Colloidal atomically-thin inorganic nanoflowers for electrocatalytic hydrogen evolution

by

Maria Sokolikova

A thesis submitted in (partial) fulfilment of the requirements

for the award of the degree

Doctor of Philosophy

from the

Imperial College London

Faculty of Engineering, Department of Materials

2019

Declaration of originality

I confirm that this Thesis, submitted in partial fulfilment of the requirements for the award of the degree of Doctor of Philosophy in the Department of Materials, Imperial College London, is a result of my own work unless referenced or acknowledged otherwise. This Thesis has not been submitted for qualifications at any other academic institution.

Maria Sokolikova

July 2019

Copyright declaration

‘The copyright of this thesis rests with the author. Unless otherwise indicated, its contents are licensed under a Creative Commons Attribution-Non Commercial 4.0 International Licence (CC BY-NC).

Under this licence, you may copy and redistribute the material in any medium or format. You may also create and distribute modified versions of the work. This is on the condition that: you credit the author and do not use it, or any derivative works, for a commercial purpose.

When reusing or sharing this work, ensure you make the licence terms clear to others by naming the licence and linking to the licence text. Where a work has been adapted, you should indicate that the work has been changed and describe those changes.

Please seek permission from the copyright holder for uses of this work that are not included in this licence or permitted under UK Copyright Law.’

Abstract

Layered metal chalcogenides include several classes of inorganic solids characterised by weak van der Waals bonding between the two-dimensional structural blocks. Bulk counterparts of layered transition metal dichalcogenides have been extensively investigated for decades for applications in catalysis and energy storage, whereas bulk pnictogen chalcogenides have attracted a significant attention due to their excellent thermoelectric properties. Following the successful isolation of graphene, the exploration of two-dimensional materials derived from bulk crystals has begun. Compared to graphene, atomically-thin sheets of layered metal chalcogenides offer a variety of disparate electronic structures, ranging from semiconductors and semimetals to topological insulators, owing to the diverse compositions and lattice symmetry of individual layers.

In order to implement the isolated layers of metal chalcogenides in novel nanoelectronics and miniaturised electrochemical devices, methods to produce two-dimensional nanosheets with high yield and in a controllable manner need to be developed. Colloidal synthesis holds a great promise for a large-scale preparation of dispersions of atomically-thin metal chalcogenide nanosheets for applications not requiring high structural perfection of the material, such as catalysis. Furthermore, wet chemical synthesis is a particularly powerful approach to obtain the material with desired morphology, crystal phase, and composition via the accurate tailoring of the precursors' reactivity. However, a controllable colloidal synthesis of metal chalcogenide nanosheets is still at a very early stage.

In this work, we design a colloidal synthesis of atomically-thin layered metal chalcogenide ($MoSe_2$, $MoTe_2$, Bi_2Te_3, WSe_2) nanoflowers from molecular precursors. We systematically investigate the effect of synthesis parameters, such as type and stoichiometry of metal precursor, coordinating solvent and growth temperature, on the morphology ($MoSe_2$) and lateral termination (Bi_2Te_3) of the colloidal branched nanosheets. We demonstrate how by optimising the precursor reactivity, the formation of chemically-unstable $MoTe_2$ and direct growth of the metastable WSe_2 polymorph can be achieved. The designed synthesis strategy was successfully modified to obtain doped material (Fe- and Cu-doped WSe_2) and ternary compositions ($W_xMo_{1-x}Se_2$), preserving the edge-rich morphology of colloidal nanoflowers. The colloidal nanoflowers were tested as a catalyst material for the hydrogen evolution reaction. Furthermore, potential improvement of the catalytic activity due to the composition variation and crystal phase engineering was examined.

Acknowledgements

I would like to thank my supervisor Dr Cecilia Mattevi for the guidance and support throughout this PhD project. The constant encouragement Cecilia provided has been of a great value. I would like to also acknowledge Dr Vincenzo Giannini for co-supervising this project.

I am especially grateful to Dr Ecaterina Ware and Dr Mahmoud Ardakani for the microscopy training and for their patient coping with the numerous knocks on their door when something miraculously was not working right. To Dr Federico Pesci for the training and assistance with the electrochemical testing, thank you. For their invaluable help with the experiments, I would like to thank Dr Peter Sherrell – for performing small-angle XRD, for assisting with the BET analysis, for numerous discussions on the catalysis results, for occasionally stealing my SEM samples from the desiccator so that the early morning microscope sessions could start on time; Mr Pawel Palczynski – for performing Raman spectroscopy on various colloidal nanoflower samples, for carrying out the XPS measurements and data analysis for the WSe_2 and ternary $W_xMo_{1-x}Se_2$ samples, for patiently unravelling the intricacy of co-existing crystal phases; Mr Mauro Och – for the XPS analysis of the $MoSe_2$ samples; Dr Victoria Bemmer – for the AFM and KPFM imaging of the semiconducting and metallic WSe_2 samples and for the guidance through data analysis.

I would like to thank all members of the Two-Dimensional Materials group, both past and present, for their friendly support and helpful discussions in the periods of (inevitable) doubts. For the great time these four years at Imperial were. Thank you.

To the crew of the Climbing Hangar and to all my climbing fellows who made sure I would not break my neck for I could have no plausible excuse to not finish this Thesis. To dear friends scattered from Daejeon to Boston who made the distance seem so infinitesimal. To my parents who never minded me hiding away from the real life for little bit longer. Thank you.

Finally, I would like to acknowledge the President's PhD Scholarship programme at Imperial College London for financial support.

Publications

Maria S. Sokolikova, Peter C. Sherrell, Pawel Palczynski, Victoria L. Bemmer, and Cecilia Mattevi, Direct solution-phase synthesis of 1T' WSe_2 nanosheets, *Nature Communications* **10** (2019), 712.

Peter C. Sherrell, Pawel Palczynski, Maria S. Sokolikova, Francesco Reale, Federico M. Pesci, Mauro Och, and Cecilia Mattevi, Large-area CVD MoS_2/WS_2 heterojunctions as a photoelectrocatalyst for salt water oxidation, *ACS Applied Energy Materials* (2019), **2**, 5877-5882.

Peter C. Sherrell, Kanudha Sharda, Chiara Grotta, Jacopo Ranalli, Maria S. Sokolikova, Federico M. Pesci, Pawel Palczynski, Victoria L. Bemmer, and Cecilia Mattevi, Thickness-dependent characterization of chemically exfoliated TiS_2 nanosheets, *ACS Omega* **3** (2018), 8655-8662.

Maria S. Sokolikova, Peter C. Sherrell, Pawel Palczynski, Victoria L. Bemmer, and Cecilia Mattevi, Room-temperature growth of colloidal Bi_2Te_3 nanosheets, *Chemical Communications* **53** (2017), 8026-8029.

Federico M. Pesci, Maria S. Sokolikova, Chiara Grotta, Peter C. Sherrell, Francesco Reale, Kanudha Sharda, Na Ni, Pawel Palczynski, and Cecilia Mattevi, MoS_2/WS_2 heterojunction for photoelectrochemical water oxidation, *ACS Catalysis* **7** (2017), 4990-4998.

Table of contents

Declaration of originality 1
Copyright declaration 2
Abstract 3
Acknowledgements 4
Publications 5
List of symbols and abbreviations 9
List of figures 13
List of tables 17
Motivation and Thesis outline 18
Chapter 1: Atomically-thin layered metal chalcogenides 21
1.1. Crystal structure of bulk layered metal chalcogenides 21
1.2. Electronic properties of atomically-thin layered metal chalcogenides 28
1.3. Application of transition metal dichalcogenides in electrocatalysis 34
1.4. Methods to produce atomically-thin transition metal dichalcogenides 39
1.4.1. Top-down approaches: Mechanical and chemical exfoliation 39
1.4.2. Bottom-up approaches: Vapour-phase and solution-phase growth 41
1.4.3. Access to the metastable crystal phases 45
Chapter 2: Experimental methodologies and characterisation techniques 49
2.1. Overview of the colloidal synthesis of semiconductor nanostructures 49
2.1.1. Spontaneous nucleation of solid phase in a supersaturated solution 50
2.1.2. Diffusion-controlled growth regime 53
2.1.3. Kinetically-controlled growth regime 55
2.1.4. Composition variation: Colloidal synthesis of hybrid nanostructures 56
2.2. Colloidal synthesis of atomically-thin layered metal chalcogenides 59
2.2.1. Experimental set-up 59
2.2.2. Choice of chalcogen precursors 60
2.2.3. Preparation of colloidal $MoSe_2$, $MoTe_2$, and WSe_2 nanostructures 62
2.2.4. Preparation of colloidal two-dimensional Bi_2Te_3 nanostructures 68
2.3. Physical characterisation techniques and instrumentation 71
2.3.1. Scanning electron microscopy 71

2.3.2. Transmission electron microscopy 74
2.3.3. Powder X-ray diffraction 81
2.3.4. X-ray photoelectron spectroscopy 83
2.3.5. Vibrational spectroscopy: Raman and Fourier transform IR spectroscopy 86
2.3.6. Optical absorption spectroscopy 89
2.3.7. Inductively-coupled plasma optical emission spectroscopy 89
2.3.8. Nitrogen adsorption 92
2.3.9. Atomic force microscopy and Kelvin probe force microscopy 93
2.3.10. Zeta-potential measurements 95
2.4. Electrocatalytic performance evaluation 97
2.4.1. Preparation of working electrodes 97
2.4.2. Electrochemical testing in a three-electrode cell 97
2.4.2.1. Experimental set-up 97
2.4.2.2. Linear sweep voltammetry and Tafel analysis 98
2.4.2.3. Electrochemical impedance spectroscopy 101
2.4.3. Optimisation of the electrode durability testing conditions 103
Chapter 3: Colloidal synthesis of inorganic metal chalcogenide nanoflowers 107
3.1. Colloidal $MoSe_2$ and $MoTe_2$ nanoflowers 107
3.1.1. Structural characterisation of $MoSe_2$ and $MoTe_2$ nanoflowers 108
3.1.2. Parametric study of the growth conditions: Colloidal $MoSe_2$ nanoflowers 113
3.1.3. Parametric study of the growth conditions: Colloidal $MoTe_2$ nanostructures 117
3.2. Colloidal Bi_2Te_3 branched nanosheets 124
3.2.1. Growth-temperature-dependent morphology of colloidal Bi_2Te_3 nanosheets 124
3.2.2. Lateral termination and insights into the growth mechanism 132
3.2.3. Effect of bismuth precursor stoichiometry on the morphology of Bi_2Te_3 nanostructures 139
3.3. Colloidal WSe_2 nanoflowers 142
3.3.1. Structural characterisation of WSe_2 nanoflowers 142
3.3.2. Conversion to the thermodynamically stable phase 148
3.3.3. Parametric study of the synthesis conditions: Insights into the growth mechanism 154
3.4. Conclusions 161

Chapter 4: Doped WSe_2 and ternary $W_xMo_{1-x}Se_2$ nanostructures 162
4.1. Doped WSe_2 nanoflowers 162
4.2. Ternary $W_xMo_{1-x}Se_2$ nanoflowers 168
4.3. Conclusions 176
Chapter 5: Application in electrochemical devices 177
5.1. Approaches to assemble colloidal TMD nanostructures on conductive supports for electrocatalytic hydrogen reduction 177
5.2. Phase engineering for improved catalytic performance: 1T' WSe_2 183
5.3. Ternary $W_xMo_{1-x}Se_2$ alloys for electrocatalytic hydrogen reduction 187
5.4. Efficiency of colloidal TMD nanosheets for catalytic hydrogen reduction 192
5.5. Stability of the active material under electrochemical testing conditions 195
5.6. Conclusions 198
Chapter 6: Concluding remarks and outlook 199
6.1. Concluding remarks 199
6.2. Future work 201
6.2.1. Solution-phase synthesis of atomically-thin binary metal chalcogenides 201
6.2.2. Composition variation via a solution-phase processing 202
6.2.3. Application in heterogeneous catalysis 202
Bibliography 203
Appendix 225
A1. List of $MoSe_2$ samples 225
A2. List of $MoTe_2$ samples 226
A3. List of WSe_2 samples 227
A4. List of Bi_2Te_3 samples 229
A5. Full list of publications 231
A6. Permissions to reuse content 233

List of symbols and abbreviations

α	Charge transfer coefficient
β	Broadening of a diffraction peak or of a spectral line
ε	Molar absorption coefficient, cm^2/mol
η	Overpotential, mV
θ	Incidence or diffraction angle, ^{o}
λ	Wavelength, nm
μ	Chemical potential
ν	Wavenumber, cm^{-1}, or frequency, Hz
σ, γ	Surface energy, J/m^2
υ, υ_m	Volume of adsorbed gas (volume of adsorbed monolayer), m^3
ϕ	Work function, eV
A	Absorbance
ABF	Annular bright-field [imaging, detector]
ac	Acetate
AC	Alternating current
acac	Acetylacetonate
ADF	Annular dark-field [imaging, detector]
AFM	Atomic force microscopy
AR	Angle-resolved [UPS and PES]
ATR	Attenuated total reflection
BET	Brunauer–Emmett–Teller [theory]
BF	Bright-field [imaging, detector]
BSE	Backscattered electron
C	Concentration, mol/L
C_{dl}	Double-layer capacitance, F
CB	Conduction band
CDW	Charge density wave
CE	Counter [auxiliary] electrode
CF	Carbon foil
CP	Carbon paper
CPD	Contact potential difference, V

CVD	Chemical vapour deposition [reaction]
C(V)T	Chemical (vapour) transport [reaction]
d_{hkl}	Interplanar distance for a set of (*hkl*) planes, nm
DC	Direct current
DF	Dark-field [imaging, detector]
DFT	Density functional theory
E	Energy [kinetic, binding], eV
E	Applied potential, V (vs RE)
E^{o}	Standard electrode potential, V
E_F	Fermi level, eV
E_g	Band gap, eV
ECSA	Electrochemically-accessible(active) surface area
EDL	Electric double layer
EDS (EDX)	Energy-dispersive X-ray spectroscopy
EIS	Electrochemical impedance spectroscopy
F	Faraday constant, ~96485 C/mol
FE(G)	Field emission (gun)
FFT	Fast Fourier transform
FTIR	Fourier-transform infrared spectroscopy
ΔG	Gibbs free energy, J
h	Planck constant, $\sim 6.626 \times 10^{-34}$ J/s
HAADF	High-angle annular dark-field [imaging, detector]
HER	Hydrogen evolution reaction
HMDS	Hexamethyldisilazane
I	Intensity (radiant flux), W
ICDD	International centre for diffraction data [database]
ICP OES	Inductively-coupled plasma optical emission spectroscopy
IR	Infrared [light, spectral region]
j	Total angular momentum
j	Catalytic current density, mA/cm^2
j_0	Exchange current density, mA/cm^2
k	Boltzmann constant, $\sim 1.38 \cdot 10^{-23}$ J/K
KPFM	Kelvin probe force microscopy

l	Orbital angular momentum
L	Optical path, cm
LSV	Linear sweep voltammetry
MBE	Molecular beam epitaxy
n-BuLi	*n*-butyllithium
N_A	Avogadro constant, ~6.022×10^{23} mol^{-1}
ND	Nanodisk
NF	Nanoflower
NP	Nanoparticle
NS	Nanosheet
OctAm	Octylamine
ODE	Octadecene
OlAc	Oleic acid
OlAm	Oleylamine
p	Partial pressure, Pa
PES, UPS	Photoelectron spectroscopy, ultra-violet photoelectron spectroscopy
Ph	Phenyl
PMMA	Poly(methyl methacrylate)
PSD	Position sensitive detector
PVT	Physical vapour transport [reaction]
r	Radius [of a nanoparticle or a crystalline domain], m
R	Ideal gas constant, 8.314 J/[mol·K]
R_c	Charge transfer resistance, Ω
R_s (R_u)	Solution (uncompensated) resistance, Ω
RE	Reference electrode
RHE	Reversible hydrogen electrode
s	Spin
s	Adsorption cross-section, m^2
S	Supersaturation
S	Specific surface area, m^2/g
SAED	Selected area electron diffraction
SDD	Silicon drift detector
SE	Secondary electron

SEM	Scanning electron microscopy
SERS	Surface-enhanced Raman scattering [or spectroscopy]
SSA	Specific surface area (m^2/g)
StAc	Stearic acid
STEM	Scanning transmission electron microscopy
STM	Scanning tunnelling microscopy
t	[Sample] thickness, nm
T	Absolute temperature, K
T_b	Boiling point, ºC
T_m	Melting point, ºC
TDPA	Tetradecylphosphonic acid
TEM	Transmission electron microscopy
TERS	Tip-enhanced Raman spectroscopy
TI	Topological insulator
TMD(s)	Transition metal dichalcogenide(s)
TOP(O)	Trioctylphosphine (oxide)
UHV	Ultra-high vacuum
UV	Ultraviolet [light, spectral region]
ΔV	Potential difference or potential window, V
VB	Valence band
V_m	Molar volume, m^3/mol
WE	Working electrode
XPS	X-ray photoemission spectroscopy
XRD	[Powder] X-ray diffraction
Z	Atomic number
Z	Electrical impedance, Ω
ZA	Zone axis

List of figures

Figure 1.1. Structural polymorphs of the group VIB TMDs. 23

Figure 1.2. Bismuth tellurides. 26

Figure 1.3. Band structure of the 2H group VIB TMDs 29

Figure 1.4. Schematic illustration of the formation of topologically non-trivial phases as represented by the dispersions of the bulk states 31

Figure 1.5. Intrinsic activity of TMDs for the electrocatalytic HER 35

Figure 2.1. Formation of colloidal nanocrystals in supersaturated solution 50

Figure 2.2. Diagram illustrating the dependence of a nanocrystal growth rate on its radius 54

Figure 2.3. Comparative sketches of possible formation mechanisms of the hybrid nanoarchitectures via the wet-chemistry approaches 57

Figure 2.4. Schlenk line used for solution-phase synthesis of the air-sensitive materials 60

Figure 2.5. Chalcogen precursors TOP:Se and TOP:Te 61

Figure 2.6 Tungsten molecular precursor 63

Figure 2.7. Transition metal complexes formed in various long-chain organic solvents 65

Figure 2.8. Modification of the tungsten precursor 66

Figure 2.9. Stoichiometric bismuth oleate used as the metal precursor in synthesis of the Bi_2Te_3 nanosheets 69

Figure 2.10. Basic principles of scanning electron microscopy 71

Figure 2.11. Basic principles of transmission electron microscopy 75

Figure 2.12. Basic operation modes of a transmission electron microscope 77

Figure 2.13. Analysis of the SAED and HR TEM data 79

Figure 2.14. Basic principles of X-ray photoelectron spectroscopy 84

Figure 2.15. A simplified diagram showing the transitions between the electronic and vibrational states 87

Figure 2.16. ICP calibration curves. 91

Figure 2.17. Contact potential difference in KPFM. 94

Figure 2.18. Simplified illustration of an electric double layer formed on the surface of a colloidal particle. 96

Figure 2.19. Assessment of the catalytic performance of the colloidal $W_xMo_{1-x}Se_2$ (x = 0-1) nanosheets 99

Figure 2.20. Modelling the potentiostatic EIS data 103

Figure 2.21. Structural characterisation of the WSe_2 working electrode after 3000 catalytic cycles....104

Figure 2.22. Optimisation of the electrochemical set-up for the long-term stability testing....105

Figure 3.1. Morphology of the colloidal $MoSe_2$ hierarchical nanostructures....109

Figure 3.2. Structural characterisation of the colloidal $MoSe_2$ nanosheets....110

Figure 3.3. Structural characterisation of the colloidal $MoTe_2$ nanostructures....112

Figure 3.4. Effect of molybdenum precursor on morphology of the colloidal $MoSe_2$ nanostructures....114

Figure 3.5. Effect molybdenum complex on morphology and crystal phase purity of the colloidal $MoSe_2$ nanostructures....115

Figure 3.6. Effect of other growth parameters on morphology of the colloidal $MoSe_2$ nanostructures....116

Figure 3.7. Effect of the transition metal precursor on the composition of the final product in the synthesis of $MoTe_2$....118

Figure 3.8. Effect of the type of solvent on the composition of the final product in the synthesis of $MoTe_2$....120

Figure 3.9. Effect of the order of mixing of the precursors on the composition of the final product in the synthesis of $MoTe_2$....121

Figure 3.10. Morphology of the colloidal Bi_2Te_3 nanosheets....125

Figure 3.11. Recrystallisation of the Bi_2Te_3 branched nanosheets observed upon annealing in solution phase....127

Figure 3.12. Stoichiometry of the bismuth telluride branched nanosheets....130

Figure 3.13. Surface oxidation of the Bi_2Te_3 nanosheets....132

Figure 3.14. Surface morphology of the Bi_2Te_3 nanosheets....134

Figure 3.15. Lateral sides of the Bi_2Te_3 branched nanoplatelets....137

Figure 3.16. Branching in the colloidal Bi_2Te_3 nanosheets....138

Figure 3.17. The effect of the bismuth precursor stoichiometry on morphology of the Bi_2Te_3 nanostructures produced at high temperature (170 ^oC)....140

Figure 3.18. The effect of the bismuth precursor stoichiometry on morphology of the Bi_2Te_3 nanostructures produced at low temperature (50 ^oC)....141

Figure 3.19. Morphology of the colloidal WSe_2 nanosheets....142

Figure 3.20. Insights into the branching observed in the colloidal WSe_2 nanostructures....143

Figure 3.21. TEM characterisation of the 1T' WSe_2 nanosheets....145

Figure 3.22. Surface distortion of the 1T' phase....146

Figure 3.23. Stability of the 1T' WSe_2 phase under TEM imaging conditions....147

Figure 3.24. Stability of the 1T' phase under ambient conditions in solution 149

Figure 3.25. 1T' to 2H phase conversion upon thermal annealing of the WSe_2 nanoflowers. 150

Figure 3.26. Phase purity of the as produced and thermally converted WSe_2 nanoflowers .. 151

Figure 3.27. Structural characterisation of the as produced and the annealed WSe_2 nanoflowers 152

Figure 3.28. Effect of various growth conditions on the crystal phase and morphology of the colloidal WSe_2 nanostructures 155

Figure 3.29. Effect of activity of tungsten complex on the crystal phase and morphology of the colloidal WSe_2 nanostructures 156

Figure 3.30. Effect of the precursor concentration on the crystal phase of WSe_2 nanostructures 158

Figure 3.31. Evidence of absence of the intercalated charged species 160

Figure 4.1. Cu-doped colloidal WSe_2 nanoflowers 164

Figure 4.2. Fe-doped colloidal WSe_2 nanoflowers 165

Figure 4.3. Crystal phase of the doped WSe_2 nanoflowers..... 166

Figure 4.4. Characterisation of the alloyed $W_xMo_{1-x}Se_2$ (x ~0.5) nanoarchitectures 170

Figure 4.5. Comparison of the $MoSe_2$ and $W_xMo_{1-x}Se_2$ (x ~0.5) branched nanosheets 171

Figure 4.6. TEM characterisation of the $W_xMo_{1-x}Se_2$ (x ~0.5) nanoflowers 172

Figure 4.7. Structural characterisation of the alloyed $W_xMo_{1-x}Se_2$ (x ~0.5) nanoflowers 173

Figure 4.8. XPS study of the produced $W_xMo_{1-x}Se_2$ nanoflowers..... 175

Figure 5.1. Working electrodes produced via drop-casting of the active material (colloidal WSe_2 nanoflowers) onto a functional substrate (CP) 178

Figure 5.2. Bottom-up synthesis of the TMD nanosheets growing directly on functional substrates..... 179

Figure 5.3. Working electrodes produced via direct growth of the active material (WSe_2 nanosheets) on a functional substrate (CP)..... 180

Figure 5.4. Comparison of catalytic performance of the WSe_2 working electrodes produced via drop-casting and via direct growth of active material on CP..... 181

Figure 5.5. Structural characterisation of the as produced 1T’ and the converted 2H WSe_2 working electrodes 184

Figure 5.6 Electronic properties of the few-layered 1T' and 2H WSe_2 nanoflowers..... 185

Figure 5.7. Comparison of catalytic activity of the 1T’ and 2H WSe_2 working electrodes .. 186

Figure 5.8. Structural characterisation of the as produced $W_xMo_{1-x}Se_2$ (x = 0-1) working electrodes 188

Figure 5.9. Comparison of catalytic performance of the $W_xMo_{1-x}Se_2$ (x = 0-1) working electrodes 190

Figure 5.10. Effect of the catalyst mass loading on performance of the working electrodes. 192

Figure 5.11. Comparison with the reported group VIB TMD electrocatalysts. 193

Figure 5.12. Change in morphology of the active material after a short (10-20 cycles) electrochemical testing..... 195

Figure 5.13. Durability test of the WSe_2 on CP working electrodes for the HER 196

List of tables

Table 1. Crystal structure parameters of bulk group VIB TMD polymorphs.....25

Table 2. Lattice parameters of the $(Bi_2)_m(Bi_2Te_3)_n$ phases. 27

Table 3. Band structure parameters of the semiconducting group VIB TMDs. 30

Table 4. Recent advances in colloidal synthesis of the group VIB TMDs. 44

Table 5. Experimental parameters varied in colloidal synthesis of the $MoSe_2$, $MoTe_2$, and WSe_2 nanosheets. 67

Table 6. Experimental parameters varied in colloidal synthesis of the Bi_2Te_3 nanosheets. 70

Table 7. Quantitative analysis of the free-standing TMD nanoflower samples and the TMD nanosheets grown on carbon paper (CP). 92

Table 8. Main characteristics of the $W_xMo_{1-x}Se_2$@CP working electrodes. 189

Motivation and Thesis outline

Developing the experimental approaches to obtain single- and few-layered metal chalcogenide nanosheets is essential for their successful implementation in novel lightweight electronics [1,2] and miniaturised energy storage devices and electrolyzers [3–5]. Moreover, certain characteristics of the final product, such as planar or hierarchal morphology, presence or absence of structural defects, and crystal phase purity, have to be pinpointed in order to target a specific practical application. In the past 30 years, a tremendous progress has been made in developing chemical and physical methods to obtain atomically-thin metal chalcogenide nanostructures. Thus, methods based on a chemical reaction and deposition from vapour phase allow synthesis of metal chalcogenide monolayers with high crystal quality and over a large area, although typically on resistive substrates, which implies arduous transfer processes for the envisioned application in electrocatalysis. Free-standing nanosheets can be obtained by cleavage from bulk counterparts, however, such exfoliation methods generally lack control over the achievable size (thickness) distribution. It is emerging that colloidal synthesis approach based on a direct reaction between the molecular precursors in solution phase can potentially allow controlling the dimensionality and morphology of growing material at atomic scale. Colloidal approach has been developed for the synthesis of monodisperse metal and semiconductor nanoparticles but remains challenging for the layered metal chalcogenides. Therefore, the aim of this PhD project was to design a reliable colloidal synthesis procedure, allowing growing and nanostructuring of the atomically-thin layered metal chalcogenides ($MoSe_2$, $MoTe_2$, Bi_2Te_3, and WSe_2) in solution phase.

In Chapter 1 of this Thesis, we provide a general overview of the layered transition metal dichalcogenide and pnictogen chalcogenide crystals. In particular, structural polymorphism of the group VIB transition metal dichalcogenides (TMDs) is discussed in conjunction with the related diversity of electronic properties. In the monolayer limit, the electronic properties of transition metal dichalcogenides differ considerably from that of the corresponding bulk phases. Recently, their monolayer counterparts have been identified as suitable catalysts for the hydrogen evolution reaction (HER) with the predicted intrinsic activities close to that of the Pt-group metals. Moreover, it has been experimentally demonstrated that the metastable polymorphs, such as the 1T(1T') phases of the group VIB TMDs, exhibit higher catalytic activity for the HER compared to the thermodynamically stable phases. We then summarise the experimental top-down and bottom-up approaches that allow synthesising atomically-thin

nanosheets of layered metal chalcogenides with a particular emphasis on approaches to the metastable polymorphs. Among these, we identify colloidal synthesis, that is just emerging for the group VIB TMD family, as especially appealing for acquiring the material compatible with the majority of processing and deposition techniques for applications in catalysis. Compared to other approaches, colloidal synthesis allows nanostructuring the free-standing material via controlling the rate of the reaction between molecular precursors.

In Chapter 2, we describe the theoretical basis of the homogeneous nucleation of solid phase from a supersaturated solution. We introduce the concepts of thermodynamically- and kinetically-driven growth processes. This allowed us to design the experimental set-up and synthesis conditions, including the choice of molecular precursors, suitable for acquiring atomically-thin $MoSe_2$, $MoTe_2$, Bi_2Te_3, and WSe_2 nanostructures in colloidal solution. Further, we cover the microscopic and spectroscopic characterisation techniques performed to investigate the morphology, crystal structure, and electronic properties of the obtained colloidal nanoflowers and the electrochemical methodologies used to assess their catalytic activity for the HER.

The development of a reaction between molecular precursors to grow binary metal chalcogenide ($MoSe_2$, $MoTe_2$, Bi_2Te_3, and WSe_2) nanoflowers in solution phase is covered in Chapter 3. These binary metal chalcogenides were obtained in the form of colloidal suspensions of edge-rich nanoflowers composed of atomically-thin petals. In order to identify the optimal synthesis conditions, we performed a parametric study varying the reactivity of molecular precursors, growth time and temperature. We suggest that the reaction conditions can be modified in such a way that the nanocrystal growth preferentially occurs in the kinetically-controlled regime. In particular, performing the growth at temperatures ranging from 20 to 170 ^{o}C allowed us to effectively control the supersaturation in the growth medium that led to controllable tailoring of the morphology of Bi_2Te_3 nanostructures from highly anisotropic to nearly equilibrium shapes. Moreover, tuning the reactivity of molecular precursors can be employed to regulate the reaction rate and therefore the kinetics of nanocrystal growth in colloidal solution. We propose that this can facilitate the formation of the metastable polymorphs provided that the energy difference between the polymorphs is relatively low, as was demonstrated in the case of colloidal WSe_2 and $MoTe_2$ nanostructures.

The solution-phase synthesis approach was further modified to alter the composition of the growing material through substitutional doping or formation of ternary alloys. This is

particularly important for enhancing the catalytic activity of the material due to modulation of its electronic structure. In Chapter 4, we demonstrate that compositional variation can be achieved during the solution-phase reaction, while preserving the overall edge-abundant morphology of the colloidal nanoflowers. In particular, we demonstrate the synthesis of doped (Cu, Fe) WSe_2 nanoflowers and ternary $W_xMo_{1-x}Se_2$ branched nanosheets.

In Chapter 5, we discuss the electrocatalytic performance of the atomically-thin TMD nanosheets produced by the colloidal method. We demonstrate that the material in the form of atomically-thin nanosheets can be grown directly on functional substrates, preserving the crystal phase and composition. Compared to other group VIB transition metal disulphides and diselenides reported for the electrocatalytic HER, colloidal WSe_2 and $MoSe_2$ nanosheets outperform the mechanically exfoliated counterparts and exhibit catalytic activities comparable to that of the chemically exfoliated nanosheets. Further, we discuss how achieving the metastable metallic phases or ternary compositions can be beneficial to enhance the activity of group VIB TMD nanostructured electrocatalysts.

Chapter 1:
Atomically-thin layered metal chalcogenides

Layered metal chalcogenides are a family of inorganic functional materials that are being extensively investigated for applications ranging from opto- and nanoelectronics [6,7] to electrocatalysis [8] and miniaturised electrochemical energy storage devices [3]. The electronic properties of two-dimensional layered crystals are strongly related to the number and the symmetry of individual layers, realising a variety of achievable band structures from direct and indirect gap semiconductors [9] to semimetals [10] and topological insulators [11,12]. Additionally, these are affected by structural defects [13] and non-stoichiometry [14] of the respective materials. In this Chapter, we provide an overview of layered metal chalcogenide crystals, their structural polymorphism, and electronic properties. Further, we discuss the potential of implementing layered transition metal dichalcogenides as active materials for the electrocatalytic hydrogen generation process. Finally, we compare different preparation methods, allowing for the controllable production of two-dimensional crystals of layered metal chalcogenides essential for majority of applications.

1.1. Crystal structure of bulk layered metal chalcogenides

Various families of inorganic compounds, such as aluminium phyllosilicates (clays), transition metal carbides and nitrides (MXenes), transition metal chalcogenides and oxides, and layered double hydroxides, possess lamellar crystal structure, exhibiting structural anisotropy along at least one crystallographic direction. Transition metal dichalcogenides (TMDs) are a class of binary compounds with the general formula ME_2, where M is a transition metal from groups IVB-VIIIB and E is a chalcogen (S, Se, or Te). Among them, group IVB–VIIB TMDs form layered structures, whereas group VIIIB TMDs are non-layered compounds [15]. Structurally, layered TMDs can be described as a stack of three-atom thick layers consisting of transition metal atoms sandwiched between two layers of chalcogen atoms [16]. The intralayer bonds between transition metal and chalcogen atoms are covalent in nature, and individual slabs are held together by weak van der Waals bonds.

TMDs display a rich variety of structural polymorphs defined by the coordination geometry of transition metal atoms. Under normal conditions, the thermodynamically stable polymorph of the majority of group VIB TMDs is the 2H phase, where H stands for the hexagonal syngony, and the integer indicates the number of single layers in a unit cell of bulk

crystal. Single layers comprising the bulk hexagonal 2H phase are commonly denoted as 1H. Characteristic to the 2H phase is the trigonal-prismatic coordination of transition metal atoms (point group D_{3h}) as shown in Figure 1.1.a. Related to the hexagonal 2H phase, the trigonal 1T structure can be visualised as a 2H three-atom thick E-M-E slab distorted along the [210] crystallographic direction owing to the gliding of one of the chalcogen planes by $\frac{a}{\sqrt{3}}$ so that the metal centres adopt perfect octahedral coordination (point group O_h) as shown in Figure 1.1.e. The crystallographic projections along the *b* (side view) and *c* (top view) axes of the 1H and 1T single layers are shown in Figure 1.1.b,f.

The preferred coordination polyhedron can be inferred from the electron count on the *d*-orbitals of the corresponding transition metal. According to the crystal field theory, in a bulk crystal, the degeneracy of the five *d*-orbitals of a transition metal is broken due to interaction with the electrostatic field of surrounding anions. In the octahedral field, the *d*-orbitals split into two sets, where the lower in energy d_{xy}, d_{xz}, and d_{yz} orbitals form the t_{2g} level, while the higher in energy $d_{x^2-y^2}$ and d_{z^2} compose the e_g, level [17]. In the trigonal-prismatic coordination, the d_{z^2} orbital becomes the lowest in energy followed by the $d_{x^2-y^2}$ and d_{xy} orbitals and then by the d_{xz} and d_{yz} orbitals. Calculations have demonstrated that the d_{z^2} level in the hexagonal 2H phase is lower in energy than the t_{2g} level in the 1T phase [18]. Progressive filling of the *d*-orbitals with the valence electrons determines the relative stability of the hexagonal and trigonal polymorphs, changing as the transition metal atomic number increases across a period. The 1T polymorph is preferred for the group IVB TMDs (d^0), while the group VB TMDs with 1 electron on the *d*-orbitals of each transition metal centre are found in both trigonal 1T and hexagonal 2H phases. In the case of the group VIB TMDs, accommodating two valence electrons on the non-bonding d_{z^2} level of the trigonal-prismatic phase is energetically more favourable than on the t_{2g} level of the octahedral phase, rendering the 2H polymorph thermodynamically stable [15,19]. That is confirmed by the first principle calculations with the only exception being bulk WTe_2 [20]. Due to the increased metal-metal interaction in bulk WTe_2, tungsten cations are displaced from the centres of the coordination polyhedra, forming a distorted octahedron as shown in Figure 1.1.h [10,21]. This minimum energy configuration is referred to as the distorted octahedral polymorph. Adding more valence electrons on the *d*-orbitals of transition metal destabilises the trigonal-prismatic coordination and the group VIIB TMDs crystallise in the trigonal 1T structure [15].

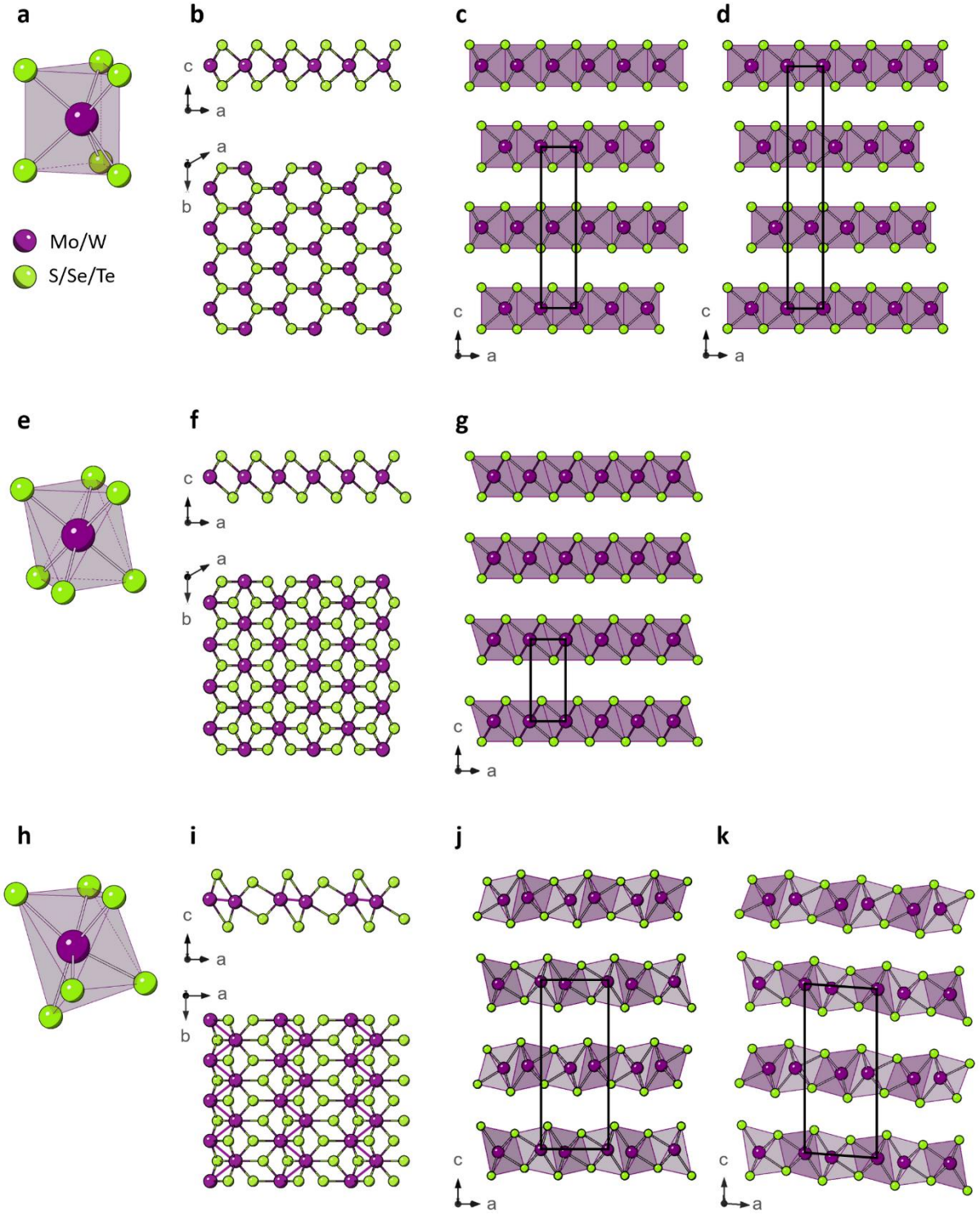


Figure 1.1. Structural polymorphs of the group VIB TMDs. **a, e, h** Coordination polyhedra around transition metal atoms in the 1H (trigonal prism, **a**), 1T (octahedron, **e**), and the distorted 1T (distorted octahedron, **h**) phases. **b, f, i** Schematic representation of the 1H, 1T, and 1T' single layers, respectively. Crystal structures are given in two projections: side view (lateral plane) and top view (basal plane); purple balls represent transition metal atoms, green balls – chalcogen atoms. **c, d, g, j, k** Bulk polymorphs produced by stacking the 1H, 1T, and 1T' single layers along the *c* axes corresponding to the hexagonal 2H (**c**), rhombohedral 3R (**d**), trigonal 1T (**g**), orthorhombic T_d (also known as the γ phase of $MoTe_2$, **j**), and monoclinic T' (also known as the β phase of $MoTe_2$, **k**) bulk phases. Black solid rectangles in panels **c, d, g, j, k** show the unit cells.

Electron transfer, for example during chemical treatment [22] or upon electrostatic gating [23], leads to an increase in electron count on the metal centres, destabilising the trigonal-prismatic coordination of the 2H phase and causing structural transformation into the octahedral 1T phase [24]. The 2H-to-1T phase transition due to accumulation of negative charge was also observed *in situ* under the continuous electron beam scanning during STEM imaging [25]. In single-layered MoS_2 nanosheets, the transition occurs through the initial formation of numerous non-parallel molybdenum zigzag chains that is followed by the chalcogen plane gliding, reducing mechanical strain and forming a domain of the trigonal 1T phase.

Unless stabilised externally by adsorbed charged species, the perfect octahedral 1T phase is the least stable phase of the group VIB TMDs [20,12]. It is prone to structural distortions, leading to clustering of transition metal atoms caused by charge density waves (CDW) [26]. Different distorted 1T structures were proposed in literature on the chemically exfoliated MoS_2 and WS_2. The most common superstructures are caused by either tetramerization ($2a \times 2a$), or trimerization ($a\sqrt{3} \times a\sqrt{3}$) of the transition metal atoms or by zigzag chain ($2a \times a$) formation. Scanning tunnelling microscopy (STM) studies of the chemically exfoliated group VIB disulphide single layers have clearly demonstrated a $2a \times a$ superstructure in the *ab* plane [26–29]. The distorted octahedral configuration of the TMD single layers with zigzag chains running through the structure is known as the 1T' polymorph (Figure 1.1.i). Three-dimensional arrangement of the 1T' single layers leads to crystals with the orthorhombic (space group $P\,nm2_1$) or monoclinic (space group $P\,2_1/m$) symmetry, depending on the stacking order (Figure 1.1.j,k). Bulk WTe_2 is found in the orthorhombic polymorph, which is referred to as the T_d phase, while $MoTe_2$ exists in the monoclinic polymorph (β-phase) at temperatures above 900 °C [30]. The higher symmetry orthorhombic T_d polymorph (γ-phase) of $MoTe_2$ can be obtained by cooling the monoclinic T' (β-) phase down to cryogenic temperatures [10,31,32] or can be stabilised at room temperature via substitutional doping with tungsten [33]. On the other hand, the T_d polymorph of WTe_2 can be transformed into the lower symmetry T' phase at pressure over 15.5 GPa [34,35]. For molybdenum and tungsten disulphides and diselenides, the 1T' polymorph is metastable under ambient conditions and can only be obtained under specific experimental conditions [20].

Similar polytypism, occurring due to variations in the stacking order of 1H single layers, leads to the hexagonal 2H (space group $P\,6_3/mmc$) and rhombohedral 3R (space group $R\,3m$) bulk phases presented in Figure 1.1.c,d. In the bulk 2H phase, two consecutive layers are shifted in such a way that the chalcogen atoms of the first layer are aligned with the transition metal

atoms of the second layer (AbA BaB). Analogously, the stacking sequence of the 3R phase can be written as AbA CaC BcB. Unlike the case of the 1H and 1T' single layers, there is only one stacking polytype reported for the 1T single layers [36]. In the bulk 1T phase (space group $P\,\bar{3}m1$), the transition metal atoms of two consecutive layers are located directly above one another as shown in Figure 1.1.g. The lattice parameters of the group VIB TMD polymorphs are summarised in Table 1.

A key symmetry characteristic defining the electronic and optical properties of various TMD polymorphs is the presence or absence of the inversion symmetry. The 3R and T_d bulk polymorphs are non-centrosymmetric, i.e. do not contain inversion symmetry centres, while the 2H and T' bulk phases are centrosymmetric [31,37]. In the case of the 2H phase, the inversion symmetry can be broken as the material is thinned down to a single layer since the 1H monolayer is non-centrosymmetric. Both the 1T and 1T' single layers and the 1T bulk polymorph are centrosymmetric. The lack of spatial inversion symmetry is critically important for potential observation of the exotic physical phenomena, e.g. Weyl fermions [31,38]. This also affords applications in non-linear optics, for example for the second harmonic generation [39].

Table 1. Crystal structure parameters of bulk group VIB TMD polymorphs. The cell parameters $a=b\neq c$ and α=β=90°, γ=120° in 2H, 3R phases; $a\neq b\neq c$ and α=β=γ=90° in T_d phase; $a\neq b\neq c$ and α=γ=90°, β≠90° in T' phase. M-M is a distance between two nearest metal atoms within one layer, layer thickness (h) is a height of the E-M-E slab, and interlayer distance (d) is a length of the van der Waals E-E bond.

Material	**Phase**	**Lattice constants**				M-M, Å	h, Å	d, Å	**Ref.**
		a, Å	b, Å	c, Å	β				
MoS_2	2H	3.16		12.294			3.19	3.47	[40]
	3R	3.164		18.39			3.15	3.50	
	1T'	5.716	3.181	?	?				[41]
WS_2	2H	3.153		12.323		3.153	3.14	3.53	[19]
	3R	3.158		18.49		3.158	3.13	3.54	
$MoSe_2$	2H	3.288		12.92			3.23	3.75	[40]
	3R	3.292		19.392					
	1T'	5.98	3.25	?	?				[42]
WSe_2	2H	3.282		12.96		3.282	3.34	3.67	[19]
	1T'	5.8	3.3	?	?				[43]
$MoTe_2$	2H (α)	3.519		13.966		3.52	3.60	3.95	[10]
	T'(β)	6.33	3.469	13.86	93.55	2.9	3.49	~3.88	[10]
		6.358	3.493	14.207	93.44				[31]
	T_d (γ)	6.33	3.469	13.83		2.87	3.48	3.86	[10]
		6.304	3.458	13.859					[38]
WTe_2	2H[1]	3.600		14.18		3.60	3.66	4.01	[10]
	T_d	6.282	3.496	14.07		2.86	3.52	3.93	

[1] Lattice parameters provided for the ideal 2H-WTe_2 are the calculated ones.

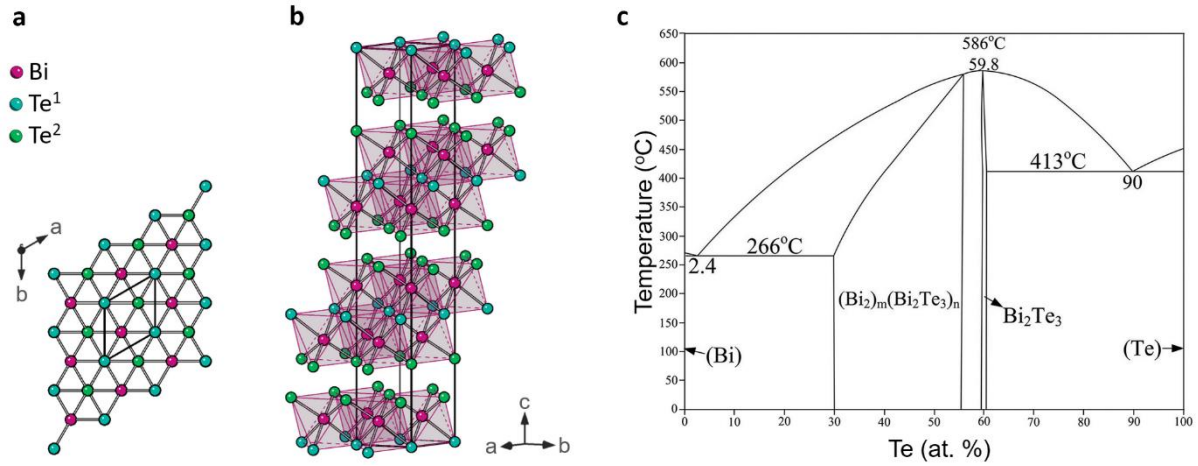


Figure 1.2. Bismuth tellurides. **a, b** Crystal structure of Bi_2Te_3viewed along the *c* axis (panel **a**) and the three-dimensional stacking of Bi_2Te_3 quintuple layers forming bulk phase (panel **b**). The hexagonal unit cell is denoted by black parallelepiped. **c** *T-x* section of the *P-T-x* phase diagram of the binary Bi-Te system, showing a series of the $(Bi_2)_m(Bi_2Te_3)_n$ phases; $(Bi_2)_m(Bi_2Te_3)_n$ phases are grouped together for clarity. Reprinted from [32], with permission from Elsevier. Copyright © 2017.

Pnictogen (Sb, Bi) chalcogenides are another class of layered binary compounds, sharing the tetradymite crystal structure shown in Figure 1.2.a,b. Bulk Bi_2Te_3 crystals belong to the rhombohedral syngony (space group $R\,\bar{3}m$) and are composed of quintuple Te^2-Bi-Te^1-Bi-Te^2 layers stacked along the *c* axis; the superscripts denote two different Te sites. Within one quintuple layer, Bi and Te atoms are covalently bound, while van der Waals interactions between the Te^2 atoms ensure binding of the adjacent layers.

Unlike bulk TMDs, bismuth tellurides do not display polytypism. Instead, depending on the synthesis conditions, they tend to form numerous $(Bi_2)_m(Bi_2Te_3)_n$ phases, which can be represented as an ordered sequence of Bi_2 bilayers inserted in van der Waals gaps between individual Bi_2Te_3 quintuple layers [44,45]. The integers *m* and *n* denote the number of corresponding Bi_2 and Bi_2Te_3 blocks in a unit cell. Accordingly, pristine Bi_2Te_3 phase can be represented as $(Bi_2)_0(Bi_2Te_3)_3$. The $(Bi_2)_m(Bi_2Te_3)_n$ phases exist in a wide range of compositions, where bismuth fraction varies from 0.4 to 1.0 [14]. This is illustrated by the *T-x* section of the *P-T-x* phase diagram of Bi-Te binary system in Figure 1.2.c. The known Bi-Te phases include Bi_2Te_3, Bi_4Te_5, BiTe, Bi_4Te_3, Bi_2Te, Bi_7Te_3, and Bi, while other predicted members, such as $Bi_{10}Te_9$, have not been obtained experimentally yet [14,45]. Tsumoite BiTe and pilsenite Bi_4Te_3 phases are the most common examples among the $(Bi_2)_m(Bi_2Te_3)_n$ homologous series. The unit cell of the BiTe phase is formed by [Bi_2Te_3-Bi_2-Bi_2Te_3] blocks stacked along the *c* axis, while in the Bi_4Te_3 phase the repeating sequence can be expressed as [Bi_2Te_3-Bi_2-Bi_2Te_3-Bi_2-Bi_2Te_3-Bi_2]. Structural parameters of the $(Bi_2)_m(Bi_2Te_3)_n$ phases discussed within this work are provided in Table 2.

Table 2. Lattice parameters of the $(Bi_2)_m(Bi_2Te_3)_n$ phases. For the rhombohedral $R\,\bar{3}m$ phases, the lattice parameters are that of the hexagonal unit cells, i.e. $a = b \neq c$ and $\alpha = \beta = 90^o$, $\gamma = 120^o$.

$(Bi_2)_m(Bi_2Te_3)_n$ phase	*m*:*n*	Space group	Lattice constants		Ref.
			a, Å	*c*, Å	
Bi_2Te_3	0:3	$R\,\bar{3}m$	4.384	30.45	[46]
BiTe	1:2	$P\,\bar{3}m1$	4.423	24.002	[47]
Bi_4Te_3	3:3	$R\,\bar{3}m$	4.451	41.888	[47]
Bi_2Te	2:1	$P\,\bar{3}m1$	4.4733	17.805	[2]

To date, only Bi_2Te_3 and Bi compounds have been extensively investigated, while the intermediate Bi-Te phases remain majorly unexplored. However, the precise control over [Bi]:[Te] stoichiometry and ordering of the corresponding structural blocks were suggested to be promising for the thermoelectric properties engineering and for tailoring the Seebeck coefficient, in particular, for implementation in microcooling devices [14].

[2] Data taken form the ICDD card 42-540.

1.2. Electronic properties of atomically-thin layered metal chalcogenides

Bulk layered metal chalcogenides cover a wide range of electronic properties from insulators (HfS_2) [16,48] and semiconductors (MoS_2 and WS_2) [49,50] to semimetals (WTe_2, TiS_2) [21,40], metals (NbS_2 and VSe_2) [40] and 3D topological insulators (Bi_2Te_3 and Bi_2Se_3) [11]. Such diversity of band structures arises from the progressive filling of the non-bonding *d*-orbitals with the valence electrons as the transition metal atomic number increases along the period [40]. In TMD crystals, six covalent bonds around a transition metal atom are formed due to mixing of its *s*-, *p*-, and *d*-orbitals with the atomic orbitals centred on the surrounding chalcogens; these contribute to the bonding σ and antibonding σ^* bands. Three remaining transition metal *d*-orbitals, that are not involved into the covalent bonding, form the non-bonding *d*-band located in the gap between the σ and σ^* bands. In the 2H phases with the trigonal-prismatic coordination around transition metal centres, the d_{xz} and d_{yz} orbitals are suitable for the covalent bonding, whereas the $d_{x^2-y^2}$ and d_{xy} orbitals, mixed with the transition metal p_x and p_y states, on one hand, and the d_{z^2} orbital, on the other, form two separated non-bonding *d*-bands between the σ and σ^* bands [40,51]. In the octahedrally coordinated 1T phases, the $d_{x^2-y^2}$ and d_{z^2} orbitals of the transition metal are mixed into the valence band, while the d_{xy}, d_{xz}, and d_{yz} form the non-bonding *d*-band [40]. Not only does this model predict the relative stability of one possible metal coordination (trigonal-prismatic or octahedral) over the other but also provides an insight into the electronic properties of the material depending on the number of the remaining valence electrons accommodated by the non-bonding *d*-bands. According to this atomic orbital model, the TMD compounds with partially occupied *d*-bands, such as 2H-$NbSe_2$ and 1T-ReS_2, exhibit metallic behaviour, while the materials with either fully filled (2H-MoS_2), or empty (1T-HfS_2), *d*-bands are either semiconductors or insulators [51]. Interestingly, due to the structural polymorphism observed in the group VIB TMDs, metallic behaviour can be achieved when the metal coordination changes to octahedral (1T-MoS_2) [52].

Bulk 2H polymorphs of the group VIB TMDs are indirect-gap semiconductors with indirect band gaps $E_g \sim 1$ eV [49,50]. The only exception is bulk WTe_2 that does not form a stable 2H phase; instead, it is found in the distorted octahedral (T_d) polymorph that exhibits semimetallic behaviour [10]. The extremums of the valence (VB) and conduction (CB) bands are located at the Γ point and at the midpoint along the Γ-K lines of the Brillouin zone, respectively. These band structure calculations were corroborated by angle-resolved ultraviolet photoelectron spectroscopy (AR UPS) studies of the valence states [49]. The optical transitions

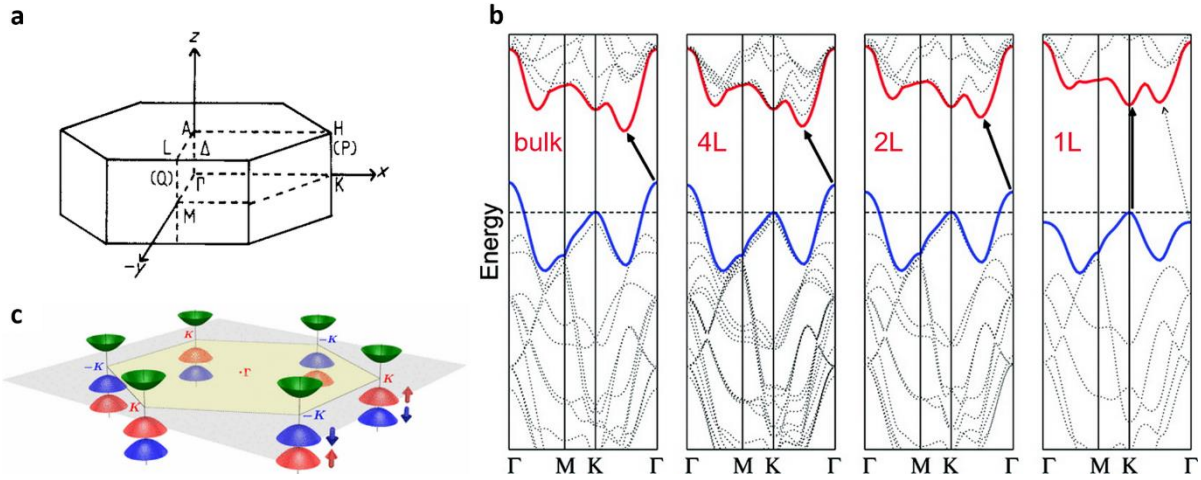


Figure 1.3. Band structure of the 2H group VIB TMDs. **a** The Brillouin zone of a hexagonal lattice with the standard symmetry notations. Reproduced with permission from [39] © IOP Publishing. All rights reserved. **b**. Calculated band structures of bulk, 4 layer, bilayer and single layer MoS_2 shownig gradual indirect-to-direct gap transformation. Reprinted with permission from [47]. Copyright © 2010, American Chemical Society. **c**. Schematic representation of the CB and VB extremums at the K points of the Brillouin zone. Reprinted with permission from [51] Copyright © 2012 by the American Physical Society.

in bulk 2H group VIB TMDs originate from the direct gaps at the K points [53]. At the K points, the valence band is split due to interlayer interactions and spin-orbit coupling, leading to the distinct excitonic transitions, A and B, between the spin-split VB maxima and the degenerate CB minimum [51,54,55,56]. Additional transitions, A' and B', appear in the optical spectra of the group VIB diselenides and ditellurides due to the splitting of the A and B exciton states. Generally, as the chalcogen atomic number increases, the main absorption edge gradually shifts to lower energies and the spin-orbit splitting increases [51]. The band structure parameters and the energies of excitonic transitions in bulk group VIB TMDs are listed in Table 3.

As the number of layers decreases, the 2H group VIB TMDs undergo the indirect-to-direct gap transition as shown in Figure 1.3.b [57]. This band structure transformation was experimentally observed in MoS_2 and WS_2 crystals by angle-resolved photoelectron spectroscopy (AR PES) [9,58]. The indirect-to-direct gap transformation is attributed to the quantum confinement of the charge carriers, as well as to the change in hybridisation between the chalcogen p_z orbitals the transition metal *d*-orbitals [15,59]. The CB states in the vicinity of the K points are composed of the transition metal *d*-orbitals. The states at the Γ point, on the other hand, originate from mixing the chalcogen p_z orbitals and the transition metal *d*-orbitals and therefore, are strongly affected by the interlayer interactions. As the number of layers decreases, the energy of the CB minimum at the Γ point changes significantly so that the indirect gap becomes larger than the direct one at the K points.

It was shown that the excitonic transitions exhibit gradual blue-shift as the material is being thinned down to single layer [55,56]. The energies of the A and B excitons weakly depend on thickness, indicating that these states are not affected by the interlayer interactions [55]. The intraband high-energy transitions (C, D bands) that involve the chalcogen *p*-orbitals demonstrate clear thickness-dependent spectral shifts. Interestingly, the shift of the A' and B' excitons was found to be more pronounced than that of the A and B excitons, indicating the strong association of the former ones with the chalcogen p_z-orbitals rather than the transition metal *d*-orbitals [55].

In the 2H group VIB TMD monolayers, the CB minima and the VB maxima are located at the corners (K points) of the Brillouin zone as shown in Figure 1.3.c. Strong spin-orbit coupling in these materials and the inversion symmetry breaking in the monolayer limit lead to the unique spin-valley coupled physics in the valence band [60]. This manifests as the electrons populating one of these valleys can be selectively manipulated by the circularly polarised light; moreover, the light emitted, when these electrons relax to the ground state, retains the same polarisation [61]. This allows for constructing optical switching valleytronic devices [15].

Table 3. Band structure parameters of the semiconducting group VIB TMDs. E_g (bulk, Γ) and E_g (bulk, K) are the indirect and direct gaps at the Γ and K points, respectively, calculated for the bulk group VIB TMDs. E_g (1ML, K) is the direct gap in the group VIB TMD single layers. Δ_{SO} is the spin-orbit splitting energy (calc. – calculated; exp. – measured experimentally, AR PES).

Material	**Fundamental gap E_g, eV**			**Optical transitions, eV**		**Δ_{SO}, meV**	
	bulk, Γ	bulk, K	1ML, K	bulk, A	bulk, B	calc.	exp.
2H-MoS_2	1.29 [62] 1.23 [63]	1.78 [62]	1.9 [64]	1.88 [65] 1.91 [66]	2.06 [65] 2.11 [66]	258 [62]	161 [62]
2H-$MoSe_2$	1.10 [62] 1.09 [63]	1.42 [62]	1.57 [67]	1.57 [65] 1.59 [66]	1.82 [65] 1.86 [66]	294 [62]	175 [62]
2H-$MoTe_2$	1.00 [62]	1.10 [62]	1.07	1.10 [65] 1.12 [66]	1.48[65] 1.43 [66]	331[62] 300 [40]	238 [62]
2H-WS_2	1.35 [63]		2	2.04 [66]	2.46 [66]		
2H-WSe_2	1.35 [68] 1.20 [63]		1.65 [67]	1.71 [69] 1.69 [66]	2.3 [69] 2.17 [66]		
2H-WTe_2	0.7 [10]			-	-	600 [40]	

As discussed in Section 1.1, bulk WTe_2 and $MoTe_2$ form the orthorhombic (T_d) and monoclinic (1T') polymorphs, respectively, with the characteristic distorted octahedral coordination around transition metal atoms. Other members of the group VIB TMD family do not naturally occur in the octahedrally-coordinated polymorphs, and methods to produce these

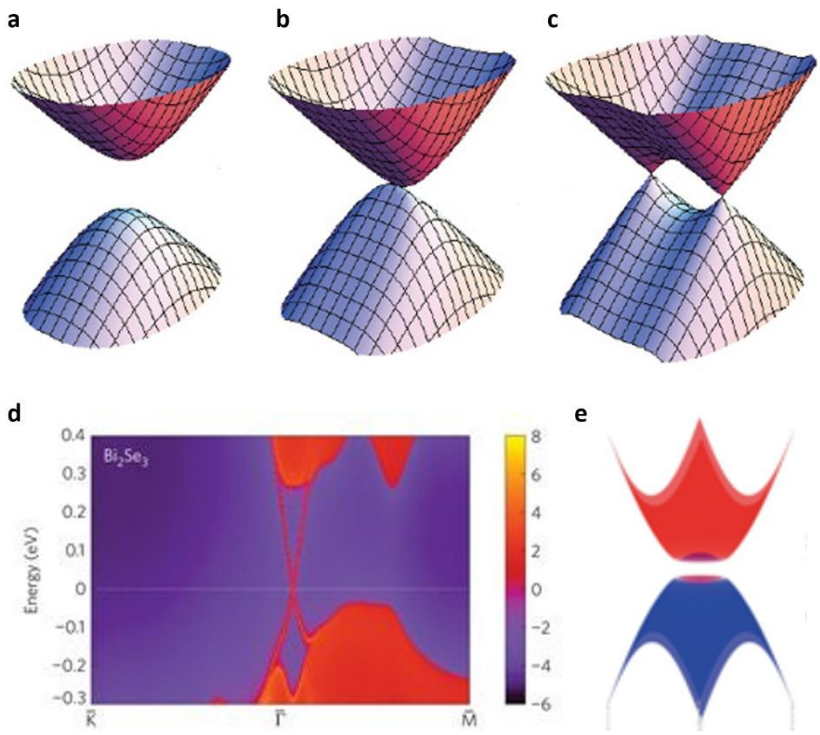


Figure 1.4. Schematic illustration of the formation of topologically non-trivial phases as represented by the dispersions of the bulk states. **a-c** Band evolution from a trivial 3D (bulk) semiconductor (panel **a**), to a trivial 3D semimetal (panel **b**), to formation of Weyl nodes in the band inversion region of a 3D topological semimetal due to the spin-orbit coupling (panel **c**). The schematics shows gradual closing of the gap between valence (blue) and conduction (red) bands. Adapted from [65]. Reprinted with permission form AAAS. Copyright © 2017. **e** Fundamental gap opening between the inverted bands of a 2D topological insulator due to the spin-orbit coupling. Reprinted by permission from Springer Nature: [66]. Copyright © 2009. **d** Local density of states illustrating the formation of topological surface state in a 3D topological insulator, Bi_2Se_3, where bands disperse through a single Dirac cone at the Γ point. Reprinted with permission from [40]. Copyright © 2016 by the American Physical Society.

metastable phases are summarised in Section 1.4.3. Unlike the corresponding semiconducting 2H counterparts, these 1T' and T_d phases are semimetallic [10] and display unique topological surface states [70]. Due to the inversion symmetry breaking, the surface electronic states of the orthorhombic group VIB TMD bulk semimetals appear to be topologically nontrivial, and these materials have been extensively investigated as potential candidates for observation of the 3D Weyl fermions [70,71,72]. Recently, the corresponding 1T' monolayers have been predicted to be large-gap quantum spin Hall insulators, displaying topologically protected edge states [12,73].

Weyl semimetals are topological semimetallic phases, in which the inversion of the conduction and valence bands forms an even number of non-degenerate Dirac cones through the points in the *k*-space called Weyl nodes as shown in Figure 1.4.c [74,75]. Topologically protected states that exist on the surface of a Weyl semimetal are the Fermi arcs in the *k*-space that connect the projections of Weyl nodes onto the surface of the Brillouin zone [76]. WTe_2,

which naturally occurs in the orthorhombic T_d polymorph, has been experimentally verified as a type II Weyl semimetal [77]. $MoTe_2$, which forms the monoclinic 1T' phase, is a topologically trivial semimetal [32]. However, the low-temperature orthorhombic γ-$MoTe_2$ that was synthesised only recently has also been identified as a possible type II Weyl semimetal candidate [78]. This was later confirmed using AR PES [79]. Moreover, it has been demonstrated that the monoclinic $MoTe_2$ can be transformed into the orthorhombic by substitutional doping with W. In particular, it was found that incorporation of ~8 at.% of W stabilised the γ-phase in $MoTe_2$ at room temperature, which according to the AR PES data exhibits the Fermi surface similar to that of WTe_2 [33].

While bulk T_d group VIB TMD phases demonstrate the properties of topological semimetals, their monolayer counterparts have been identified as 2D topological insulators (TI), exhibiting a large intrinsic quantum spin Hall effect. 2D TI are characterised by the insulating bulk with an energy gap opening in the band inversion region due to the spin-orbit coupling, while topologically protected metallic states, that bridge the bulk gap, exist at the edges (Figure 1.4.e). In the 1T' monolayers, the intrinsic band inversion at the Γ point of the Brillouin zone (~0.6 eV) is attributed to the lowering of the transition metal *d*-orbitals owing to the zigzag chain formation and doubling of the period [12]. The spin-orbit coupling opens up a fundamental gap at the bands crossing points near the Fermi level that is tunable by the applied electric field. Opening of a ~55 meV bulk gap has been experimentally revealed in epitaxially grown WTe_2 monolayers [80]. Later, opening of a measurable gap in monolayer 1T' WSe_2 (120-129 meV) [43,81] has been reported. The gap energies achievable in the 1T' group VIB TMD monolayers exceed the thermal energy kT (~26 meV) that makes these materials potentially interesting for applications in spintronic devices.

Bulk Bi_2Se_3, Bi_2Te_3, and Sb_2Te_3 represent a class of 3D topological insulators [11]. 3D topological insulators exhibit large (~0.3 eV) insulating gaps, opening in the band inversion region, in the bulk and topologically protected gapless surface states (Figure 1.4.d) [11]. It should be noted that these surface states arise from the topologically-nontrivial bulk bands and therefore are not affected by non-magnetic doping, localised structural defects, and also surface modification due to interaction with adsorbed species.

In order to implement these layer-dependant semiconducting properties (2H phase of group VIB TMDs) and the unique topologically non-trivial states (1T' and T_d phases of group VIB TMDs; Bi_2Te_3) in the devices, methods to produce structurally perfect layered metal chalcogenides in a controllable manner and with a precise control over the morphology

(number of layers), composition (avoiding formation of non-stoichiometric phases), and crystal phase purity (2H vs 1T' or T_d) are required. Additionally, achieving a controllable transition between the thermodynamically stable semiconducting (2H) and the metastable semimetallic (1T', T_d) phases is particularly interesting for switchable devices, like resistive memories. Recently, a successful phase modulation via the electric-field-controlled lithiation has been demonstrated in MoS_2 [2]. Furthermore, in $MoTe_2$ and alloyed $Mo_xW_{1-x}Te_2$ systems, the reversible electric-field-driven phase transformation was used for the resistive random access memory (RRAM) devices [82]. In these devices, resistive switching reproducibly occurred within 10 ns and the on/off ratio was found to be close to 10^6.

1.3. Application of transition metal dichalcogenides in electrocatalysis

Electrocatalytic hydrogen generation in acidic medium is a two-step process. The initial reduction of solvated protons by electrons from the external circuit leads to the formation of adsorbed neutral H_{ads} on the catalyst surface ($H^+_{solv} + e^- \rightarrow H_{ads}$). This step is known as the Volmer reaction. Formation of molecular hydrogen proceeds through either the Tafel reaction between two adsorbed surface hydrogen atoms $H_{ads} + H_{ads} \rightarrow H_2$, or the Heyrovsky reaction when the adsorbed hydrogen reacts with the solvated proton followed by reduction by electrons from the external circuit $H_{ads} + H^+_{solv} + e^- \rightarrow H_2$ [83]. It is important to note that during the Heyrovsky reaction, the solvated proton is not adsorbed at the active site, instead it directly binds to the adsorbed H_{ads} [84]. Depending on the catalyst nature, either the initial proton reduction (Volmer step) or the following formation of molecular hydrogen (Tafel and Heyrovsky reactions) is the rate limiting stage of the catalytic hydrogen evolution reaction (HER). The widely accepted descriptor for the reaction rate is the Gibbs free energy ΔG_H of the hydrogen adsorption on the active site [85]. If the hydrogen binding to the catalyst surface is too weak then the adsorption is ineffective and the initial proton reduction (Volmer reaction) will limit the HER rate. On the other hand, if the binding is too strong then the formation and desorption of molecular hydrogen is the limiting step. This concept is known as the Sabatier principle and it states that the optimum catalyst binds the substrate neither weakly nor strongly. Graphically, this is represented by plotting the reaction rate as a function of the adsorption free energy ΔG_H as shown in Figure 1.5.a [86]. The materials exhibiting high activity for the catalytic HER, such as Pt and Pd, display the ΔG_H close to 0 eV and are grouped in the vicinity of the tip of the "volcano" plot. Recently, DFT calculations identified MoS_2 to be a promising candidate to replace the Pt-group metals for the catalytic HER [87]. Measuring the catalytic activity of MoS_2 islands produced by the UHV sputtering approach revealed a correlation between the reaction rate and the fraction of edge sites [8]. Thus, the edges of semiconducting 2H MoS_2 nanosheets have been suggested as the primarily active sites for the electrocatalytic HER, however, the origin of this activity remained unclear until recently. The DFT calculations have demonstrated that the lattice corrugation expected to occur at the edges of MoS_2 structures gives rise to a distinct edge electronic state facilitating the catalytic HER, which was experimentally observed in lower Tafel slope and higher exchange current density compared to the bulk MoS_2 counterpart [88]. The localised electronic states at the edges of few-layered 2H MoS_2 nanosheets have been distinguished spectroscopically by X-ray absorption

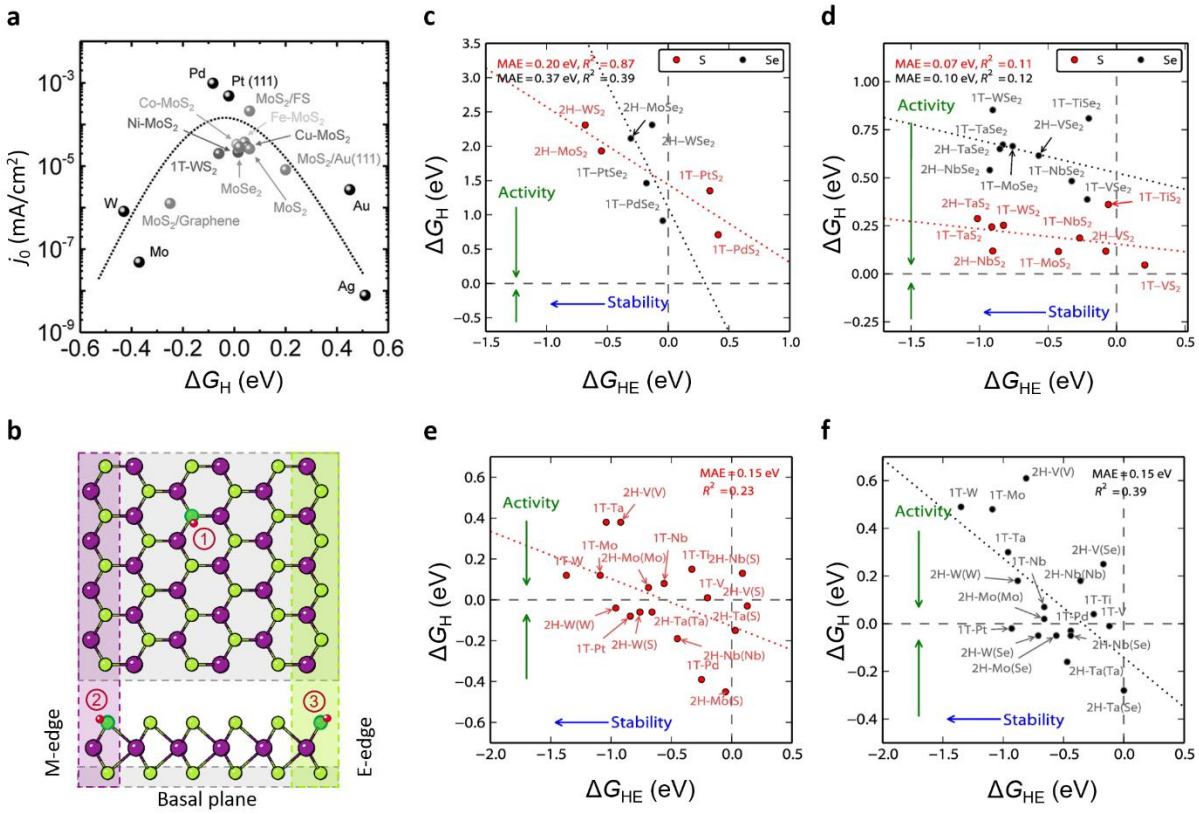


Figure 1.5. Intrinsic activity of TMDs for the electrocatalytic HER. **a** The "volcano" plot displaying the exchange current density as a function of the hydrogen adsorption free energy estimated for various noble metal catalysts (Pt, Pd), free-standing edges of the 2H TMD and the 2H TMDs assembled on Au, graphene, Fe, Cu, Ni, Co, and basal plane of the 1T TMD. Reprinted with permission from [78]. Copyright © 2016, John Wiley and Sons. **b** A schematic representation of the hydrogen adsorbed on the basal plane (1), on the metal M-edge (2), and on the chalcogen E-edge (3) sites of TMDs. Hydrogen atoms are represented by red dots. **c-f**. Catalyst activity-stability ΔG_H-ΔG_{HE} plots for the basal planes of the semiconducting (panel **c**) and the metallic (panel **d**) TMD catalysts; for the edges of the transition metal disulphides (panel **e**) and diselenides (panel **f**). Green arrows indicate the optimum hydrogen binding ($\Delta G_H = 0$ eV) for the efficient HER; blue arrows show the increasing stability of the catalyst surface over the vacancy formation; red and grey dotted lines are provided as visual guides. Reprinted from [83], with permission from Elsevier. Copyright © 2015.

spectroscopy and the spatial localisation of these electronic states has been evidenced using scanning transmission X-ray microscopy imaging at the corresponding energies.

Basal planes of group VIB disulphides and diselenides are found to be catalytically inert, displaying the differential hydrogen adsorption free energies ΔG_H close to 2 eV [89]. Among the four materials, $MoSe_2$ is expected to demonstrate the highest catalytic activity since both metal (M) and chalcogen (E) edge sites have ΔG_H close to thermoneutral (0.02 and -0.05 eV, respectively) [89]. $MoSe_2$ is closely followed by WS_2, both edges of which are potentially active for the catalytic HER (-0.04 and -0.05 eV), whereas only the Se edge of WSe_2 (-0.05 eV) and the Mo edge of MoS_2 (0.06 eV) were identified as catalytically active [89].

Further theoretical modelling has shown that the catalyst activity is inversely proportional to the catalyst stability [90]. Under reducing conditions, hydrogen evolution reaction, occurring on the surface of transition metal disulphides and diselenides, competes with the formation of sulphur or selenium vacancies [91]. Both reactions involve first binding of hydrogen onto the chalcogen sites in either the basal or the lateral planes as shown in Figure 1.5.b. This is followed by desorption of either molecular hydrogen, in case the HER dominates, or H_2S (H_2Se) if the vacancy formation is energetically preferred. The suggested descriptor for the catalyst degradation is the adsorption free energy of the HE (E = S, Se) species, ΔG_{HE}. Using ΔG_H and ΔG_{HE} descriptors, Tsai *et al* investigated 26 single-layered TMD catalysts [90]. According to their findings, basal planes of the semiconducting 2H TMDs bind hydrogen too weakly (Figure 1.5.c). The hydrogen adsorption free energy can be tuned by weakening the metal-chalcogen binding, for example through substitutional doping, yet the increasing ΔG_{HE} indicates a significant decline in the catalyst stability before basal planes of the semiconducting phases become active for the HER. On the other hand, basal planes of the metallic TMDs display much stronger hydrogen binding (Figure 1.5.d). Moreover, the general trend is that binding onto sulphides is stronger than onto selenides, suggesting the metallic transition metal disulphides (1T MoS_2, 2H NbS_2) to be promising candidates for the HER. In contrast to the inert basal planes, edge sites of numerous TMD catalysts display optimum hydrogen binding (ΔG_H close to 0 eV). However, a similar inverse relationship between the activity and stability was found for the edge sites of the TMD catalysts, regardless of the chalcogen type, the edge structure (1T, 2H metal edge, 2H chalcogen edge) and the material bulk metallicity as demonstrated in Figure 1.5.e,f.

In the group VIB TMD family, the superior catalytic activity of metallic phases has been generally ascribed to high affinity of basal planes of the 1T(1T') polymorphs to hydrogen [90,92,93]. The activation of basal plane in the metallic 1T polymorph has been experimentally demonstrated by partial oxidation of chemically exfoliated MoS_2 nanosheets [94]. The pristine 1T MoS_2 nanosheets outperformed the 2H counterpart, exhibiting significantly lower onset overpotentials (100 vs 250 mV) and lower Tafel slopes (40 vs 85 mV/dec, respectively). Following the oxidative treatment, the catalytic activity of the 2H phase decreased substantially, while the performance of edge oxidised 1T MoS_2 nanosheets remained unaffected. Based on these findings, the edges of the 1T nanosheets were suggested not to be the main reaction sites and the activation of the basal plane has been proposed.

From a thermodynamic point of view, the overall catalytic hydrogen reduction reaction, occurring on both the 2H metal edges and the 1T basal planes of group VIB TMDs, is reported to follow the Volmer-Heyrovsky mechanism. [90,92]. These models are based on using the hydrogen adsorption free energies of the reaction intermediates as the major thermodynamic descriptor. However, Chen *et al* have pointed out that under typical HER conditions, the difference between the hydrogen coverage of catalyst surface and the concentration of hydrogen in the electrolyte solution would lead to predominant hydrogen desorption through the Tafel reaction rather than the Heyrovsky reaction [95]. The authors suggest that a reasonable thermodynamic model of the heterogeneous HER mechanism should involve the catalyst/water interface structure instead.

In practice, the properties of a catalyst-functional substrate interface, as well as the electron transport across the catalyst material, influence the performance of a working electrode, perhaps, even more than pure thermodynamics of the catalytic reaction. Compared to the semiconducting 2H counterparts, the metallic polymorphs, such as 1T' MoS_2 and WS_2, greatly benefit from the removal of the Schottky barrier as the catalyst-substrate interface becomes essentially metal-metal, leading to lower charge dissipation and more effective electron injection into the catalyst material. This has been evidenced in the experiments with two model catalysts, mechanically exfoliated WTe_2 and CVD grown MoS_2 [96]. The interface modulation has greatly affected the performance of semiconducting MoS_2, while had no measurable effect on the efficiency of semimetallic WTe_2 catalyst. Similarly, it has been reported that lowering the catalyst-substrate contact resistance has led to the activation of existing catalytic sites (sulphur vacancies) in the basal plane of the 2H MoS_2 [97]

Assembling the catalyst on a TI support platform can potentially have a positive effect on the catalytic activity [98]. However, this approach has not been applied to the experimental TMD systems yet. The activity of transition metal clusters supported on a Bi_2Se_3 substrate for the HER and the effect of topologically protected surface states on the hydrogen adsorption free energy have been studied theoretically. It was found that the catalysts with low intrinsic hydrogen binding strength, for instance the metal edge of WSe_2, could potentially benefit from coupling with the topologically protected surface states, leading to an optimised hydrogen adsorption.

The general strategy for designing an effective catalyst based on the 2H phase TMDs is by increasing the number of exposed edge sites since the basal planes are practically inert for the HER. This can be achieved, for example, by reducing the lateral size of mechanically

exfoliated nanosheets. Indeed, the performance of thin film working electrodes made of mechanically exfoliated WS_2 nanosheets improved as the nanosheet size decreased [99]. Fraction of the edge sites can also be increased by introducing structural defects in the basal plane via etching [100], annealing in a reducing atmosphere [101], or treating with oxygen plasma [102]. Another route to increase the number of accessible edge sites is a direct bottom-up synthesis of nanostructures with branched morphologies [103,104].

To date, the reported approaches to tune the intrinsic catalytic activity of a given TMD material include variation of its chemical composition through substitutional doping [105,106] or alloying [107,108], inducing the crystal phase transition into the metallic polymorph [109], and intercalation of alkali metal into the van der Waals gaps of few-layered TMDs [110]. It has been established that the addition of small amounts of dopants, typically transition metals, can effectively enhance the catalytic activity of both the semiconducting 2H [111] and the metallic 1T [92] polymorphs. The effect of substitutional doping is generally attributed to the alteration of the electronic states of pristine phases, leading to modification of the hydrogen binding strength. An overview of the recent experimental studies on substitutional doping in TMDs for the electrocatalytic HER is provided in Section 4.1. The difficulties in preparation of the doped catalysts are associated with an insufficient control over composition and spatial distribution of the dopants, e.g. clusterisation. These can be successfully overcome by the formation of TMD alloys. The methods to achieve isostructural and hetero-phased ternary and quaternary TMD alloys are introduced in Section 4.2, while the principle works on the application of alloyed TMD in the catalytic hydrogen production are cited in Section 5.3. Initiating the 2H-to-1T(1T') phase transitions in the group VIB TMDs that allow for activation of basal planes in the metallic polymorphs is perhaps the best investigated strategy for the catalytic activity enhancement. The pioneering works reported the improved catalytic activity in chemically exfoliated MoS_2 [94] and WS_2 [109] nanosheets. Moreover, the improvement was found to directly correspond to the fraction of metallic phase attained during the chemical exfoliation process [112]. Interestingly, the activity of the metallic 1T polymorph can be further enhanced via the intercalation of alkali metal cations into the van der Waals gaps as was shown for the 1T MoS_2 [110]. The enhancement was assigned to the optimisation of the hydrogen binding strength as corroborated by the first principles calculations. It should be noted that the possibility of stabilisation of the metastable 1T polymorph is majorly overlooked in these studies. In Sections 3.3 and 5.2, we discuss the direct solution-phase synthesis of the metastable 1T' polymorph (WSe_2) as a perspective alternative approach to the effective HER catalyst.

1.4. Methods to produce atomically-thin transition metal dichalcogenides

Producing TMDs in a form of atomically-thin nanosheets is a crucial requirement to employ their unique size-dependent electronic properties in novel opto- and nanoelectronic devices and in electrochemical devices for energy storage and catalysis. Generally, two-dimensional TMD structures can be obtained by either top-down techniques involving thinning bulk crystals down to few- and single-layered flakes or through bottom-up approaches based on the direct chemical reaction between molecular building blocks.

1.4.1. Top-down approaches: Mechanical and chemical exfoliation

Exfoliation of atomically-thin nanosheets is based on the preferential cleavage of layered metal chalcogenide crystals between the adjacent layers held by van der Waals interactions. Similarly to the pioneering work on graphene [113], high quality TMD and pnictogen chalcogenide single layers can be achieved by scotch tape assisted peeling from the bulk crystals [6,46,55,57]. Although the scotch tape exfoliation allows for producing single-layered flakes of excellent crystallinity that are suitable for both fundamental characterisation and for device fabrication, the yield of exfoliated material is typically low and the lateral size of isolated flakes rarely exceeds a few μm [64,114]. The recently proposed method of gold-assisted scotch tape exfoliation enables isolation of ultra-large group VIB TMD flakes (tens of mm^2) from natural crystals [115]. Strong van der Waals interaction between the freshly deposited Au (111) film and the basal chalcogen plane of TMDs facilitates the exfoliation of the topmost TMD layer allowing for the selective transfer of single layers from their parent crystals.

High-throughput mechanical exfoliation can be achieved in liquid phase by ultrasonication. Solution phase exfoliation of bulk powders yields dispersions of single- and few-layered TMD nanosheets in common solvents with concentrations reaching 40 mg/mL [116]. Moreover, by simple mixing different bulk materials prior to exfoliation or by mixing the starting TMD compound with functional additives, composite materials can be formed through the restacking of exfoliated nanosheets. Liquid phase exfoliation is usually carried out in organic solvents, such as isopropanol, ethanol, and N-methyl-pyrrolidone, [117] or in aqueous solutions of appropriate surfactants (polymers) [118]. The dispersibility of exfoliated material strongly depends on the solvent properties. It has been found that the successful exfoliation down to monolayers and the formation of stable concentrated dispersions can only be achieved if the surface energy of material matches that of the solvent [119]. The liquid exfoliation process typically results in the dispersions of TMD flakes of heterogeneous lateral sizes and thickness

[117,118]. Recently, the statistical analysis of different layered materials exfoliated via liquid-phase approach has demonstrated that the area of exfoliated nanosheets follows a power-law scaling relationship with their thickness [120]. The reduction of the lateral size, that greatly affects the applicability of exfoliated material in nanoelectronics, is commonly attributed to the sonication induced scission and is typical for highly concentrated dispersions prepared at prolonged sonication times [116]. The interplay of the in-plane tearing and out-of-plane peeling energies and the in-plane and out-of-plane Young's moduli sets the limitations on the achievable lateral sizes of monolayered TMD flakes produced via liquid-phase exfoliation [120]. On the other hand, size selective precipitation by cascade centrifugation allows for separating the monolayer enriched fractions of the exfoliated material [121] essential for formulating inks for printable electronics [122].

The insertion of charged or neutral species in the van der Waals gaps of TMD bulk crystals weakens the interaction between layers and so facilitates the exfoliation down to single layers. Typically, chemical exfoliation occurs in two stages. First, bulk TMD powders are intercalated with alkali metal cations; lithium compounds, such as *n*-butyllithium (*n*-BuLi) and lithium borohydride, are commonly used [28,123]. This is followed by hydrolysis of the intercalated TMD powders. The reaction between water and intercalated lithium leads to generation of H_2 gas bubbles that separate TMD layers [26,28]. Exfoliation to single- and few-layered flakes can be achieved by gentle manual shaking. Chemical exfoliation typically yields in high fraction of single-layered flakes; however, the process is time-consuming and highly sensitive to the environment as it requires an inert atmosphere. Lateral size of the exfoliated TMD flakes reaches a few μm and is majorly defined by the grain size of the parent bulk crystals. Additionally, the reaction with lithium compounds during the intercalation step leads to the reduction of TMDs. This induces structural distortion of the pristine trigonal-prismatic coordination of transition metal atoms in the 2H phase. Combined scanning tunnelling microscopy (STM) and electron diffraction structural studies have demonstrated that the exfoliated MoS_2 adopts either the 1T [22] or the 1T' [26] phase depending on the amount of intercalated lithium, while the chemically exfoliated WS_2 single- and few-layered flakes are found in the 1T' phase [26,28]. As a consequence of the partial phase transformation, the chemically exfoliated TMDs display metallic behaviour. The semiconducting phase can be restored via mild thermal annealing [124]. Generally, the quality of exfoliation strongly depends on the uniformity of intercalant distribution. Electrochemical intercalation has proved to be a promising approach to achieve large area TMD nanosheets with narrow thickness distribution.

Moreover, the intercalation of quaternary ammonium salts does not affect the crystal phase of the TMD material, thus making possible large-scale solution phase production of the phase-pure semiconducting nanosheets [125].

1.4.2. Bottom-up approaches: Vapour-phase and solution-phase growth

The bottom-up approaches, such as deposition from vapour phase and solution-phase chemical synthesis, are based on a direct reaction between the transition metal and chalcogen molecular precursors either in vapour or in liquid phase. Chemical vapour deposition (CVD) emerged as a synthesis method to produce electronic-grade atomically-thin TMD crystals [126] and continuous films, reaching tens of cm^2 in some cases [127]. CVD process involves a reaction between the co-evaporated precursors of required transition metal and chalcogen, occurring on various substrates, including Si/SiO_2, sapphire, quartz, and graphitic carbon. The growth process is carried out in a horizontal tube furnace at temperatures typically in the range 650-950 °C. The growth can be performed either at low (10^{-2} mbar) or at atmospheric pressure, however, low pressure in the reactor ensures lower concentrations of residual gases, moisture, and possible impurities that leads to higher quality crystals being produced. Transition metal trioxides [128–132] or the corresponding acids [126], oxychlorides [133], chlorides [130,134,135], and foils [127] are commonly chosen as metal precursors for the synthesis of the group IVB-VIB TMDs. On the other hand, bulk chalcogen (S, Se, Te) powders serve as a chalcogen source. The reaction rate strongly depends on the generation of a steady vapour flux of both precursors that requires optimisation of many growth parameters, including the reactor pressure, carrier gas flow rate and temperature profiles. Moreover, the wetting properties of a growth substrate can be modified by adding organic species (seeding promoters) to lower the energy barrier for nucleation [136].

It has been shown that using gaseous precursors instead of solid trioxide and chalcogen powders helps to improve the uniformity of the TMD crystals, although significantly slows down the reaction rate. The CVD approach based on using the volatile sources of transition metal (carbonyls, chlorides) or chalcogen (hydrogen chalcogenides, dialkyl chalcogenides) is referred to as metal-organic CVD and has been successfully employed to synthesise large-scale highly-crystalline mono- and few-layered MoS_2 [137,138], WS_2 [137], and WSe_2 [139] crystals, demonstrating high carrier mobilities at room temperature (30-100 $cm^2/[V \cdot s]$ in MoS_2; 18 $cm^2/[V \cdot s]$ in WS_2).

Large-area uniform TMD films can be achieved via the chalcogenation of pre-deposited transition metal or transition metal oxide films as was demonstrated for MoS_2, WS_2, $MoSe_2$, and WSe_2 systems [103,140–143]. Although this approach generally requires lower temperatures and allows for the fast production of wafer-scale TMD films with precisely controlled thickness, the materials exhibit low carrier mobilities (~0.04 $cm^2/V \cdot s$ in the case of MoS_2 films) due to the high degree of polycrystallinity and small size of single-crystalline grains, as well as due to the presence of unreacted metal or metal oxide inclusions [141]. However, the chalcogenation route is potentially promising for a wafer-scale production of a phase-controlled TMD polymorphs. A phase-selective synthesis of homogenous few-layered 2H and 1T' $MoTe_2$ films was achieved by changing metal precursor from MoO_3 to Mo [144]. The stabilisation of the metastable phase was attributed to the compressive strain owing to the smaller parameters of the Mo lattice compared to the MoO_3.

Although CVD approach is suitable for synthesis of high-quality atomically-thin TMDs for nanoelectronic devices [130,132], the structural defects, such as dislocations and twin boundaries, commonly observed in the CVD grown materials hinder their application in optical devices [145,146]. High optical quality TMD monolayers can be produced via the physical vapour transport (PVT) route. This synthesis method is based on the sublimation of the required bulk TMD powders followed by their recrystallisation on a substrate [39,147]. Similarly, the PVT approach has been applied to synthesise high quality ultrathin TI flakes (Bi_2Te_3, Bi_2Se_3), that are not achievable via the direct reaction due to high reactivity of the precursors [148].

The wet chemistry approach involves a reaction between the respective molecular precursors, occurring at elevated temperatures in liquid phase. Due to its scalability and generally high reaction yields, the solution-phase synthesis is appropriate for production of concentrated (aqueous or non-aqueous) suspensions of mono- to few-layered TMD nanosheets compatible with numerous deposition techniques, such as spin- and spray-coating, ink-jet and roll-to-roll printing, for application in non-volatile memory devices [149], switchable absorbents of heavy metal and organic contaminants [150,151]; electrochemical energy storage devices [152], and electro- and photocatalytic hydrogen production [153–156]. However, precise control over the thickness of TMD nanosheets is exceptionally challenging since it requires an effective suppression of the vertical growth mode (along the *c* direction), which is particularly difficult to achieve due to the inertness of chalcogen terminated basal planes to the covalent functionalisation. The solution-phase growth of TMD nanomaterials is performed either via the hydrothermal (solvothermal) or via the colloidal synthesis route. Both routes require

moderately high temperatures (150-300 ºC). Hydrothermal (solvothermal) synthesis is carried out in an aqueous (non-aqueous) solution in a sealed container at high pressure and at temperatures exceeding the boiling point of the solvent. Whereas, colloidal synthesis is typically performed at normal pressure in an inert atmosphere. Growth mechanisms, proposed for these two solution-phase approaches, differ significantly. Colloidal growth is based on a burst heterogeneous nucleation of solid phase in a supersaturated solution, which is followed by the growth stage (Section 2.1), whereas in hydro- and solvothermal syntheses, the nucleation and growth processes are not separated in time [157]. Also, the key feature of colloidal synthesis is the presence of capping ligands in the reaction medium that mediate the particle growth and ensure colloidal stability of the final suspensions.

Recently, hydro- and solvothermal synthesis of the group VIB disulphide and diselenide nanostructures from the respective trioxides (MoO_3, WO_3) [158,159], ammonium molybdates and tungstates ($(NH_4)_6Mo_7O_{24}\cdot 4H_2O$, $(NH_4)_{10}W_{12}O_{41}\cdot xH_2O$) [160–163], carbonyls ($Mo(CO)_6$, $W(CO)_6$) [151], and chlorides ($MoCl_5$, WCl_6) [161] have been successfully demonstrated. Common chalcogen precursors include thiourea, thioacetamide, and elemental sulphur and selenium; however, the hydrolysis of chalcogen precursors, occurring under the hydrothermal conditions and leading to the evolution of H_2S and H_2Se, is assumed to be crucial for the synthesis of atomically-thin TMD structures. The solvothermal synthesis of pnictogen chalcogenides is commonly performed from the respective oxides (Bi_2O_3, SeO_2, TeO_2) [164], chlorides ($BiCl_3$, $SbCl_3$) [164,165], sodium selenite and tellurite (Na_2SeO_3, Na_2TeO_3) [166] in ethylene glycol in the presence of a surfactant (polyvinylpyrrolidone) to prevent agglomeration. Compared to the colloidal synthesis approach, hydrothermal (solvothermal) synthesis requires longer growth times (10-48 hours) and generally yields branched or agglomerated nanostructures. Colloidal synthesis, on the other hand, requires more accurate tuning of the growth conditions, such as precursor concentrations and temperature, in order to achieve the control over the morphology, size, and uniformity of the grown material. In the case of group IVB disulphides, fine control over the thickness of colloidal nanosheet has been achieved by tuning the chalcogen (*in situ* generated H_2S) influx rate [167].

Only a few experimental protocols of the colloidal synthesis of molybdenum [149,153,168–171] and tungsten [154,156,168,169,172] dichalcogenides have been reported recently. These are summarised in Table 4. Typically, molybdenum and tungsten chlorides ($MoCl_5$ and WCl_6) are used as the respective sources of transition metal [149,156]; however, carbonyls ($Mo(CO)_6$ and $W(CO)_6$) [169] and molybdates and tungstates (Na_2MoO_4 and $(NH_4)_2WO_4$) [170,154] have also

been successfully employed for the synthesis of colloidal TMD nanostructures. Commonly used chalcogen precursors include carbon disulphide [149,156], thiourea [154], thioacetamide [168] and diphenyl diselenide [169]. The morphology of the final product is reported to vary from irregular nanodisk-like shapes (NDs) [154,169] and nanosheets (NSs) [149,169] to more regularly shaped nanoflowers (NFs) [170,171]. It appears that the material produced from either chlorides [156,172] or carbonyls [168,169] tends to acquire the morphology of few-layered nanodisks. Moreover, individual nanostructures are often found to form chains of closely-stacked disks [154] or even continuous micron-sized quasi-2D agglomerates [172]. It is only emerging that the lateral extension of colloidal TMD nanodisks can be potentially achieved if oleic acid is present in the reaction medium [149,169], however, its role in the TMD synthesis remains unclear. The choice of molecular precursors used in this work and the details of the designed synthesis protocols are provided in Sections 2.2.2 and 2.2.3.

Table 4. Recent advances in colloidal synthesis of the group VIB TMDs.

Material	**Growth conditions**			**Morphology**			**Crystal phase**	**Reference**
	precursors: transition metal; chalcogen	organic solvent(s)	T_{growth}, °C	nanoparticle shape	thickness, layers	lateral size, nm		
MoS_2	$MoCl_5$ + TDPA + OlAc + OlAm; CS_2	OlAm	320	NSs	≥2		2H	[149]
	$[Mo(ac)_2]_2$ + StAc; $CH_3(NH_2)CS$	OlAm, TOPO	330	NDs	1-5	15-40	2H	[168]
$MoSe_2$	$MoO_2(acac)_2$; Ph_2Se_2	OlAm	240	NFs	2-5	100-200	2H	[153]
	$Mo(CO)_6$ + TDPA; Ph_2Se_2	OlAc	350	NSs	1	200	2H	[169]
	Na_2MoO_4; ODE:Se	OlAc, OctAm	300	NFs		50-250	2H	[170]
WS_2	$(NH_4)_2WO_4$; $(NH_2)_2CS$	OlAm	280	NDs		160	1T'/ 2H	[154]
	WCl_6 (+HMDS)+ OlAc + OlAm; CS_2	OlAm	320	NDs	1	100	1T'/ 2H	[156]
	$W(CO)_6$ +StAc; $CH_3(NH_2)CS$	ODE, TOPO, squalane	330	NDs	1-5		2H	[168]
	WCl_6; OlAm:S	OlAm, ODE	300	NDs			2H	[172]
WSe_2	$W(CO)_6$ + TDPA; Ph_2Se_2	OlAm (or OlAc)	330	NDs (NS)s	4-8 (1)	5 (200)	2H	[169]
$MoTe_2$	$MoCl_5$ + OlAc; TOP:Te	TOP, OlAm, HMDS	300	NFs		100-150	1T'	[171]

Additionally, a few reports indicate that subtle variations in the molecular precursors chemistry may result in the formation of metastable crystal phases [154,156]. Approaches to the metastable phases of group VIB TMDs, including the recent examples of colloidal synthesis, are discussed in Section 1.4.3.

1.4.3. Access to the metastable crystal phases

The metastable crystal phases can be either accessed through destabilisation of the thermodynamically stable polymorphs, for instance, due to electron transfer, or synthesised directly, when the growth conditions are optimised in such a way that the metastable product is kinetically preferred. The first reports on the metallic 1T(1T') group VIB TMD polymorphs date back to the pioneering works on chemical exfoliation of these materials [28,173]. It has been suggested that the electron transfer from the intercalated alkali metal species leads to an increased electron count on the transition metal *d*-orbitals [26]. Upon chemical reduction, the coordination around transition metal centres changes from trigonal-prismatic to octahedral. The resulting crystal phase is commonly denoted as the metallic 1T, however, STM studies of chemically exfoliated nanosheets have verified distortions in the *ab* plane, characteristic to the distorted-octahedral 1T' phase [27]. Generally, the 1T(1T') phases produced via chemical exfoliation approach are attained as small crystalline (< 1 μm) domains embedded into the 2H matrix. Moreover, the ratio between the converted 1T(1T') and pristine 2H phases strongly depends on the type and concentration of reducing agent (alkali metal) and the composition of TMD material [112]. One of the drawbacks of the chemical exfoliation approach is that thus produced metastable 1T(1T') phases gradually decay into the 2H polymorph upon aging and especially in the restacked films once the ions have been removed [27,174,175]. Recently, it has been demonstrated that this instability can be mitigated via the hydrogenation of intercalated lithium species [176]. According to the DFT calculations, LiH is a good electron donor that stabilises the 1T' phase in multi-layered flakes for over 3 months. Although LiH, encapsulated between the TMD layers, is stable, the surface bound hydride easily converts into Li_2CO_3 and Li_3N, what makes this approach unsuitable for stabilisation of the 1T' phase in chemically exfoliated single layers. Another disadvantage of the lithium intercalation of TMD powders is attributed to the non-uniform distribution of intercalated lithium that hinders the control over the dimensions of the converted 1T(1T') patches. However, the 2H-to-1T' phase transformation can be precisely controlled over micron-sized areas if lithium migration within the van der Waals gaps is regulated by an external electric field. Such controllable phase switching has been demonstrated in lithiated MoS_2 films for neuromorphic memory devices [2]

and in the ultra-thin (~2-50 nm) MoS_2 nanosheets upon a reversible electrochemical lithiation [177].

Similarly, phase conversion can be achieved via a post-growth treatment of CVD grown 2H TMD flakes and films with solutions of *n*-BuLi in nonpolar solvents. Taking into account generally larger lateral sizes of the CVD grown flakes compared to that of the chemically exfoliated ones, this potentially allows for production of larger domains of the metastable 1T/1T' phases. *n*-BuLi treatment of polycrystalline films of 2H-MoS_2 and 2H-$MoSe_2$ grown on Si/SiO_2 wafers led to partial conversion into the metallic 1T phase with the overall conversion efficiency of ~50% [178]. Furthermore, the lithium-induced structural transformations in the CVD grown 2H-MoS_2 flakes appear to be thickness-dependent with the monolayers exhibiting strong resistance to the phase conversion [179]. This, therefore, paves the way to the 2D metal-semiconductor junctions in CVD grown TMD devices by controlling the exposure to lithiating agent (*n*-BuLi). In case of the 2H-WSe_2 monolayers, a complete conversion into the metallic 1T phase can be achieved [180]. Interestingly, depositing a PMMA mask has allowed for creating patterned 2H/1T heterojunctions in WSe_2 monolayers. Finally, the 2H-to-1T phase conversion can be induced by exposure to the vapours of electron donating compounds, such as butylamine and trimethylamine, as was demonstrated in the case of MoS_2 and $MoSe_2$ [181]. This can be potentially employed in a novel type of passive sensing devices based on detecting the abrupt changes in material conductivity in the presence of strong donor analytes, such as nerve gas.

It has been predicted that the semiconductor-to-semimetal phase transition can be achieved by electrostatic gating [23]. For example, the gate voltage of ~2-4 V is required to induce the 2H-to-1T' structural transformation in $MoTe_2$. Although such controllable phase switching is potentially interesting for non-volatile memory devices, the approach can hardly be extended to other members of the group VIB TMD family since it would require greater energy input due to the larger energy difference between the 2H and 1T' polymorphs for lighter dichalcogenides [20]. The required gate voltages, however, can be substantially reduced by substitutional doping and alloying.

Direct growth techniques such as vapour phase deposition and solution-phase reactions, commonly rely on a facile tuning of the synthesis conditions. For example, ~100 nm islands of the 1T' WSe_2 have been synthesised on bilayer graphene terminated 6H-SiC(0001) substrates by molecular beam epitaxy (MBE) [81,43]. The phase-selective growth was achieved by controlling the deposition temperature. Keeping the temperatures below 280 ºC, a mixture of

the 1H and 1T' phases was attained, while only 1H-phased WSe_2 islands were observed at higher (400 °C) temperatures. Substrate functionalisation has been found beneficial for growing the metastable phases of materials with larger energy difference between the stable and metastable polymorphs (0.55 eV in MoS_2; 0.33 eV in $MoSe_2$[3]). Thus, the 1T' $MoSe_2$ islands were selectively formed on Au (111) substrates that were treated with selenium prior to deposition [42]. Otherwise, if a layer of selenium was not pre-deposited, only the thermodynamically stable 1H polymorph has been obtained. Such a difference in the resulting crystal phase was attributed to the formation of an electron donating Mo layer between the Au substrate and the pre-sputtered Se overlayer that facilitated growth of the 1T' phase. MBE deposition of 1T' MoS_2 nanoclusters (30-50 atoms) on Au (111) substrates has also been reported [41]. The gold substrate itself was presumed to serve as an electron reservoir that stabilised the nucleating 1T' phase.

Bulk (mm-sized) crystals of the 1T' group VIB TMDs can be obtained through a direct chemical reaction between the alkali metal containing molybdenum or tungsten precursors, such as potassium or sodium molybdate, and elemental sulphur or selenium annealed in an inert atmosphere in an ampoule [182]. Similarly, vapour transfer and deposition techniques allowing for the synthesis of bulk 1T' phases (~100 μm in lateral size) are generally based on the first sulphurisation or selenisation of the required alkali metal molybdate that is followed by a thermal decomposition of thus prepared precursors in a reducing atmosphere [183]. High purity 1T' monolayers can then be mechanically [183] or chemically exfoliated [182] from the 1T' bulk crystals; in case of chemical exfoliation the 1T' phase content in the final product reaches 97%. Moreover, a phase-selective CVD growth of MoS_2 monolayers based on using a similar type of precursor, potassium thiomolybdate, K_2MoS_4, has been proposed recently [184]. The crystal phase control was achieved by changing the atmosphere from inert to reducing by adding H_2 into the carrier gas. Interestingly, depending on the H_2 concentration, either the 1T' or 2H phase-pure monolayers and 1T'/2H heterobilayers could be selectively produced.

Alternatively, CVD growth of the metastable 1T polymorph can be aided by a specific catalyst as has been demonstrated in the synthesis of 1T WS_2 [185]. In this case, adding a mixture of Fe_3O_4 and NaCl, serving as a catalyst and a growth promoter, into the standard CVD set-up (WO_3 and elemental S as material precursors) has led to formation of the 1T/2H WS_2 butterflies with one of the laterally stitched wings being 1T and the other 2H phase. Single crystalline

[3] Energy difference between the 2H and 1T' polymorphs is taken from [20].

domains in these butterfly-like WS_2 monolayers reached 80 μm. It has also been shown that these 1T/2H WS_2 structures could serve as seeds for the laterally expanded 1T/1T and 2H/2H WS_2/MoS_2 planar heterostructures.

Similarly to vapour deposition approaches, the reported protocols of hydro- or solvothermal syntheses of the metastable 1T(1T') group VIB TMD polymorphs commonly involve either reacting ammonium containing salts, like $(NH_4)_2WO_4$ [154], $(NH_4)_{10}W_{12}O_{41}\cdot H_2O$ [163], and $(NH_4)_6Mo_7O_{24}$ [162], with the chalcogen precursor, such as thiourea or thioacetamide, or thermal decomposition of ammonium thiomolybdate [186] in solution phase. The final product is attained as suspensions of the ultra-thin mixed-phase 1T/2H nanosheets or nanoribbons with nm-sized single-crystalline domains. The 1T(1T') phase content in these nanosheets reaches ~61.6% [162]. The metastable phase is stabilised by charged precursor residues trapped between the layers of few-layered nanosheets. Specifically, the presence of intercalated ammonium uniformly distributed across the nanosheets has been repeatedly verified by elemental mapping and XPS analysis [162,163,187]. The solvothermal strategy can be adapted to form arrays of the 1T'-rich (60%) nanosheets (MoS_2) on conductive support (single wall carbon nanotubes) for the application in electrochemical devices [187].

Recently, using an external magnetic field has been proposed for the phase-selective solution-phase synthesis of the 1T MoS_2 and WS_2 nanosheets [161]. The preferential nucleation of the metastable 1T polymorph in high magnetic fields was assumed to be caused by its higher magnetic susceptibility compared to the 2H phase, so the energy barrier of the heterogeneous nucleation of the 1T phase is lowered in the magneto-hydrothermal process.

Colloidal synthesis of the metastable polymorphs of group VIB TMDs remains majorly undeveloped. The few reported protocols are very similar to the hydro- and solvothermal reactions between ammonium salts and thiourea but carried out in oleylamine as a solvent [154]. However, the direct synthesis of pristine metastable phases not stabilised by charged species is challenging, and no reliable strategy has been developed so far. Tuning the reactivity of molecular precursors of transition metal and chalcogen can be potentially utilised for targeting the phase-selective growth in solution phase [156]. The basics of kinetically-driven growth of colloidal nanocrystals will be discussed in Section 2.1.3. In the TMD systems, the effects of nanocrystal nucleation and growth kinetics on the preferential formation of one polymorph over the other remain unexplored.

Chapter 2:
Experimental methodologies and characterisation techniques

In this Chapter, we present the colloidal synthesis that we have designed to obtain $MoSe_2$, $MoTe_2$, Bi_2Te_3, and WSe_2 nanostructures in solution phase. Over the past decades, colloidal synthesis has been majorly employed to obtain colloidal suspensions of high quality $A^{II}B^{VI}$ and $A^{IV}B^{VI}$ semiconductor nanostructures [188,189] but remains significantly undeveloped for the TMD systems. Here, we describe the theoretical model of homogeneous nucleation and growth of the solid phase in supersaturated solution, which provides a sufficient, although fairly simplified, basis of the growth process of the layered metal chalcogenides ($MoSe_2$, $MoTe_2$, Bi_2Te_3, and WSe_2). This is followed by a discussion of the experimental approaches to grow colloidal $MoSe_2$, $MoTe_2$, Bi_2Te_3, and WSe_2 nanostructures designed within this work, including a detailed description of the experimental set-up, choice of suitable molecular precursors, and the range of the experimental conditions varied in the synthesis of these binary systems. Further, we cover the characterisation techniques used to investigate the morphology, crystal structure, and optical properties of the obtained colloidal nanostructures. Finally, we focus on the fundamentals of the electrochemical methods and particular experimental methodologies applied to assess the catalytic activity of the produced materials for the hydrogen reduction reaction.

2.1. Overview of the colloidal synthesis of semiconductor nanostructures

In general terms, colloidal synthesis of semiconductor nanoparticles is based on a homogeneous nucleation of the crystal phase in the supersaturated monomer solution in the presence of a capping ligand that acts as a steric barrier, preventing nanoparticles from aggregation and ensuring their colloidal stability. Developed in early '90s to synthesise nearly monodispersed spherical CdSe nanocrystals (colloidal quantum dots) [188,190], the colloidal approach has been extended to a huge variety of semiconductor systems ranging from binary heavy metal (Cd, Zn, Cu, Ag, Sn, Pb) chalcogenides [191–193] to metal halide perovskites [194] and more exotic transition metal-based chalcospinels [195]. However, it has seen very little application for the synthesis of TMD nanostructures. A significant understanding of the nanocrystal formation process has been gained experimentally that allowed for achieving an unprecedented control over the morphology of the colloidal semiconductor nanocrystals. This has been demonstrated by successful growth of the highly uniform anisotropic nanostructures,

e.g. nanorods [196], branched tetrapod- and octapod-shaped nanocrystals [197,198], nanoribbons [199,200], and more recently two-dimensional semiconductor nanosheets (colloidal quantum wells) [201–204]. Strict theoretical modelling of the formation mechanism of colloidal nanocrystals is complicated due to a high fraction of surface atoms that are prone to interaction with solvent and capping ligand molecules. This may significantly alter the stability of the nucleated species and energetics of their crystal facets. However, general thermodynamic description of the nucleation and growth processes can be extrapolated to various types of materials. This can provide insights into potential synthesis routes to achieve nanocrystals with required shape and composition.

2.1.1. Spontaneous nucleation of solid phase in a supersaturated solution

Growth of colloidal nanoparticles occurs through a series of consecutive stages. The growth process starts with a reaction between the respective molecular precursors, leading to accumulation of the monomer, which is the building block of the growing nanocrystals. This is followed by homogeneous nucleation and growth in solution phase. At the very final stages of reaction the system may enter the Ostwald ripening stage [205,206].

A typical solution-phase crystallisation follows the same route regardless of the material chemistry. Graphically, this can be illustrated by LaMer plot showing change of the monomer concentration over time in solution (Figure 2.1.a) [207,208]. The initial chemical reaction between the molecular precursors leads to the steady monomer accumulation that corresponds to the linear section of the LaMer curve in the region I. Even though the monomer concentration C (mol/L) exceeds that of a saturated solution C_{sat} (bulk solubility), the activation barrier is still

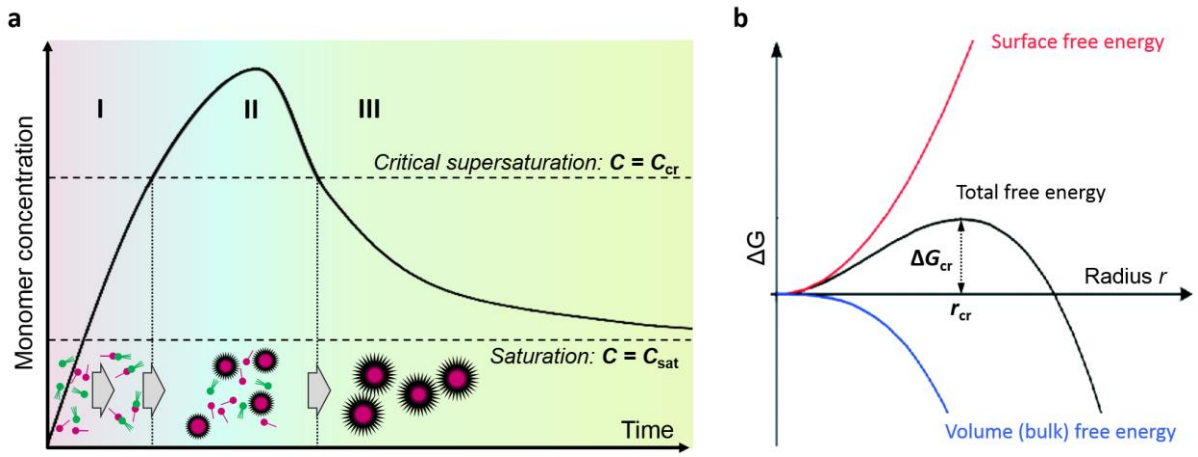


Figure 2.1. Formation of colloidal nanocrystals in supersaturated solution. **a** LaMer plot illustrating changes in the monomer concentration occurring during the nucleation and growth stages of the colloidal synthesis. **b** Formation of the activation barrier of homogeneous nucleation ΔG_{cr} as a difference between the bulk and surface terms of the Gibbs free energy.

too high for the homogeneous nucleation and the formation of solid phase does not occur in the region I. In the region II, the supersaturation $S = {}^{C}/_{C_{\mathrm{sat}}}$ reaches the critical level $S_{\mathrm{cr}} = {}^{C_{\mathrm{cr}}}/_{C_{\mathrm{sat}}}$ high enough to overcome the activation barrier and spontaneous nucleation of the solid phase occurs. At this stage the free monomer is consumed during the nucleation and the subsequent growth processes. Since the consumption rate exceeds the rate of the chemical reaction between the molecular precursors and so of the monomer supply, the monomer concentration eventually drops below the critical supersaturation level S_{cr}. At this stage, although the monomer solution remains supersaturated, the net homogeneous nucleation rate turns to zero (no new nuclei produced) and the reaction entries the growth phase (region III). Growth of the nanoparticles continues as long as the monomer concentration C is higher than C_{sat}.

The activation barrier of homogeneous nucleation, when the system spontaneously changes from the homogeneous to the heterogeneous state, arises because the nuclei of the solid phase are less stable than either the well solvated monomer or the formed nanocrystals [205,209]. Applied to the case of two-dimensional materials, formation of a disk-like nucleus with the radius r (m) and thickness h (m) creates a phase interface with the area $2\pi r(r+h)$ and the surface energy σ (J/m^2). At the same time, formation of a seed is associated with the transition of the supersaturated solution into a stable solid state and therefore is accompanied by a reduction of the chemical potential $\Delta\mu$ (J/mol). The total change of the Gibbs free energy ΔG (J) can be written as a sum of these two, surface and bulk, terms:

$$\Delta G = 2(1+a)\pi r^2\sigma - a\pi r^3\frac{\Delta\mu}{V_{\mathrm{m}}} \qquad (1)$$

where a is a dimensionless coefficient defining the aspect ratio of a disk-like nucleus, i.e. a is equal to ${}^{h}/_{r}$; V_{m} is the molar volume of condensing phase (m^3/mol). As shown in Figure 2.1.b, the Gibbs free energy ΔG as a function of a nucleus dimension r has an extremum at the critical size of the nuclei r_{cr} [210]. For a given monomer supersaturation S in the system, only the seeds with the radius exceeding r_{cr} can spontaneously nucleate and grow in the supersaturated solution, while smaller clusters formed by random collision of the monomer are unstable and dissociate into the constituent monomer blocks. For an effective homogeneous nucleation, the supersaturation in solution should be high enough to maintain the nucleation rate at the level at which the number of seeds increases even if the smaller seeds dissolve away. Numerical analysis of the Gibbs free energy as a function of the nanocrystal size is complicated since both

nanocrystal surface energy and chemical potential are size-dependent; moreover, nanocrystal solubility rapidly increases as its diameter decreases. In real systems, the exact level of the critical supersaturation, at which the formation of stable nuclei occurs, is hard to define and the dissolution of the nuclei with the $r > r_{cr}$ can happen due to the local fluctuations in temperature or in monomer concentration [205].

To prepare monodisperse colloidal nanocrystals, the nucleation and subsequent growth stages have to essentially be separated in time. This concept became known as a "burst nucleation" approach and was first proposed by V. LaMer [207]. In burst nucleation, sudden high supersaturation is commonly achieved by a rapid injection of the molecular precursors that leads to a large number of small stable nuclei being immediately formed in the solution. Rapid depletion of the free monomer causes termination of the nucleation process and the seeds start growing. Separation of the nucleation and growth stages suggests that all nucleated nanoparticles have the same growth history and so the final size distribution is defined only during the nucleation stage and does not change during the growth stage.

The discussed thermodynamic model of the homogeneous nucleation in solution is, however, significantly simplified, and it does not consider factors associated with the chemical reaction kinetics that provide an additional, kinetic, barrier to the nucleation. For example, in very insoluble inorganic crystals the monomer concentration exceeding the solubility of the smallest possible clusters (~1 nm) allowed in the system can be easily achieved. This suggests that there is virtually no thermodynamic barrier for the spontaneous homogeneous nucleation to occur [210]. In practice, the nucleation in such systems is determined by the formation of "magic-sized clusters", which are stable nanoclusters, possessing closed electron shells [211,212]. Once formed, these clusters are thermodynamically trapped and the following growth via the addition of a few building block (monomer) is unfavourable. Instead, the growth of nanocrystals is commonly reported to proceed through the oriented attachment of the magic-sized clusters [212,213].

Finally, it should also be pointed out that even when the nucleation process goes through the classical nucleation route (thermodynamically-limited nucleation), there is a strong driving force to minimise the surface area of a nanocrystal due to exceptionally high surface-to-bulk atom ratio characteristic to the nanostructures that leads to a considerable surface reconstruction. This surface reconstruction may occur through a lattice compression and introduction of defects, i.e. stacking faults, [190] or even through a spontaneous [214] or ligand-driven [215] phase transition into a different crystal structure.

2.1.2. Diffusion-controlled growth regime

When the level of supersaturation drops below critical, the homogeneous nucleation of the new seeds of solid phase is suppressed and the system enters the growth stage. In the early '50s, H. Reiss developed a simple model of the diffusion-controlled growth of spherical particles in solution phase [205,216]. In this model, growth of spherical particles is assumed to occur under steady state conditions, specifically, when the growing particles do not interact, and the monomer concentration is accepted as constant at a certain fixed distance from the particle centre. The growth rate is proposed to be solely limited by the monomer flux to the particle surface. The amount of monomer reaching the surface of a particle with the radius r increases proportionally to r^2, while the volume of a particle increases proportionally to r^3 as a result of the monomer deposition on the particle surface. Thus, the growth rate of a spherical particle is inversely proportional to its radius, suggesting that smaller particles grow faster than the larger ones. As a consequence, Reiss model predicts that in an ensemble of growing spherical particles the size distribution always decreases as long as all particles are growing, and no additional nucleation events take place. In real systems, however, particle growth rate depends on the chemical reaction kinetics of the monomer adsorption and desorption on its surface. Qualitatively, the effect of the change in the chemical potential during the particle growth can be described as the smaller the particle radius r, the harder it is to deposit monomer on its surface, therefore dissolution of the particle becomes preferential [205]. Dependence of the particle growth rate on its radius as a result of the competing mass transport and the chemical reaction processes is depicted in Figure 2.2 [217]. Particles with the size smaller than critical r_{cr} exhibit negative growth rates ($\frac{\partial r}{\partial t}$) due to a large fraction of the surface atoms that renders them prone to dissolution back into the free monomer species. The growth rate turns positive once the particle size exceeds the critical value r_{cr}. The peak in the corresponding plot of the growth rate as a function of the particle radius is commonly explained by a geometric factor as increasing the radius of larger particles requires deposition of more monomer than for the smaller ones that explains the difference in growth rates.

At high monomer concentrations, significant difference in the growth rates of small and large particles leads to the gradual "focusing" of the size distribution due to the fact that smaller particles grow faster than the larger ones resulting in an increase of the monodispersity in the system. This effect is represented by the red curve in Figure 2.2. At low monomer concentration, the growth rates are rather slow and do not differ considerably in the broad range

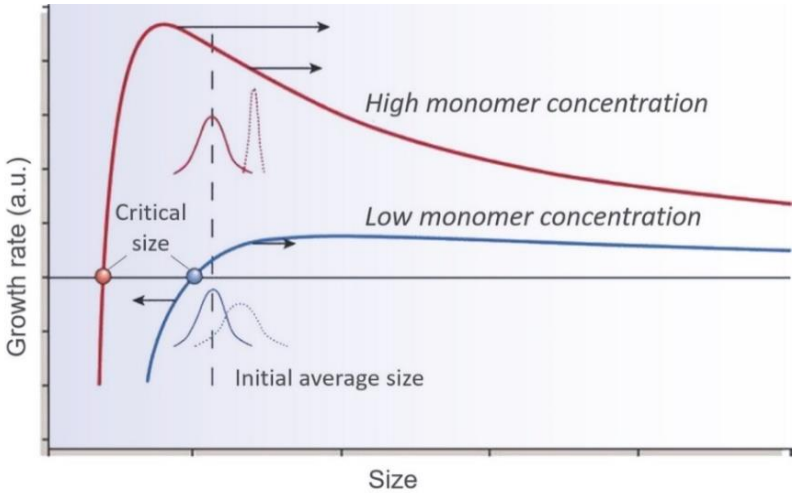


Figure 2.2. Diagram illustrating the dependence of a nanocrystal growth rate on its radius. Reprinted by permission from Springer Nature: [200]. Copyright © 2004.

of the particle sizes present in the system, as illustrated by the blue curve in Figure 2.2. These considerations lead to a major observation: slow growth rates characteristic to the crystallisation under low supersaturation (low monomer concentration) typically produce equilibrated, barely faceted, crystals exhibiting broad size distributions.

It should be noted that the critical radius r_{cr} defining the minimum size of a stable particle in the system strongly depends on the monomer concentration. In the late stages of the solution-phase crystal growth, when the free monomer is depleted down to the saturation level and the critical size falls within the range of particle sizes present in the system, growth of the particles with radius exceeding r_{cr} continues due to dissolution of the smaller ones that results in the "defocusing" (broadening) of size distribution. This process is also referred to as Ostwald ripening. Strictly speaking, Ostwald ripening can occur at any free monomer concentration as long as there are crystals with the size smaller than r_{cr} present in the system.

Overall, the diffusion-controlled solution-phase crystal growth typically favours the minimisation of the excessive surface energy and results in formation of nearly spherical (equilibrium) crystals. In practice, ensembles of particles with narrow size distribution can be achieved if the reaction is arrested when the supersaturation is still high and before the system enters the Ostwald ripening stage. Additionally, the size distribution can be refocused by the addition of extra monomer shifting the critical size to smaller values and inducing "focusing" as long as the monomer concentration remains sufficiently high (high supersaturation) [218]. Interestingly, at even higher monomer concentrations and, as a consequence, higher growth rates particles with more complex, anisotropic, morphologies can be grown as will be discussed in the next section.

2.1.3. Kinetically-controlled growth regime

Unlike the growth under low supersaturation (steady state conditions), which is also referred to as a thermodynamically- or diffusion-controlled growth regime that yields equilibrium shaped crystals with low aspect ratios, the growth at high supersaturation levels results in considerably higher crystal growth rates that allows for formation of highly anisotropic crystals. In such kinetically-controlled growth processes, the rate limiting step is the monomer deposition reaction, and the morphology that the growing particle acquires depends on the difference in growth rates of the crystal facets. Kinetically-controlled crystal growth occurs at supersaturation levels just above the size distribution focusing regime [217] and the tailored monomer-concentration-dependant morphology (aspect ratio) of the colloidal nanocrystals has been successfully demonstrated experimentally [196,219].

We should point out that a facet growth rate is defined as the rate at which this facet propagates from the centre of the crystal nucleus. The growth rate of a specific facet, along a specific crystallographic direction, depends on the corresponding surface energy since the kinetic barrier of the monomer deposition reaction is inversely proportional to the intrinsic surface energy of the facet at which the reaction occurs [220]. Under non-equilibrium conditions (high monomer flux), the monomer deposition preferentially takes place at the least stable facets exhibiting high surface energies and providing the favourable pathway to the not necessarily most stable final products. This can lead to formation of highly anisotropic morphologies [220,221]. Furthermore, the anisotropic crystals growing under the non-equilibrium conditions can stably expose the high energy facets due to the minimal formation energy barrier [222].

Difference in the growth rates of various crystal facets can be controllably modulated by adding a capping ligand selectively passivating certain crystal facets thus impeding their growth and facilitating the crystal extension in other directions. Precise tailoring of the relative growth rates, and hence the shape of the growing nanocrystals, can be achieved by varying the type [223] and the amounts [224,225] of capping ligand as well as by adjusting the ratio between various capping ligands [219]. Using this approach, colloidal semiconductor nanoparticles with various morphologies ranging from one-dimensional nanorods with high aspect ratios [226] to two-dimensional platelets [227] have been synthesised. The capping ligands (surfactants) used in the colloidal synthesis play a dual role: dynamically solvating nanocrystals and preventing their aggregation serving as a mechanical barrier. At the nanocrystal growth temperatures, surfactants adsorb on and desorb off the nanocrystal facets thus the nanocrystal surface is

transiently accessible for the monomer deposition, while at room temperature, when the reaction is arrested, form a steric barrier ensuring colloidal stability of the synthesised nanoparticles. Most commonly used capping ligands include long chain carboxylic acids and amines, alkyl phosphines and alkyl phosphonic acids. In these ambipolar molecules, polar functional head groups coordinate nanocrystals saturating the dangling bonds at the surface sites, whereas non-polar long chain organic tails interact with organic solvents providing stabilisation of the colloidal suspension. The binding energies of various capping ligands were explicitly modelled for the cadmium chalcogenides system with the general trend being that alkyl phosphines and to lesser degree primary aliphatic amines effectively passivate the chalcogen terminated crystal facets, while alkyl phosphonic acids demonstrate high affinity to the transition metal rich facets [228]. For the TMD system, information on the capping ligand binding energies is significantly limited in the recent literature. Among commonly used surfactants, oleic acid is assumed to have lower binding energy to both the {100} and {110} lateral facets compared to that of oleylamine or oleyl alcohol, while all three capping ligands show very low affinity to the chalcogen terminated {001} basal planes [169].

Gradual monomer consumption during the nanoparticle growth process results in a shift of the dominant mechanism from the kinetically-controlled to the thermodynamically-controlled that eventually leads to the nanoparticle shape evolution into the more equilibrium ones due to adsorption and desorption processes, occurring concurrently. In order to achieve highly anisotropic morphologies, growth of the colloidal nanoparticles needs to be arrested while the system is still in the kinetically-controlled mode (high monomer supersaturation).

2.1.4. Composition variation: Colloidal synthesis of hybrid nanostructures

Not only the morphology of colloidal nanocrystals but also their composition and spatial distribution of the constituent counterparts within a single nanoarchitecture can be effectively controlled during the solution-phase synthesis. The experimental wet chemistry approaches allowing for the selective modification of the composition of colloidal nanostructures can be divided into three main groups, namely, seeded growth, cation (or less commonly reported anion) exchange, and direct formation of mixed compositions, and are summarised through the comparative sketches in Figure 2.3.

Seeded growth is the most straightforward two-step approach to synthesise heterostructured hybrid nanoparticles. In this process, nanoparticles of material A are formed first (product 0) that then serve as “seeds” for the deposition of material B that is being slowly

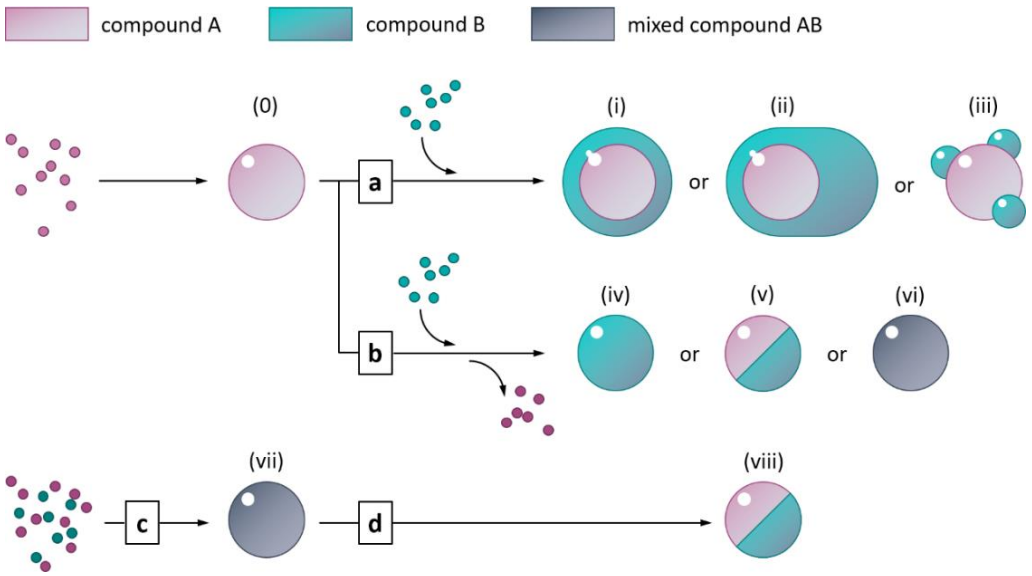


Figure 2.3. Comparative sketches of possible formation mechanisms of the hybrid nanoarchitectures via the wet-chemistry approaches. **a** Formation of the isotropic (i) or anisotropic (ii) core-shell heterostructures or the asymmetrical heterodimers (iii) via the seeded growth route. **b** Formation of the fully (iv) or partially (v) substituted, including the alloyed (vi), nanostructures via the cation exchange route. **c** Direct formation of the uniform ternary alloys (vii) and **d** the spontaneous phase segregation leading to the heterostructured nanoarchitectures (heterodimers, viii).

added into the colloidal suspension of nanoparticles A [229] as depicted by the pathway a in Figure 2.3. Deposition of material B occurs selectively on the surface of nanoparticles A since the energy barrier of the heterogeneous nucleation is considerably lower than that of the homogeneous nucleation and thus nucleation of a separate phase B in the solution is unfavourable. The formation of a heterostructured nanocrystal involves creation of an interface between two structurally different materials. Depending on the subtle balance between the intrinsic surface energies of individual phases A and B, the effect of capping ligands, and the surface energy of the A/B interface, the heterogeneous deposition can result in the formation of heterostructures with either isotropic (i) or anisotropic (ii) core/shell geometries [230,231] as well as heterodimers (iii) consisting of adjacent domains A and B [232]. The latter type of hybrid architectures has been recently achieved in the CVD grown layered transition metal dichalcogenide systems as vertical [233,234] or in-plane [234,235] two-dimensional heterostructures.

Another type of chemical transformation reported to take place in the suspensions of colloidal nanoparticles when one solid phase is being transformed into another via the replacement of its ions [236] is known as ion exchange and it is illustrated by the pathway b in Figure 2.3. Thermodynamically, the exchange process is driven by the relative stabilities of the starting phase A and the product phase B as well as by the difference in solvation, or in a

broader context, ligation, energies of the respective substituting B and the liberated A monomer species in the colloidal suspension [191]. The kinetics of ion exchange is notoriously faster at the nanoscale compared to the case of bulk solids [236]. As a result, cation exchange in ionic semiconductor nanocrystals can lead to a complete conversion of the host crystal phase (product iv). However, if incomplete, the replacement reaction leads to the formation of heterostructured (v) or alloyed (vi) transient nanoarchitectures depending on the nature and the propagation kinetics of the interface between the starting and product phases A and B, respectively. Provided that the anion framework is robust enough, sequential cation exchange allows for the realisation of anisotropic shapes, dictated by the morphology of the parent nanocrystals, in the highly symmetric crystal systems that lack the unique crystallographic direction and therefore are otherwise attained in a form of isotropic particles [192]. Additionally, cation exchange in ionic semiconductor nanocrystals has been used to acquire the product structures in the metastable crystal phases templated and locked by the symmetry of the starting material [236]. Furthermore, more complex binary heterostructures can be produced during the partial transformation occurring owing to the selective diffusion along certain crystallographic directions thus creating separate domains [237,238]. Such selectivity of the cation exchange reaction is reported to emerge due to the crystallographic relationship between two crystal phases, starting and the product, and can be amplified through the choice of suitable capping ligands modifying the surface energy of the selected crystal facets. Cation exchange can also be achieved in covalent crystals [239], however, the cation diffusion and replacement rate are expected to be significantly slower [240].

Finally, initiating homogeneous nucleation of the solid phase in the solution, containing monomer species of different compounds as illustrated by the pathway c in Figure 2.3, was successfully employed to incorporate dopants into the pristine crystal lattice [241] as well as to synthesise isostructural ternary alloys [242] as long as the mixing enthalpy remains negative. Destabilisation of the alloyed phases causes spontaneous decomposition (phase segregation) and consequently formation of the heterostructured dimers (pathway d in Figure 2.3). In Sections 4.1 and 4.2 we discuss how this experimental approach developed for the colloidal $A^{II}B^{VI}$ hybrid nanocrystals can be adapted to produce doped and alloyed TMD (WSe_2) nanostructures in solution phase.

2.2. Colloidal synthesis of atomically-thin layered metal chalcogenides

2.2.1. Experimental set-up

Synthesis of all materials discussed in this work ($MoSe_2$, $MoTe_2$, WSe_2, Bi_2Te_3, doped WSe_2 and ternary $W_xMo_{1-x}Se_2$ nanostructures) was carried out in a standard Schlenk line shown in Figure 2.4 in an inert atmosphere to minimise oxidation of both starting precursors and the material produced at relatively high growth temperatures (up to 300 ºC). In the presented set-up, the vacuum line of the double manifold (1) is connected to a rotary vane pump (4) through two traps: an absorbing trap (2) filled with finely ground KOH granules, which serve as an absorber of the gaseous HCl produced as a side-product in the syntheses from metal chlorides ($MoCl_5$, WCl_6), and a cold trap (3) cooled with liquid nitrogen during the experiment to condense evacuated organic vapours and moisture to prevent them from entering the vacuum pump. Dynamic vacuum in the system is monitored by a Pirani gauge (5); solvent degassing and metal complex formation were normally performed at 1-1.5×10^{-1} mbar. The gas line of the Schlenk manifold is connected to a nitrogen cylinder (not shown in the picture). Before entering the gas line and the reaction flasks, the inert gas is passed through a Drierite^{TM} gas-drying unit (6) to eliminate traces of moisture. The excess of nitrogen gas is vented out through a mineral oil bubbler that also acts as a liquid seal between the inert atmosphere in the gas line and the oxidising atmosphere outside. The reactions were carried out in a three-neck 50 mL flask heated by one of the heating mantles (7) placed on top of a magnetic stirrer; reaction temperature was controlled by a temperature controller (8) equipped with a thermocouple. Reaction flasks were connected to the Schlenk manifold through an antisplash adapter (9) to prevent condensed heavy organic products from returning into the reaction flask.

Both metal and chalcogen precursors used in solution-phase synthesis of transition metal chalcogenide nanostructures must satisfy two experimental criteria: firstly, to be available in a liquid form; secondly, to be reactive enough to form monomer essential for the nucleation of the material. Existence in a liquid form is an essential requirement for the molecular precursors in order to ensure homogeneous nucleation of the material in solution rather than heterogeneous nucleation that would otherwise occur on the surface of solid precursors and to allow for a precise control over the loaded precursor amounts, and hence over the stoichiometry of growing material. Molecular precursors of choice are discussed in the following sections.



Figure 2.4. Schlenk line used for solution-phase synthesis of the air-sensitive materials.

2.2.2. Choice of chalcogen precursors

In contrast to the rich sulphur-containing precursor chemistry developed for solution-phase synthesis of quantum dots, their selenium and tellurium analogues remain underdeveloped or in some cases unavailable. Elemental selenium and tellurium are known to dissolve in tertiary organic phosphines forming the corresponding selenides and tellurides upon a reaction $R_3P + E \leftrightarrow R_3P{=}E$, where E is chalcogen, R is an organic ligand [243]. Although commonly described as solutions, organic phosphine chalcogenides do not contain free elemental chalcogens, instead in this reaction the tertiary phosphine undergoes a chemical oxidation covalently binding chalcogen atoms [244]. It should be noted that in an isolated form phosphine chalcogenides are prone to dissociation, however their stability can be significantly improved if used in the presence of substantial amounts of the parent phosphine [245]. 1M trioctylphosphine selenide (TOP:Se) and trioctylphosphine telluride (TOP:Te) solutions in trioctylphosphine (TOP) were chosen as the chalcogen precursors for synthesis of the transition metal selenide and telluride nanosheets. The stock solutions were prepared by dissolution of 5 mmol of selenium (Aldrich, 99.99% trace metals basis) or tellurium (Aldrich, 99.8% trace metal basis) powder, respectively, in 5 mL of TOP (Aldrich, 90%) at 100-250 ^{o}C in an inert atmosphere of nitrogen gas, then transferred into the nitrogen filled vials with septa caps and stored in a drying desiccator (Figure 2.5.a).

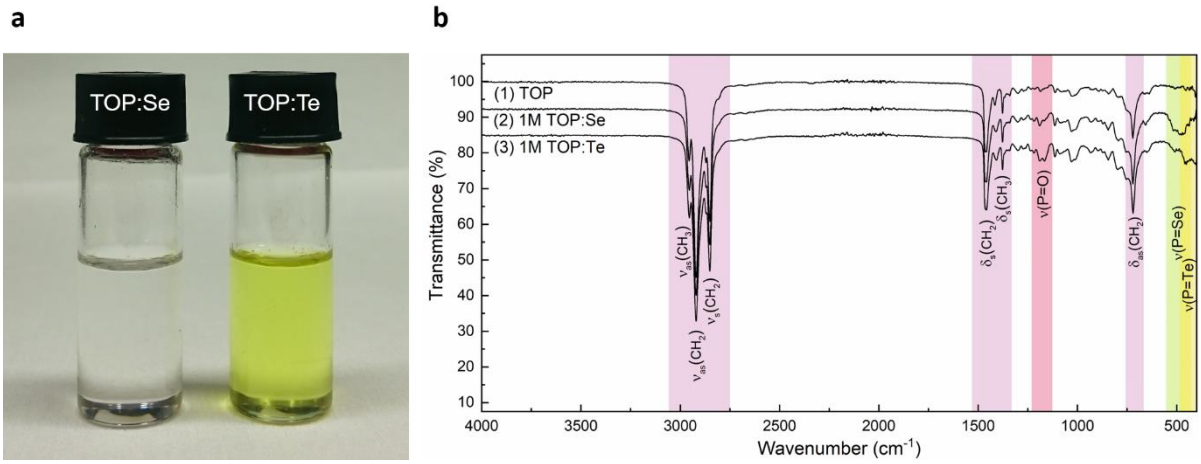


Figure 2.5. Chalcogen precursors TOP:Se and TOP:Te. **a** Photograph of 1M TOP:Se and 1M TOP:Te solutions. **b** ATR FTIR spectra of TOP (1), 1M TOP:Se (2) and 1M TOP:Te (3). Spectra are offset for clarity. Vibration modes are labelled as following: ν – stretching; δ – in-plane bending; γ – out-of-plane bending.

The dissolution of elemental chalcogens in TOP was monitored by Fourier-transform infra-red (FTIR) spectroscopy (Figure 2.5.b). The ATR FTIR spectra of 1M TOP:Se and TOP:Te demonstrate new bands appearing in the fingerprints region that are absent in the spectrum of TOP and can possibly be attributed to the stretching modes of the P=Se (centred at 490 cm^{-1}) and P=Te (observed at 420 cm^{-1}) bonds [246]. The strongest IR peaks can be assigned to the C-H bond vibrations: symmetric ν_s and asymmetric ν_{as} stretching modes of the CH_3 (at 2870 and 2955 cm^{-1}) and the CH_2 (at 2850 and 2919 cm^{-1}) groups, symmetric δ_s bending of the CH_3 (umbrella, at 1377 cm^{-1}) and symmetric δ_s (scissoring, at 1463 cm^{-1}) and asymmetric δ_{as} (rocking, at 722 cm^{-1}) in-plane deformations of the CH_2 groups of the alkyl chains. A weak vibration mode found at 1180 cm^{-1} in TOP:Te and nearly absent in TOP:Se can be assigned to a stretching mode of the P=O bond [247] and can indicate a minor oxidation of the phosphine during the reaction with tellurium occurring at 250 ^{o}C.

The alternative selenium precursors used in this work to investigate the role of precursor reactivity in colloidal synthesis of the $MoSe_2$ and WSe_2 nanostructures were elemental selenium and a solution of elemental selenium in oleylamine (OlAm). It has been reported that elemental selenium can be dissolved in many organic solvents through a series of reactions at the C-H and double -C=C- bonds of aliphatic hydrocarbons [244,248] or by oxidation of the N-H and $^{\alpha}$C-H bonds of aliphatic amines [249]. Active forms of selenium in the organoselenium intermediates produced in these reactions are still being investigated, however a number of studies have clearly demonstrated that heating of the elemental selenium in long-chain organic solvents commonly used in colloidal synthesis of the semiconductor nanoparticles

(hexadecane, octadecene, octylamine, oleylamine) results in formation of gaseous H_2Se as one of the products, which, although rarely mentioned in literature on colloidal synthesis, can induce higher reactivity of the "dispersed" selenium compared to the tertiary phosphine selenides [250]. In this work, 1M Se:OlAm stock solution was prepared by dissolving 5 mmol of selenium powder (Aldrich, 99.99% trace metals basis) in 5 mL of OlAm (Aldrich, 70%) at 250 °C in a nitrogen atmosphere and was used within an hour after preparation to minimise any possible change of the reactivity which occurs over time [248].

Finally, elemental selenium, used in a few syntheses of the $MoSe_2$ and WSe_2 nanostructures discussed in Chapter 3, supposedly melts (T_m = 221 °C, [251]) and then reacts with a coordinating solvent, oleic acid (OlAc), leading to the H_2Se evolution. Presence of the *in situ* generated H_2Se can possibly explain the experimentally observed higher reactivity of the elemental selenium compared to TOP:Se. This hypothesis is supported by the fact that a thin layer of the brick-red amorphous selenium was repeatedly observed on cold parts of the glassware (cold neck of the reaction flask, adaptors, antisplash condenser) after the syntheses from elemental selenium, whereas no evidence of selenium contamination of the glassware was found after syntheses from TOP:Se, while the reaction temperature (300 °C) was not high enough for the elemental selenium to evaporate (685 °C, [251]).

2.2.3. Preparation of colloidal $MoSe_2$, $MoTe_2$, and WSe_2 nanostructures

The approach to synthesise colloidal $MoSe_2$, $MoTe_2$, and WSe_2 branched nanosheets introduced in this work is based on the reaction between a transition metal precursor and a chalcogen precursor occurring in the solution phase. In a typical synthesis, nucleation of the material followed by the growth from molecular precursors is induced by a rapid injection of the chalcogen precursor into a hot solution containing the metal precursor. Designing the synthesis protocol, we have chosen to avoid commonly used di-*t*-butyl selenide [252] or diphenyl diselenide [153,169] due to their toxicity and tungstate or molybdate salts [163,170] potentially leading to the increased content of oxidised material owing to incomplete selenisation/tellurisation process. Chalcogen precursors of choice were introduced in Section 2.2.2. Transition metal molecular precursors were prepared by dissolving inorganic transition metal complexes ($W(CO)_6$, WCl_6, $Mo(CO)_6$, $MoCl_5$) in long chain organic solvents (oleic acid, oleylamine, octadecene). The organic solvents were degassed prior to the synthesis in order to minimise the amount of dissolved oxygen, which otherwise could lead to undesirable oxidation of the growing material, and the transition metal complexes were normally transferred under nitrogen into the degassed solvent and then were kept at 200 °C under vacuum until complete

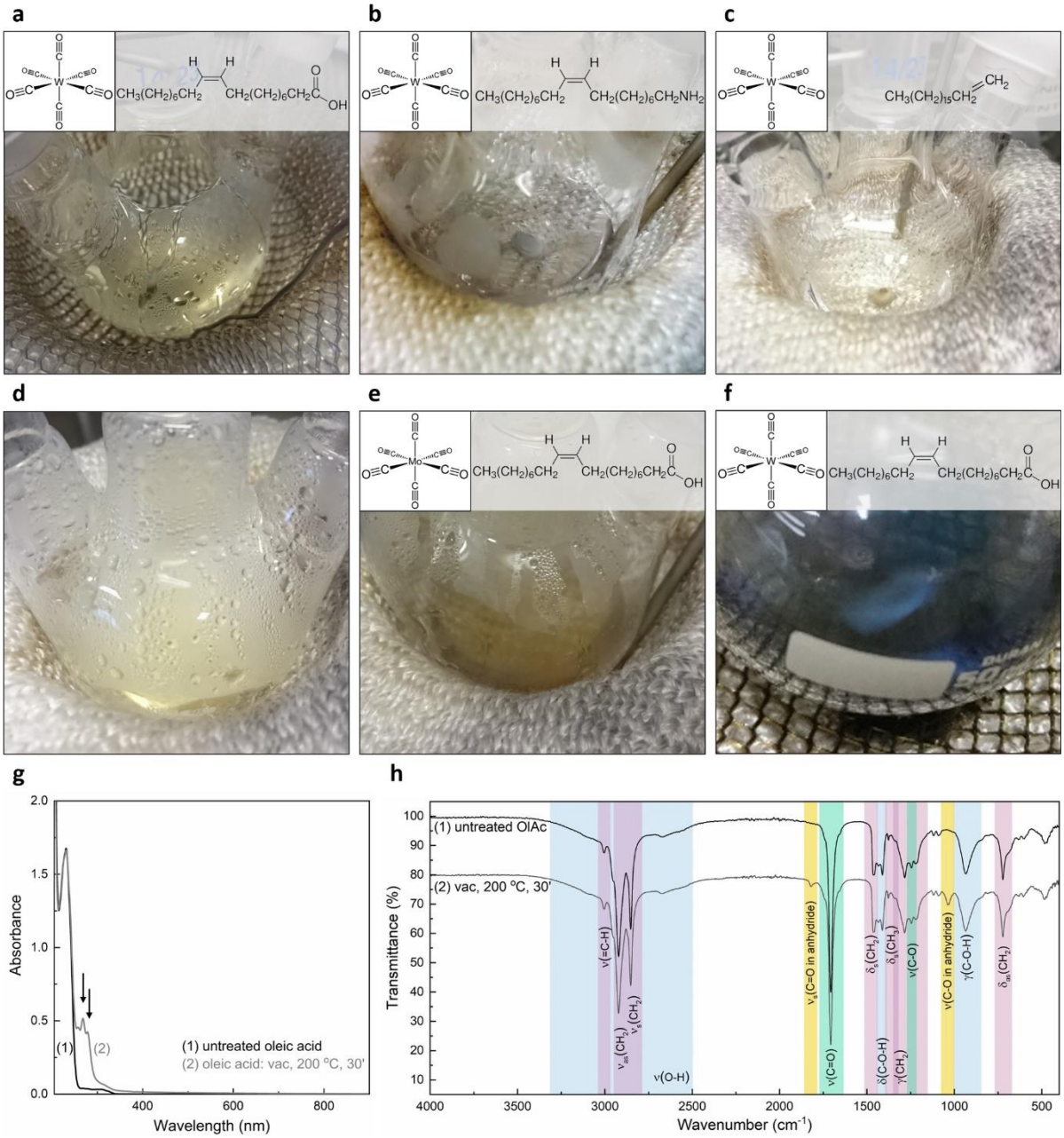


Figure 2.6 Tungsten molecular precursor. **a-c** Photographs of tungsten complex formed by dissolving tungsten carbonyl in either oleic acid, or oleylamine, or 1-octadecene (in presence of minimum amount of oleic acid), respectively; photograph in panel **f** shows tungsten carbonyl complex dissolved in untreated oleic acid. **d** Photograph of oleic acid after 30 minutes treatment at 200 °C under vacuum. **e** Photograph of molybdenum complex formed by dissolving molybdenum carbonyl in oleic acid. **g, h** UV-vis absorption spectra and ATR FTIR spectra of untreated oleic acid (1) and oleic acid after 30 minutes treatment at 200 °C under vacuum (2), respectively.

dissolution. The growth of $MoSe_2$, $MoTe_2$, and WSe_2 nanosheets was performed at 300 °C. This growth temperature was chosen as no nucleation of the material was observed at lower temperatures, which is in good agreement with previous reports [168], and higher temperatures would cause solvent boiling (oleic acid T_b = 360 °C; 1-octadecene T_b = 315 °C). After three

hours at this temperature, the reaction was quenched by rapid cooling the reaction flask to room temperature and the produced material was isolated from the unreacted precursors by centrifugation at 5000 rpm for 15 minutes, repeatedly washed with ethanol/acetone mixture (1:1 volume ratio), and then redispersed in ethanol. A standard reaction duration of 3 hours was chosen after a series of preliminary experiments that have shown that shorter growth times did not allow accumulating enough material for a successful isolation from the unreacted precursors mixture by centrifugation, whereas extending the reaction time up to 19 hours did not lead to the observable changes in either amount or morphology of the produced final products as discussed in Sections 3.1.2 and 3.3.3 and therefore was found unnecessary in a standard reaction.

Tungsten and molybdenum carbonyls are white, translucent crystals stable in air and therefore were the preferred source of transition metal in the oxidation state 0 as they led to lower oxide content in the final product. Both carbonyls can be solubilised in non-polar organic solvents forming nearly colourless (tungsten carbonyl) or slightly brownish (molybdenum carbonyl) complexes as presented in Figure 2.6.a-c,e. Dissolution is supposedly accompanied by partial substitution of one or a few carbonyl ligands and so by a coordination of the transition metal centres with long chain organics. It should be noted that the observed brownish tint of the molybdenum solutions can possibly be attributed to partial dissociation of the less thermally robust molybdenum carbonyl suggested by lower first carbonyl dissociation energy compared to that of $W(CO)_6$ [253] rather than caused by formation of Mo^{IV} or Mo^{V} species [254] in inert atmosphere of nitrogen gas. The pale-yellow colour of tungsten carbonyl dissolved in oleic acid is attributed to oleic acid itself. Unlike oleylamine or octadecene, oleic acid undergoes a condensation reaction with formation of the corresponding anhydride when heated under vacuum; the resulting solution appears to be pale-yellow in colour (Figure 2.6.d). As demonstrated in Figure 2.6.h, the condensation reaction is accompanied by the anhydride in-plane C=O and -C-O stretching vibration modes appearing at 1819 and at 1038 cm^{-1}, respectively; while in the corresponding absorption spectrum a number of new peaks arise in the range 268-280 nm (marked with black arrows in Figure 2.6.g) in addition to the absorption bands of a double C=C bond centred at 230 nm [255]. Similar changes were observed in the absorption spectra of $Mo(CO)_6$ dissolved in oleic acid (indicated by black arrows in Figure 2.7.a). Formed as a side-product of the condensation and not completely removed adventitious water could cause oxidation of the $MoSe_2$, $MoTe_2$, or WSe_2 product directly during the growth in solution phase. It should also be mentioned that the tungsten carbonyl complex in oleic acid,

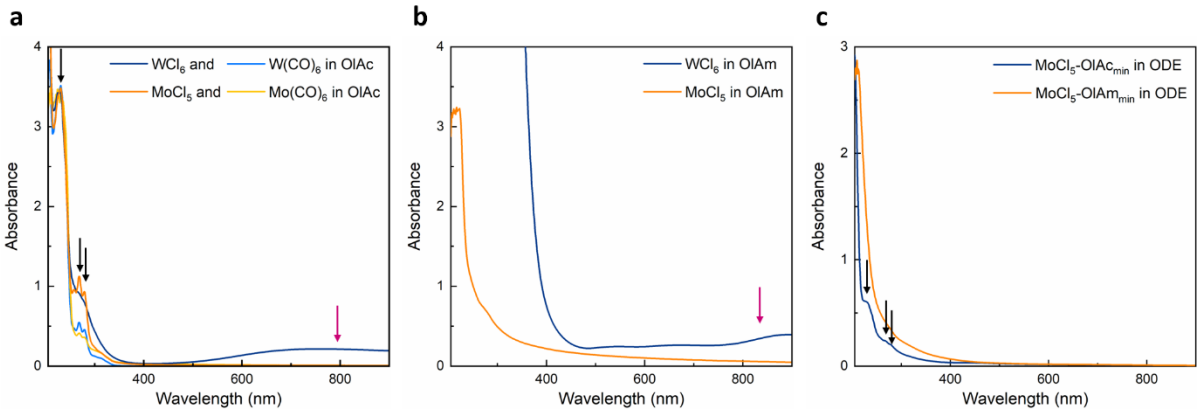


Figure 2.7. Transition metal complexes formed in various long-chain organic solvents. UV-vis absorption spectra of transition metal carbonyls ($W(CO)_6$ and $Mo(CO)_6$) and chlorides (WCl_6 and $MoCl_5$) dissolved **a** in oleic acid, **b** in oleylamine, and **c** in octadecene in presence of minimum amount of oleic acid at 200 °C under vacuum.

if formed at room temperature or if oleic acid was not degassed beforehand, would turn dark-blue when heated up to the reaction temperature (300 °C) as shown in Figure 2.6.f; this deep-blue colour can possibly be attributed to the W^V/W^{VI} oxidised species [256] and can be explained by formation of the W^V bronzes through the reaction with dissolved oxygen and adventitious water. Similar experiments were not conducted for molybdenum carbonyl dissolved in oleic acid.

Considering the similarity in the first transition metal-ligand bond dissociation energies, tungsten (VI) and molybdenum (V) chlorides are expected to demonstrate activities close to that of the respective carbonyls [257]. However, transition metal chlorides were seldom used for synthesis within this work as both are readily hydrolysed even by moist air that led to formation of highly oxidised TMD material. In the long-chain organic solvents selected within this work both chlorides form dark solutions; rapid oxidation of the starting transition metal precursors with formation of brightly coloured (yellow to orange) oxychlorides became evident, for example, when transition metal chlorides were solubilised in oleylamine or oleic acid in a nitrogen filled vial.

The UV-vis absorption spectra of tungsten and molybdenum inorganic complexes dissolved in various long-chain organic solvents are provided in Figure 2.7. Interestingly, complexes formed from either carbonyls, where the starting oxidation state of transition metal is 0, or from the corresponding chlorides containing transition metal in the highest oxidation state +5 or +6 do not display absorption transitions in the visible range apart from those associated with oleic acid and its anhydride (pointed with black arrows in Figure 2.7.a); broad band centred around 800 nm (highlighted with purple arrow) observed in the spectrum of WCl_6

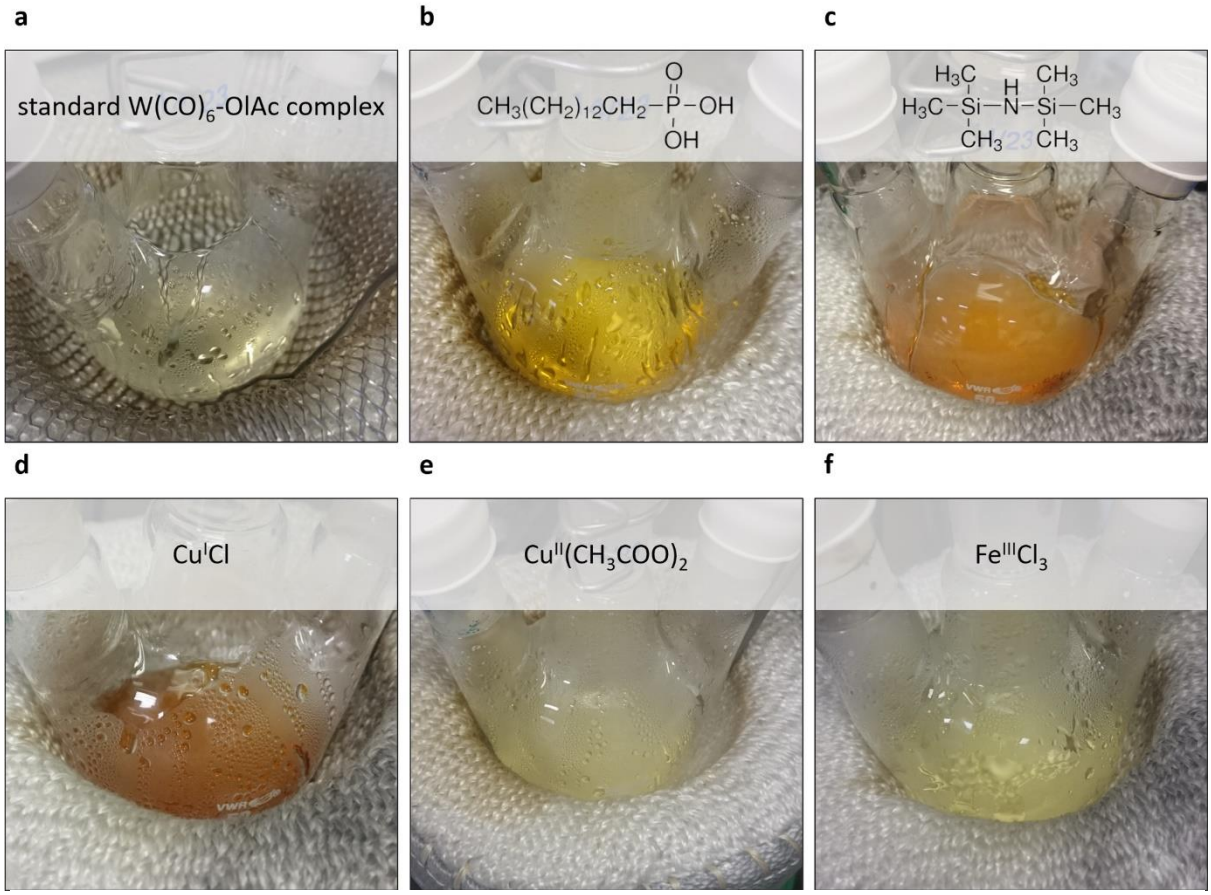


Figure 2.8. Modification of the tungsten precursor. **a** Standard tungsten carbonyl complex in oleic acid. **b, c** Tungsten carbonyl complex in oleic acid formed in presence of TDPA and HMDS, respectively. **d, e, f** Tungsten carbonyl complex in oleic acid formed in presence of $Cu^{I}Cl$, $Cu^{II}(CH_3COO)_2$, and $Fe^{III}Cl_3$, respectively, used in syntheses of the doped WSe_2 nanosheets.

dissolved in oleic acid can be attributed to the presence of oxidised tungsten species. When the solvent was changed to oleylamine, only a strong absorption band of the amino-group is recorded in the UV region in the corresponding spectra (Figure 2.7.b); broad band of oxidised tungsten species was reproducibly observed (marked with purple arrow). Similar features corresponding to oleic acid or oleylamine were observed in the spectra of transition metal complexes dissolved in octadecene in presence of minimum amount of oleic acid or oleylamine as shown in Figure 2.7.c. The absence of absorption bands, corresponding to the transition metal complexed with long-chain organic ligands, in the respective UV-vis spectra hindered the direct investigation of the reaction between the solubilised transition metal precursor and the chalcogen precursor.

The reactivity of transition metal complexes in oleic acid was modified through complexing with two additives, namely tetradecylphosphonic acid (TDPA) and hexamethyldisilazane (HMDS, Figure 2.8.a-c). Being a stronger binding ligand compared to

oleate [258], TDPA is expected to increase thermal robustness of the tungsten precursor and so to lower its reactivity. TDPA is widely reported in the shape-selective colloidal synthesis of the $A^{II}B^{VI}$ quantum dots, however, it is seldom mentioned in the current literature on the solution-phase growth of TMD nanoarchitectures [169]. In its turn, HMDS was suggested to increase reactivity of the tungsten complex due to weaker binding to a transition metal compared to carboxylic acid [156] and has recently been identified as a crucial component allowing for obtaining well-defined TMD nanostructures [171,259,260]. To obtain the modified transition metal complex, the respective additives were transferred into the reaction flask containing degassed oleic acid prior to the addition of transition metal carbonyl; the mixture was then kept under vacuum for additional 15 minutes. Then the transition metal complex was formed as described in the standard synthesis.

Table 5. Experimental parameters varied in colloidal synthesis of the $MoSe_2$, $MoTe_2$, and WSe_2 nanosheets.

Synthesis parameter		**Range**
Metal precursor	- transition metal carbonyls	$Mo(CO)_6$ and $W(CO)_6$ as powders
	- transition metal chlorides	$MoCl_5$ and WCl_6 as powders and as solutions in OlAc or OlAm
	- transition metal oxo complex	$MoO_2(acac)_2$
Chalcogen precursor	- tellurium precursor	1M TOP:Te
	- selenium precursor	1M TOP:Se; Se powder; freshly prepared 1M Se:OlAm
Solvent	- coordinating	OlAc; OlAm
	- non-coordinating	ODE
Growth time	- t_{growth}	180-1140 minutes
Additives	- modification of the transition metal complex	TDPA; HMDS
	- doping of the final material	CuCl, $Cu(ac)_2$; $FeCl_3$

In a similar way, transition metal complex was modified in order to achieve ternary composition and doped material discussed in Chapter 4. Ternary $W_xMo_{1-x}Se_2$ alloys were obtained through a reaction between TOP:Se and mixed transition metal complex in oleic acid formed from tungsten and molybdenum carbonyls taken in the desired molar ratio. Synthesis of the Cu- and Fe-doped material was attempted by adding a certain amount (<16 at.% in all three cases) of salt containing the required cation along with transition metal carbonyl into degassed oleic acid; the following steps of the procedure were as described above. Salts chosen to modify the transition metal complex were CuCl, $Cu(ac)_2$, and $FeCl_3$. Photographs of the

modified transition metal precursor are presented in Figure 2.8.d-f. Upon dissolution of bluish-green $Cu^{II}(ac)_2$ and brownish $Fe^{III}Cl_3$ chloride in excess of oleic acid, formation of the respective coloured oleates is expected, however, both tungsten precursors formed in presence of copper acetate and iron chloride appear pale-yellow in colour similar to the standard tungsten carbonyl complex complexed with oleic acid (Figure 2.8.e,f), absence of visual changes can be explained by low concentration of copper and iron oleates in the modified tungsten precursor. On the other hand, formed in presence of greenish-grey $Cu^{I}Cl$ tungsten complex gradually turns brown upon heating to 200 °C under vacuum (Figure 2.8.d). Since the modified transition metal complex was prepared at high temperature under vacuum, the side products, such as HCl and CH_3COOH, were completely removed from the reaction medium before the chalcogen precursor was injected.

The scope of the experimental conditions studied in this work is summarised in Table 5.

2.2.4. Preparation of colloidal two-dimensional Bi_2Te_3 nanostructures

In a standard synthesis, Bi_2Te_3 nanosheets were produced through a reaction between *in situ* formed bismuth oleate and TOP:Te in a non-coordinating solvent ODE. In this work, oleylamine was not used as a solvent since it is expected to reduce bismuth salts, inducing nucleation of bismuth nanoparticles in solution phase [[261]]. Bismuth oleate was obtained via the following exchange reaction:

$$Bi(CH_3COO)_3 + xC_{17}H_{33}COOH \rightarrow Bi(C_{17}H_{33}COO)_x(CH_3COO)_{3-x} + xCH_3COOH\uparrow.$$

For that, 0.5 mmol of bismuth (III) acetate (Sigma-Aldrich, 99.99% trace metals basis) and 0.5-3.5 mmol of OlAc (Aldrich, 90%) were added in 10 mL of ODE (Aldrich, 90%) and the mixture was degassed under vacuum for 30 minutes. The mixture was then heated to 150-160 °C under a nitrogen flow and was kept at this temperature until complete dissolution of bismuth acetate. The solution of bismuth oleate in ODE was degassed one more time to extract free acetic acid.

Formation of bismuth oleate was studied by ATR FTIR spectroscopy (Figure 2.9.b). The ligand exchange reaction was accompanied by the symmetric ν_s and asymmetric ν_{as} stretching modes of the deprotonated -COO^- group of oleic acid appearing at 1404 and 1536 cm^{-1}, respectively, while presence of the C-H bond vibrations assigned to the CH_2 (ν_s at 2850 cm^{-1} and ν_{as} at 2920 cm^{-1}) and =C-H (3005 cm^{-1}) groups, which are absent in the spectra of acetic acid and acetates, prove that the ligands were indeed unsaturated long-chain oleyl radicals. At the same time, the disappearance of the strong C=O stretching vibration (1710 cm^{-1}), characteristic of the uncharged oleic acid, and absence of the broad O-H stretching (3500-

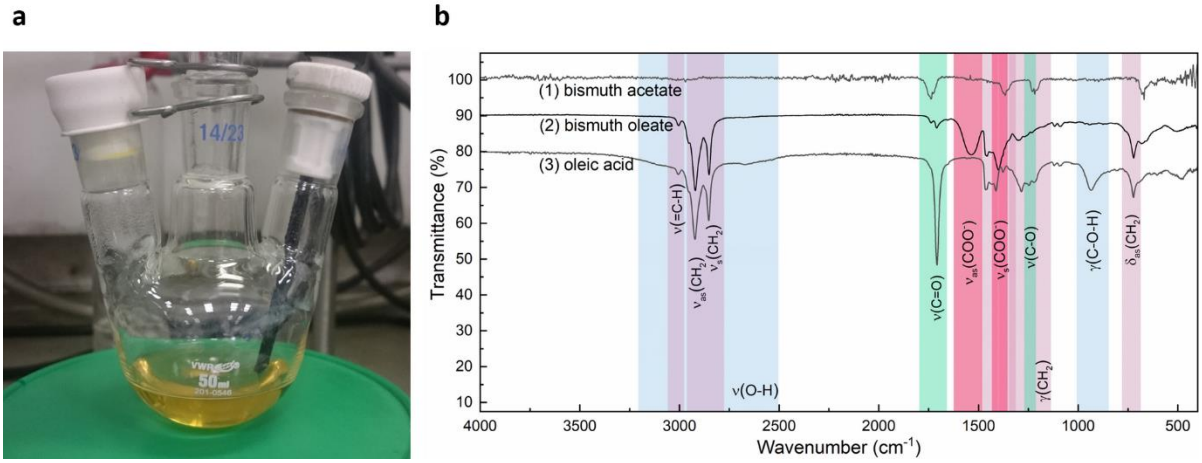


Figure 2.9. Stoichiometric bismuth oleate used as the metal precursor in synthesis of the Bi_2Te_3 nanosheets. **a** Photograph of stoichiometric bismuth oleate. **b** ATR FTIR spectra of bismuth acetate (1), stoichiometric bismuth oleate (2), and free oleic acid (3). Spectra are offset for clarity.

2500 cm^{-1}) and bending (at 930 cm^{-1}) bands was a good indication that the exchange reaction was complete, and that free acetic acid was removed from the bismuth precursor.

Bismuth oleate, that appeared as a clear, pale-yellow to bright-yellow, solution in ODE (Figure 2.9.a), was then brought to the growth temperature T_{growth} ranging from 20 to 170 ºC and 0.75 mmol of 1M TOP:Te was quickly injected into the reaction flask to initiate nucleation of the Bi_2Te_3 nanosheets. Following the swift injection of trioctylphosphine telluride, the colour of the reaction mixture slowly changed to light-brown and then black, indicating the formation of Bi_2Te_3 nanosheets at 20 ºC; the colour change was nearly instantaneous at higher growth temperatures (70-170 ºC). The growth was stopped by rapid cooling to room temperature. As produced Bi_2Te_3 nanosheets were isolated from the reaction medium via centrifugation at 3000 rpm for 15 minutes, washed with ethanol/acetone (1:1) mixture and then redispersed in 4 mL of hexane. The produced suspensions in ethanol and dried powders for analysis were stored in a drying desiccator to prevent degradation as a contact with moisture and not with molecular oxygen was identified as the key reason for the material quality deterioration [262].

The growth conditions, such as growth temperature and time, type of solvent (coordinating vs non-coordinating) and type of bismuth precursor (partially substituted bismuth acetate, stoichiometric bismuth oleate, and bismuth oleate containing the excess of free oleic acid), were varied in a wide range as summarised in Table 6. Full list of samples and the corresponding synthesis conditions is provided in Appendix A4.

Table 6. Experimental parameters varied in colloidal synthesis of the Bi_2Te_3 nanosheets.

Synthesis parameter		**Range**
Growth temperature	- T_{growth}	20-180 ºC
Growth time	- t_{growth}	0.25-1440 minutes
Bismuth precursor	- $[Bi(CH_3COO)_3]$:[OlAc]	1:1; 1:3; 1:7

2.3. Physical characterisation techniques and instrumentation

The synthesised colloidal $MoSe_2$, $MoTe_2$, Bi_2Te_3, and WSe_2 free-standing nanostructures and their ensembles grown directly on conductive substrates were characterised by various spectroscopic and microscopic techniques including optical absorption, FTIR, and Raman spectroscopies and scanning and transmission electron microscopies. In this section we explain the basic principles of these techniques and describe the relevant sample preparation procedures.

2.3.1. Scanning electron microscopy

Scanning electron microscopy (SEM) was employed to study the morphology of the free-standing nanostructures and the surface topography of the samples grown directly on carbon-based conductive substrates.

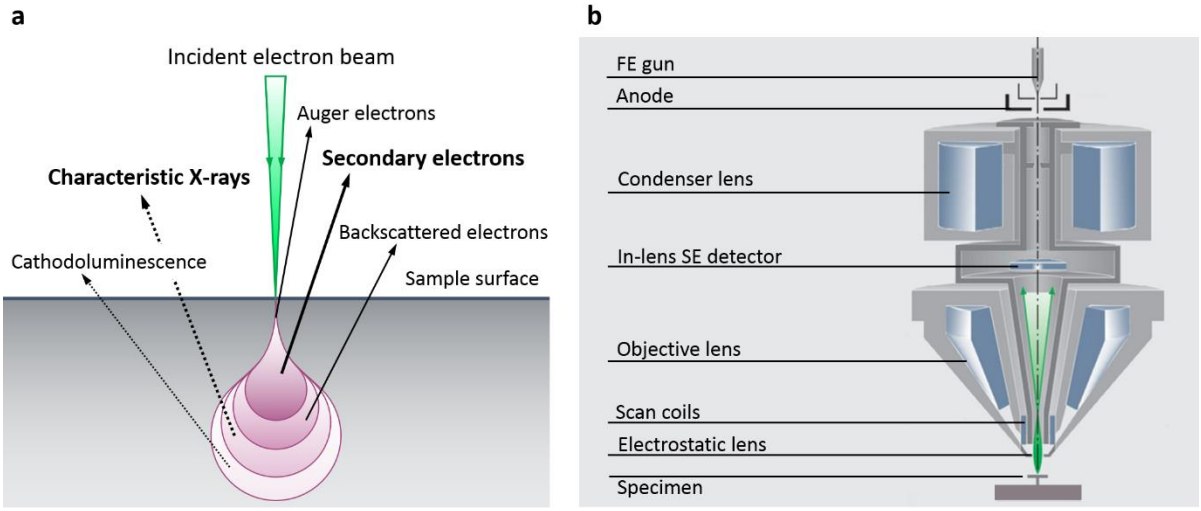


Figure 2.10. Basic principles of scanning electron microscopy. **a** A diagram showing the variety of electron-matter interactions, occurring in thick samples. The electron and radiation signals used to produce SEM images and elemental spectra/maps are given in bold. **b** A schematic cross-section of the Zeiss Sigma FEG-SEM column. Adapted from *www.zeiss.com*.

SEM is an analytical method to produce enlarged images of samples by scanning their surface in a raster scan pattern with a focused electron beam. When interacting with the sample, the electron beam generates numerous analytical signals used to acquire information about sample topography and chemical composition. The detected signal intensity is correlated to the beam position to form an image or the corresponding elemental map.

The interaction of focused electron beam (probe) with the atoms of the sample generates various signals including Auger, secondary (SE) and backscattered (BSE) electrons and the characteristic X-rays and visible light photons (cathodoluminescence) at different depths in the

sample as shown in Figure 2.10.a. Both the penetration depth of the primary electron beam and the interaction volume depend on the kinetic energy of electrons and density of the specimen [263]. Generally, the interaction volume is greater at higher accelerating voltages, while decreases with the material density increasing. Secondary electrons are the electrons produced by the ionisation of the sample atoms by the primary electrons of scanning beam. Since the kinetic energy of secondary electrons is one to two orders of magnitude lower than that of the incident beam electrons, the distance that a secondary electron travels between the consecutive inelastic collisions in solids is typically only a few nanometres and therefore only a small fraction of secondary electrons, generated within vicinity of the sample surface, escape to vacuum, while the majority of them is being reabsorbed [264]. Thus, the secondary electron imaging provides the information on the sample topography. On the other hand, the backscattered electrons are the primary beam electrons that have been deflected and scattered through high angles by the nuclei of atoms in the specimen. The probability of elastic scattering process increases for heavier elements and so the intensity of BSE signal is strongly related to the atomic number, showing variation in chemical composition of the sample. The kinetic energy of backscattered electrons is close to that of the primary beam and the BSE signal originates within the tens to hundreds nanometres depth from the sample's surface [264].

In a typical SEM, electrons of the primary beam are either emitted thermally or extracted by the applied electrostatic field. Thermionic emission can be assisted by applying an electrostatic field to the cathode that allows lowering the work function of emitter material and so achieving the emission at lower operating temperature. The extracted electrons are then accelerated by electric field generated between the emitter and the anode parallel to the optic axis (Figure 2.10.b). The kinetic energy of the primary beam electrons typically ranges from 2 to 30 keV. Passing through a set of condenser and then objective lenses, the beam is focused to a very small probe about a few nm in diameter (on a flat surface). The probe is scanned in two perpendicular directions in a raster fashion over the sample surface by the scanning (deflecting) coils located just above the objective (electrostatic) lens in the electron column. The generated signal, secondary and backscattered electrons, is recorded by the respective detector; rich three-dimensional morphology of the colloidal branched nanosheets was imaged using the SE signal. Essentially, the SE detector consists of a scintillator placed inside a Faraday cage in the specimen chamber of an SEM. Since the kinetic energy of secondary electrons is typically lower than 50 eV, a small potential is applied to the Faraday cage to draw the SE, escaping from the sample surface to the detector. The backscattered electrons have

higher kinetic energy close to that of the primary beam and so are not attracted to the SE detector by this potential. Once reached the scintillator, the SE signal is converted into the visible light photons that travel outside the microscope chamber through the waveguide to a photomultiplier. The amplified signal is then guided to a photocathode, where the photons are absorbed to generate an electrical signal corresponding to the SE signal intensity at the particular spot of a raster image. In contrast to the conventional side-mounted Everhart-Thornley SE detectors, the in-lens SE detectors are located directly above the sample surface, and so the images recorded using this type of detectors are not affected by the intensity asymmetry artefacts. Moreover, due to their unmatched sensitivity to of the low-energy electrons, the in-lens SE detectors allow detecting the signal from the top-most layer of a sample at low accelerating voltage [265,266]. For this reason, imaging of the atomically-thin TMD nanostructures was performed in the SE detection mode using an in-lens detector.

Interacting with the sample, an electron of the primary beam may knock out a core level electron. The hole in the inner shell is then filled with an electron from the outer shell. The excess of energy is carried away by an emitted X-ray photon. The energy of emitted X-rays is characteristic to a particular atom and can be used for elemental analysis (energy-dispersive X-ray spectroscopy, EDS) [263,267]. In SEM, characteristic X-rays, generated by scanning the sample's surface with a focused electron probe, are detected with an integrated energy-dispersive detector. Commonly used detectors are silicon drift detectors (SDD) that convert the X-ray signal into current due to ionisation of a semiconductor sensor [268]. The number of charges created in the detector is proportional to the energy of individual incoming X-ray photon. The EDS spectra are recorded by counting the number of X-rays per energy interval. The continuous background in EDS spectra arises from the gradual deceleration of the primary electrons due to interactions with the atom nuclei as they pass through the sample. Maximum in the spectrum of deceleration radiation (Bremsstrahlung) corresponds to the energy of incident electrons. The characteristic X-rays appear as sharp peaks at the corresponding energies. EDS spectra provide essential information about the sample composition. However, quantitative elemental analysis using EDS is complicated due to the losses of X-rays before they escape the surface due to reabsorption or deflection by the atoms in the bulk of the sample.

The samples for SEM imaging and elemental analysis were prepared by drop-casting the dilute dispersions of synthesised colloidal nanostructures in ethanol onto the acetone cleaned Si/SiO_2 substrates and dried overnight. Thus prepared samples were mounted on the SEM stubs using a carbon tape and grounded using silver paint to minimise charging effects. Preliminary

imaging and qualitative elemental analysis were performed on a JEOL JSM-6010LA InTouchScope scanning electron microscope at 20 kV accelerating voltage and working distances between 13 and 15 mm. For high resolution SEM imaging, the experiments were carried out on a Zeiss Sigma 300 field emission scanning electron microscope, while Zeiss LEO Gemini 1525 field emission scanning electron microscopes equipped with an Oxford x-act EDS detector was used for the acquisition of the elemental maps. Images were typically recorded using an in-lens secondary electron detector at 5 kV accelerating voltage at working distances below 8 mm. EDS maps were obtained at 20 kV and working distance of 10-12 mm.

2.3.2. Transmission electron microscopy

Transmission electron microscopy (TEM) was performed to investigate the morphology of colloidal $MoSe_2$, $MoTe_2$, Bi_2Te_3, and WSe_2 free-standing nanostructures; local lattice symmetry and structural defects in these ultra-thin nanosheets; and spatial distribution of the chemical components of colloidal alloyed $W_xMo_{1-x}Se_2$ nanosheets.

Similarly to scanning electron microscopy, transmission electron microscopy is based on using various electron signals produced due to the interaction of a high energy incident electron beam with ultra-thin samples. In contrast to SEM, only the electrons that have passed through the specimen are analysed in TEM [263]. These transmitted electrons that do not deviate far from the direction of the incident beam contain information about sample morphology, chemistry and crystal structure (Figure 2.11.a). Passing through a thin sample, the electrons are scattered due to interactions with the electrostatic field of nuclei or with the electron clouds of specimen atoms. Those that remain unaffected and exit the sample in the direction of the incident beam are referred to as the direct beam, whereas scattered electrons are those that are deviated from their initial trajectory through small angles [269]. Scattering can be classified as elastic if the electron interacts with the sample without losing its energy or inelastic if the energy loss is measurable. Additionally, in ultra-thin crystalline samples, describing the electron scattering on electron clouds of atoms as diffraction of the plane wave is more informative as this explains formation of the direct and the diffracted beams when the lattice planes are suitably oriented to satisfy the Bragg's condition [269].

Interacting with the crystal lattice, the incident electron wave can change its amplitude and its phase; this gives rise to amplitude and phase contrast in TEM images. These contrast formation mechanisms contribute simultaneously, however, the imaging conditions can be optimised in such a way that only one of these mechanisms would dominate thus producing an

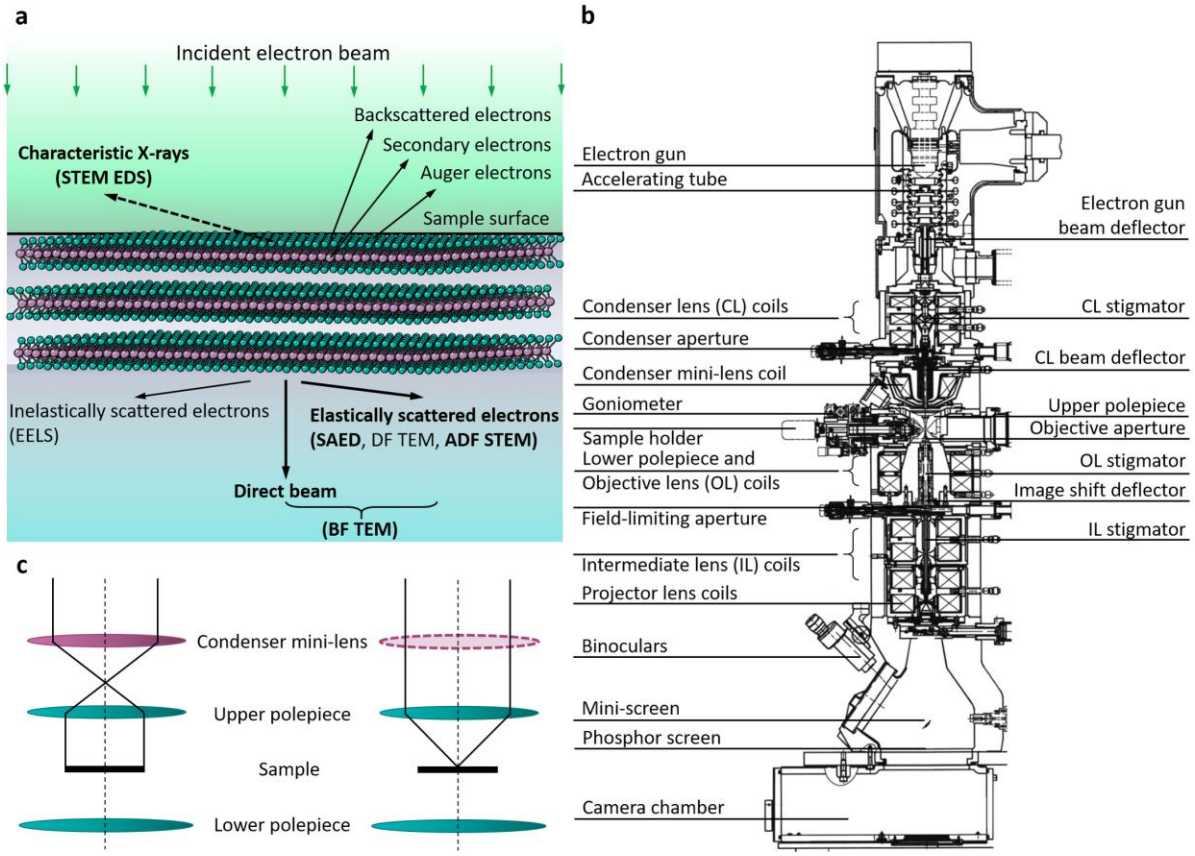


Figure 2.11. Basic principles of transmission electron microscopy. **a** A diagram illustrating the variety of electron-matter interactions, arising in a thin crystalline sample. The electron and radiation signals used to produce TEM images and elemental spectra/maps are given in bold. **b** Schematic cross-section of a TEM column. Adapted from *www.zeiss.org*. **c** A diagram demonstrating the condenser mini-lens system operating in TEM (left panel) and STEM (right panel) modes.

interpretable contrast in the image. The amplitude of the plane electron wave passing through a thin sample can change due to variations in sample thickness or composition (density) since thicker areas of the sample or domains, containing heavier chemical elements, would scatter electrons more effectively, resulting in darker areas in TEM images. This type of contrast is referred to as mass-thickness contrast. The diffraction contrast in TEM imaging is achieved by selecting only one, either the direct or the diffracted, beam to pass to the detector to form either a bright-field (BF) or a dark-field (DF) image, respectively. Selecting only the central (direct) beam would produce the amplitude contrast between scattering and non-scattering areas in the image whether the sample is crystalline or amorphous. The phase contrast arises when more than one of the diffracted beams contribute to the image. Constructive interference of the diffracted beams results in formation of contrasting fringes. At high magnification, if the crystalline specimen is oriented in such a way that the incident beam is parallel to a low-index zone axis (ZA), the interference pattern of two and more selected diffracted beams produces lattice fringes. The on-axis lattice fringe images cannot be treated as a direct visualisation of

atomic columns in the sample. Instead, they shall be used to characterise the local crystal structure and orientation.

A schematic cross-section of a TEM column is presented in Figure 2.11.b. The optical system of a transmission electron microscope consists of the illumination (probe forming) system, including the electron gun (source) and a sequence of condenser lenses, deflector coils, apertures and stigmators; image forming system composed of the objective, intermediate, and projector lenses; and a set of various detectors. In this work, TEM imaging was performed using two JEOL microscopes: a JEM-2100Plus with a thermionic LaB_6 source and a JEM-2100F with a Schottky type field emission (FE) gun. Compared to a thermionic emitter, a Schottky type FE gun is characterised by higher brightness (4×10^8 vs 5×10^6 A/cm^2·sr at 200 kV), much smaller size of the virtual source (~10 nm vs ~10 μm), and narrower energy spread (~0.7 vs ~2 eV) that makes it particularly suitable for scanning TEM (STEM).[4].

Below the electron gun there is a system of electromagnetic lenses, apertures and stigmators that serve to form either a parallel or convergent probe on the sample in TEM and STEM modes, respectively. The first condenser lens is used to form a demagnified image of the gun crossover. The second condenser lens controls the diameter of the illuminated area and the beam convergence angle on the sample. Located inside the second condenser lens, the condenser aperture limits the fraction of electron beam passing down to the sample and so the intensity and the size of the beam. A condenser mini lens is essential in the TEM/STEM machines as it allows switching between the respective modes, providing either a parallel or a convergent illumination on the specimen as shown in Figure 2.11.c. The double deflection coils, that introduce an effective magnetic field perpendicular to the optic axis, are used to tilt and to shift the electron beam. In STEM mode, a second set of deflection coils is required to tilt the beam twice so that the probe always remains parallel to the optic axis, while scanning across the sample surface [269].

In a side-entry TEM, the specimen is inserted between two polepieces, forming the objective lens system. The upper (pre-specimen) part of the objective lens effectively acts as the final condenser lens, while the bottom part (post-specimen) forms a diffraction pattern of the sample in the back focal plane and a focused image in the first image plane. The objective (high-contrast) aperture is located in the back focal plane of the objective lens. Below the objective lens, there is a sequence of intermediate lenses that further magnify the focused image

[4] Cathode characteristics are taken from the Glossary of TEM terms at https://www.jeol.co.jp/en/words/emterms/

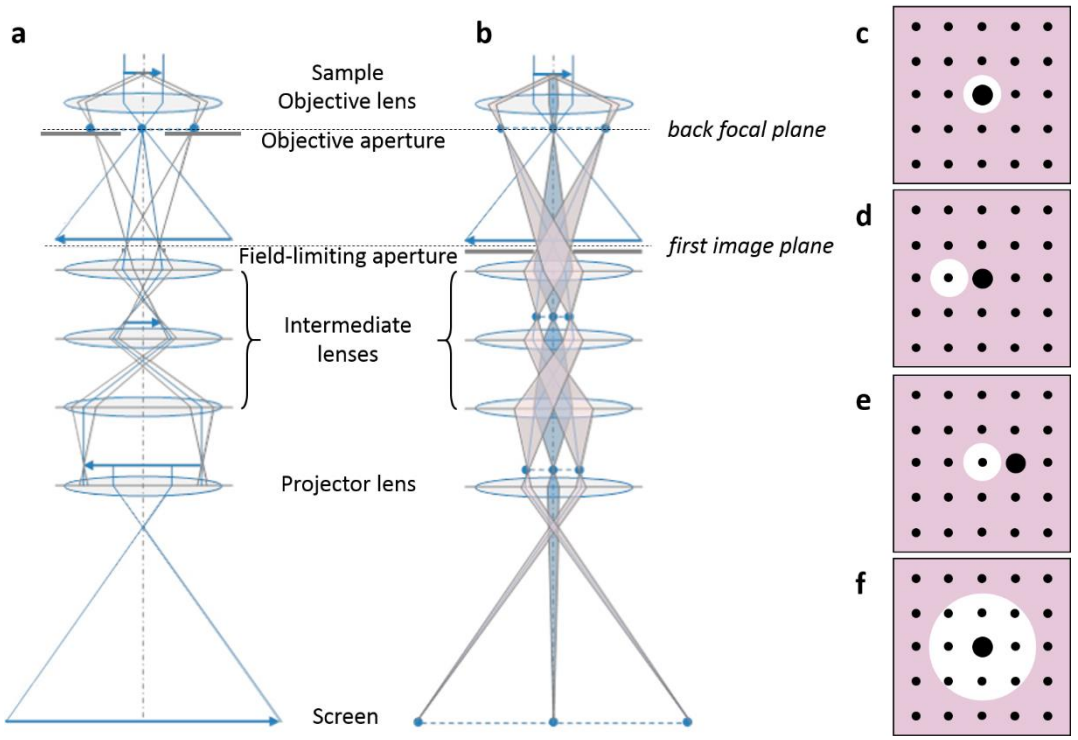


Figure 2.12. Basic operation modes of a transmission electron microscope. **a, b** Ray diagrams illustrating the formation of a magnified image in imaging mode (panel **a**) and a diffraction pattern in diffraction mode (panel **b**). Adapted from *www.jeol.co.jp*. **c-f** Selection of certain diffracted beams to form a BF TEM image (panel **c**), off-axis DF TEM image (panel **d**), centred DF TEM image (panel **e**), and TEM image with enhanced phase contrast (panel **f**). In schemes **c-f** small black spots represent the diffracted beams, larger black spots represent the direct beam, the objective aperture position is marked with a white circle.

of the sample that is then projected onto the viewing screen or a CCD camera by the projector lens. In TEM, switching between the imaging and diffraction modes is achieved by changing the excitation of the intermediate lens. If the strength of the intermediate lens is adjusted such that the image plane of the objective lens serves as its object plane, then a magnified image of the sample is projected onto the screen or detector (Figure 2.12.a). Similarly, if the intermediate lens is set so that the back focal plane of the objective lens becomes its object plane then a diffraction pattern can be viewed on the screen (Figure 2.12.b). The field-limiting aperture allows selecting the area of interest to form selected area electron diffraction (SAED) patterns. This aperture is positioned in the first image plane of the objective lens and so once in place it casts a virtual aperture on the sample. Recording SAED patterns enables to determine the local crystal structure and crystallographic orientation of the selected area. On the other hand, the objective aperture can be used to select only certain diffracted beams to form the image. BF TEM images are formed if only the direct beam is selected (Figure 2.12.c), while DF TEM images are obtained by selecting a fraction of diffracted electrons (Figure 2.12.d,e). In HR

TEM images, the phase contrast can be amplified by selecting a number of diffracted beams as shown in Figure 2.12.f. Cutting off the electrons that travel far off the optic axis allows us to decrease the aberrations and hence to improve the image resolution.

In contrast to the stationary beam in TEM mode, a focused probe is scanned over an ultra-thin specimen to generate the analytical signal in STEM mode. The intensity of the transmitted or scattered/diffracted wave, exiting from each point of the specimen, is detected with an annular bright-field (ABF) or annular dark-field (ADF) detector, respectively. In the microscope column, the annular detectors are located in the plane conjugate to the stationary convergent beam diffraction pattern formed in the back plane of the objective lens. The contrast in ADF STEM images often originates from the mass-thickness variation in the sample.

TEM samples were prepared by drop-casting dilute suspensions of nanostructures on carbon-coated copper grids (Agar Scientific, 200 nm thick holey carbon film) and dried overnight under ambient conditions. TEM imaging was performed on a JEOL JEM-2100Plus or JEOL JEM-2100F microscopes operated at 200 kV accelerating voltage. For high-resolution TEM (HR TEM) imaging, the areas of nanoflowers partially suspended on holes in the carbon films were selected in order to reduce the contribution from the electrons inelastically scattered by the amorphous carbon film. Annular dark-field (ADF) images were acquired in scanning transmission electron microscopy (STEM) mode on a JEOL JEM-2100F microscope using a JEOL annular dark-field/bright-field detector; ADF STEM scans were typically 2048×2048 pixels in size, dwell time was 10 µs per pixel. Corresponding elemental mapping was performed in STEM mode using an Oxford X-MaxN 80 mm^2 SDD detector for energy-dispersive X-ray spectroscopy (EDS). Acquired EDS data were analysed using the AZtec or INCA software packages (Oxford Instruments).

Statistical analysis of the dimensions of the synthesised metal chalcogenide ($MoSe_2$, $MoTe_2$, Bi_2Te_3, WSe_2, and $W_xMo_{1-x}Se_2$) nanoflowers is complicated due to partial aggregation of the material in dispersions and due to the solvent evaporation-driven agglomeration of colloidal nanostructures that occurs during TEM sample preparation [270,271]. In the corresponding TEM images, the nanoflowers often appear resting upon one another and the exact projection of individual nanostructures is hard to determine. The diameters of $MoSe_2$, WSe_2, and $W_xMo_{1-x}Se_2$ nanoflowers reported further in this work in Sections 3.1.1, 3.3.1, and 4.2 are the approximate values measured across a few representative nanostructures in a sample. For the same reason the lateral dimensions of individual petals composing the nanoflowers were not determined since the boundaries between overlapping petals are hard to

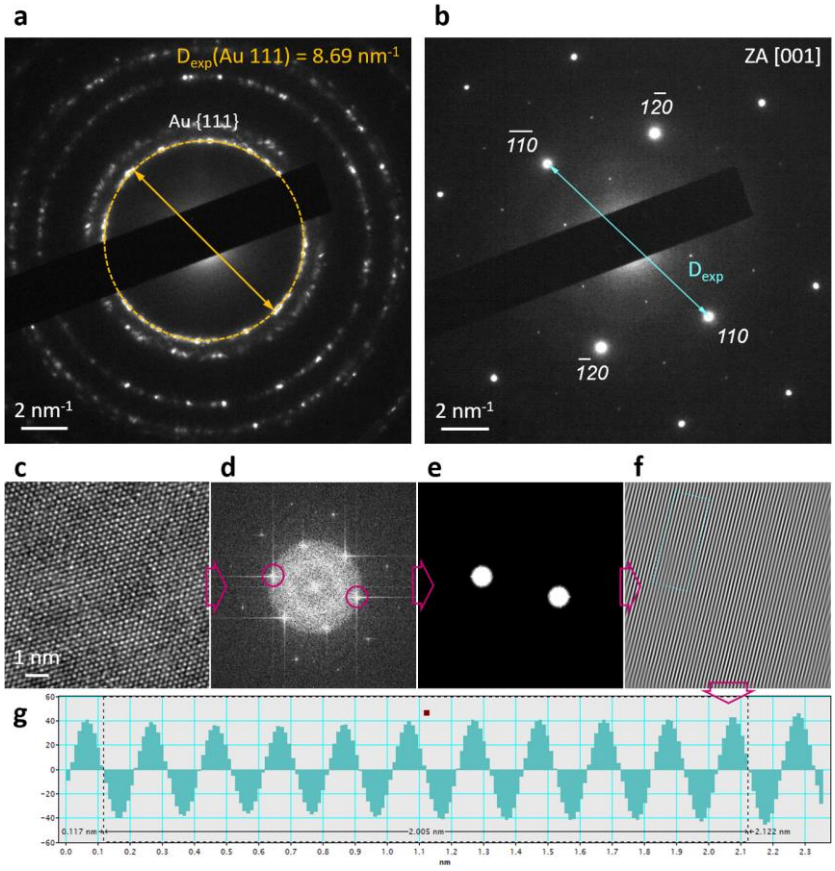


Figure 2.13. Analysis of the SAED and HR TEM data. **a** SAED pattern of a polycrystalline gold film used as a standard for the camera length calibration. **b** Representative diffraction pattern of a Bi_2Te_3 nanoplate (as in Figure 3.14.g) taken along the [001] zone axis; the blue arrow shows the distance between the $(\mathbf{110})$ and $(\mathbf{\bar{1}\bar{1}0})$ diffraction spots used to calculate the interplanar distance corresponding to the {110} planes. **c-g** A series of steps performed to measure the interplanar distances from the HR TEM images: **c** – the original TEM image (of a Bi_2Te_3 nanoplate shown in Figure 3.14.g); **d** – the corresponding FFT pattern, purple circles highlight a pair of diffraction spots chosen for the analysis; **e** – the applied Spot mask; **f** – the inverted FFT showing the lattice fringes; **g** – the intensity profile used to measure the corresponding interplanar distance.

establish. Statistical analysis was performed for the Bi_2Te_3 samples only. To obtain a dataset for analysis, a series of low-magnification TEM images of the ensembles was acquired, capturing about 200 well-resolved particles. In order to ensure that the set is representative, the frames were recorded at different spots across the sample. The sources of the error associated with the particle size determination include pixel resolution of the recorded images, insufficient contrast between particles and support film, image distortions due to unoptimized imaging conditions and improper magnification calibration [272]. The microscope alignment was routinely performed prior to any image acquisition, while the magnification calibration was carried out during the instrument servicing. The image acquisition was performed in BF TEM mode in order to increase the particle-to-background contrast. It is recommended that the TEM

images for analysis are acquired with the resolution greater than 2 pixels/nm; in this case, the image resolution contribution into the measurement uncertainty is less than 0.5 nm [270,272]. To satisfy this criterion, the magnification was typically chosen between 40000× and 100000× (pixel size between 0.33 and 0.13 nm) and all the frames within the set were recorded at the same magnification. Nanoparticle sizes were measured manually using a Ruler tool in the ImageJ software package. The produced set of values was fitted with a Gaussian function. The fitting results are reported in a form of μ±σ, where μ is the mean value (nanoplate thickness), σ is the standard deviation (Section 3.2.1).

SAED patterns and HR TEM images were analysed using the Gatan DigitalMicrograph software package. The interplanar distances d_{hkl} can be calculated from the SAED data using the equation:

$$d_{hkl} = \lambda L \frac{1}{r_{hkl}}, \quad (2)$$

where λ is the wavelength of the electrons in the incident beam, L is the camera length, r_{hkl} is the. radius of the (*hkl*) diffraction ring or the distance of the (*hkl*) diffraction spot from the origin [269]. The camera length calibration was performed by recording the diffraction pattern of a standard specimen (polycrystalline gold film, Figure 2.13.a). The experimental *d*-spacing corresponding to the {111} planes of Au, d_{exp}(Au 111), can be calculated by the equation:

$$d_{\exp}(Au\ 111) = \frac{2}{D_{\exp}(Au\ 111)}, \quad (3)$$

where D_{exp}(Au 111) is the measured diameter of the diffraction ring (nm^{-1}). In the example shown in Figure 2.13.a, the corresponding d_{exp}(Au) is equal to 2.30 Å, whereas the standard value d_{st}(Au) is 2.35 Å (ICDD 4-784). The ratio between the standard and the experimentally found Au {111} interplanar distances was used as a calibration coefficient when the diffraction patterns of the synthesised nanostructures were analysed. In the case of single crystal diffraction patterns, the r_{hkl} was measured as a half of the distance between the (hkl) and $(\overline{hkl})$ diffraction spots as shown in Figure 2.13.b. The distances reported in this work are the average values of three measurements. The experimental SAED patterns used for the estimation of interplanar distances were recorded with the resolution no less than 58 pixels/nm^{-1} (pixel size 0.017 nm^{-1}), providing the measurement precision $\frac{\Delta d}{d}$ of 0.3%.

In the case of colloidal $MoSe_2$, WSe_2, Bi_2Te_3 nanoflowers, individual petals of which are composed of single crystalline patches of approximately 5-50 nm in diameter, the lattice

parameters were obtained from the HR TEM images. The interplanar distances were determined based on the diffraction spot positions in the fast Fourier transform (FFT) patterns of digital HR TEM images [273]. A square area of a HR TEM image recorded at a microscope magnification setting between 400000× and 1000000× was selected using a Rectangle ROI selection tool in the Gatan DigitalMicrograph (512×512 pixels, Figure 2.13.c). The corresponding FFT pattern is shown in Figure 2.13.d. By applying a Spot mask, only a symmetric pair of diffraction spots is selected (Figure 2.13.e). The Inverse FFT of this pair of diffraction spots forms a real-space image of the corresponding lattice fringes (Figure 2.13.f). The interplanar distance was then measured using a Profile tool as shown in Figure 2.13.g. To increase the precision of lattice parameters evaluation, it is advised that the HR TEM images are collected at lower magnification, typically, between 300000× and 400000×, since in this case the distances r_{hkl} in the corresponding FFT patterns can be measured more precisely [274]. For the HR TEM image acquisition settings used throughout this work, the diffraction vector r_{hkl} measurement precision was 0.6%, 1.2%, and 1.7% for the microscope magnification settings of 400000×, 800000× and 1000000×, respectively.[5] However, the 400000× was often found unsuitable for the colloidal $MoSe_2$, Bi_2Te_3, and WSe_2 nanoflowers with small (~5 nm) single-crystalline domains. Compared to the results obtained from the analysis of SAED patterns, the lattice spacings measured from HR TEM images substantially deviate from the standard values; in some cases the absolute measurement error was found to be as high as 8%. It is known that the accuracy of interplanar distance measurements depends on the method of calibration [273]. In the case of Bi_2Te_3 nanoplates, the recorded HR TEM images were recalibrated using an interplanar distance, typically, (110), measured from the SAED pattern acquired on the same nanoplate, as an internal standard; this allowed us to reduce the absolute error to 0.5%. However, this approach is not suitable for the colloidal $MoSe_2$, WSe_2, and $W_xMo_{1-x}Se_2$ nanoflowers.

2.3.3. Powder X-ray diffraction

Powder X-ray diffraction (XRD) was used for the structural characterisation of the colloidal nanosheets as well as for the macroscopic analysis of sample crystallinity and crystal phase purity. XRD is based on the diffraction of the X-rays on the atomic planes of crystal lattice under examination. The Bragg's law sets the condition on the incidence angles θ (°), at

[5] For measuring the *d*-values of about 2 Å.

which the constructive interference of the elastically scattered X-rays is observed for any set of crystallographic planes (*hkl*) with the interplanar distance d_{hkl} (nm):

$$2d_{hkl} \sin\theta = \mathrm{n}\lambda, \quad (4)$$

where λ is the wavelength of the incident X-day photons (nm), n is integer [275].

Samples for XRD analysis were prepared on Si/SiO_2 or glass substrates. Concentrated suspensions of colloidal nanosheets ($MoSe_2$, $MoTe_2$, Bi_2Te_3, WSe_2) in ethanol were used for deposition. The surface of samples was flattened prior to the measurements. The X-ray diffractograms were recorded on a Bruker D2 Phaser diffractometer (Cu K_α source) in the range 6-50 $^o2\theta$, step size of 0.026 $^o2\theta$. Small-angle diffraction data were collected using a PANalytical X'PERT-PRO X-ray diffractometer (Cu K_α source) in the range 3-20 $^o2\theta$, step size of 0.03 $^o2\theta$. The diffraction data were analysed using the PANalytical HighScore software package. The reference diffraction patterns of the 1T and 1T' bulk phases of WSe_2 were simulated using the CrystalDiffract software package.

The diffractometers were operated in the θ-θ reflection scan geometry. In this case, the sample is located on the axis of the diffractometer, while the X-ray source and the detector (scintillation counter) move simultaneously in the angular range θ around the stationary sample. In both diffractometers, the X-ray tubes with copper anodes are used as a source of X-rays. The source wavelength, corresponding to the energy of the Cu $K\alpha_{1,2}$ lines, is 1.54184 Å; the Cu Kβ component was eliminated by a graphite monochromator.

The phase analysis of crystalline solids is performed by comparing the set of diffraction peaks observed in experimental diffractograms to the standard diffraction patterns (ICDD database). Both the positions and the relative intensities of the diffraction peaks are employed for phase analysis. If numerous crystal phases are present in the sample, the diffraction pattern is always a superposition of the individual phases that allows for identification of the ratio between the phases.

The broadening of diffraction peaks contains information on the average crystallite sizes and strain in the system. The experimentally observed broadening of the diffraction peaks is attributed to a combination of factors, including imperfections of the crystal lattice, inhomogeneous strain at the grain boundaries, and finite (sub-micron) crystallite sizes. The broadening associated with the crystallite size is described by the Scherrer equation:

$$r = \frac{\mathrm{K}\lambda}{\beta \cos\theta}, \quad (5)$$

where r is the mean size (radius) of a crystalline domain (nm), K is the shape factor, λ is the wavelength of the incident beam (nm), β is the broadening of the diffraction peak corresponding to the diffraction angle θ after subtracting the instrument broadening [275]. The Scherrer equation provides the lower bound on the crystallite size since beside the finite crystallite sizes the diffraction peaks are typically broadened due to chemical inhomogeneities and lattice strain caused by structural defects, such as point defects, dislocations, stacking faults, grain boundaries, present in samples. The analysis of peak broadening is additionally complicated due to the asymmetry of diffraction peaks caused by the instrumental factors and non-ideal reflection geometry. The asymmetry is especially prominent at low diffraction angles (15-25° 2θ) [275].

The shift of diffraction peaks from their reference positions that is commonly observed in experiments is generally attributed to the mechanical strain leading to either expansion or contraction of the crystal lattice. Changes in the lattice constants can be caused, for example, by partial substitution or by inclusion of dopant atoms with radius that differs from that of the atoms of pristine phase. Thus, chemical inhomogeneity of the crystalline samples can be inferred from XRD data.

2.3.4. X-ray photoelectron spectroscopy

X-ray photoelectron spectroscopy (XPS) provides information about the surface chemistry of the material under examination, including its elemental composition and chemical state of its constituent elements. In this work, XPS analysis was majorly used to quantify the ratio between the 1T' and 2H crystal phases in the colloidal WSe_2 and ternary $W_xMo_{1-x}Se_2$ nanostructures based on the observed chemical shifts in the core electron spectra of W (4*f*), Mo (3*d*), and Se (3*d*). Additionally, chemical composition and purity of the synthesised nanostructures was inferred from the XPS data. This included estimating the area-averaged atomic ratio of the transition metal cations in the alloyed $W_xMo_{1-x}Se_2$ nanoflowers and evaluating the oxidised material content.

In X-ray photoelectron spectroscopy, a sample is irradiated by a monochromatic X-ray beam and the photoelectrons ejected from the surface atoms are detected [276]. When a soft X-ray photon is absorbed by an atom of the sample, a core level electron can be knocked out as shown in the left diagram in Figure 2.14.a. The measured kinetic energy E_{kinetic} (eV) of the emitted photoelectron depends on the energy of incident irradiation hv and the binding energy

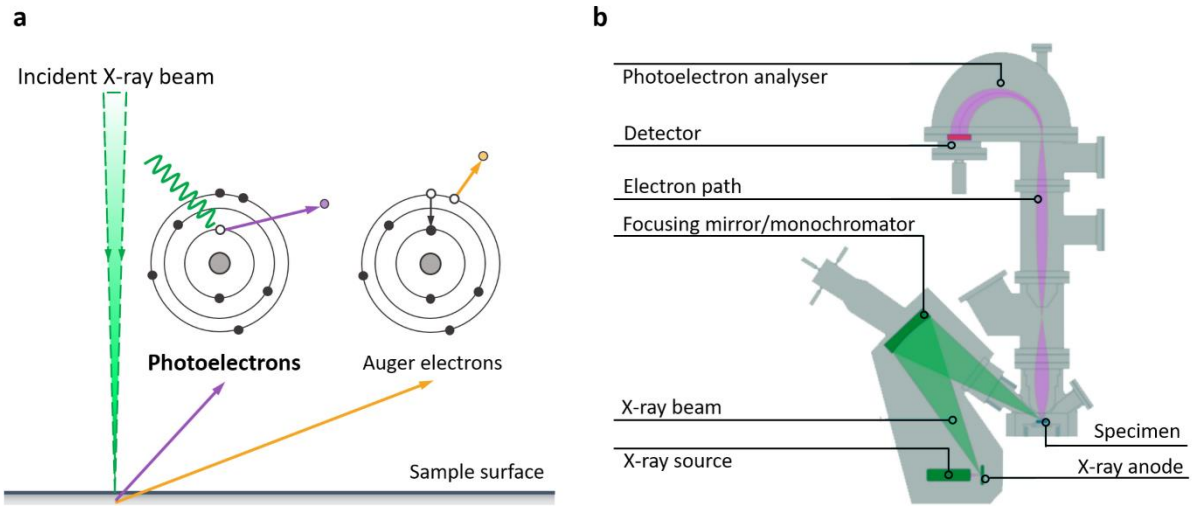


Figure 2.14. Basic principles of X-ray photoelectron spectroscopy. **a** Schematic diagram of the photoelectron emission and Auger emission processes. **b** Cross sectional schematics of an XPS spectrometer. Adapted from *www.EnviroESCA.com*.

E_{binding} (eV) of the atomic orbital, from which the photoelectron was ejected. This is given by equation:

$$E_{\text{kinetic}} = h\nu - E_{\text{binding}} - \phi_s, \tag{6}$$

where ϕ_s is the instrument work function (eV) [276]. Therefore, measuring the kinetic energy of the ejected photoelectrons allows for accurate determination of the binding energy of the electron shell the photoelectron originates from. The binding energy is often considered as the energy difference between the initial and the final states of the photoelectron, in other words, between either of the electron shells (K, L, M) and the Fermi level, E_F. Because each chemical element is characterised by a unique set of binding energies, XPS can be used for elemental analysis considering that the spectrum of a multielement compound is a sum of the individual spectra of its constituents. Moreover, the atom binding energy values are exceptionally sensitive to its chemical environment, thus providing an important insight into the chemical and electronic states of any element composing the material.

Since the mean free path of photoelectrons in solids is rather short, only the photoelectrons generated in the vicinity of sample's surface escape into vacuum and can be detected. In XPS, depth of analysis does not exceed 10 nm below the surface for most solid materials [276]. Thus, XPS is normally used to investigate the surface chemistry of bulk material. Although when applied to low dimensional materials, like atomically-thin nanosheets (< 10 nm thick), XPS provides representative information about the nanomaterial itself. Photoelectron spectrum is generated by counting the number of electrons per an energy interval

over a broad range of kinetic energies. The photoelectrons, that escaped the sample without any collisions with the atoms, produce distinct peaks in the spectrum, while those, that experienced inelastic scattering before they reached the surface, contribute to the background [277]. The spin-orbit coupling leads to the splitting of the *p*-, *d*-, and *f*-orbitals into pairs of states with the angular momentum $j = l + s$, where l is the orbital angular momentum (1 for the *p*-, 2 for the *d*-, and 3 for the *f*-orbitals), and s is the electron spin (±½). This causes the corresponding peaks becoming split (doublets) in XPS spectra. Photoelectron lines have general notation nl_j, where n is the principle quantum number. Thus, upon ionisation, the *p*-, *d*-, and *f*-orbitals form the $np_{3/2}$ and $np_{1/2}$, $nd_{5/2}$ and $nd_{3/2}$, $nf_{7/2}$ and $nf_{5/2}$ doublets, respectively. The intensity ratio between the doublet components is proportional to the ratio of their respective populations, which is defined as $(2j+1)$. Therefore, the intensity ratio is 1:2 for the *p*-, 2:3 for the *d*-, and 3:4 for the *f*-orbitals [276].

Once the photoelectron is emitted from the inner (core) shell, the ionised atom relaxes due to the outer shell electron compensating the vacancy in the core level; this may be accompanied by the emission of an X-ray photon. However, it is also possible that the atom relaxes via the Auger process that is shown in the right scheme in Figure 2.14.a. In this case, an outer shell electron falls into the core level vacancy produced as a result of the initial photoionisation-photoelectron emission process, and the excessive energy is carried off by a second electron (Auger electron) ejection. The kinetic energy of an Auger electron corresponds to the energy difference of the initially ionised and double ionised atom.

XPS spectra were acquired using a Thermo Fisher K-Alpha+ equipped with an Al anode (Kα 1486.6 eV). The generated X-ray beam was monochromated and then focused down to 200-400 μm spot on the sample. All measurements were performed at room temperature. Since the spectrometer operates in ultra-high vacuum (10^{-9} mbar), all samples for analysis were drop-cast onto Si/SiO_2 substrates and dried either overnight under ambient conditions or in a tube furnace at 200 ºC in order to remove the residual solvent (ethanol) and to prevent outgassing in the spectrometer chamber. Samples were grounded using carbon tape to prevent charging of the sample surface. The emitted photoelectrons pass through a series of transfer electrostatic lenses and then enter a hemispherical electron energy analyser as shown in Figure 2.14.b. The analyser consists of two concentric hemispherical electrodes and the multichannel detector in the output plane. Photoelectrons travel in the gap between two hemispheres. The potential difference ΔV_0 between the hemispherical electrodes sets the limit on the kinetic energy E_0 of photoelectrons that can reach the detector, which is known as pass energy. The electrons with

higher (lower) energy will follow a trajectory of larger (smaller) radius and will not reach the detector. In this work, 20 eV pass energy was used for all measurements. In the scanning mode, the potential difference applied across the hemispherical analyser is kept constant, while the voltage on the electrostatic lenses is scanned in such a way that only the electrons with selected kinetic energy are counted on the detector for the selected time. The survey spectra were recorded with the energy step of 0.1 eV, while high-resolution spectra of the W 4*f*, Mo 3*d*, and Se 3*d* core level electrons were collected with 0.05 eV resolution. XPS spectra were analysed using the Avantage software package.

2.3.5. Vibrational spectroscopy: Raman and Fourier transform IR spectroscopy

Raman and IR spectroscopies provide information on the fundamental vibrational states of a molecule or a crystal. The vibrational energy levels correspond to the respective motion of individual atoms or group of atoms within a molecule or a crystal, and the combination of vibrational states and electronic states represents the total set of the energy levels. When matter (a molecule or a crystal) is placed into electromagnetic field (light), a quantum of energy can be absorbed if its energy $h\nu$ is equal to the energy difference between two levels ΔE. Since the energy separation between the electronic states is generally much larger than that of the vibrational states, the former ones are typically observed in the range between ultraviolet (UV) and near infrared (IR), 100-1000 nm (10^6-10^4 cm^{-1}), while the latter ones appear in the IR region (10^4-10^2 cm^{-1}) [278]. Graphically, the transitions between the electronic energy levels and between the vibrational energy levels are represented in the diagrams in Figure 2.15. The electronic transitions will be discussed in Section 2.3.6 (optical absorption spectroscopy). IR spectroscopy is similar to optical absorption spectroscopy and is based on measuring the direct absorption of IR light by a sample that is irradiated by a polychromatic beam (Figure 2.15.b). The IR transitions occur within the ground electronic state at the resonant frequencies, i.e. matching the frequencies of vibrations of groups of atoms. On the other hand, in Raman spectroscopy, the information on vibrational modes is inferred from the analysis of the inelastically scattered fraction of the incident monochromatic light. In the Raman scattering process, a photon of the incident beam is absorbed by matter and then reemitted as a low-energy (scattered photon), and the excess of energy is carried away by an optical phonon (Figure 2.15.c, S). The observed change in the photon frequency (Stocks shift) corresponds to the energy difference between the vibrational states. It is also possible that due to interaction with the lattice phonons, the incident photon may gain energy (Figure 2.15.c, A). In this case, the anti-Stocks shift is observed. The process of energy exchange between a photon and a lattice

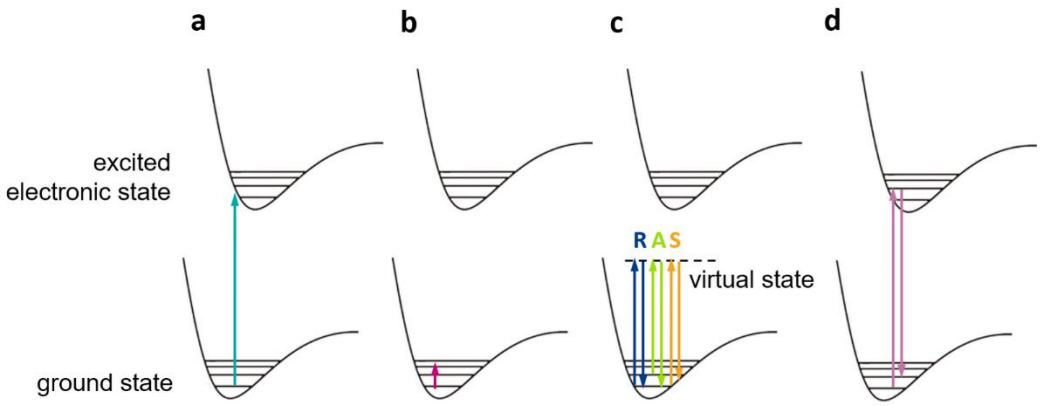


Figure 2.15. A simplified diagram showing the transitions between the electronic and vibrational states. **a** Optical (UV-vis) absorption; **b** IR absorption; **c** Rayleigh scattering (R), anti-Stocks (A) and Stocks (S) Raman scattering; **d** resonance Raman scattering. Adapted from *www.silmeco.com*.

optical phonon is commonly represented as occurring through a virtual state. If the excitation energy matches the energy difference between the ground and the excited electronic states, the Raman scattering is referred to as the resonance process (Figure 2.15.d).

Not all transitions between the vibrational and the electronics levels are allowed. The selection rules that identify the set of allowed transitions can be determined based on the symmetry of a molecule (point group analysis) [278] or a crystal (space group analysis) [279].

Although IR and Raman spectroscopies are complementary techniques allowing for the complete analysis of atomic vibrations in molecules and lattice dynamic of crystals, IR-active and Raman-active vibration modes have different physical origin. The vibration modes that lead to changes in the electric dipole moment of a molecule or a group of atoms induced by the electric field (light) are IR active. If the polarizability of a molecule or a group of atoms, that is the ability to response to the electric field, changes then the vibration is Raman active. In practice that means that in centrosymmetric molecules and crystals, the IR-active modes are Raman-inactive and *vice versa*.

In this work, Fourier transform IR (FTIR) spectroscopy was majorly used to investigate molecular precursors, and in particular the coordination of transition metals in these complexes. Unlike conventional absorption IR spectroscopy, Fourier transform IR spectroscopy is based on measuring the interference of various frequencies of transmitted irradiation. The FTIR spectrometers are designed as interferometers, where the incident beam from the IR source is split into two rays of equal intensity by a beamsplitter. Each of the rays of IR light is then guided to the mirrors, one of which is fixed, while the other is moving. Depending on the position of a moving mirror, either constructive or destructive interference of two rays is

recorded (interferogram). The sample is generally located between the interferometer and the detector. Applying the Fourier transform to the recorded interference pattern, a single beam transmission spectrum can be produced. The IR spectrum of a sample is then obtained as a ratio of the single beam spectra recorded with and without sample (background). The advantages of FTIR spectroscopy over the conventional IR absorption spectroscopy include multiplicity as the signal is collected at all frequencies simultaneously that allows for quick acquisition and averaging of the spectra; and higher sensitivity originating from lower reflective losses owing to fewer mirrors and slits in the construction of an interferometer. The FTIR spectra were collected using a Thermo Scientific Nicolet iS10 spectrometer equipped with a tungsten-halogen lamp as the IR source and a KBr/Ge mid-IR beamsplitter. A HeNe laser is used to control the motion of the moving mirror. The samples were characterised via attenuated total reflectance (ATR). For that, the solutions under examination were placed directly on the surface of the ATR crystal (diamond) and the spectra were collected by averaging 32 scans in the range of 4000-400 cm^{-1} with a typical resolution of 4 cm^{-1}. The ATR correction was performed using the OMNIC Specta software package.

Structural features of the colloidal $MoSe_2$, $MoTe_2$, Bi_2Te_3, and WSe_2 nanostructures, such as polymorphism (Sections 3.1 and 3.3) and crystal structure defects, including replacement of transition metal atoms in the lattice nods (in $W_xMo_{1-x}Se_2$ alloys, Section 4.2) and trapping of the non-stoichiometric species in van der Waals gaps (in Bi_2Te_3 nanostructures, Section 3.2) were studied using Raman spectroscopy. To acquire a Raman spectrum, a sample is irradiated by monochromatic (laser) light and the inelasically scattered radiation is dispersed onto a CCD detector, while the elastically scattered (Rayleigh) component is filtered out. Raman spectra were recorded using a Renishaw inVia Qontor confocal Raman microscope at excitation wavelength of 532 nm. In a confocal Raman microscope, the laser beam is focused on the sample surface by the microscope objective lens allowing for spatial resolution under 1 μm. In all experiments, a 1800 lines/mm grating was used, providing ~1.5 cm^{-1} spectral resolution. Samples were drop-cast on Si/SiO_2 substrates from the ethanol suspensions of colloidal nanosheets. To avoid damage to the samples due to low heat conductivity of Si/SiO_2 substrates, the laser power was kept under 0.195 mW, while 5-10 consecutive acquisitions were performed to increase the signal-to-noise ratio. The observed Raman shifts were calibrated based on the characteristic band of crystalline Si at 520 cm^{-1}.

2.3.6. Optical absorption spectroscopy

Optical transitions of the semiconducting TMD nanostructures were studied using UV-vis (ultraviolet-visible) absorption spectroscopy. That is a spectroscopic technique based on measuring the wavelength-dependent attenuation of the incident light as it passes through the sample. Absorption of visible light (400-700 nm) occurs due to the electronic transitions between the ground and the excited states of the material under examination (Figure 2.15.a). In case of the semiconducting TMD nanostructures, these correspond to the interband (excitonic) transitions between the conduction (CB) and the valence (VB) bands.

Absorbance A is defined as the common logarithm of the incident to transmitted beam intensities ratio. In a homogeneous isotropic medium, absorbance is proportional to the concentration of absorbing species C (mol/cm^3) as stated by the Beer-Lambert law:

$$A = \log\frac{I_o}{I} = \varepsilon CL, \tag{7}$$

where I_o and I are the intensities (radiant flux, W) of the incident and the transmitted beam, respectively; ε is the molar absorption coefficient (cm^2/mol) that, strictly speaking, depends on the concentration; L is the optical path (cm) [280].

Absorption spectra of the dispersions of colloidal TMD nanoflowers in ethanol were collected using a PerkinElmer Lambda 25 UV-vis spectrometer. Spectra were recorded between 1100 and 200 nm with 1 nm spectral resolution. In order to resolve features associated with the organic ligands, quartz cuvettes, that are transparent in the near-UV region, were used.

2.3.7. Inductively-coupled plasma optical emission spectroscopy

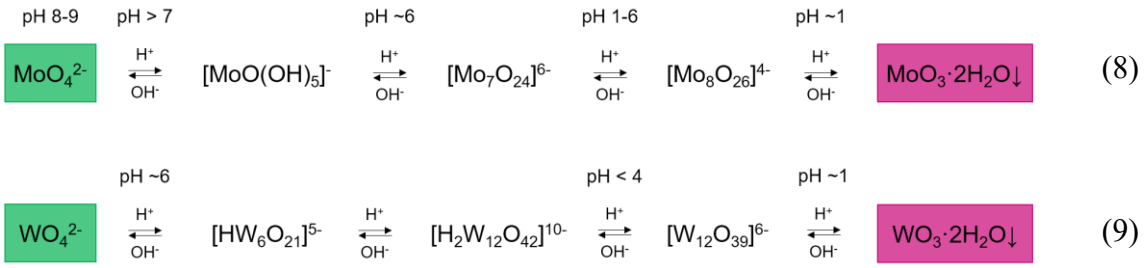
Inductively-coupled plasma optical emission spectroscopy (ICP OES) allows for the qualitative and quantitative analysis of the sample composition. It is a spectroscopic technique that uses inductively-coupled plasma to ionise atoms of the sample and the constituent elements are detected by the characteristic emission produced during the recombination. Intensity of the characteristic emission lines is proportional to the element concentration in the sample.

Aqueous solution of the analyte is driven into a nebulizer by a peristaltic pump. Here, an aliquot of the analyte is sprayed into the flame of a plasma torch (Ar). Due to collision with the electrons and ions of argon plasma, the sample molecules are ionised and then emit light upon recombination. The emitted light is focussed on a diffraction grating, and then the component wavelengths are detected by an array of photodetectors that accumulate the charge proportional to the light intensity. For quantitative elemental analysis, the solutions containing known

amount of the required elements (standards) are analysed first and the calibration curves, assigning the measured intensities to the known concentration values, are obtained. The sample composition is then interpolated based on the calibration curves. The quantitative elemental analysis of the colloidal TMD nanoflowers was carried out on a Thermo Scientific iCAP 6000 Series ICP spectrometer equipped with an ASX-520 autosampler. The data analysis was performed using the iTEVA software package.

The key part of an accurate elemental analysis is sample preparation. Samples of colloidal TMD nanoflowers were digested in a 45% HNO_3 solution over 24 hours and then the aliquots were diluted to analytical concentrations by a required amount of Milli-Q water.

At room temperature, the group VIB TMDs are stable in dilute non-oxidising acids (HCl) [281]. However, tungsten and molybdenum disulphides react readily with boiling H_2SO_4 (MoS_2) [17] and mixtures of HNO_3 and HF or HCl (WS_2) [281]. Both diselenides can dissolve in mineral acids upon heating [281]. The analytical work with acidic solutions of tungsten and molybdenum is complicated since, upon digestion in concentrated mineral acids (HNO_3), both $MoSe_2$ and WSe_2 are likely to form insoluble trioxides. In weakly acidic solutions, polymeric molybdate and tungstate anions are formed (Equations 8, 9), these polyanions are insoluble in water. In strongly acidic solutions, polyanions depolymerise, forming molybdic $MoO_3 \cdot 2H_2O$ and tungstic $WO_3 \cdot 2H_2O$ acids.



The formation of insoluble trioxides in both the digested TMD samples (pH 1) and the standards (pH 8-9), which were brought to the same matrix (same HNO_3 concentration as in the samples) for the measurement, could potentially lead to the underestimation of the transition metal concentrations. Therefore, the range of working concentration has to be carefully chosen in order to avoid the crystallisation of MoO_3 and WO_3 and as a result their elimination from the analyte solutions due to precipitation. On the other hand, concentrated HNO_3 is likely to oxidise Se^{-2} to Se^{+4} forming selenous acid, which is highly soluble in water, and so the selenium signal can be used for quantitative analysis in a wide range of concentrations. Possible digestion reactions are as following:

$$MoSe_2 + 14HNO_{3\ conc,\ hot} \rightarrow \mathbf{MoO_3}\downarrow + 2\mathbf{H_2SeO_3} + 14NO_2\uparrow + 5H_2O \quad (10)$$
$$\uparrow\downarrow$$
$$[HSeO_3]^- \rightleftarrows [SeO_3]^{2-} \rightleftarrows [Se_2O_5]^{2-}$$

$$WSe_2 + 14HNO_{3\ conc,\ hot} \rightarrow \mathbf{WO_3}\downarrow + 2\mathbf{H_2SeO_3} + 14NO_2\uparrow + 5H_2O \quad (11)$$
$$\uparrow\downarrow$$
$$[HSeO_3]^- \rightleftarrows [SeO_3]^{2-} \rightleftarrows [Se_2O_5]^{2-}$$

Tungsten, molybdenum, and selenium standards for ICP OES were prepared in the range of concentrations 0-10 ppm; 0-25 ppm and 0-50 ppm (Figure 2.16). In the highly acidic matrix (8.1 vol.% HNO_3), yellowish WO_3 instantly precipitates from the 50 ppm standard solution, whereas at lower concentration the crystallisation appears to be slower and the 25 ppm standard solution becomes murky due to the oxide formation only after one week, while no precipitation is observed in the 0-10 ppm standards. At lower acid content (0.6 vol.% HNO_3), all 0-50 ppm standard solutions demonstrate good stability over a course of a few weeks. The signal intensities measured for the 0-10 ppm standards in either 3.6 or 8.1 vol.% HNO_3 matrices demonstrate good reproducibility. For the standard ICP OES analysis of the colloidal TMD nanoflowers, 0-10 ppm or 0-25 ppm standard solutions in 3.6 vol.% HNO_3 were chosen for the calibration fit.

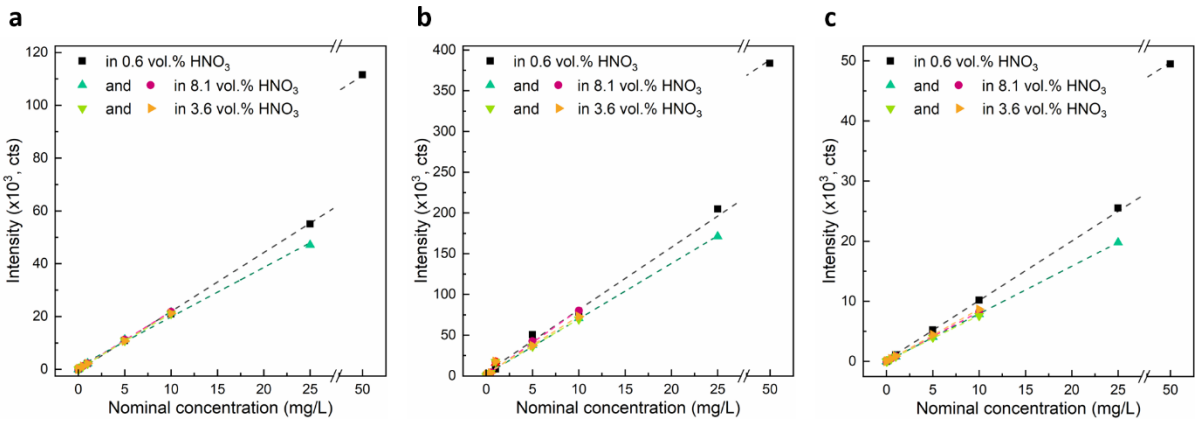


Figure 2.16. ICP calibration curves. **a, b, c** Tungsten, molybdenum, and selenium standards, respectively. Standards prepared in the concentration ranges 0-10ppm, 0-25ppm, and 0-50ppm in various matrixes (0.6, 3.6, 8.1 vol.% of HNO_3).

The results of ICP OES analysis of colloidal suspensions of the free-standing TMD nanoflowers (for the reaction yield) and of the TMD working electrodes produced by the direct growth approach (for the catalyst mass loading) are summarised in Table 7.

Table 7. Quantitative analysis of the free-standing TMD nanoflower samples and the TMD nanosheets grown on carbon paper (CP).

Sample	Concentration in suspension, mg/L – mmol/L						Reaction yield, %
	[W]		[Mo]		[Se]		
WSe_2 (#41)	12.9	0.08			101.1	1.25	2.5
WSe_2 (#42)	13.9	0.08			99.8	1.25	2
$MoSe_2$ (#20)			156.5	1.63	274.2	3.48	7
$W_xMo_{1-x}Se_2$ (#03)	27.6	0.15	276.5	2.88	1266.2	16.03	16
	Surface coverage, µg/cm² – µmol/cm²						
	[W]		[Mo]		[Se]		
WSe_2 (#58) @CP	21.01	0.114			53.1	0.672	1[6]
$MoSe_2$ (#23) @CP			5.94	0.062	13.6	0.172	0.3
$W_xMo_{1-x}Se_2$ (#04) @CP	14.72	0.08	15.88	0.166	67.9	0.86	1.4

2.3.8. Nitrogen adsorption

Physical adsorption of inert gas molecules (N_2, Ar) on a surface of the materials under study allows for measuring their specific surface area (m^2/g). The experimental method is based on the Brunauer-Emmett-Teller (BET) theory, which considers formation of an adsorbate monolayer on the adsorbent surface [282]. The theory considers the adsorbates as not chemically interacting with the adsorbent, moreover, the adsorbate molecules do not interact with each other within the adsorbed layer. In the BET theory, the adsorption isotherm of the inert gas is described by equation:

$$\frac{1}{\upsilon(\frac{p_0}{p}-1)} = \frac{c-1}{\upsilon_m c}\left(\frac{p}{p_0}\right) + \frac{1}{\upsilon_m c}, \quad (12)$$

where p_0 and p are the adsorbate saturation (condensation) and equilibrium pressures (Pa) at the temperature of adsorption, c is the BET constant, υ is the volume of adsorbed gas (m^3), υ_m is the volume of an adsorbed monolayer (m^3). Experimentally, the volume of adsorbed gas υ is measured as a function of the relative pressure p/p_0 at a constant temperature of adsorption (typically 77 K) that allows for estimating the volume of the adsorbed monolayer $\upsilon_{m.}$ and then the number of adsorbate molecules in the monolayer. If the adsorption cross-section s (m^2), which is the area occupied by a single adsorbate molecule on the adsorbent surface, is known, the total surface area S_{total} (m^2) is calculated by the equation:

$$S_{total} = \frac{\upsilon_m N_A s}{V_m}, \quad (13)$$

[6] The yield is calculated based on the amount of material dissolved from CP only; it does not include the free-standing flowers formed in the solution phase.

where N_A is the Avogadro constant (~6.022×10^{23} mol-1), V_m is the molar volume of the adsorbate gas (m^3/mol) [282]. The specific surface area S (m^2/g) can then be obtained by normalising the S_{total} by mass of the material. The specific surface area determined from the results of physical adsorption should not be treated as a true value since it strongly depends on the adsorption cross-section s of the adsorbate, which appears to vary from solid to solid [283].

The nitrogen adsorption measurements were carried out using an Autosorb iQ-AG static chemisorption analysis station (Quantachrome instruments). Dried powders of the WSe_2, $MoSe_2$, and $W_xMo_{1-x}Se_2$ (x ~0.5) nanoflowers and the materials grown directly on CP were used for analysis.

2.3.9. Atomic force microscopy and Kelvin probe force microscopy

Atomic force microscopy (AFM) is a type of microscopy, where high-resolution images of sample topography are obtained based on registering the probe-sample interaction, when a mechanical probe is scanned in a raster pattern across the sample surface [284]. An AFM is composed of four major systems: a mechanical probe, a sample stage, a probe-sample monitoring system (laser and position sensitive detectors, PSD), and a feedback system that controls the cantilever position. A mechanical probe consists of a fine micro-fabricated tip, typically made of Si or Si_3N_4 for the topography imaging, mounted on a cantilever. The tip radius of curvature is of the order of a few nanometres that allows for the accurate topography imaging with a nanometre-scale resolution. An AFM can be operated in either contact, intermittent contact, or non-contact mode [285]. In contact operation mode, the tip is dragged across the sample's surface. This is achieved by controlling the sample stage position in x, y, and z directions with respect to the AFM tip apex; however, an independent xyz drive that controls the mechanical probe position can be present depending on the microscope make. The contact mode AFM is performed in firm contact, when the tip-sample interactions are dominated by the repulsive forces. The resulting deflection of the cantilever is registered by the monitoring system as the reflection of a laser beam off the upper surface of the cantilever. The signal from the PSD, which is essentially a photodetector, is used as an input signal of the electronic feedback loop regulating the position of the tip through piezo-electric actuators. In a contact mode, the information about sample's topography can obtained from the direct monitoring of the cantilever deflection as long as the tip remains in contact with the sample. However, height variation is more commonly calculated from the output signal of the feedback loop that is employed to continuously adjust the cantilever height to maintain a user-defined tip-sample separation (the setpoint), while the sample is being scanned in a raster xy pattern.

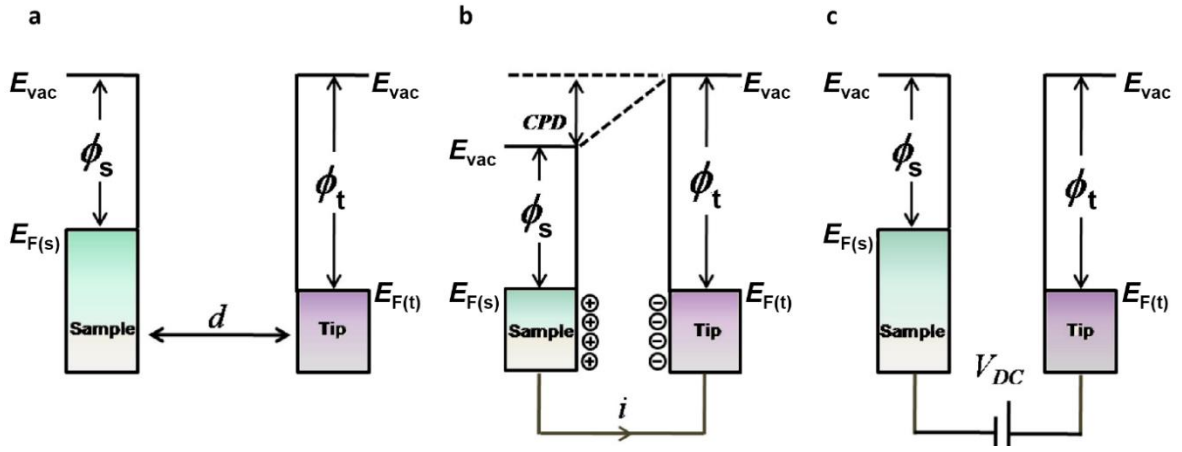


Figure 2.17. Contact potential difference in KPFM. Energy level diagrams showing **a** AFM tip and sample surface before the electric contact; **b** equilibration of the Fermi levels upon the electric contact between the tip and the sample; **c** nullification of the CPD by applying an external bias. Reprinted from [255], with permission from Elsevier. Copyright © 2011.

In contrast to the static contact mode, the intermittent contact (tapping) and non-contact modes are dynamic. Since the tip is not brought to contact with the sample surface, the damage to the sample (and the tip) is reduced. Also this minimises the "snap-in" imaging artefacts, appearing when the attractive forces between the tip and the sample may cause the tip to dig into the sample surface. Instead, the cantilever is externally oscillating at a frequency close to the resonance one. The interaction between the sample surface and the tip apex due to van der Waals, dipole-dipole, or electrostatic forces induces changes in the cantilever oscillation amplitude and frequency. These changes with respect to the reference amplitude and frequency are used as a feedback signal to obtain the sample topography in tapping and non-contact modes, respectively [285]. In the amplitude modulation regime, the feedback loop is set to maintain the amplitude of the oscillation constant, whereas in the frequency modulation regime, the feedback loop adjusts the tip-sample separation to keep the difference between the tip oscillation frequency and the reference (setpoint) frequency constant.

Kelvin probe force microscopy (KPFM) is used to measure the contact potential difference (CPD) between the sample and a conducting tip. When the AFM tip is brought to electrical contact with the sample surface, the tunnelling current flows between the tip and the sample until the Fermi levels of two materials, $E_{F(t)}$ and $E_{F(s)}$, respectively, are equilibrated as shown in Figure 2.17.b. The CPD, which is equal to the difference between the sample and the tip work functions, ϕ_s and ϕ_t, identifies the electrostatic force acting in the contact area. This force can be nullified by applying an external bias to eliminate the surface charge in the contact

area (Figure 2.17.c). Thus, measuring the bias potential allows for calculating the material work function ϕ_s if the AFM tip work function ϕ_t is known.

In this work, surface topography and surface potential imaging of the WSe_2 nanostructures were performed on an Asylum MFP-3d microscope. A PtIr coated Si tip (Bruker SCM-PIT-V2) mounted onto a PPP-NCHR 20 (Nanosensors) cantilever was used as a probe. The initial scanning was performed over 16 μm^2 scan area at 256 points per line and at a scan rate of 1 Hz. The resolution was increased to 1024 points per line for detailed imaging of individual nanostructures. Samples for KPFM were prepared on p-doped Si wafers, p-Si was used as a reference material. The work function of WSe_2 ϕ_{WSe_2} was calculated with respect to the work function of p-doped Si ϕ_{Si} following the equation:

$$\phi_{WSe_2} = \phi_{Si} - e \times (CPD_{WSe_2} - CPD_{Si}) \quad (14)$$

The AFM and KPFM data were analysed using the Gwyddion software package.

2.3.10. Zeta-potential measurements

The surface charge of nanoflowers in colloidal suspensions was assessed based on the ζ-potential value obtained from the electrophoretic velocity measurements.

When dispersed in polar solvents, particles will spontaneously acquire a surface charge. This can be caused by various factors, for example by unequal ion adsorption from the dispersing medium resulting in a non-zero net charge, by preferential dissolution of the crystal lattice, or by ionisation of surface groups if surfactant is present [286,287]. Similar ionisation mechanisms are expected to take place in non-aqueous polar solutions. This surface charge is neutralised by the counterions attracted to the particle surface from the bulk solution, forming the electric double layer (EDL) [209,288]. The detailed description of the EDL is complicated; however, two distinct regions can be identified (Figure 2.18). The layer closest to the particle surface, Stern layer, is formed by the ions carrying the charge opposite to that of the particle surface (counter-ions). This layer is considered as immobile and can also include the adsorbed ions. Further from the particle surface is the diffuse layer that allows diffusion of co-ions and counter-ions loosely bound to the particle. The boundary within the diffuse layer, which corresponds to the stationary layer that moves with the particle, is called the slipping plane. The ζ-potential defines the potential within the diffuse layer at the slipping plane.

Experimentally, laser Doppler electrophoresis is used to measure the ζ-potential value [289]. The method is based on applying an electric field across the dispersion of charged

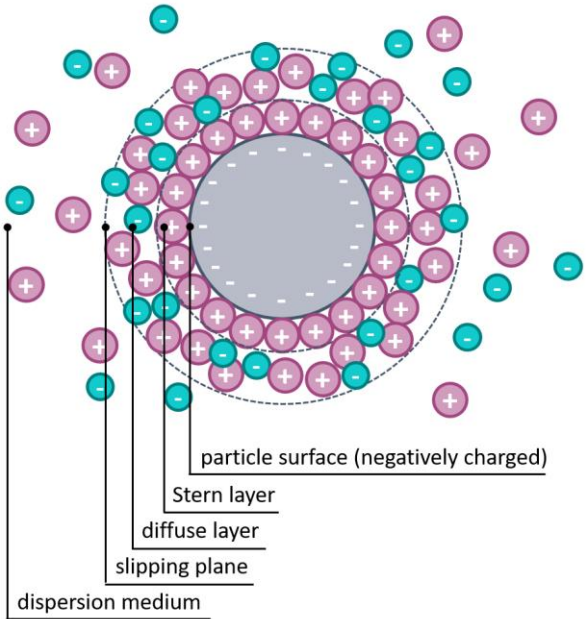


Figure 2.18. Simplified illustration of an electric double layer formed on the surface of a colloidal particle.

particles and measuring the velocity of particle migration to the electrode of opposite sign. If a laser beam is passed through the suspension, the migrating particles will cause changes in frequency of the incident irradiation. This spectral shift is proportional to the particle velocity that is then used to calculate the ζ-potential. In this work, the ζ-potential of WSe_2 suspensions in ethanol was measured using a Zetasizer Nano-Z (Malvern Instruments Ltd.). All measurements were performed at room temperature (22.5 ºC).

2.4. Electrocatalytic performance evaluation

2.4.1. Preparation of working electrodes

Working electrodes for catalytic hydrogen evolution reaction (HER) were prepared by two techniques – deposition of thin films from colloidal suspensions and direct growth of active material on conductive support. In order to grow WSe_2, $MoSe_2$ and $W_xMo_{1-x}Se_2$ nanoflowers directly on an arbitrary conductive substrate, a piece of either carbon paper (CP), or carbon foil (CF) or Au foil (~4 cm^2) was placed in the reaction flask containing the metal (tungsten molybdenum, or mixed) complex in oleic acid, left soaking for 30 minutes at 300 ^oC and then the heterogeneous nucleation was induced by a rapid injection of the chalcogen precursor. After three hours of growth, the substrate with the nanosheets assembled on its surface was removed from the reaction solution, repeatedly washed with ethanol to remove the oleic acid residue and dried under ambient conditions before electrochemical testing.

2.4.2. Electrochemical testing in a three-electrode cell

2.4.2.1. Experimental set-up

The catalytic performance of the colloidal $W_xMo_{1-x}Se_2$ (x = 0-1) nanosheets was tested in a standard three-electrode cell configuration using a Gamry Interface 1000 potentiostat. 1M H_2SO_4 (95%, VWR) or 1M H_3PO_4 (85%, Sigma Aldrich) solutions in Milli-Q water were chosen as an electrolyte. The working electrodes produced either by drop-casting or by direct growth of active material on a conductive support (~4 cm^2) were tested as fabricated without any preliminary treatment. The electrode active area typically varied between 0.25 and 0.3 cm^2. Carbon foil (~14 cm^2, 99.8%, Aldrich) was mainly used as a counter electrode that protects the reference electrode serving as a current drain. However, in the series of experiments on the testing conditions optimisation described in Section 2.4.3, an alternative auxiliary electrode made of platinum gauze (100 mesh, 99.9%, Alfa Aesar) was used. All potentials E (V) were applied vs a commercial $Ag/AgCl_{\ 3M\ KCl}$ (BASi, MF-2052) or $Hg/Hg_2Cl_{2\ sat\ KCl}$ (ALS, RE-2BP) reference electrode. The potentials were converted to vs Reversible Hydrogen Electrode (RHE) following the equation:

$$E\ (vs\ \mathrm{RHE}) = E\ (vs\ \text{reference electrode}) + 0.059 \times \mathrm{pH} + E^{o}, \qquad (15)$$

where E^o is a standard electrode potential: $E^o_{Ag/AgCl\ 3M\ KCl}$ = +0.21 V; $E^o_{Hg/Hg2Cl2\ sat\ KCl}$ = +0.2444 V.

2.4.2.2. Linear sweep voltammetry and Tafel analysis

Two primary electrode performance characteristics, the overpotential at the catalytic current density of -10 mA/cm^2 (η_{10}, mV) and the Tafel slope, were obtained from linear sweep voltammetry (LSV) data. LSV is an electrochemical method where the potential between the working electrode and the reference electrode is swept linearly at a constant scan rate, while the current at the working electrode is being measured. The processes occurring at the auxiliary electrode are not monitored. The polarisation curves were recorded by sweeping the applied potential cathodically from 0 to -0.8 V vs reference electrode at a scan rate of 5 mV/s. Before testing, the working electrodes were soaked in aqueous electrolyte of choice (1M H_2SO_4 if not stated otherwise) for 1 hour to ensure wetting of the high surface area of branched TMD catalyst. Ten consecutive LSV scans were performed prior to the characterisation to condition the working electrodes and to ensure that the delivered catalytic current is stable (Figure 2.19.a,b). The measured current was normalised to the geometric active area of working electrode to obtain the catalytic current densities j (mA/cm^2). The geometric active area is equal to the area of working electrode immersed into electrolyte and typically varied in the range 0.25-0.3 cm^2. It should be noted that normalising measured current to the geometric active area provides reliable values for working electrodes with smooth and planar surfaces, however, for nanostructured catalysts, like arrays of vertically aligned TMD nanosheets grown on conductive substrates discussed in Chapter 5, it leads to overestimating the catalyst activity. It has been suggested that the actual surface area of the electrode-electrolyte interface may be used instead to calculate catalytic current density [290]. The specific surface area (SSA) of a nanostructured TMD catalyst can be determined from the results of nitrogen adsorption (Section 2.3.8). However, this method of evaluating the current density as a catalyst activity metric is considered highly inaccurate since the catalytically-active area of a catalyst differs from its specific surface area; moreover, the density of catalytically-active sites varies considerably from catalyst to catalyst. For these reasons, current densities obtained by normalising to the SSA are not discussed in this work. Alternatively, electrochemically-accessible(active) surface area (ECSA) can be used to obtain specific current densities. Although having been developed for noble metal catalysts [291,292], the refined protocols on assessing the ESCA of TMD catalysts are lacking in literature. Relative ECSA can be measured from the double-layer capacitance of the interface [293] but this parameter cannot be used to compare catalyst activities from different studies [290]. Furthermore, double-layer capacitance corresponds to the non-Faradaic ion adsorption processes at the electrode-electrolyte interface,

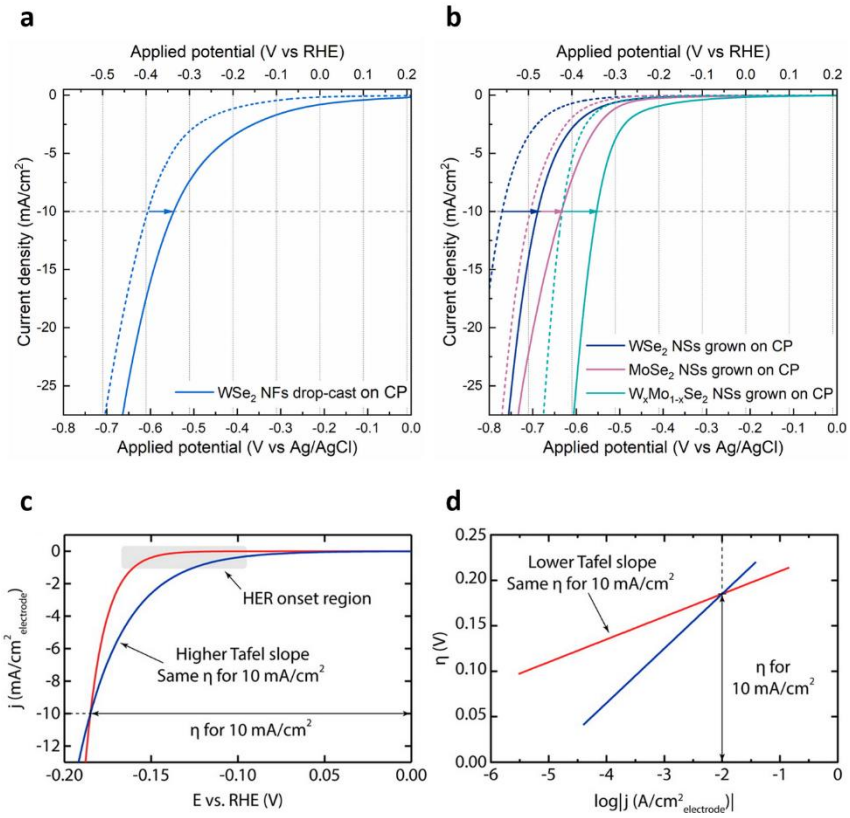


Figure 2.19. Assessment of the catalytic performance of the colloidal $W_xMo_{1-x}Se_2$ (x = 0-1) nanosheets. **a, b** Polarisation curves recorded on the drop-cast WSe_2 (panel **a**) and the directly grown WSe_2, $MoSe_2$, and $W_xMo_{1-x}Se_2$ (panel **b**) working electrodes before (initial scan, dashed lines) and after (10^{th} cycle, solid lines) ten cathodic sweeps from 0 to -0.8 V (vs Ag/AgCl). **c, d.** Polarisation curves and the corresponding Tafel slopes, respectively, of two theoretical catalysts. Reprinted with permission from [157]. Copyright © 2014, American Chemical Society.

while the catalytic HER is a Faradaic process, and so may not reflect the catalyst activity. The current densities presented in this work are geometric current densities at the nanostructured TMD working electrodes. In order to account for the synthesis-to-synthesis variations in the achieved mass loadings, we also provide catalytic current densities normalised by the mass of active material as discussed in Section 5.3. In this case, the mass loadings (μg/cm^2) were obtained by ICP OES (Section 2.3.7).

Reaction overpotential is the potential difference between the thermodynamic potential E^o of the electrochemical reaction and the experimental potential E at which the electrochemical reaction occurs. At thermodynamic equilibrium, the reversible potential for the HER E^o is 0 V. Overpotential can be written as $\eta = E$ (vs RHE) – 0. There are two special overpotentials for the HER commonly discussed in literature. The onset overpotential η_0 is the overpotential, at which the catalytic reaction begins, or in other words, at which the catalytic current becomes measurable. Due to the ambiguity of the onset overpotential definition, this

value is hard to determine (Figure 2.19.c) and so the η_0 is rarely used for the actual comparison of catalyst materials [294]. The overpotential required to achieve a certain catalytic current density is used instead. Often, -10 mA/cm^2 is chosen as the benchmarking value and the overpotential at this current density η_{10} is used as a total electrode performance metrics to compare the activity of different catalysts [290,294,295]. It should be pointed out that two different catalysts may achieve the benchmarking current density at the same η_{10} overpotential values as shown in Figure 2.19.c, however, the reaction kinetics may differ considerably in these two cases (Figure 2.19.d). For this reason, two crucial characteristics of the catalyst activity, Tafel slope and exchange current density, are usually reported in combination with the reaction overpotential to provide an accurate and complete overview of the electrode performance.

Tafel analysis provides information on the inherent kinetics of the catalytic reaction on the catalyst surface. The Tafel slope illustrates how fast the process occurs at the catalyst interface, while the exchange current density corresponds to the current density at equilibrium (the forward reaction balances the reverse reaction) and can be treated as a background current of the electrolysis reaction. For a simple redox reaction $Ox + ne^- \leftrightarrow Red$ at the catalyst-electrolyte interface, the dependence of catalytic current density on a working electrode j on the electrode potential E is given by the Butler-Volmer equation [83,290,296]:

$$j = j_0 \left[-e^{\frac{-\alpha \mathrm{n} F}{RT}(E-E^o)} + e^{\frac{(1-\alpha)\mathrm{n}F}{RT}(E-E^o)} \right], \tag{16}$$

where j_0 is the exchange current density (mA/cm^2); α and 1-α are the charge transfer coefficients of the forward and the reverse reactions, respectively; F is the Faraday constant (~96485 C/mol); R is the ideal gas constant (~8.314 J/[mol·K]); T is absolute temperature (K); the difference E-E^o is the overpotential η (V). At high polarisations (Tafel region), when only one of the processes prevails (the rate of reverse reaction is negligible compared to the rate of forward reaction), the Butler-Volmer equation is approximated by the Tafel equations for the anodic and the cathodic processes, respectively:

$$j \sim \begin{cases} j_0 e^{\frac{(1-\alpha)\mathrm{n}F}{RT}\eta} \text{ if } \eta \gg \dfrac{RT}{\mathrm{n}F} \\ -j_0 e^{\frac{-\alpha \mathrm{n} F}{RT}\eta} \text{ if } \eta \ll -\dfrac{RT}{\mathrm{n}F} \end{cases} \tag{17}$$

From these, the overpotential η can be derived as:

$$\eta \sim \begin{cases} \frac{RT}{(1-\alpha)\mathrm{n}F} \ln\left|\frac{j}{j_o}\right| & \text{if } \eta \gg \frac{RT}{\mathrm{n}F} \\ -\frac{RT}{\alpha \mathrm{n}F} \ln\left|\frac{j}{j_o}\right| & \text{if } \eta \ll -\frac{RT}{\mathrm{n}F} \end{cases} \quad (18)$$

The overpotential η linearly depends on the ln|j|; however, Tafel plots are normally presented in the η vs log|j| coordinates. For a cathodic process, such as the HER, Tafel slope is determined as $-\frac{2.303RT}{\alpha \mathrm{n}F}$ and its physical meaning is the additional voltage required to gain an order of magnitude increase in the catalytic current density; the widely-accepted Tafel slope unit is mV/dec. On the other hand, extrapolating the linear region of a Tafel plot until the interception with the x axis (η=0) allows for estimating the exchange current density j_0.

Since the electrocatalytic performance is usually tested in the three-electrode cell configuration, the solution resistance R_s strongly affects the potential values. Compensating the iR drop is thus considered essential for the assessment of the ideal electrode performance; however, for practical reasons reporting the uncompensated overpotential values is preferred. The R_s value depends on numerous factors, such as the distance between the reference and the auxiliary electrodes and the ionic strength of electrolyte solution [290]. Additionally, the contact resistance of electrical connections, for example of the electrodes to the potentiostat, contribute to the resistance losses. The total uncompensated resistance R_u is therefore used to compensate the iR drop in experimental polarisation curves. The dropped potential is calculated at each data point of the polarisation curve by multiplying the R_u by the corresponding current density value; then the iR-compensated potential $E_{\text{iR free}}$ can be obtained by subtracting the potential drop from the experimental potential value E. The uncompensated resistance value R_u is measured using electrochemical impedance spectroscopy (EIS) discussed in Section 2.4.2.3.

In this work, in order to reflect the performance of working electrodes, the iR-uncompensated overpotentials η_{10} are discussed. On the other hand, to avoid overestimating the Tafel slopes, Tafel analysis is performed only after compensating the iR drop.

2.4.2.3. Electrochemical impedance spectroscopy

Electrochemical impedance spectroscopy (EIS) is a technique allowing for studying the bound or mobile charges in the systems, electrochemical response of which is based on numerous and often connected transfer processes. The method is especially crucial for investigating the charge transfer across the interfaces, such as electrode surfaces, microstructure and grain boundaries, and phase boundaries, in the heterogeneous systems [297].

Electrical impedance (complex impedance) is a frequency-dependent measure of the resistance of alternating current (AC) driven circuits. Electrical impedance Z is a complex quantity characterised by the magnitude and the phase. The real part of impedance Z' is the electrical resistance of the circuit, while the imaginary part of impedance Z'' is the electrical reactance of the circuit that is caused by the electrostatic charge storage (capacitive reactance) and by the electrical current induced by the changing magnetic field of the alternating current (inductive reactance). In application to a three-electrode electrochemical cell, performing the EIS characterisation allows for probing and separating the contributions of several processes taking place in the cell that often include the electrolyte resistance, the capacitance of the double layer formed at the electrolyte-electrode interface, the charge-transfer resistance associated with the current of electrochemical reaction occurring at the electrode surface, and the ion diffusion. Impedance is commonly measured by applying a single-frequency signal (potential or current) to the interface under examination and to measure the phase shift and the amplitude change at the same frequency [297]. In an electrochemical cell, the potential is kept at a certain value since there is a reaction taking place on the working electrode and a small AC (voltage) signal is applied to probe the impedance of a cell [298]. An impedance spectrum is obtained by changing the signal frequency in a wide range. In this work, the potentiostatic EIS measurements were performed at the DC voltage required to achieve the current density of -10 mA/cm^2, typically -0.5-0.6 V vs reference electrode for all tested nanostructures. The AC voltage with the amplitude of 20 mV was swept in the frequency range from 10^6 to 10^{-2} Hz.

The potentiostatic EIS data are commonly presented as the impedance hodograph (Nyquist plot), where each point in the Z'-Z'' plane corresponds to the impedance at one frequency. An alternative representation is the Bode plot, where the absolute values of impedance and the phase shift are plotted as a function of the signal frequency. The analysis of the EIS data requires modelling the equivalent circuit using serial and parallel combinations of common elements, such as a resistor, a capacitor, an inductor, and a Warburg element. In this work, the EIS data were fitted to a Randles equivalent circuit. The fitting was performed using the Echem Analyst software package (Gamry).

The Randles cell includes contributions of the solution (uncompensated) resistance R_s (R_u), the charge transfer resistance R_c and the double layer capacitance C_{dl}. The equivalent circuit diagram is shown in Figure 2.20.a. The corresponding Nyquist plot for a Randles cell is always a semicircle (Figure 2.20.b). The high frequency intercept with the real impedance axis corresponds to the solution (uncompensated) R_s (R_u) resistance, while the low frequency

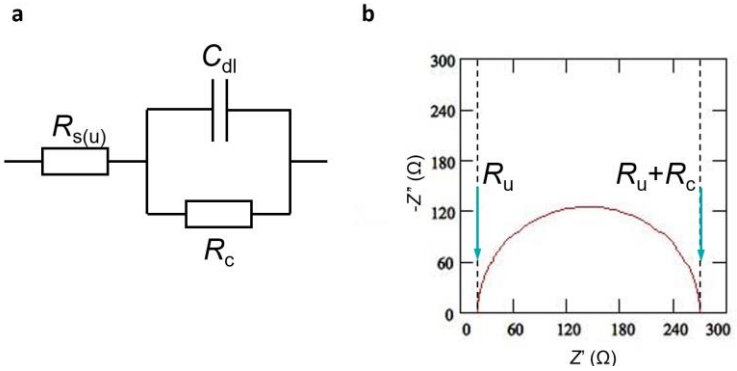


Figure 2.20. Modelling the potentiostatic EIS data. **a** The equivalent circuit of a Randles cell. **b**. The corresponding Nyquist plot. Adapted from *www.gamry.com*.

intercept is the sum R_u+R_c [299]. In general, the parallel combination of a capacitor and a resistor is characterised by the time constant $\tau = R \cdot C$. The appearance of multiple semicircles (arcs) in the impedance hodographs is caused by numerous complex processes with different time constants taking place in the system. These can include the electrical transfer across grain boundaries and phase interfaces or processes occurring inside the pores of the electrode coating. It should be noted that the same set of experimental data can be often fitted with more than one equivalent circuit, therefore a prior modelling of the system under examination is required [297]. Also, the arcs in impedance hodographs may appear significantly distorted due to multiple relaxation processes with comparable time constants (less than 2 orders of magnitude difference) taking place or the centre of the arc can be displaced below the real axis due to a distribution in relaxation times, for example caused by the microscopic inhomogeneities of electrode structure.

2.4.3. Optimisation of the electrode durability testing conditions

Prior to testing the electrocatalytic properties of the colloidal $W_xMo_{1-x}Se_2$ nanosheets, we have performed a series of experiments in order to identify the optimal electrochemical testing set-up. We found the commonly reported set-up, when testing is performed in 1M sulphuric acid solution using a commercial Ag/AgCl reference electrode, unsuitable for a long-term stability testing since the continuous cycling (3000 cycles) under reducing potentials has led to deposition of silver contaminants onto the working electrode surface. The elemental analysis (Figure 2.21.b) performed on the WSe_2 nanosheets after 3000 catalytic HER cycles between 0 and -0.8 V vs $Ag/AgCl_{3M\ KCl}$ reveals a significant amount of silver present in the sample post-testing. The corresponding SEM image (Figure 2.21.a) clearly demonstrates numerous quasi-rectangular Ag nanoparticles covering the surface of working electrode. The issue of silver ions leaking from the Ag/AgCl reference electrodes into the electrolyte solution

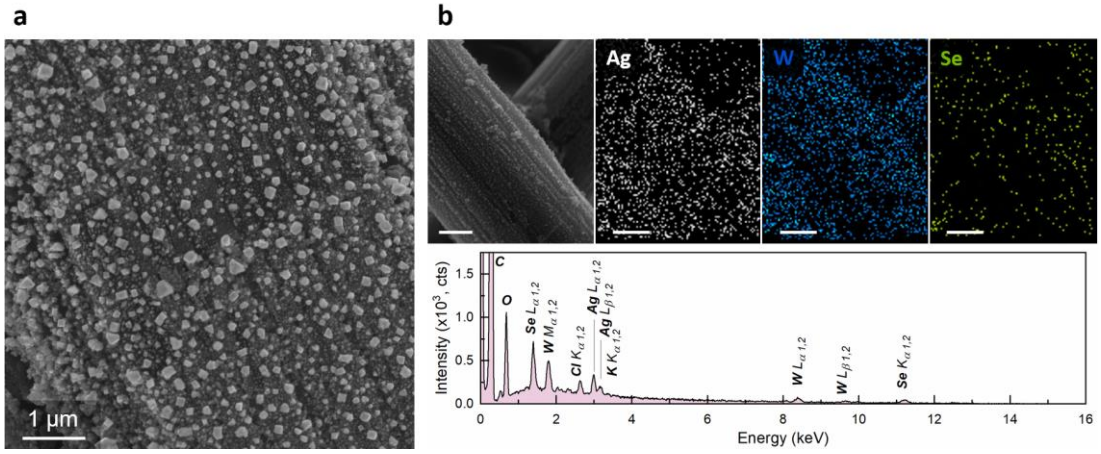


Figure 2.21. Structural characterisation of the WSe_2 working electrode after 3000 catalytic cycles. **a** SEM image and **b** corresponding EDS maps (top panel; Ag, W, and Se) and spectrum (bottom panel) acquired on the WSe_2 working electrode after long-term stability testing preformed in 1M H_2SO_4 using a Ag/AgCl reference electrode. Scale bars 2 µm.

resulting in the reduction of Ag^+ followed by its deposition as neutral Ag nanoparticles on the working electrodes has been raised recently [300]. In the cited work, deposition of silver nanoparticles resulted in current densities of over -5 mA/cm^2 achieved at relatively low overpotentials (500 mV) after several hours of potentiostatic electrolysis. However, this is rarely discussed in works on TMD catalysis.

It should be noted that no measurable signal of silver is detected in the EDS spectra of the working electrodes after basic electrochemical testing (10-20 catalytic cycles). Therefore, the initial increase of the catalytic current observed during a few first catalytic cycles (Figure 2.19.a,b) is likely to be attributed to the gradual wetting of high surface area of the branched nanosheets involving higher number of the active sites into the catalytic reaction. However, in order to explicitly exclude the false positive results arising due to deposition of catalytically active impurities the conditions of long-term stability testing had to be optimised.

We performed a series of model experiments, where the working electrode was replaced by the catalytically inert carbon foil (CF) and the varied parameters were the following: type of counter electrode (Pt mesh vs carbon foil), type of reference electrode (Ag/AgCl vs Hg/Hg_2Cl_2) and type of electrolyte (1M H_2SO_4 vs 1M H_3PO_4). The effect of each of these parameters was assessed based on the variation of the current density at the working electrode after 100 of cathodic sweeps from 0 to -0.8 V (vs reference electrode) at a 10 mV/s scan rate as shown in Figure 2.22.b-e. The CF working electrode (WE) – CF counter electrode (CE) – $Ag/AgCl_{(3M\ KCl)}$ reference electrode (RE) – 1M H_2SO_4 electrolyte set-up represents the standard electrochemical testing scheme used throughout this work. Initially inert CF starts exhibiting a

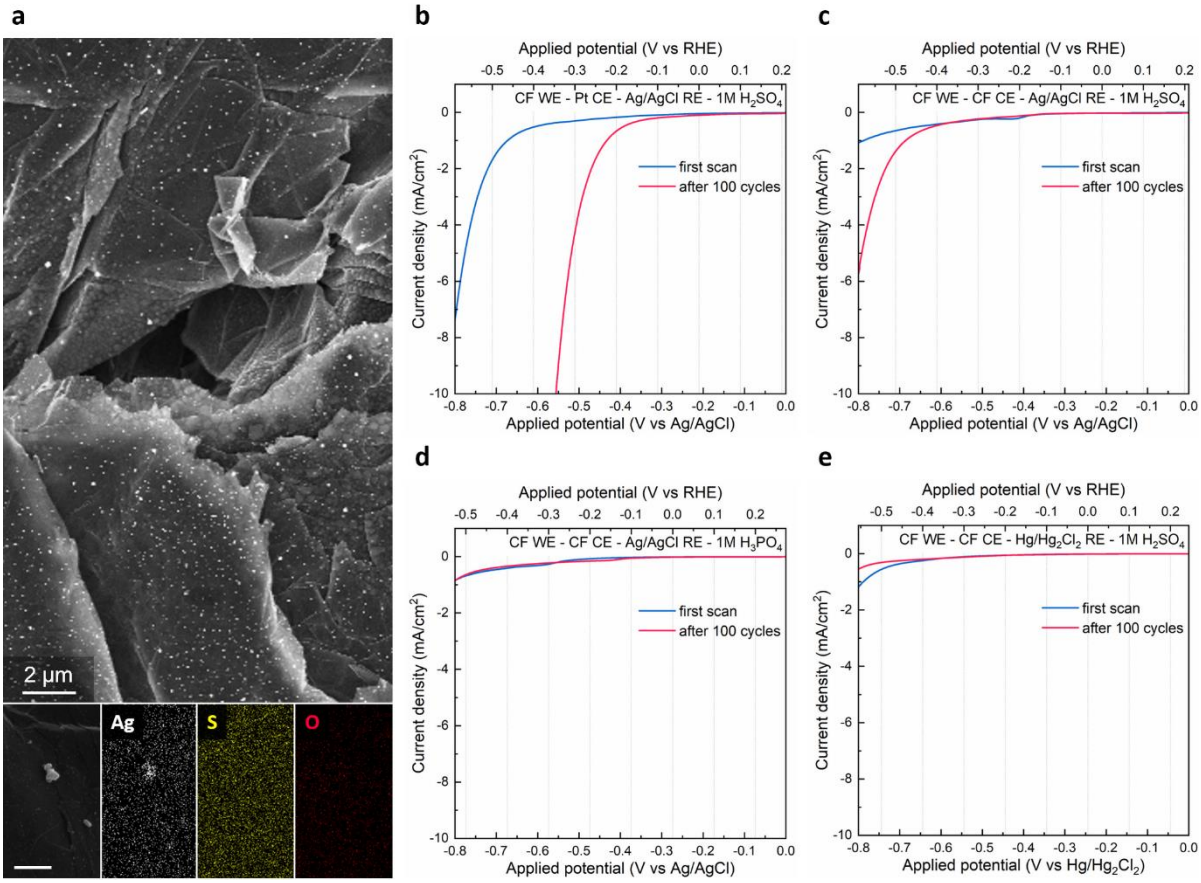


Figure 2..22. Optimisation of the electrochemical set-up for the long-term stability testing. **a** SEM image and the EDS maps (scale bar 500 nm) of the CF WE after 100 catalytic cycles in the CF WE – CF CE – Ag/AgCl RE – 1M H_2SO_4 configuration demonstrating deposition of silver nanoparticles; S and O signals in the elemental maps arise from the surface contamination of the CF WE with electrolyte residues. **b-e** Polarisation curves of the CF WE before (blue) and after (red) 100 catalytic cycles in the following configurations: **b** CF WE – Pt CE – Ag/AgCl RE – 1M H_2SO_4; **c** CF WE – CF CE – Ag/AgCl RE – 1M H_2SO_4; **d** CF WE – CF CE – Ag/AgCl RE – 1M H_3PO_4; **e** CF WE – CF CE – Hg/Hg_2Cl_2 RE – 1M H_2SO_4.

measurable catalytic activity after 100 of cycles (Figure 2.22.c) reaching the maximum current density of -5 mA/cm^2 at 580 mV overpotential. SEM imaging and elemental analysis shown in Figure 2.22.a reveal numerous silver nanoparticles appearing on the surface of the tested CF as a result of reductive electrodeposition. Surprisingly, using Pt mesh as a counter electrode has led to significantly higher current densities at the CF working electrode exceeding - 10 mA/cm^2 at the overpotentials over 350 mV (Figure 2.22.b). To supress silver ion leakage from the Ag/AgCl reference electrode Roger *et al* suggested using phosphoric acid as an alternative electrolyte based on the lower solubility of the corresponding silver salt in water at room temperature [[300]]. Indeed, performing the catalytic cycling in 1M H_3PO_4 resulted in a significantly more stable current densities not exceeding -1 mA/cm^2 at 525 mV overpotential (Figure 2.22.d). Alternatively, a calomel reference electrode can be used to exclude

electrodeposition of metallic silver completely (Figure 2.22.e); the observed decrease in the measured current density at the CF working electrode can be in fact attribute to the local depletion of the electrolyte since the catalytic cycling was performed in a conventional electrochemical cell without magnetic stirring.

The durability testing of the WSe_2 working electrodes discussed in Section 5.5 was carried out in 1M phosphoric acid electrolyte using carbon foil as a counter electrode and a commercial Ag/AgCl reference electrode.

Chapter 3:
Colloidal synthesis of inorganic metal chalcogenide nanoflowers

This Chapter covers the development of a bottom-up solution-phase synthesis approach to grow binary metal chalcogenide, specifically $MoSe_2$, $MoTe_2$, Bi_2Te_3, and WSe_2, hierarchical nanosheets, also referred to as nanoflowers or branched nanosheets within this Thesis, from molecular precursors. We investigate the effect of synthesis conditions on the morphology, degree of crystallinity, and crystal structure of the produced nanosheets. To achieve this, a parametric study of the colloidal synthesis conditions, including reactivity of both metal and chalcogen precursors, type of the solvent, growth temperature and synthesis time, has been carried out. We demonstrate that the selected materials ($MoSe_2$, $MoTe_2$, Bi_2Te_3, and WSe_2) can be obtained in the form of well-defined nanoflowers with atomically-thin petals, exhibiting edge-abundant morphology. The latter is beneficial for a number of practical applications, such as catalysis and electrochemical energy storage devices. We explore how the synthesis parameters, such as growth temperature in the case of Bi_2Te_3 synthesis, can be employed to attain a controllable tuning of the morphology of the growing material. Further, we shed light on how growth in the solution phase can facilitate formation of the metastable polymorphs, for instance the monoclinic phases of WSe_2 and $MoTe_2$, providing an extra tool to control the electronic properties of a given material.

3.1. Colloidal $MoSe_2$ and $MoTe_2$ nanoflowers

Colloidal $MoSe_2$ hierarchical nanosheets were synthesised by adding trioctylphosphine selenide complex into a hot solution of molybdenum hexacarbonyl in oleic acid. We chose to use molybdenum hexacarbonyl as a source of the transition metal as in contrast to the corresponding chloride, $MoCl_5$, and molybdates, Na_2MoO_4 and $(NH_4)_6Mo_7O_{24}{\cdot}4H_2O$, previously reported in the literature on solvothermal synthesis of molybdenum disulphides and diselenides [160,170,260], carbonyls are more robust and air-stable and therefore would result in the formation of less oxidised material. Colloidal synthesis of the $MoTe_2$ nanostructures has also been attempted, however, we found that a more reactive form of molybdenum precursor, such as molybdenum pentachloride, ought to be used in order to achieve nucleation of crystalline $MoTe_2$. The experimental set-up and the detailed procedures are described in Section 2.2.3. Full list of performed syntheses and the corresponding conditions are provided in Appendix A1 and A2.

3.1.1. Structural characterisation of $MoSe_2$ and $MoTe_2$ nanoflowers

The produced $MoSe_2$ nanostructures were isolated from the reaction medium and then dispersed in ethanol for storage. A photograph of a freshly prepared colloidal suspension of $MoSe_2$ nanoflowers is shown in Figure 3.1.a. The suspension is dark-grey in colour and the scattering of the visible light (Tyndall effect) suggests that the dispersed $MoSe_2$ nanostructures are in the order of a few hundred nanometres in size. Indeed, low-magnification SEM imaging (Figure 3.1.a) shows that being roughly spherical in nature the produced particles exhibit branched, flower-like, morphology. The agglomeration of $MoSe_2$ branched nanoparticles, occurring upon solvent evaporation during the SEM samples preparation, hinders the direct investigation of their morphology. TEM analysis, on the other hand, reveals that the majority of individual $MoSe_2$ nanoflowers do not exceed 200 nm in diameter with an average size of approximately 50-100 nm (Figure 3.1.d). The obtained hierarchical nanoarchitectures are made of two-dimensional nanosheets of variable thickness. The thickness of the constituent nanosheets accounts for 10-15 monolayers near the core of a nanoflower and is progressively thinning down to 3-4 layers at the edges. This thickness observed for the vertically aligned petals is, however, in stark contrast with the appearance of the flat petals, which according to a very faint contrast in the TEM images, are likely to be ultra-thin. A top-view high resolution TEM image presented in Figure 3.1.b illustrates how the petal rims are composed of single- and few-layered regions. The moiré patterns observed in the few-layered areas are indicative of the rotational misalignment of restacked layers. In Figure 3.1.c, a HR TEM image of the produced $MoSe_2$ nanosheets displays the three-fold symmetry of the crystal lattice with the *d*-spacing of 2.6 Å. Taking into account the absolute measurement error (<8%, Section 2.3.2), this value is close to that of the {100} planes of bulk hexagonal $MoSe_2$ (2.84 Å, ICDD 29-914). The results of elemental analysis indicate a slight excess of selenium in the as produced material ([Mo]:[Se] atomic ratio is 1:2.28). In addition to that, the crystallinity of $MoSe_2$ nanosheets is quite low as is evidenced by the ~nm^2-sized single crystalline patches composing the basal plane (Figure 3.1.c), which cause blurring of the diffraction spots in the corresponding FFT pattern (Figure 3.1.c inset), and the sub-nm voids present in the single-layered areas (marked with yellow arrows in Figure 3.1.b). It should be noted that in the $MoSe_2$ samples a fraction of the nanostructures is found in a more complex branched morphology (Figure 3.1.e). These structures (‘brushes’) can be described as intertwined branched nanosheets with thick multi-layered ‘stems’ and thin petals stemming off them (Figure 3.1.f).

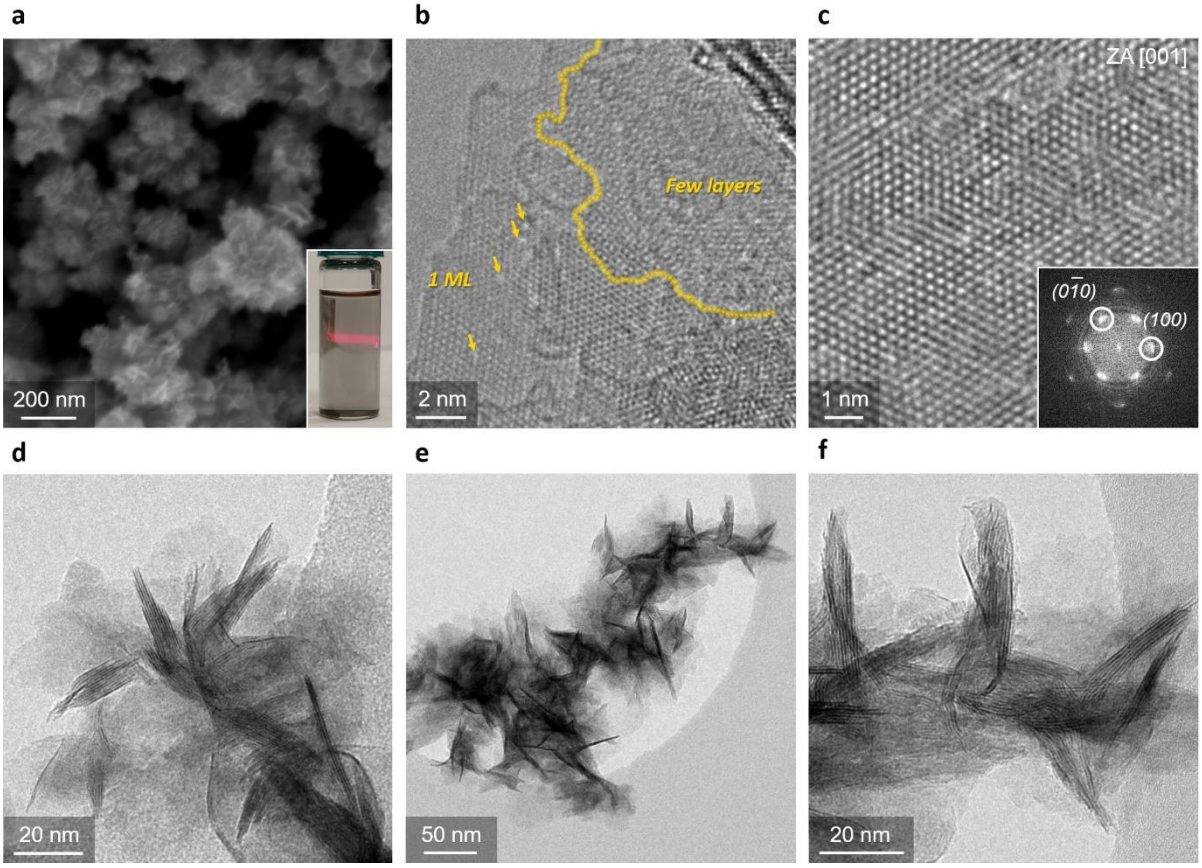


Figure 3.1. Morphology of the colloidal $MoSe_2$ hierarchical nanostructures. **a** SEM image of an ensemble of the $MoSe_2$ branched nanosheets, inset shows a photograph of a suspension of the $MoSe_2$ branched nanosheets in ethanol. **b, c** High resolution TEM images taken from the rims of individual $MoSe_2$ petals and the corresponding FFT pattern (inset in panel **c**) demonstrating crystalline nature of single petals. **d** TEM image of a $MoSe_2$ nanoflower. **e, f** TEM images of the $MoSe_2$ "brushes" of ultra-thin petals sprawling off the thicker "stems".

The representative experimental XRD pattern of the produced colloidal $MoSe_2$ nanosheets is shown in Figure 3.2.a and matches well the reference pattern of bulk $MoSe_2$ (ICDD 29-914). The diffraction peaks are broadened due to the small size of crystalline domains and a strain caused by curling and folding of the thin $MoSe_2$ nanosheets. The most prominent reflections observed in the experimental diffractogram at 13.9, 31.8, and 38.1 degrees 2θ correspond to the (002), (100) and (103) planes of the hexagonal phase of $MoSe_2$. The strong (002) reflection confirms multi-layered nature of the 'bulk' of the produced material.

The Raman spectrum of the synthesised $MoSe_2$ nanosheets (Figure 3.2.b) demonstrates two well-resolved signatures centred at 239 and 285.6 cm^{-1} as well as complex overtone peaks at ~435 and ~580 cm^{-1}. The sharp peak observed at ~240 cm^{-1} is commonly assigned to the out-of-plane A_{1g} vibrational mode of the hexagonal $MoSe_2$. In bulk $MoSe_2$ powder, A_{1g} is blue-

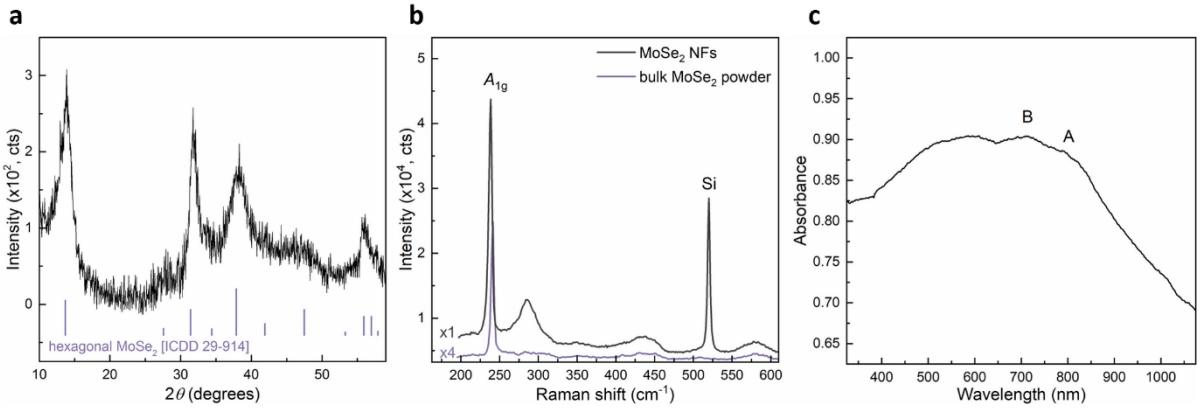


Figure 3.2. Structural characterisation of the colloidal $MoSe_2$ nanosheets. **a, b, c** X-ray diffractogram, Raman spectrum, and optical absorption spectrum of the produced $MoSe_2$ hierarchical nanosheets, respectively. A reference diffraction pattern of bulk $MoSe_2$ (ICDD 29-914) is shown in **a** for comparison. Raman spectrum of bulk $MoSe_2$ powder in panel **b** is given in x4 scale, the spectra are offset for clarity.

shifted compared to that of the colloidal $MoSe_2$ nanoflowers and appears at 241.1 cm^{-1} (Figure 3.2.b); this experimental value is in good agreement with the reported position of the A_{1g} mode of bulk $MoSe_2$ (~242 cm^{-1}, [301]). The characteristic softening (red shift) of the out-of-plane vibrational mode is generally observed with the thickness of material decreasing [54], ultimately reaching the single-layer limit where the A_{1g} mode is normally found in the range 239-240.5 cm^{-1} [67,169,302]. The peak at 285.6 cm^{-1}, which is not detected in bulk $MoSe_2$, can be assigned to the in-plane E^1_{2g} vibration mode, similarly to [303,304]. However, this mode has been demonstrated to have very low intensity even in monolayers and can only be detected when its intensity is enhanced under a short-wavelength excitation [301], suggesting a resonant character of this mode. Recently, tip-enhanced Raman spectroscopy (TERS), which allows for the nanometre-sized lateral resolution of the heterogeneities in samples, has unambiguously shown that this resonant mode at ~287 cm^{-1} is significantly enhanced in polycrystalline $MoSe_2$ monolayers, while is nearly absent in single-crystalline monolayers of ~100 μm size [302]. Thus, the polycrystalline nature of the colloidal $MoSe_2$ nanoflowers made of nanoscale domains (within individual petals), and thus being abundant in grain boundaries, is likely to cause the observed enhancement of the in-plane Raman signature that has not been reported in the single-crystalline $MoSe_2$ monolayers[169].

The semiconducting 2H phase of $MoSe_2$ nanoflowers is evidenced by the results of optical absorption spectroscopy. A typical UV-vis absorption spectrum of the produced $MoSe_2$ hierarchical nanosheets is presented in Figure 3.2.c and demonstrates the characteristic excitonic transitions of the semiconducting phase. The interband transitions are labelled

according to the conventional notions introduced by J. Wilson and A. Yoffe [40]. The A and B excitons near the optical absorption edge originate from the transitions between the spin-orbit split valence band and conduction band and in the case of synthesised $MoSe_2$ nanoflowers are found at 805 and 710 nm, respectively. The observed positions are red-shifted from the reported monolayer positions [53,305] that agrees well with the few-layered nature of the synthesised material determined from the TEM data.

The synthesis approach developed to grow $MoSe_2$ hierarchical nanosheets in solution phase has been further extended to synthesise colloidal $MoTe_2$ nanostructures. The main difficulty to synthesise $MoTe_2$ directly from the corresponding molecular precursors is associated with the extreme instability of available tellurium precursors that are suitable for a solution-phase reaction. In the following section, we provide a detailed parametric study of the growth conditions we optimised to obtain the colloidal $MoTe_2$ nanostructures.

The morphology of the produced colloidal $MoTe_2$ nanostructures resembles that of the $MoSe_2$ nanoflowers discussed above. A representative TEM image is shown in Figure 3.3.a and reveals irregular quasi-flowerlike shape of the synthesised $MoTe_2$ with lateral dimensions in the range 100-200 nm. TEM analysis, and especially high-resolution imaging, of the material is complicated due to a rather quick degradation and, as a consequence, amorphization of colloidal $MoTe_2$ nanostructures in the course of a few hours of air exposure. The phase analysis of the produced $MoTe_2$ was performed using powder X-ray diffraction data instead. A typical diffractogram of $MoTe_2$ nanostructures is presented in Figure 3.3.c. It clearly shows two distinct phases present in the sample. A set of rather broad diffraction peaks can be ascribed to $MoTe_2$. Although the experimental peaks are substantially broadened due to the nanoscale dimensions of the crystalline domains, the overall diffraction pattern of colloidal $MoTe_2$ nanostructures does not match that of the hexagonal phase. Instead, synthesised in the solution phase $MoTe_2$ seem to be acquired in the monoclinic 1T' phase, also referred to as β-$MoTe_2$. Calculations have identified that the thermodynamically stable phase of $MoTe_2$, both in bulk material and in a monolayer limit, is the hexagonal 2H phase [12,20]. However, the calculated energy difference between the 2H and 1T' polymorphs is only 0.04 eV per formula unit [20]. This suggests that formation of the metastable polymorph is quite possible under favourable growth conditions. Additionally, interaction with organic ligands and solvents can alter the surface energy and so further lower the energy barrier for obtaining the metastable phase. The most prominent peak in the diffraction pattern of the obtained 1T' $MoTe_2$ corresponds to the unresolved (201), ($\bar{1}$12), and (112) reflections observed at 29.42, 31.73, and 32.53° 2θ,

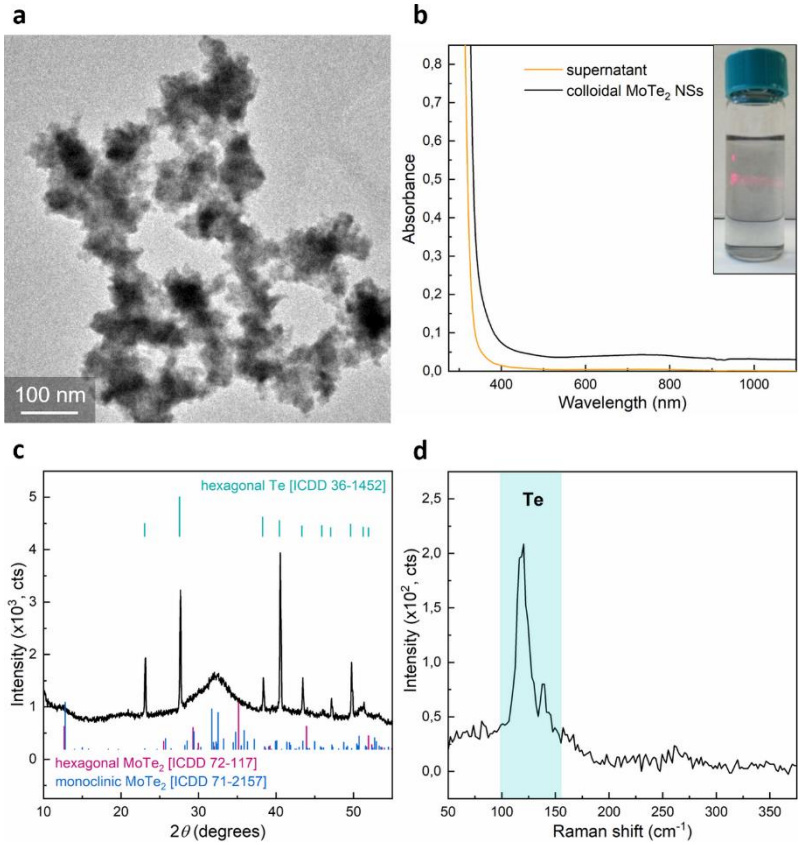


Figure 3.3. Structural characterisation of the colloidal $MoTe_2$ nanostructures. **a** TEM image of the produced $MoTe_2$ nanostructures. **b** Optical absorption spectra of the final $MoTe_2$ product and the reaction medium (supernatant); inset is a photograph of a freshly prepared suspension of the colloidal $MoTe_2$ nanostructures in ethanol. **c, d** XRD pattern and Raman spectrum of the final $MoTe_2$ product, respectively. In panel **c**, standard diffraction patterns of the hexagonal tellurium (ICDD 36-1452), hexagonal (ICDD 72-117) and monoclinic (ICDD 71-2157) $MoTe_2$ are given for reference.

respectively, in bulk β-$MoTe_2$. Unlike the case of the $MoSe_2$ hierarchical nanosheets, the (002) reflection at 12.79 $^{o}2\theta$ is nearly absent in the diffractogram of colloidal $MoTe_2$ nanostructures, indicating the small thickness of their petals. A second set of sharp diffraction peaks perfectly matches the reference pattern of metallic tellurium. Indeed, micron-sized needles of highly crystalline tellurium have been repeatedly observed in the SEM images of the produced material (will be discussed in more details in Section 3.1.3). We attribute the crystallisation of tellurium side-product to the decomposition of phosphine telluride complex at elevated temperatures rather than to the instability of transition metal ditellurides, and molybdenum ditelluride in particular, as in the latter case the formation of amorphous tellurium clusters could be expected.

The Raman spectrum of $MoTe_2$ product shown in Figure 3.3.d exhibits two strong bands at 120 and 140 cm^{-1} that are related to the A_1 and E vibrational modes of elemental tellurium [306]. The Raman spectra were acquired from the areas containing only small agglomerates of

$MoTe_2$ nanoflowers and away from the optically-visible Te side-products. Therefore, the appearance of the Te vibrational modes in Raman spectra of $MoTe_2$ nanoflowers is likely due to the material degradation under laser irradiation. The degradation of transition metal ditelluride samples accompanied by the formation of Te metalloid clusters is commonly reported [307]. In the cited report, for instance, it was demonstrated that the fingerprints of the 1T' phase disappear completely in the Raman spectrum of the 1T' $MoTe_2$ single layer after the first 30 seconds of signal acquisition (1 mW power focused to the 1 μm laser spot on the sample), while the intensity of the Te metalloid bands steadily increases over the next 4 minutes of exposure until it reaches saturation. Due to the low symmetry, the monoclinic 1T' polymorph displays a wider set of characteristic Raman features compared to the hexagonal 2H phase. From the group theory, bulk 1T' $MoTe_2$ has 18 Raman active modes, only 9 of which are allowed in the Raman spectrum of the corresponding monolayers [308]. Indeed, 3 modes with the B_g symmetry (along the zigzag chains of Mo atoms in the *b*-axis direction) at 92, 102, 190 cm^{-1} and 6 modes with the A_g symmetry (vibrations in the *ac* plane perpendicular to the zigzag chains) at 85, 113, 128, 164, 253, and 270 cm^{-1} were experimentally observed in the Raman spectra of the high-quality CVD grown 1T' $MoTe_2$ single layer recorded at different incident light polarisation and signal collection geometries [307]. In the case of colloidal 1T'$MoTe_2$ nanostructures discussed in this Chapter, low crystal quality and rapid degradation of the produced material hindered the direct study of its lattice.

In contrast to the hexagonal polymorph, which in the bulk form is an indirect gap semiconductor and becomes a direct gap semiconductor with the optical band gap of 1.1 eV in the monolayer limit [309], bulk monoclinic 1T' $MoTe_2$ is semimetallic in nature and exhibits a narrow band gap (~60 meV) opening once the material is thinned down to 1-10 layers [310]. As expected for the semimetallic 1T' polymorph, the optical absorption spectrum of the produced colloidal $MoTe_2$ nanostructures shown in Figure 3.3.b does not display any excitonic bands in the IR-region. Compared to the solution of the unreacted molecular precursors (supernatant), it exhibits only a considerable scattering in the entire visible range owing to the metallic nature of the 1T' polymorph. Strong band in the high-energy region, which is present in the optical spectra of both the final product and the supernatant, is attributed to the absorption of free oleic acid, which was not removed completely during the post-growth washing process.

3.1.2. Parametric study of the growth conditions: Colloidal $MoSe_2$ nanoflowers

To better understand the tunability of the proposed synthesis process of colloidal $MoSe_2$ nanostructures, we have carried out a series of experiments varying the growth conditions.

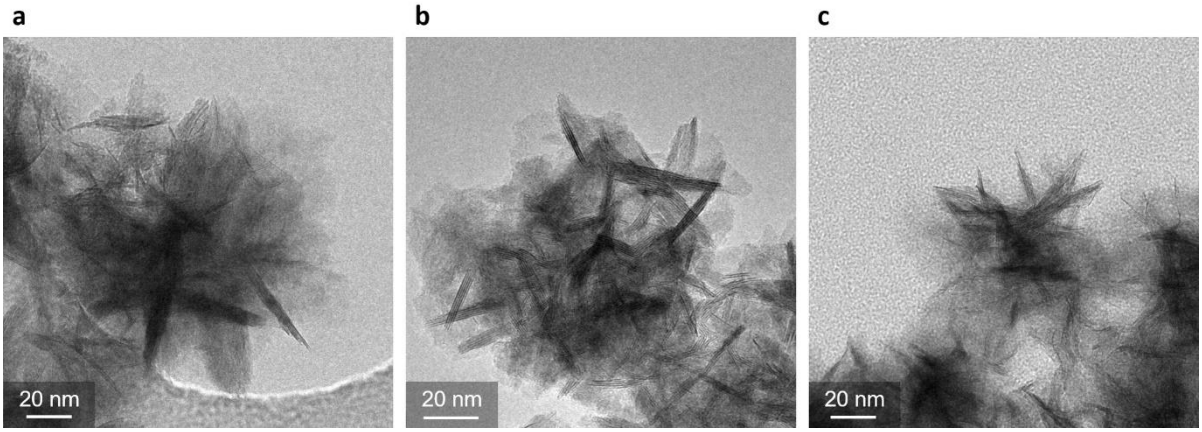


Figure 3.4. Effect of molybdenum precursor on morphology of the colloidal $MoSe_2$ nanostructures. Representative TEM images of individual $MoSe_2$ nanoflowers grown through the reaction between 1M TOP:Se and **a** $Mo(CO)_6$, **b** $MoCl_5$, and **c** $MoO_2(acac)_2$ in hot oleic acid.

Firstly, the effect of transition metal precursor was investigated. We have performed a series of syntheses using molybdenum hexacarbonyl $Mo(CO)_6$, molybdenum pentachloride $MoCl_5$, and molybdenyl acetylacetonate $MoO_2(acac)_2$, to form the molybdenum complex, while other growth conditions (selenium precursor, solvent, growth temperature and time) were kept unchanged. The representative TEM images of the corresponding $MoSe_2$ nanostructures are shown in Figure 3.4.a-c. Replacing molybdenum carbonyl with the respective dioxydiacetylacetonate led to formation of smaller $MoSe_2$ nanostructures with the apparent diameter changed from over 150 nm to just under 100 nm (Figure 3.4.a,c), while the well-defined flower-like morphology was preserved. On the other hand, using $MoCl_5$ as a source of transition metal resulted in the formation of branched nanostructures composed of agglomerated $MoSe_2$ nanosheets (Figure 3.4.b).

We further investigate the effect of coordinating solvent on the morphology of $MoSe_2$ nanosheets. To do so, three molybdenum complexes, $Mo(CO)_6$ dissolved in oleic acid, $Mo(CO)_6$ in oleylamine, and $MoCl_5$ in oleylamine, were compared (Figure 3.5.a-c). In contrast to the well-shaped nearly-spherical $MoSe_2$ branched nanostructures produced by reacting the selenium precursor with the $Mo(CO)_6$ complex in oleic acid (Figure 3.5.a), coordinating $Mo(CO)_6$ with oleylamine resulted in the formation of agglomerated nanosheets (Figure 3.5.b). It should be noted that similar continuous branched structures of agglomerated nanosheets were grown through a reaction between the selenium precursor and $MoCl_5$ in oleylamine (Figure 3.5.c). The lateral size of individual $MoSe_2$ nanosheets decreased to about 20 nm as illustrated by TEM image in the inset in Figure 3.5.c.

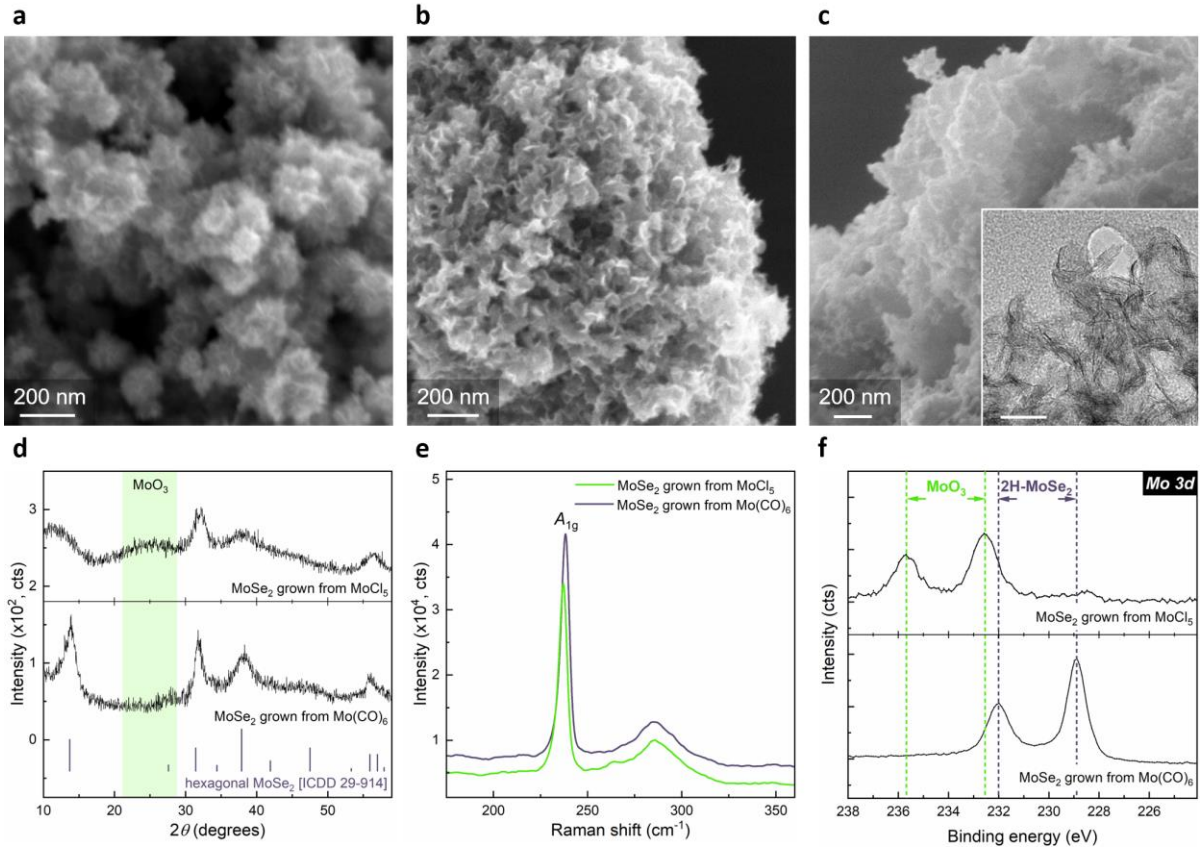


Figure 3.5. Effect molybdenum complex on morphology and crystal phase purity of the colloidal $MoSe_2$ nanostructures. **a-c** Representative SEM images of the ensembles of $MoSe_2$ nanostructures grown from **a** $Mo(CO)_6$ in oleic acid, **b** $Mo(CO)_6$ in oleylamine, and **c** $MoCl_5$ in oleylamine. Inset in panel **c** shows a TEM image of the ultra-thin $MoSe_2$ nanosheets; scale bar 20 nm. **d-f** XRD patterns, Raman spectra and high resolution XPS spectra of the Mo 3*d* core level electrons, respectively, of the $MoSe_2$ nanoflowers synthesised from $Mo(CO)_6$-OlAc and $MoCl_5$-OlAm complexes.

The effect of solvent type on the morphology of $MoSe_2$ nanostructures can be two-fold. First, oleic acid is assumed to be a stronger complexing ligand compared to oleylamine, and so the transition metal complexes formed in oleic acid are less reactive than the ones in oleylamine [156]. Second, compared to oleylamine, oleic acid was found to exhibit a weaker affinity to the lateral surfaces of the group VIB TMDs and so does not inhibit the lateral extension of TMD nanosheets growing in colloidal solution [169]. We suggest that the apparent reduction of the lateral dimensions of $MoSe_2$ nanostructures might be attributed to the difference in reactivity of molybdenum source. When the reaction is performed from more reactive molybdenum complex formed in oleylamine, faster monomer accumulation and so higher supersaturation in the system cause the formation of higher number of smaller nuclei and result in the final nanostructures with smaller lateral sizes. Whereas when low reactive molybdenum complex in oleic acid is used, the monomer is accumulated gradually. This leads to lower supersaturation,

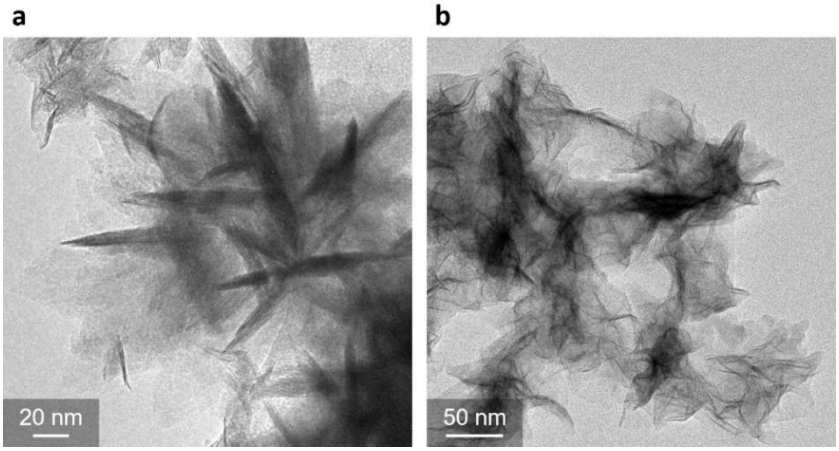


Figure 3.6. Effect of other growth parameters on morphology of the colloidal $MoSe_2$ nanostructures. **a** growth time increased to 19 hours, **b** reactivity of the $Mo(CO)_6$ precursor increased by complexing with HMDS.

allowing for the formation of fewer $MoSe_2$ nuclei. The residual precursor not consumed during the nucleation stage is available for the growth of larger well-defined nanostructures.

The difference in morphology of $MoSe_2$ branched nanosheets grown from the metal complexes in OlAc and OlAm is additionally illustrated by the results of powder X-ray diffraction and Raman spectroscopy shown in Figure 3.5.d,e. The Raman spectra of the synthesised $MoSe_2$ nanosheets (Figure 3.5.e) display similar well-resolved out-of-plane A_{1g} and in-plane E^1_{2g} modes discussed in Section 3.1.1. However, the red shift of the out-of-plane vibrational mode ($\Delta\omega$ = 1.2 cm^{-1}) suggests the decrease in thickness of the nanosheets produced from the more reactive $MoCl_5$-OlAm precursor. This is corroborated by the XRD results demonstrating much lower intensity of the (002) peak (at ~13.8 $^o2\theta$) in the thin $MoSe_2$ nanosheets synthesised from the $MoCl_5$-OlAm precursor compared to the material grown from the less reactive $Mo(CO)_6$-OlAc as shown in Figure 3.5.d. Despite the fact that the $MoCl_5$ precursor has evidently led to the formation of thinner $MoSe_2$ nanosheets, it has not been used throughout this work as the material produced by this route contained a considerable fraction of oxidised molybdenum. The formation of MoO_3 may be due to the reaction of highly active $MoCl_5$ with air occurring during the transfer stage and initial solubilisation in oleylamine. The presence of MoO_3 phase in the samples synthesised from $MoCl_5$ is demonstrated by a broad reflection observed at ~27 $^o2\theta$ in the experimental diffractograms, while this reflection is absent in the XRD patterns of the $MoSe_2$ samples grown from carbonyl (Figure 3.5.d). Moreover, only a distinct Mo^{+6} doublet at 232.6 and 235.7 eV corresponding to the MoO_3 phase is present in the XPS spectrum of the Mo 3*d* core level electrons of the $MoSe_2$ nanosheets grown from $MoCl_5$ (Figure 3.5.f). On the contrary, a single Mo^{+4} doublet of the hexagonal $MoSe_2$ is found

at 228.9 and 232.0 eV in the corresponding XPS spectrum of the material grown from $Mo(CO)_6$.

Finally, as shown in Figure 3.6.a, the increase in growth time from 3 to 19 hours did not affect the morphology of the synthesised $MoSe_2$ nanostructures. On the other hand, slight modulation of the reactivity of the $Mo(CO)_6$-OlAc precursor by complexing with hexamethyldisilazane (HMDS) allowed us to decrease the degree of branching in the colloidal $MoSe_2$ nanostructures, while leading to a noticeable lateral extension of the individual nanosheets (Figure 3.6.b).

3.1.3. Parametric study of the growth conditions: Colloidal $MoTe_2$ nanostructures

The main challenge in the solution-phase growth of transition metal ditellurides arises from the instability of the available chalcogen precursors. Although tertiary phosphine selenides are thermally robust, their telluride counterparts tend to decompose even at room temperature, releasing metallic tellurium [[244]]. This reaction is promoted considerably upon exposure to air, however, the formation of tellurium 'mirror' has been repeatedly observed even on the walls of a nitrogen filled vial containing stock solution of 1M TOP:Te. At the growth temperature (300 ºC) used throughout this work, tellurium precursor dissociates and then recrystallises in a form of micron-sized needles repeatedly observed in the SEM images of the final products (as shown in Figure 3.7). This Te phase gives rise to a second set of sharp diffraction peaks in the experimental diffractograms (see Figure 3.3.c). In the recently published protocols on colloidal synthesis of molybdenum and tungsten tellurides [[171,259]], highly uniform branched nanostructures were attained through a reaction of the transition metal chloride based precursor dropwise injected into a hot solution of the TOP:Te complex in primary amine in the presence of hexamethyldisilazane (HMDS). HMDS was indicated as an essential component of the synthesis, leading to formation of highly crystalline ditelluride nanoflowers, however, no explanation of the role of HMDS has been provided so far. Used as an additive in the colloidal synthesis of the hexagonal SnS plates, HMDS is believed to help removing the *in situ* built HCl from the reaction mixture, eventually leading to the formation of highly-crystalline SnS nanosheets [[311]]. Additionally, in the synthesis of colloidal WS_2, HMDS was suggested to improve reactivity of the transition metal complex essential for the formation of high-quality nanostructures [[156]]. In this study we, however, limited the set of experimental conditions to the direct reaction between the transition metal and tellurium precursors occurring in a hot solvent, excluding the investigation of the effect of additives from the scope of current work.

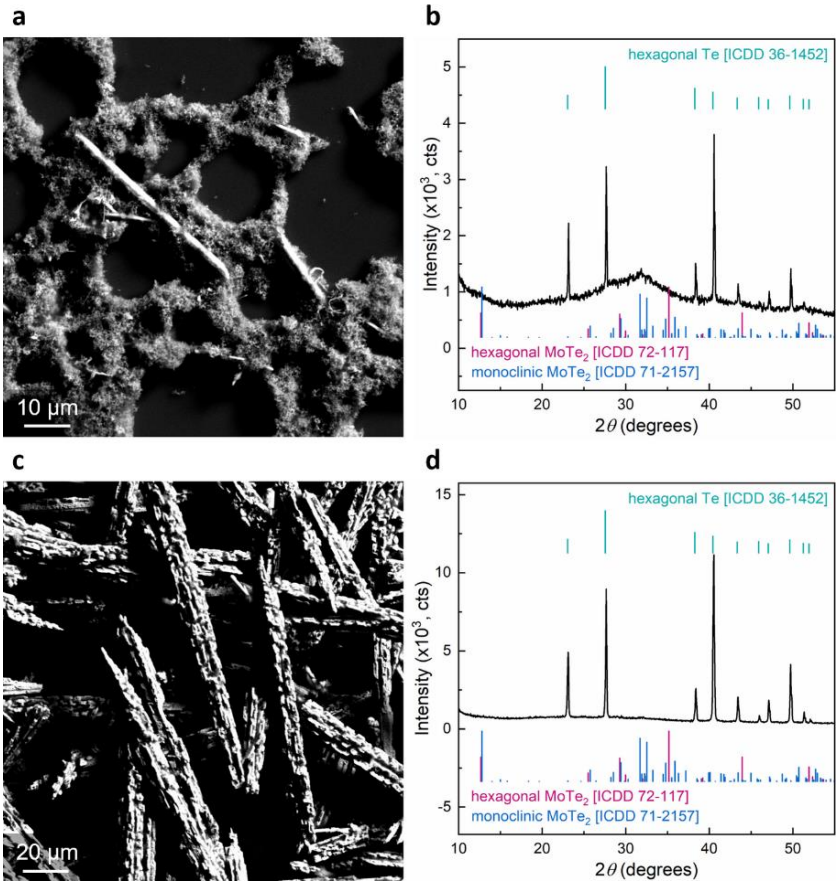


Figure 3.7. Effect of the transition metal precursor on the composition of the final product in the synthesis of $MoTe_2$. SEM images and XRD patterns of the final $MoTe_2$ products obtained through a reaction between 1M TOP:Te and **a, b** $MoCl_5$ and **c, d** $Mo(CO)_6$ dissolved in oleic acid.

Three experimental parameters, namely, type of molybdenum precursor, type of solvent and order of mixing of molecular precursors, were studied in order to identify the synthesis conditions, allowing for the preferential growth of molybdenum ditelluride nanostructures. The reactions were performed at fixed temperature (300 ºC) and time (2 hours); concentrations of the tellurium and molybdenum precursors were also kept fixed throughout the series of experiments. The final products of each of the model experiments were characterised using powder X-ray diffraction and scanning electron microscopy coupled with energy-dispersive spectroscopy revealing morphology, elemental composition and crystallinity of their various components.

In Figure 3.7, the final products of the reaction between trioctylphosphine telluride and either $MoCl_5$ (panels a, b) or $Mo(CO)_6$ (panels c, d) in oleic acid are shown. The reaction with $Mo(CO)_6$ did not lead to formation of any measurable amount of the $MoTe_2$ product. SEM images shown in Figure 3.7.c display only tellurium needles present in the final product. This conclusion is verified by the results of X-ray diffraction, revealing a single set of sharp

diffraction peaks corresponding to highly-crystalline tellurium (Figure 3.7.d). The elemental analysis has further supported the observation that no reaction occurred between TOP:Te and $Mo(CO)_6$ since the molybdenum signal is absent in the EDS spectra of the final product.

On the other hand, when a more reactive form of molybdenum, $MoCl_5$, is used in the colloidal synthesis of $MoTe_2$, the reaction between trioctylphosphine telluride and molybdenum precursor becomes energetically favourable, competing with the precursor decomposition and recrystallisation of tellurium micron-sized needles. The SEM imaging (Figure 3.7.a) confirms that the final product attained through the reaction between TOP:Te and $MoCl_5$ predominantly contains $MoTe_2$ branched nanosheets and a minor fraction of the micron-sized tellurium needles. Accordingly, two sets of diffraction peaks, of the nanometre-sized 1T'-$MoTe_2$ and of highly-crystalline tellurium side-product, are observed in the corresponding diffraction pattern (Figure 3.7.b). EDS analysis of the agglomerates of $MoTe_2$ nanostructures identified the approximate [Mo]:[Te] molar ratio being close to 1:2, while the TEM imaging (Figure 3.3.a) reveals the flower-like morphology of individual $MoTe_2$ nanostructures.

Next, the effect of two types of coordinating solvents, namely, oleic acid and oleylamine, and of a non-coordinating solvent, octadecene, on the composition of the final product was studied. For this set of experiments, a required amount of $MoCl_5$ was dissolved in a small amount of oleic acid (typically, no more than 1 mL) under nitrogen; thus prepared molybdenum precursor was then transferred into the degassed solvent of choice and heated up to the growth temperature (300 ^{o}C). The growth of $MoTe_2$ product was initiated by a swift injection of tellurium precursor. In the pioneering work on solution-phase synthesis of two-dimensional WSe_2 and $MoSe_2$ nanosheets, both oleic acid and oleylamine capping ligands were identified to selectively coordinate the transition metal (Mo or W) centres at the lateral sides of a TMD nanosheet; moreover, strongly binding ligands, like oleylamine, were suggested to inhibit the lateral extension of the growing nanosheet leading to a preferential vertical growth of multi-layered material, while the nanosheets obtained in the presence of weakly binding ligands, such as oleic acid, are predominantly monolayered [[169]]. For this reason, oleic acid was initially selected as a weakly binding coordinating solvent for the solution-phase growth of the $MoTe_2$ nanostructures (Figure 3.8.a). Replacing oleic acid with oleylamine has, however, led to a significant decrease in the amount of crystalline tellurium found in the final products. In fact, only two types of molybdenum containing nanostructures are repeatedly found in the $MoTe_2$ samples synthesised in oleylamine. Among them, $MoTe_2$ branched nanosheets forming

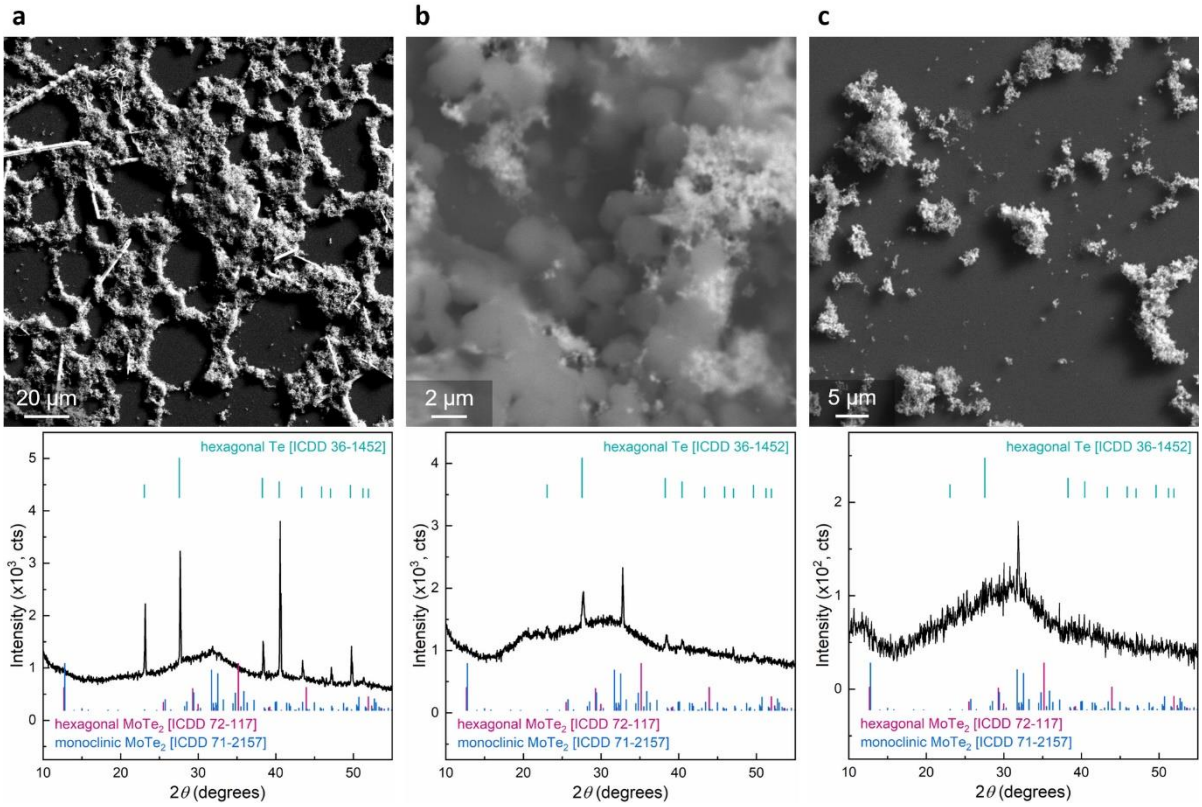


Figure 3.8. Effect of the type of solvent on the composition of the final product in the synthesis of $MoTe_2$. SEM images and XRD patterns of the final products obtained through a reaction between 1M TOP:Te and $MoCl_5$ in **a** oleic acid, **b** oleylamine, and **c** octadecene.

micron-sized agglomerates seen in the SEM images (Figure 3.8.b) account for the major part of the synthesised material. In addition to them, disk-like electron-transparent structures with lateral dimensions of a few microns are present in the final product (Figure 3.8.b). According to the results of elemental analysis, the disk-like structures are made of carbon and chlorine and thus are likely to be attributed to the organic-bound chloride by-products formed through a reaction between the residual chloride and oleylamine. Powder X-ray diffraction further confirms that, in contrast to the material synthesised in oleic acid, the $MoTe_2$ product obtained in oleylamine does not contain any significant fraction of crystalline tellurium. Further, we found that the quality of the $MoTe_2$ product can be significantly improved if the reaction between the molybdenum and tellurium precursors is carried out in a non-coordinating solvent. In particular, the reaction between $MoCl_5$ dissolved in a minimum amount of oleic acid and 1M TOP:Te performed in a non-coordinating solvent octadecene yielded high quality $MoTe_2$ nanostructures demonstrating no traces of the crystalline tellurium side-products (Figure 3.8.c). It should be noted that similar results were obtained when the transition metal complex was formed in a minimum amount of oleylamine instead of oleic acid.

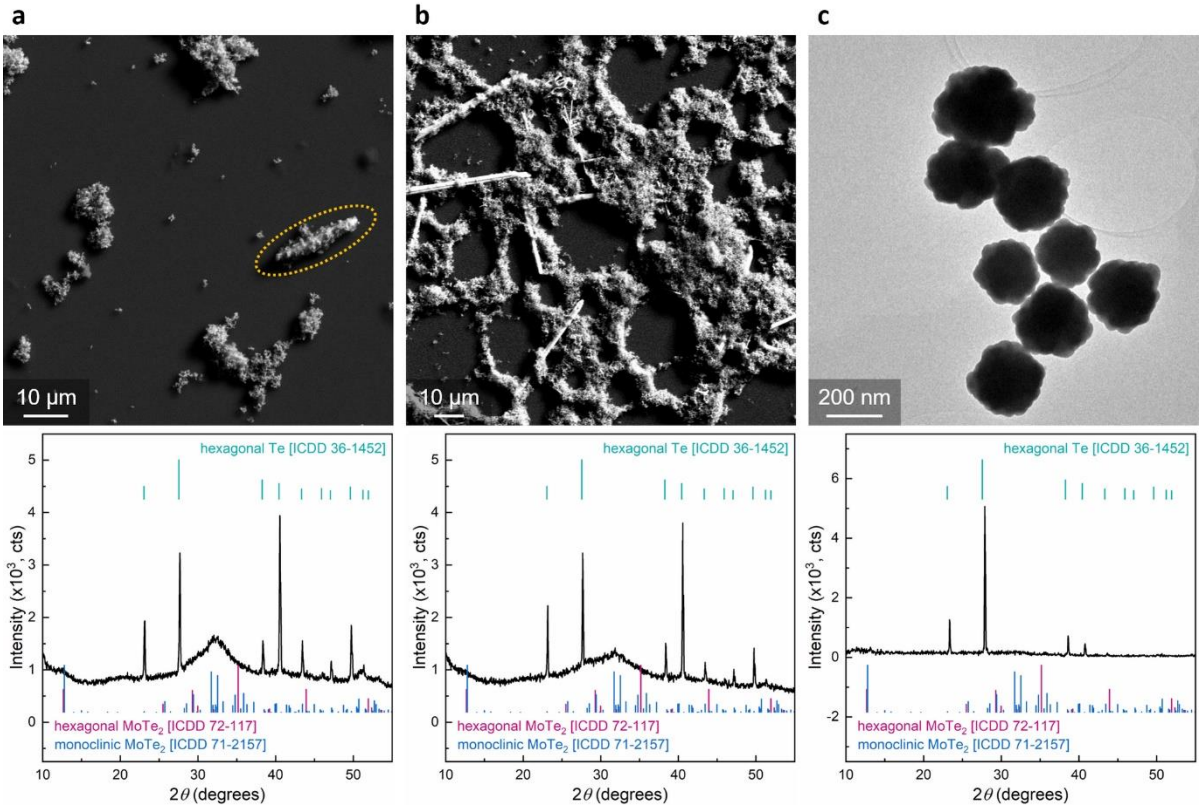


Figure 3.9. Effect of the order of mixing of the precursors on the composition of the final product in the synthesis of $MoTe_2$. SEM (TEM in panel **c**) and XRD patterns of the final products obtained through a reaction between 1M TOP:Te and $MoCl_5$ in oleic acid: **a** transition metal precursor is swiftly injected into hot solution of the chalcogen precursor; **b** chalcogen precursor is swiftly injected into a hot solution of the transition metal precursor; **c** chalcogen precursor is injected dropwise into a hot solution containing the transition metal precursor.

The order of mixing of the molecular precursors does not seem to significantly affect the quality of the final product. In a standard synthesis, a required amount of 1M TOP:Te stock solution is rapidly injected into a hot solution of the $MoCl_5$ complex in oleic acid and then the material is left to grow for 2 hours at 300 ºC. The final product contains two distinct components, one of which is micron-sized highly anisotropic tellurium needles, while the second component is the nanostructured 1T' $MoTe_2$ acquired in a form of branched nanosheets (Figure 3.7.a,b; Figure 3.8.a; Figure 3.9.b). Similarly, two components, the 1T'-$MoTe_2$ nanostructures and highly anisotropic tellurium micron-sized crystals, were found in the final product obtained through a reaction between the *in situ* generated tellurium precursor, produced via dissolution of a required amount of tellurium powder in a mixture of hot oleic acid and trioctylphosphine, and $MoCl_5$ in minimum amount of oleic acid quickly injected into a tellurium-containing solution (Figure 3.9.a). Notably, in the latter case the tellurium needles appear to be serving as seeds for the $MoTe_2$ nucleation and as a result are densely coated by the $MoTe_2$ nanosheets growing on their surface as shown in Figure 3.9.a (feature highlighted

with orange ellipse). The fact that such seeded growth of the $MoTe_2$ nanostructures was not observed in the syntheses when the chalcogen precursor was injected into a solution containing the transition metal complex, suggests that nucleation of the $MoTe_2$ nanostructures and tellurium by-products are temporally separated. Moreover, formation of the crystalline tellurium by-products themselves can be indicative of a slow reaction rate between the molybdenum and tellurium species leading to accumulation of a considerable amount of the excessive, unconsumed in the prime reaction, tellurium and as a result to the homogeneous nucleation of tellurium phase.

We further assumed that a dropwise injection of a thermally unstable tellurium precursor can potentially impede the formation of tellurium side-products since in this case the chalcogen precursor, added into the system in small portions, is likely to be fully consumed in the reaction with the excess of molybdenum precursor before the crystallisation of free tellurium in a form of highly-anisotropic needles becomes possible. In contrast to our expectations, dropwise injection of the chalcogen precursor did not yield any measurable nucleation of the $MoTe_2$ product; instead, only quasi-spherical tellurium nanoparticles were found in the final product (Figure 3.9.c). The change in morphology of the tellurium structures becomes evident from the corresponding diffraction patterns. When the chalcogen precursor is added into the reaction medium in a dropwise manner, the growth of the tellurium by-products is limited by the diffusion of the reactive species to the surface of growing tellurium crystals (thermodynamically-controlled growth regime) and so the material acquires the equilibrium shape, which is nearly spherical. The experimental diffraction pattern closely matches that of the bulk tellurium with the strongest reflection at 27.9 $^{o}2\theta$ corresponding to the (101) planes (presented in Figure 3.9.c above the experimental XRD pattern) similarly to the Te spheres via the laser ablation approach [312]. On the other hand, the anisotropic Te needles, obtained at higher concentrations of the tellurium precursor, display the strongest XRD peak at 40.3 $^{o}2\theta$ of the (110) planes of the hexagonal tellurium (Figure 3.7.a,b; Figure 3.8.a; Figure 3.9.a,b) in agreement with the earlier reports [313].

To summarise, growth of the phase-pure $MoTe_2$ nanostructures is significantly hindered by the instability of the available tellurium precursors prone to a prompt dissociation at high temperatures and by the slow reaction rate between the molecular molybdenum and tellurium species, eventually leading to the nucleation of considerable amounts of highly crystalline tellurium side-products. Using more reactive forms of molybdenum, like $MoCl_5$ instead of $Mo(CO)_6$, and replacing the excess of coordinating solvent with non-coordinating one, such as

octadecene (in other words, dissolving the starting inorganic complexes of molybdenum in a minimum amount of coordinating oleic acid or oleylamine), seemingly helps to lower down the energy barrier of the direct reaction between the molecular precursors, and leads to formation of the $MoTe_2$ nanostructures.

3.2. Colloidal Bi_2Te_3 branched nanosheets

Colloidal Bi_2Te_3 branched nanosheets were synthesised in a non-coordinating organic solvent from *in situ* generated stoichiometric bismuth oleate and trioctylphosphine telluride complex. For this reaction, oleic acid was chosen as a capping ligand, mediating the growth of the Bi_2Te_3 nanoparticles, while the reaction was carried out in a non-coordinating solvent. Oleic acid readily reacts with bismuth salts facilitating the solubilisation of bismuth precursor, and at the same time, in contrast to commonly used oleylamine, it does not reduce bismuth ions to elemental bismuth thus preventing the formation of undesired bismuth nanoparticles. As opposed to the colloidal synthesis of the $MoSe_2$ and $MoTe_2$ nanostructures discussed in Section 3.1, where oleic acid played the role of a coordinating solvent, we found it absolutely necessary to avoid the presence of free oleic acid in the reaction medium during the Bi_2Te_3 growth. This crucial change allowed us to attain the Bi_2Te_3 two-dimensional nanosheets in a wide temperature range from 20 ºC to 170 ºC in a stark contrast to the majority of growth protocols relying on the use of bismuth salts dissolved in oleic acid [[314,315]]. We provide further evidence to this claim by varying the molar ratio between oleic acid and bismuth acetate to demonstrate the change in morphology of the growing Bi_2Te_3 nanostructures. The experimental set-up and the detailed procedures are described in Section 2.2.4. The full list of performed syntheses and the corresponding conditions are provided in Appendix A3.

3.2.1. Growth-temperature-dependent morphology of colloidal Bi_2Te_3 nanosheets

Colloidal Bi_2Te_3 nanostructures were obtained through a synthesis approach introduced in Section 2.2.4. Here, we investigate the effect of growth temperature alone on the morphology of the produced Bi_2Te_3 nanosheets; other growth parameters, such as type and concentration of the molecular precursors, solvent, and the amount of free oleic acid in the reaction mixture were kept constant. Presented in Figure 3.10.a-c are the representative TEM images of the Bi_2Te_3 nanosheets grown at 20, 70, and 170 ºC, respectively. The material formed at room temperature (20 ºC) demonstrates a branched flower-like morphology with the curled two-dimensional nanosheets emanating from the central core. The approximate lateral dimensions of the individual Bi_2Te_3 petals reach 200 nm. At higher growth temperatures, the shape of the produced Bi_2Te_3 nanostructures becomes more defined, approaching nearly perfect regular hexagons at 170 ºC. Interestingly, two types of Bi_2Te_3 nanostructures are found in the samples grown at high temperature (170 ºC): hexagonal platelets, lateral size of which significantly exceeds their thickness, and branched platelets (inset in Figure 3.10.c) composed of multiple

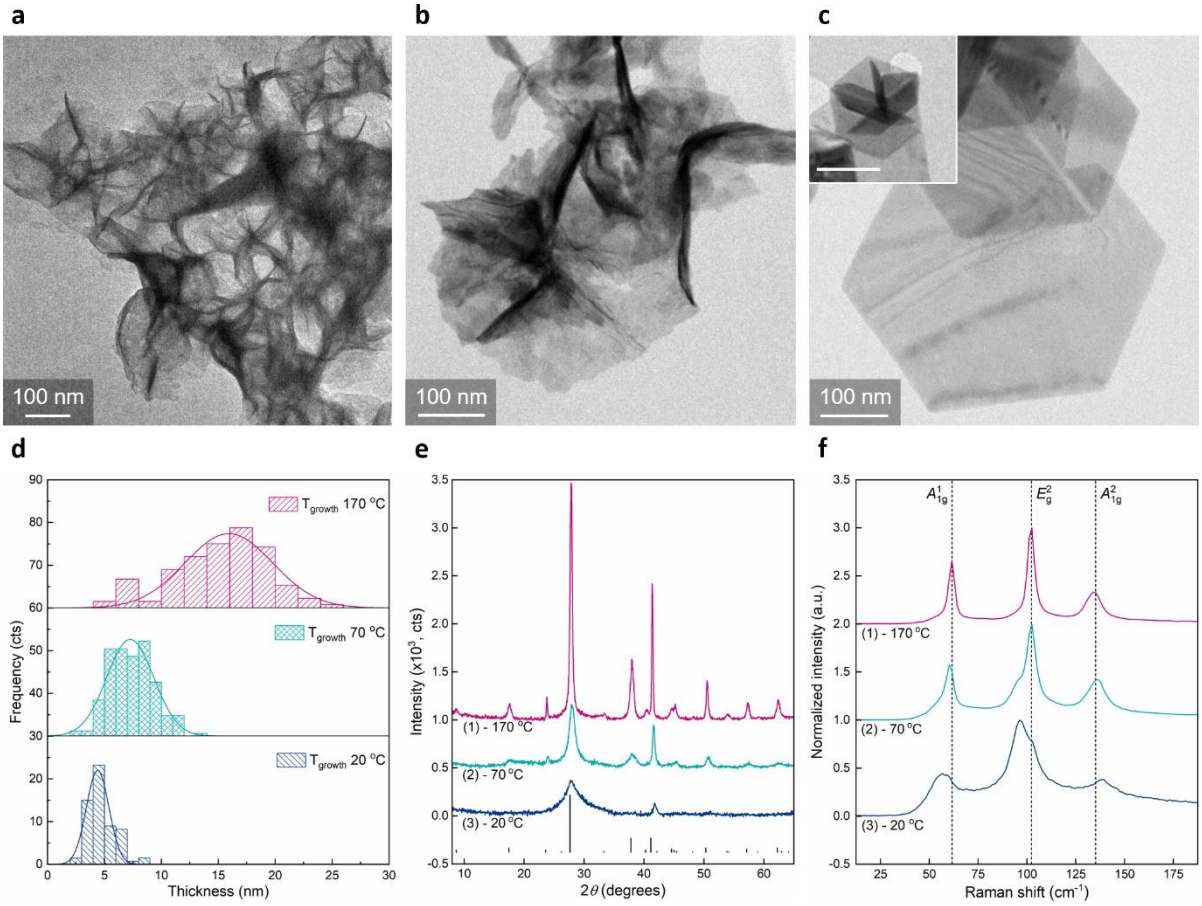


Figure 3.10. Morphology of the colloidal Bi_2Te_3 nanosheets. **a, b, c** Representative low-magnification TEM images of the Bi_2Te_3 nanosheets grown at 20 ºC, 70 ºC, and 170 ºC, respectively. Inset in panel **c** shows a branched nanocrystal composed of four individual hexagonal plates (scale bar 200 nm). **d, e, f** Thickness histograms, X-ray diffraction patterns and Raman spectra of the Bi_2Te_3 branched nanosheets, respectively. The diffractograms and Raman spectra are offset for clarity. In panel **e**, standard diffraction peaks of the rhombohedral Bi_2Te_3 (ICDD 15-863) are provided as a reference. In panel **f**, vertical dashed lines denote positions of the Raman active mode of bulk Bi_2Te_3 taken from reference [304].

nearly identical single-crystalline hexagonal platelets. The overall hexagonal shape of the synthesised nanostructures is governed by the three-fold symmetry of the *ab* plane of Bi_2Te_3 crystal lattice, while an anisotropic disk(plate)-like morphology is also expected considering the layered crystal structure of bulk Bi_2Te_3 when the lateral extension of the growing nanocrystals perpendicularly to the *c*-axis is energetically preferred compared to the vertical growth along the *c*-axis [193,316]. The complex shape of branched platelets, consisting of up to four intersecting hexagonal platelets, closely resembles that of the CuS (covellite) and $LiCoO_2$ concaved cuboctahedrons [317,318]. The formation of such complex morphologies was attributed to selective pitting of the high energy facets of crystal nuclei during the early stages of solution-phase growth that enables to expose the more stable facets and thus to minimise the nanocrystal

surface energy. The lateral dimensions of Bi_2Te_3 platelets increase to over 600 nm at the growth temperature of 170 ºC.

The thickness of the produced Bi_2Te_3 nanosheets was also found to progressively increase with the synthesis temperature. The side-view TEM images of approximately 150 nanosheets grown at each specified temperature were analysed and the corresponding histograms are shown in Figure 3.10.d. The average thickness of the branched nanosheets grown at 20 ºC does not exceed 4±1 nm that accounts for approximately four Bi_2Te_3 quintuple layers. With the growth temperature raised to 70 ºC, the thickness of Bi_2Te_3 nanosheets increases to 7±2 nm and reaches 16±4 nm at growth temperature of 170 ºC. Since the thickness of nanosheets was determined solely from the statistical analysis of the side-view TEM images, the measured values can exceed the actual ones due to the slight variation in inclination angles of the vertically oriented platelets so that their edges are not perfectly perpendicular to the incident beam. This effect is expected to be more pronounced for the rigid thick platelets grown at 170 ºC than for the flexible thin nanosheets obtained at room temperature, causing the size distribution to appear significantly broadened.

The XRD data shown in Figure 3.10.e confirm that the produced bismuth telluride nanosheets possess the rhombohedral crystal structure of Bi_2Te_3 belonging to the $R\,\bar{3}m$ space group (standard diffraction pattern of bulk rhombohedral Bi_2Te_3 is included for reference). The degree of crystallinity, however, strongly depends on the growth temperature. Two broad diffraction peaks, observed at 27.9 and 41.6º 2θ in the experimental diffractogram of the nanosheets grown at room temperature, can be assigned to the (015) and (110) planes of Bi_2Te_3. The significant broadening of these reflections can imply the polycrystalline nature of the material obtained at this low temperature. As the synthesis temperature increases, numerous reflections appear in the corresponding diffraction patterns, suggesting the improved crystallinity of the material, while the increased size of crystalline domains is evidenced by the higher intensities and narrower widths of the diffraction peaks. These findings agree well with the TEM observations discussed earlier. It is worth mentioning that the synthesised branched nanosheets exhibit lattice compression in the *ab* plane as is evidenced by the shift of the diffraction peaks towards higher diffraction angles with respect to the reference positions. For the Bi_2Te_3 platelets attained at 170 ºC, the (110) and (015) interplanar distances do not deviate considerably from the bulk values and are found to be 2.18 and 3.2 Å, respectively, which is only 0.5% smaller than the corresponding spacings in bulk material. This shift becomes more evident in the case of nanosheets grown at lower temperatures, and the (110) and (015)

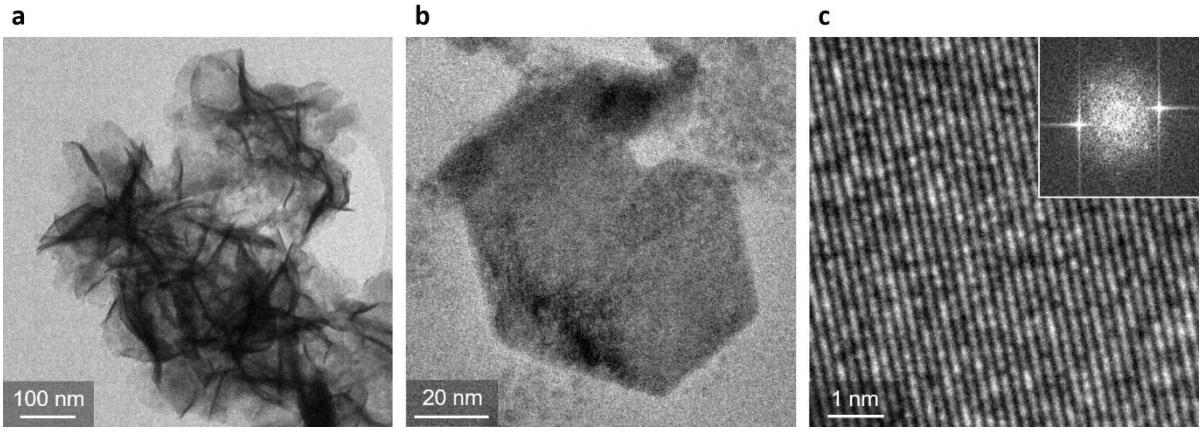


Figure 3.11. Recrystallisation of the Bi_2Te_3 branched nanosheets observed upon annealing in solution phase. **a, b** TEM images of the Bi_2Te_3 nanosheets grown at room temperature before and after the post-growth annealing at 100 ºC. **c** High-resolution TEM image and the corresponding FFT (inset) demonstrating the improved crystallinity of the annealed Bi_2Te_3 nanosheets.

interplanar distances appear to be decreased by up to 2% – 2.17 and 3.19 Å for the nanosheets obtained at 70 ºC and 2.15 and 3.17 Å for the material grown at room temperature, respectively. The observed lattice compression can be attributed to the presence of Te vacancies and substitutional Bi_{Te} defects, where Bi atoms occupy the Te lattice nods, in the grown material.

Interestingly, the crystallinity of the material grown at room temperature can be improved via the post-growth annealing in solution phase. Compared in Figure 3.11.a,b are TEM images of the Bi_2Te_3 nanosheets before and after thermal annealing. The annealing was performed at 100 ºC in octadecene as a non-coordinating solvent and in the presence of a small amount of TOP as a capping ligand required to prevent aggregation of the nanosheets. Upon annealing, the material undergoes recrystallisation with the polycrystalline branched nanosheets being replaced by single crystalline platelets with hexagonal shape. High resolution TEM imaging (Figure 3.11.c) reveals the lattice fringes with uniform spacing of 2 Å close to that of the {110} planes of bulk Bi_2Te_3 (2.19 Å, ICDD 15-863).

Raman spectroscopy was employed to investigate the thickness-dependent behaviour of the lattice vibrations of the produced material. Typical Raman spectra of the nanosheets grown at 20, 70, and 170 ºC are reported in Figure 3.10.f. According to the group theory, four intrinsic Raman active modes are expected for bulk to few-layered Bi_2Te_3: two in-plane E_g and two out-of-plane A_{1g} vibrations. Three vibrational modes observed at 61.4, 102.1, and 134.2 cm^{-1} in the spectrum of the platelets grown at 170 ºC can be assigned to the A_{1g}^1, E_g^2, and A_{1g}^2 modes of Bi_2Te_3; moreover, the observed frequencies are close to those reported for the bulk material [304,319]. The E_g^1 peak becomes distinct when the material is thinned down to two quintuple

layers and is claimed to be very weak in thicker flakes [319], therefore is not expected in the Raman spectrum of the synthesised Bi_2Te_3 hexagons with the average thickness of 16 nm (14-16 quintuple layers). In contrast to the in-plane E_g^2 mode, out-of-plane A_{1g}^1 and A_{1g}^2 lattice vibrations demonstrate a clear thickness-dependent behaviour (peak frequency shift and broadening) with the thickness of the synthesised material progressively decreasing at lower growth temperatures (Figure 3.10.f). Specifically, in thinner Bi_2Te_3 nanosheets obtained at room temperature, the out-of-plane modes are centred at 56.6 and 138.7 cm^{-1}. These values correlate well with the reported frequencies of the three quintuple layer thick Bi_2Te_3 [319] that agrees with the average thickness estimated from the TEM data (4 nm).

Although the in-plane E_g^2 mode is less sensitive to the number of layers and thus cannot be used for the direct determination of the material thickness, it seems to provide an important insight into the material non-stoichiometry. In the ~7 nm thick Bi_2Te_3 nanosheets grown at 70 ºC, the E_g^2 mode is centred at 102.2 cm^{-1} and is not substantially shifted compared to the ~16 nm thick Bi_2Te_3 platelets (170 ºC). However, a shoulder peak appearing at the lower frequency side of the E_g^2 peak can be indicative of the inclusion of excessive bismuth atoms between Bi_2Te_3 quintuple layers. Bismuth telluride exists in numerous phases that can be generally described as a combination of Bi_2 bilayer and Bi_2Te_3 quintuple layer blocks stacked along their *c*-axes forming $(Bi_2)_m(Bi_2Te_3)_n$ structures, where *m* and *n* are integers (see Section 1.1). To date, Raman studies of the members of Bi-Te binary system, other than Bi_2Te_3, remain limited [320]. It has been shown that Bi-rich phases produced via pulsed laser deposition (PLD) technique display gradual decrease in the intensity of the Bi_2Te_3 characteristic modes with the increase in Bi content; additionally, new features appear in the Raman spectra [320]. The new modes (unassigned in [320]) are red-shifted relative to the E_g^2 mode of the stoichiometric Bi_2Te_3. Specifically, a new peak at ~88 cm^{-1} is found in the Raman spectrum of the tsumoite BiTe (50% Bi), this mode is further red-shifted to ~83 cm^{-1} with the Bi content increasing to 57% in the pilsenite Bi_4Te_3. It should be noted that in the cited work [320], all reported peak positions experience a systematic red-shift ($\Delta\omega$ ~5 cm^{-1}), therefore the new features of Bi-rich phases are to be expected at ~93 and ~88 cm^{-1} in tsumoite and pilsenite, respectively. Indeed, Raman study of the MBE grown 50 nm thick Bi_4Te_3 films has confirmed the presence of two extra features at 87.7 and 114.9 cm^{-1} in addition to four vibrational modes of the pristine Bi_2Te_3 [321]. These new peaks were assigned to the E_g and A_{1g} modes of the single Bi_2 bilayer covalently bonded to the Bi_2Te_3 slabs. The shoulder peak observed in the experimental Raman spectra of the branched nanosheets obtained at 70 and 20 ºC is centred at ~95 cm^{-1}. This suggests that the

material produced in this temperature range is in fact a mixture of the pristine Bi_2Te_3 phase and a Bi-excessive phase yet, considering the frequency of the shoulder peak, this Bi-rich phase does not contain more than 50% of bismuth. The formation of polycrystalline material abundant in structural defects that result into formation of the non-stoichiometric phases is likely to occur at the higher supersaturation of the monomer solution, i.e. low synthesis temperature; this is evidenced by the increased intensity of the shoulder peak that becomes dominant in the Raman spectrum of the branched nanosheets grown at 20 °C, thus denoting the higher content of the Bi-rich phase compared to the stoichiometric Bi_2Te_3.

High-resolution TEM imaging of the lateral facets of the Bi_2Te_3 nanosheets presented in Figure 3.12.a-c further corroborates the assertion that the excess of Bi atoms is more likely to be trapped between the quintuple Bi_2Te_3 slabs at lower growth temperatures. Although not being atomically-resolved, the side-view TEM images of the edge-on oriented Bi_2Te_3 nanosheets provide information on periodicity of the layered structure of the produced material. The nanosheets grown at 170 °C display a uniform periodicity of 9.9 Å along the *c*-axis closely matching the (003) planes of the stoichiometric Bi_2Te_3 (10.16 Å). In the nanosheets obtained at lower temperatures (20 and 70 °C), the periodicity along the [001] direction is increased to 10.8-11.5 Å that can be attributed to the lattice expansion due to the intercalation of excessive Bi during the crystal growth, corroborating the non-stoichiometry of the synthesised material inferred from the Raman spectroscopy data. In order to obtain a direct proof of the growth-temperature-dependent composition variation, we also performed a semi-quantitative (standardless) elemental analysis (Figure 3.12.d). The results, however, indicate a measurable Bi over-stoichiometry in the material synthesised at high (170 °C) as well as at lower (70 °C) temperature.[7] The atomic [Bi]:[Te] ratio was determined from the intensities of the corresponding L$\alpha_{1,2}$ lines, and the average stoichiometry was the following: 2.25:3 and 2.35:3 for the nanosheets grown at 70 and 170 °C, respectively. Being a local probe, the results of energy-dispersive spectroscopy can be affected by various factors, including geometry of the sample and possible degradation of the material under the beam during the signal acquisition. In its turn, nanostructured Bi_2Te_3 is known to have low thermal conductivity [322], what is commonly considered as the main factor causing its instability under the focused probes as the induced heat does not dissipate effectively and causes local lattice melting. For instance, local

[7] In the case of Bi_2Te_3 samples grown at 20 °C, EDS analysis was not performed due to unavailability of a sufficiently purified final product. Strong contamination with the unreacted bismuth precursor, appearing as micron-sized bismuth acetate crystals, was repeatedly observed in the corresponding SEM images of the Bi_2Te_3 nanosheets obtained in the low temperature growths.

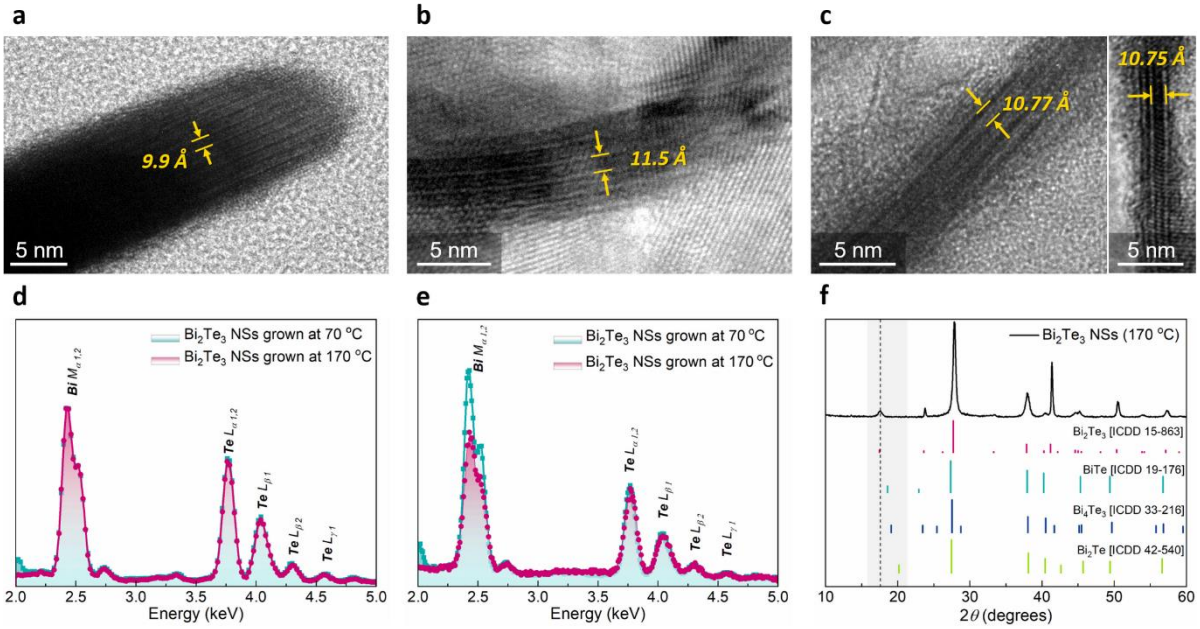


Figure 3.12. Stoichiometry of the bismuth telluride branched nanosheets. **a, b, c** side-view TEM images of the Bi_2Te_3 branched nanosheets produced at 170, 70, and 20 °C, respectively. **d** TEM EDS spectra taken from the individual branched nanosheets grown at 70 and 170 °C. **e** SEM EDS spectra taken from the representative spots in the ensembles of branched nanosheets grown at 70 and 170 °C. **f** Comparison of the experimental diffractogram of the Bi_2Te_3 nanosheets (170 °C) with the reference patterns of various Bi-rich phases.

melting and loss of structural integrity was observed in the exfoliated single- and few-layered Bi_2Te_3 flakes under laser excitation [46]. The increased number of structural defects, such as grain boundaries, is expected to increase scattering of the acoustic phonons and so to further decrease the thermal conductivity of the material. Indeed, we have repeatedly observed the decomposition of thin polycrystalline nanosheets obtained at low growth temperatures (20-35 °C) under the laser irradiation (532 nm, 1.4-2.5 mW) with the two strong bands of tellurium metalloid (similar to those discussed in Section 3.1.1) appearing at 122 and 140 cm^{-1} in the Raman spectra. Such laser-induced decomposition was not observed in thicker single-crystalline Bi_2Te_3 platelets grown at 170 °C. Moreover, the sublimation of two-dimensional Bi_2Te_3 nanocrystals was directly visualised upon heating the material in the TEM column [323]. In this case, the authors also state that even before the loss of structural integrity becomes apparent, the sublimation of tellurium precedes the detachment of bismuth atoms that eventually leads to the removal of entire sections of the nanocrystals. The electron beam damage to the sample is expected to be reduced at lower accelerating voltages (lower kinetic energy of the incident electrons) and, indeed, the elemental analysis performed in the SEM mode at 20 kV accelerating voltage (Figure 3.12.e) indicates higher bismuth content in the samples obtained at lower growth temperatures.

To summarise this, the stoichiometry of the synthesised material appears to be close to 2:3, although a slight excess of bismuth is detected even in the case of high temperature growth. This intrinsic bismuth over-stoichiometry is likely to arise due to the presence of Te vacancies and antisite defects, specifically, bismuth atoms in the tellurium positions (Bi_{Te}), in the synthesised material. Since the formation energy of the antisite defects is rather low (~0.4 eV [324,325]), they can be anticipated to be the dominant structural defects for the high temperature growths. The presence of Bi atom inclusion between the Bi_2Te_3 slabs in the case of platelets grown at 170 °C was ruled out based on the results of the TEM analysis (discussed earlier) and X-ray diffraction. Shown in Figure 3.12.f is the experimental diffractogram of the Bi_2Te_3 platelets, demonstrating a perfect match with the reference pattern of bulk Bi_2Te_3 accounting for all diffraction peaks observed in the experiment. Notably, the position of the (006) diffraction peak, which depends on the periodicity in the *c*-axis direction, matches that of Bi_2Te_3 and deviates strongly from the reported positions for various Bi-rich phases (area highlighted with a grey shaded box in Figure 3.12.f). This allows us to conclude that the material produced at high temperature (170 °C) is a phase-pure Bi_2Te_3, however rich with antisite defects causing slight Bi over-stoichiometry. On the contrary, the non-stoichiometric polycrystalline branched nanosheets obtained at low growth temperatures (20-70 °C) are more likely to result from the inclusion of the excessive bismuth atoms and Bi_2 bilayer slabs between the layers of pristine Bi_2Te_3 as is evidenced by Raman spectroscopy data and corroborated by TEM.

Our nanostructured Bi_2Te_3 nanosheets are prone to degradation occurring on a time scale of a few weeks if exposed to moist air. This is in agreement with observations that bulk Bi_2Te_3 crystals are affected by surface oxidation if exposed to moist air, while the effect disappear if exposed to dry air, suggesting a key role played by water molecules [262]. The SEM images of the Bi_2Te_3 platelets taken with a time interval of two weeks (Figure 3.13.a) illustrate how initially sharp platelets' edges, normally observed in the freshly prepared samples, become "fused" after a two-week exposure to moist air. TEM imaging also confirms the formation of a layer of amorphous surface oxide (Figure 3.13.b).

Further, the XRD experiments show that the nanosheets lose their crystallinity and become partially amorphous due to oxidation. In Figure 3.13.c we compare degradation rates of the Bi_2Te_3 samples in air and in a non-polar organic solvent. For this experiment, an aliquot of the Bi_2Te_3 nanosheets (~25 μmol) was divided into halves; one half was drop-cast onto a glass substrate and the prepared film was examined (this is a reference diffractogram of a fresh

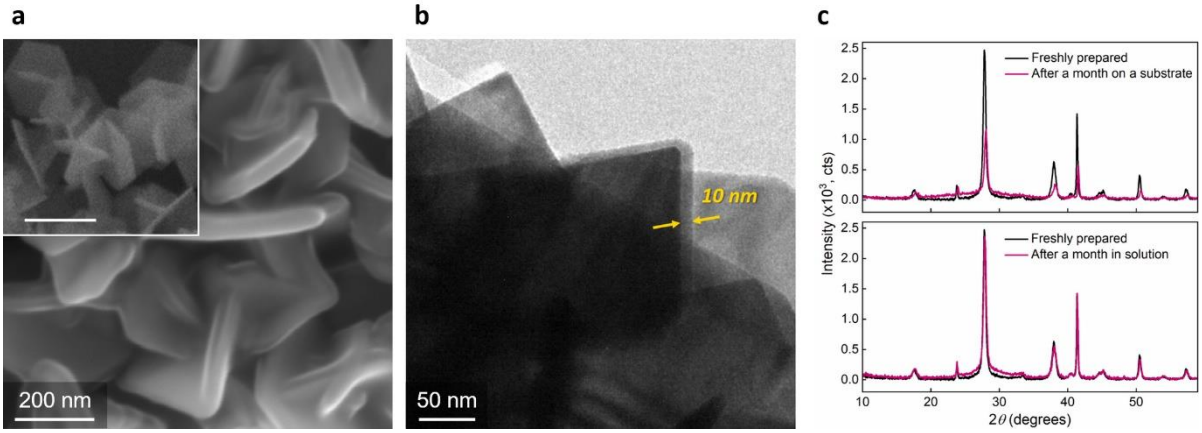


Figure 3.13. Surface oxidation of the Bi_2Te_3 nanosheets. **a** SEM images of the freshly prepared (inset, scale bar 300 nm) and two weeks old samples of the Bi_2Te_3 branched nanosheets. **b** TEM image of a Bi_2Te_3 branched nanosheets revealing a thin (~10 nm) layer of the surface oxide. **c** XRD patterns of the Bi_2Te_3 samples, either dried to powders (top panel) or stored as a suspension in ethanol (bottom panel), after a month long exposure to the moist air.

sample), then left for a month under ambient conditions. The second half was stored as a suspension in hexane in a sealed vial in a drying desiccator. After one month, diffractograms of the samples were compared to the initial one. The diffractogram of a film of the Bi_2Te_3 nanosheets assembled on a glass slide (Figure 3.13.c, top panel) demonstrates a substantial decrease in the diffraction peak intensities after one month of exposure to the atmospheric air. The changes in the diffraction pattern of the material suspended in a non-polar solvent were found to be negligible manifesting low degradation rate (Figure 3.13.c, bottom panel). Our observations are in a good agreement with the reported study of the surface oxidation of bulk Bi_2Te_3 crystals [262], claiming that the surface oxidation only occurs after simultaneous adsorption of oxygen and water molecules. Therefore, the structural quality of the synthesised Bi_2Te_3 nanosheets can be preserved if the material is stored in non-polar organic solvents in absence of moisture.

3.2.2. Lateral termination and insights into the growth mechanism

In addition to control over morphology, the growth temperature appears to affect the lateral termination of the synthesised Bi_2Te_3 nanosheets. In all cases, the basal planes of the two-dimensional Bi_2Te_3 nanosheets were found to be {001} facets as can be expected for the layered van der Waals systems [326], where the planes perpendicular to the unique *c*-axis do not have dangling bonds and therefore possess the lowest surface energy [15]. In stark contrast to the majority of the existent reports on the CVD [148] or solvothermal [164,327] synthesis of the two-dimensional Bi_2Te_3 nanostructures and Bi_2Te_3-based heterostructures exhibiting the

morphology of trigonal or hexagonal prisms with the lateral facets enveloped by either the {010} or the {110} planes, we found out that the lateral termination of the colloidal Bi_2Te_3 nanosheets could be effectively altered from the high-index {015} to the low-index {110} by changing the growth temperature from 20-70 ºC to 170 ºC.

The surface morphology of the colloidal Bi_2Te_3 nanosheets was studied using high-resolution TEM (Figure 3.14). The material obtained at low growth temperatures (20 and 70 ºC) exhibits a distinct flower-like morphology as shown in panels a and d in Figure 3.14. The selected area electron diffraction (SAED) pattern in panel b confirms the polycrystalline nature of the colloidal Bi_2Te_3 grown at room temperature as revealed by the numerous crystallite orientations forming continuous diffraction rings. The most prominent among them corresponds to the (015) planes of Bi_2Te_3 in agreement with the results of XRD analysis discussed earlier. Further, high resolution TEM imaging (Figure 3.14, panel c) indicates that individual petals of Bi_2Te_3 nanoflowers consist of single crystalline patches of over 100 nm^2 in size. The interplanar distance estimated from the HRTEM image is 3.16 Å and the corresponding FFT pattern (inset in Figure 3.14.c) can be indexed in the $[5\bar{5}1]$ zone axis. Therefore, the atomic columns resolved in the HRTEM images appear to correspond to the (015) and $(\bar{1}05)$ crystal planes, although the interplanar distance was found to be smaller than in bulk Bi_2Te_3. The lattice compression that possibly arises due to the presence of structural defects, such as Te vacancies, in the ultra-thin Bi_2Te_3 nanosheets was also inferred from the XRD data (the (015) spacing was found to be 3.17 Å) and can explain the observed discrepancy. It is worth noting that the $\{015\}$ termination is seldom observed in the two-dimensional Bi_2Te_3 nanostructures and to date was only reported for the Bi_2Te_3 nanoribbons [328]. With the growth temperature increased to 70 ºC, the crystallinity of the Bi_2Te_3 branched nanosheets improves as clearly evidenced by fewer diffraction spots observed in the SAED pattern (Figure 3.14.e). However, the material displays the same {015} lateral termination with the interplanar spacing of 3.2 Å (Figure 3.14.f).

Obtained at high growth temperature, Bi_2Te_3 predominantly adopts the morphology of hexagonal platelets (Figure 3.14.g), however a minor fraction of branched platelets, which will be discussed later, is also consistently found in the samples. Sharp diffraction spots with higher order reflections observed in the SAED patterns of the Bi_2Te_3 hexagons (Figure 3.14.h) are indicative of their single crystalline nature. The experimental SAED pattern indexed in the [001] zone axis displays the three-fold symmetry of the *ab* plane enclosed by the $\{110\}$ lateral facets. The faint dots observed in the SAED pattern (highlighted with dashed circles) can be

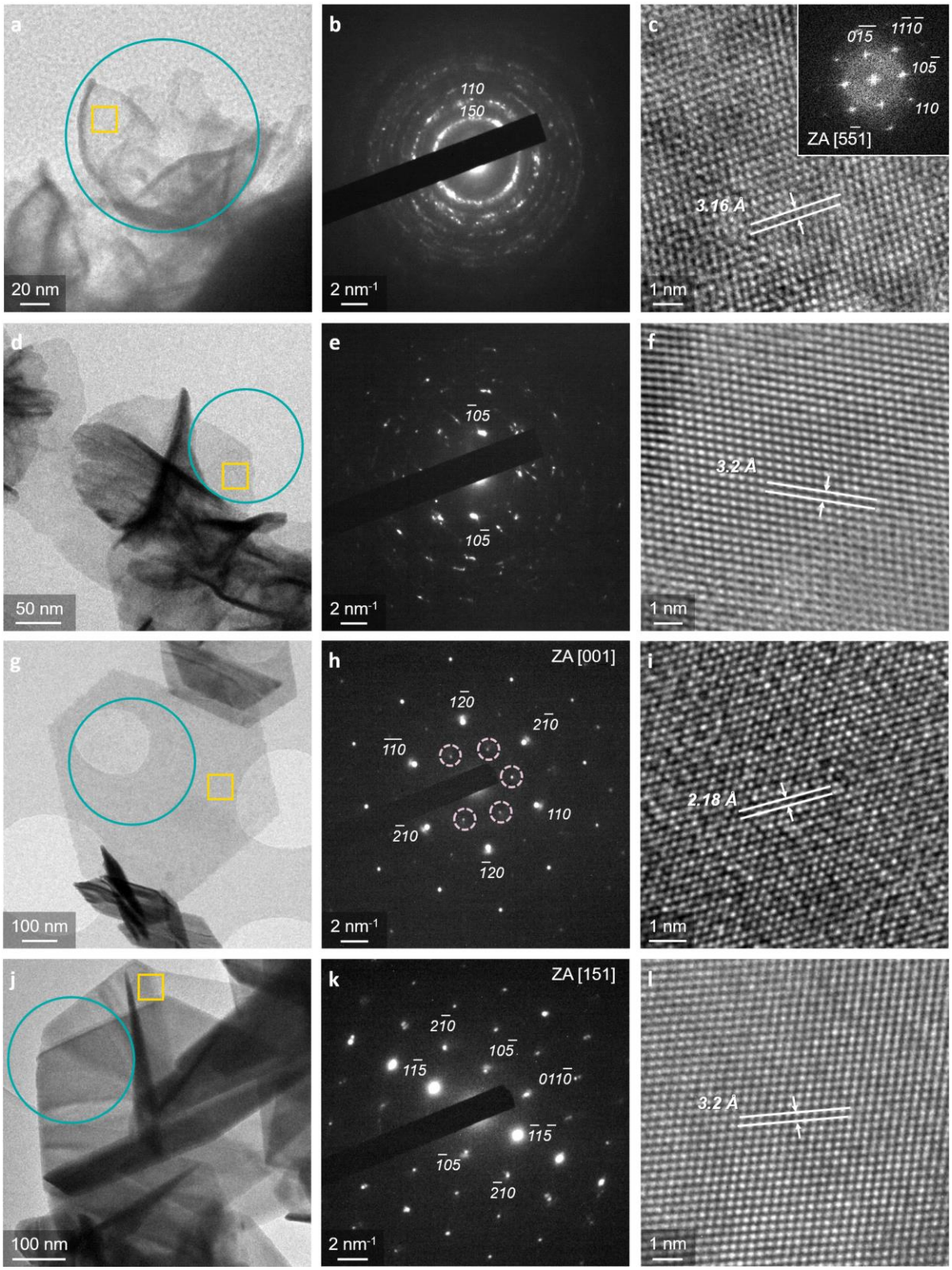


Figure 3.14. Surface morphology of the Bi_2Te_3 nanosheets. **a, d, g, j** representative TEM images, **b, e, h, k** SAED patterns, and **c, f, I, l** high-resolution TEM images of the Bi_2Te_3 nanosheets grown at 20 ºC (**a-c**), 70 ºC (**d-f**) and 170 ºC (**g-l**). SAED patterns are recorded from the areas highlighted with teal circles, while the high-resolution TEM images are taken from the regions marked with yellow squares in **a, d, g, j**. Inset in panel **c** shows the corresponding FFT pattern.

assigned to the kinematically-forbidden {100} reflections possibly arising due to the antisite defects present in the nanostructured material [329]. This observation is consistent with the results of the elemental analysis, revealing a slight excess of bismuth in the as produced Bi_2Te_3 hexagonal plates attributed to the Bi_{Te} antisite defects. High-resolution image of the basal plane of a single crystalline Bi_2Te_3 hexagon (Figure 3.14.i) shows the hexagonal arrangement of atomic columns with the uniform interplanar spacing of 2.18 Å matching well the (110) planes of Bi_2Te_3.

The shape of the branched platelets (Figure 3.14.j, Figure 3.10.c inset), consisting of multiple intersecting single crystalline hexagonal plates, resemble that of the branched nanosheets obtained at lower growth temperature (Figure 3.14.d, Figure 3.10.b), however the platelet edges appear sharper compared to the ragged outline of the Bi_2Te_3 nanoflowers grown at 70 ºC. The SAED pattern shown in Figure 3.14.k is taken from a single crystalline area of an individual platelet comprising the branched platelet and can be indexed in the [151] direction, demonstrating the same {015} lateral termination observed in the two-dimensional petals of the Bi_2Te_3 branched nanosheets grown at 20-70 ºC. Further, the HR TEM image of an individual platelet (Figure 3.14.l) displays the lattice fringes with the uniform interplanar distance of 3.2 Å matching that of the (015) planes.

The driving force, defining the shape and faceting that a nanocrystal acquires during the growth process, is the supersaturation at a given temperature [205]. When the supersaturation in the system is low, the crystal growth is governed by the monomer diffusion to each of the growing facets. The monomer diffusion rate is typically much slower than the rates of the adsorption/desorption and migration of monomer species, occurring at a growing crystal facet. As a consequence, the nanocrystals grown under lower supersaturation (also referred to as a thermodynamically-controlled growth) generally acquire the shapes close to the equilibrium ones. On the other hand, when the supersaturation in the system is high, there is always an excess of the monomer species in vicinity of the growing crystal facet and so the facet growth rate is mostly defined by its excessive surface energy. This type of crystal growth, known as a kinetically-controlled regime, commonly leads to the formation of highly anisotropic nanoparticles since in this case the shape of a growing crystal strongly depends on the difference in the facet growth rates [197,330]. A clear transition from the kinetically-controlled to the thermodynamically-controlled growth mode, occurring when the concentration of the monomer in the system is reduced, can be illustrated by the shape transformation of the tellurium by-products produced in the synthesis of $MoTe_2$ nanostructures (Section 3.1.3). At

high monomer concentration (swift injection), the crystals adopted highly anisotropic needle-like shape, while at low monomer concentration (dropwise injection), the crystal shape changed into the equilibrium quasi-spherical. A similar reasoning can be applied to explain the difference in the morphology of Bi_2Te_3 nanostructures obtained at low (20 °C) and high (170 °C) growth temperatures. Since the growth conditions, including the monomer concentrations, were kept the same in this series of experiments, the supersaturation is expected to be lower at higher reaction temperatures due to the temperature dependent solubility of the monomer; therefore at high reaction temperature (170 °C, low supersaturation) growth of the Bi_2Te_3 nanostructures is mediated by the monomer diffusion and the crystals acquire regular equilibrium shapes. At low growth temperature (20 °C, high supersaturation), the crystal growth is likely to be governed by the difference in the surface energies of its facets, yielding highly anisotropic shapes. However, crystal growth, occurring predominantly in either the kinetically- or the thermodynamically-controlled regime, cannot provide an explicit explanation for the formation of the branched structures.

The dominance of the kinetic reaction control over thermodynamic reaction control can, however, explain the difference in lateral termination of the synthesised Bi_2Te_3 nanosheets. Under the non-equilibrium conditions, the crystal growth is assumed to preferentially occur at the most unstable facets (higher excessive surface energy) since this provides a favourable pathway to the final product, however, does not necessarily lead to the formation of the most stable product [331]. The first-principles calculations have demonstrated that the surface energies of various pristine facets of the group VB chalcogenides follow the order $\gamma(001) < \gamma(015) < \gamma(110) < \gamma(010) << \gamma(01\bar{4})_{Bi/Te} < \gamma(02\bar{5})_{Bi/Te}$ [165,332]. Moreover, compared to other pnictogen chalcogenides, such as Sb_2Te_3 and Bi_2Se_3, the energy difference between the (015) and (110) planes in bulk Bi_2Te_3 is rather small [165]. Grown at high temperature (170 °C), when the reaction system is much closer to the equilibrium compared to the low temperature growths, Bi_2Te_3 predominantly exhibits the morphology of hexagonal platelets enveloped by the {001} and perpendicular to them {110} planes, forming the basal and lateral surfaces, respectively, ensuring the lowest surface energy of the produced Bi_2Te_3 nanostructures. On the other hand, in the low-temperature syntheses (20-70 °C), when the crystal growth is driven by the balance between the reactions occurring at different facets and their respective kinetics, reactions at the high-index polar facets, i.e. the $(01\bar{4})$ planes, exhibiting a higher number of dangling bonds (0.12 per atom on the surface) are likely to be more favourable than deposition of either bismuth or tellurium species onto less active (015) or (110) lateral facets (0.08 and 0.1 dangling bonds

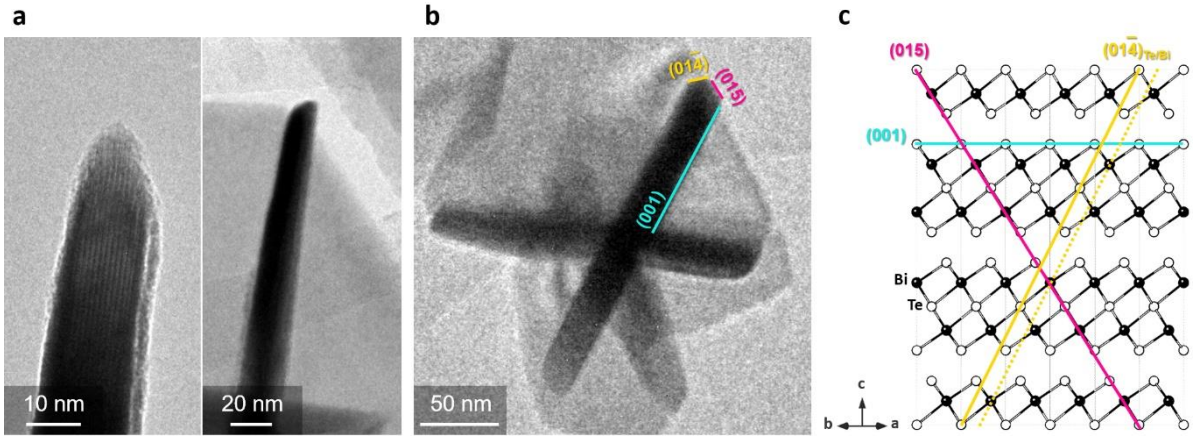


Figure 3.15. Lateral sides of the Bi_2Te_3 branched nanoplatelets. **a, b** side-view TEM images of the Bi_2Te_3 branched nanoplates demonstrating the inclination angle between the basal and lateral sides of the individual plates. **c** Schematic representation of the (001) basal and non-polar (015) and polar $(\mathbf{01\bar{4}})_{Bi/Te}$ lateral surfaces.

per atom of the surface, respectively) and even less so onto the practically inert {001} basal planes.[8] Fast monomer deposition at the high energy crystal facets and so their fast propagation from the centre of the growing crystal leads to a considerable areal extension of the more stable {001} and {015} planes and in the end to the observed {015} lateral termination of the branched nanosheets; however, the exact growth mechanism requires a more dedicated study. This hypothesis is supported by the side-view TEM images (Figure 3.15.a), revealing the lateral and basal sides of the Bi_2Te_3 branched nanosheets and branched nanoplatelets being not orthogonal. The formation of truncated nanoarchitectures have been reported in the CVD growth of Bi_2Te_3 and Bi_2Se_3 planar and vertical nanoplates enclosed by the {001}, {015}, and $\{01\bar{4}\}$ facets [333]. The direct assessment of the angles between the lateral surfaces and between them and the basal plane from the side-view TEM images is not reliable due to the variation in orientation of the individual hexagons. In addition to that, the amorphous layer of the surface oxide (when present) blurs sharp edges of the Bi_2Te_3 platelets, further complicating the direct investigation of the lateral surfaces. The angles between either of the (015) and $(01\bar{4})$ lateral facets and the (001) basal planes are close to 60° (Figure 3.15.c) that is in a fairly good agreement with the experimental observations (Figure 3.15.b). Interestingly, thermal annealing of the Bi_2Te_3 branched nanosheets performed in the solution phase in the absence of available free monomer led to restoration the equilibrium hexagonal shape and the concomitant recrystallisation of the material resulted into changes in the lateral termination from the {015} to the equilibrium {110} (Figure 3.11).

[8] The number of dangling bonds per atom of the corresponding surface is taken from ref. [332].

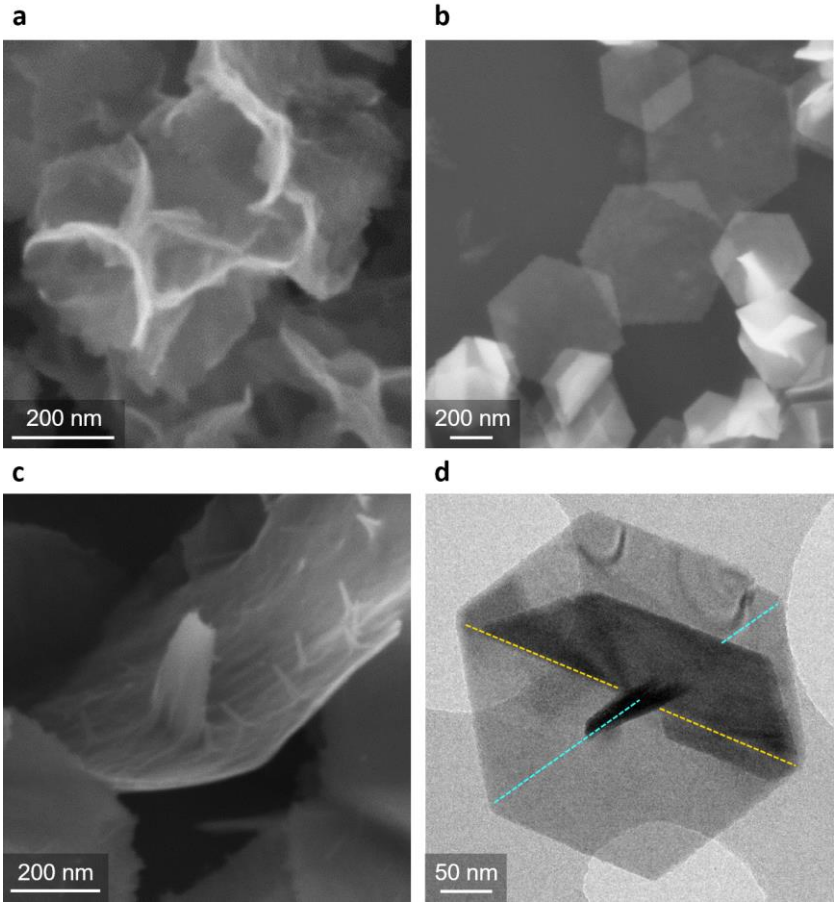


Figure 3.16. Branching in the colloidal Bi_2Te_3 nanosheets. **a, b** SEM images of the final products obtained at the growth temperatures of 70 ºC and 170 ºC, respectively, demonstrating a lower degree of branching in the Bi_2Te_3 nanosheets at higher growth temperatures. **c** SEM image of a secondary petal growing off the primary Bi_2Te_3 platelet. **d** TEM image of a branched Bi_2Te_3 platelet illustrating the secondary hexagonal platelets growing through the middle of the primary platelet.

The formation mechanism of Bi_2Te_3 branched nanostructures appears to be more complex than a simplified secondary nucleation. First, the apparent branching is effectively suppressed when the material is attained at higher growth temperatures (lower supersaturation) as illustrated by the SEM images of the respective samples in Figure 3.16.a,b. Taken from the reaction medium after just a few seconds into the growth, the Bi_2Te_3 nanostructures display distinct secondary petals stemming off the primary hexagonal platelet (Figure 3.16.c). Remarkably, the secondary petals almost exclusively grow along the main diagonals of the primary hexagonal platelet as shown in Figure 3.16.d. This implies that the crystal growth, yielding branched Bi_2Te_3 nanoplatelets, is likely to be a seed-mediated process rather than a mere random secondary nucleation. As mentioned in Section 3.2.1, similar geometries of concaved cuboctahedrons were previously reported for the CuS and $LiCoO_2$ nanocrystals [317,318]. The proposed mechanism includes the growth through adsorption and desorption of structural blocks, inducing a selective pitting of the less stable facets, thus leading to

minimisation of the exposed high-energy edges and to increase of the surface area of more stable facets [317]. Although the morphology of the Bi_2Te_3 seeds has not been studied within this work, nucleation of the Bi_2Te_3 polygons, which could serve as a shape-templating seeds leading to the growth of the branched nanostructures, can be expected in a kinetically-controlled growth regime. In fact, synthesis of the Bi_2Te_3 nanooctahedra, exhibiting the high-index {015} termination, has been reported recently [334].

To conclude, the morphology of the Bi_2Te_3 nanostructures grown in the solution phase can be effectively controlled by varying the synthesis conditions. This can be appealing for tailoring the topological properties of the material providing an access to the high-index surfaces that are not normally attained under nearly equilibrium conditions of the CVD process.

3.2.3. Effect of bismuth precursor stoichiometry on the morphology of Bi_2Te_3 nanostructures

In contrast to the chemically inert basal planes, lateral sides of Bi_2Te_3 nanostructures are terminated with the unsaturated dangling bonds and so are susceptible to the presence of free capping ligand. An excess of strongly binding capping agent, such as oleic acid or oleylamine, can effectively passivate the undercoordinated sites of the lateral planes and as a consequence inhibit lateral growth of the Bi_2Te_3 nanostructures. In this study, we chose not to use oleylamine as a solvent or a capping ligand as it is known to reduce bismuth salts, causing nucleation of bismuth nanoparticles [335] and thus hindering the formation of high quality two-dimensional nanostructures. As we mentioned earlier, using stoichiometric bismuth oleate as a source of bismuth ions allowed us to reduce the growth temperature down to 20 ºC and to attain two-dimensional Bi_2Te_3 nanostructures in the entire temperature range (20-170 ºC). This differs significantly from the majority of works, where low temperature (under 40 ºC) growth in oleic acid, which is used as a coordinating solvent, yields in quasi-spherical Bi_2Te_3 nanoparticles only or no material nucleation is observed at all [314,315].

We further investigate the effect of the $[Bi(CH_3COO)_3]$:[oleic acid] molar ratio on the morphology of the growing Bi_2Te_3 nanostructures. To do so, we have prepared solutions of bismuth precursor in octadecene, varying the ratio between bismuth acetate and oleic acid from 1:7 (excess of free oleic acid) to 1:3 (stoichiometric bismuth oleate) and to 1:1 (partially substituted bismuth acetate). Figure 3.17.a-c shows the representative SEM images of Bi_2Te_3 products obtained from these bismuth precursors. With the amount of free oleic acid decreased when the molar ratio is changed from 1:7 to the stoichiometric 1:3, the degree of branching of

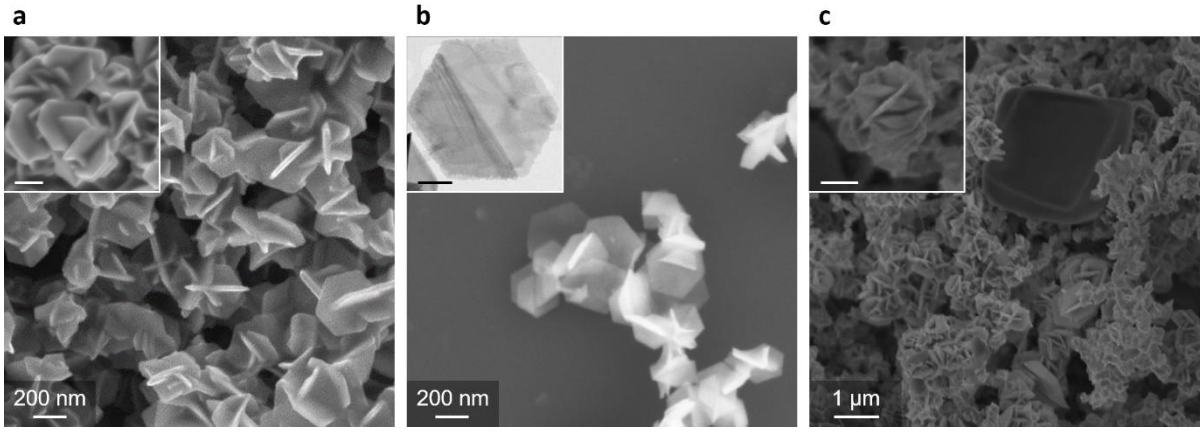


Figure 3.17. The effect of the bismuth precursor stoichiometry on morphology of the Bi_2Te_3 nanostructures produced at high temperature (170 ºC). Representative SEM images of the Bi_2Te_3 nanostructures synthesised from **a** 1:7, **b** 1:3, and **c** 1:1 $[Bi(CH_3COO)_3]$:[OlAc] mixtures. Insets show SEM and TEM images of the individual Bi_2Te_3 branched platelets grown under the specified conditions; scale bars 200 nm (panel **a**); 100 nm (panel **b**); 50 nm (panel **c**).

the Bi_2Te_3 platelets is also visibly decreased as is evidenced by the increased fraction of either single-crystalline hexagonal platelets or branched platelets made of only two intersecting hexagons present in the samples (Figure 3.17.b; 3.16.b). Further reduction of the oleic acid content (Figure 3.17.c) led to formation of the partially substituted bismuth acetate precursor resulting in considerable contamination of the final product with unreacted bismuth acetate. Bismuth acetate is present in the samples in a form of micron-sized rectangular particles. EDS analysis performed on individual rectangular particles confirms the presence of only Bi, C, and O in their structure. The Bi_2Te_3 nanostructures acquired under these conditions display highly branched morphology as shown in Figure 3.17.c. The excessive branching observed in the Bi_2Te_3 product synthesised from the 1:1 $[Bi(CH_3COO)_3]$:[oleic acid] mixture can be attributed to the presence of unremoved acetate ligands, similar to [336], where the presence of acetate and acetic acid was found to be essential for the formation of well-defined highly-branched Bi_2Te_3 flowers.

A similar trend of the reduced branching in Bi_2Te_3 nanostructures was also observed at lower growth temperatures (50 ºC) when the amount of free oleic acid was minimised. This is illustrated by the representative TEM images of Bi_2Te_3 nanosheets obtained from the 1:7 and 1:3 mixtures shown in panels a and b in Figure 3.18, respectively. However, in contrast to the high temperature growths (see Figure 3.17.c), no material nucleation was observed at low growth temperature when the $[Bi(CH_3COO)_3]$:[OlAc] precursor ratio was 1:1 (Figure 3.18.c).

Overall, we have studied the effect of the free oleic acid present in the reaction medium on the morphology of the growing Bi_2Te_3 nanostructures. We have found that reducing the

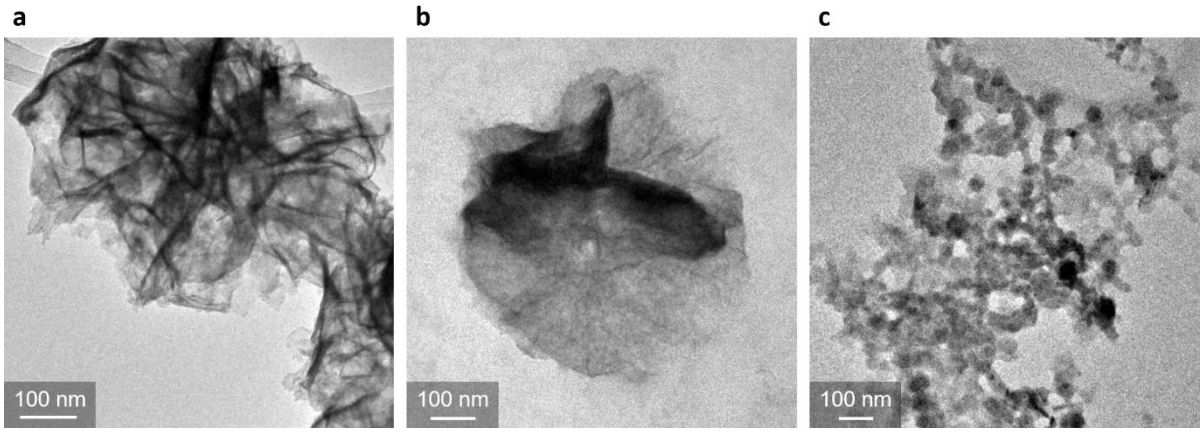


Figure 3.18. The effect of the bismuth precursor stoichiometry on morphology of the Bi_2Te_3 nanostructures produced at low temperature (50 °C). Representative SEM images of the Bi_2Te_3 nanostructures synthesised from **a** 1:7, **b** 1:3, and **c** 1:1 [$Bi(CH_3COO)_3$]:[OlAc] mixtures.

amount of free oleic acid to a minimum necessary to form the stoichiometric bismuth oleate allowed us to obtain two-dimensional Bi_2Te_3 nanostructures in a wide range of growth temperatures varying from 170 °C down to room temperature.

3.3. Colloidal WSe_2 nanoflowers

Similar to $MoSe_2$ nanostructures discussed in Section 3.1, colloidal WSe_2 hierarchical nanosheets were obtained through a solution-phase reaction between trioctylphosphine selenide complex and tungsten hexacarbonyl dissolved in hot oleic acid. The full details of the experimental procedure are given in Section 2.2.3. Full list of samples and the corresponding synthesis conditions are provided in Appendix A4.

3.3.1. Structural characterisation of WSe_2 nanoflowers

Under the described growth conditions, WSe_2 is produced in a form of the edge-rich flower-like nanostructures, similar to the ones observed in the bottom-up synthesis of the colloidal $MoSe_2$ (Section 3.1). However, the morphology of the colloidal WSe_2 nanostructures appears to be more uniform compared to that of the $MoSe_2$ nanostructures that were commonly attained in a variety of forms ranging from the well-defined nanoflowers to continuous branched nanosheets (nanobrushes).

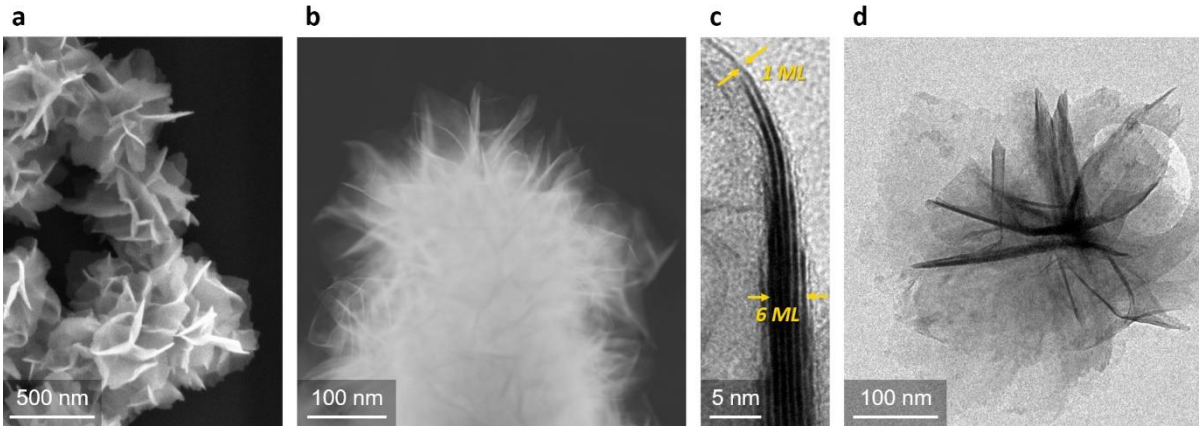


Figure 3.19. Morphology of the colloidal WSe_2 nanosheets. **a** SEM image of the ensemble of WSe_2 nanoflowers. **b** ADF STEM image of a WSe_2 nanoflower. **c** Side-view TEM image of an individual petal of a WSe_2 nanoflower. **d** TEM image of the core region of a WSe_2 nanoflower.

A representative SEM image shown in Figure 3.19.a. demonstrates rich three-dimensional morphology of the colloidal WSe_2 nanoflowers, consisting of two-dimensional petals emerging from the central core. In the ADF STEM images, individual WSe_2 petals appear curled and folded (Figure 3.19.b) due to a small thickness of the nanosheets compared to their lateral dimensions. The diameter of the synthesised WSe_2 nanoflowers varies from 300 nm up to 700 nm, significantly exceeding lateral dimensions of the $MoSe_2$ nanoflowers obtained under similar growth conditions. The side-view TEM imaging (Figure 3.19.c) reveals the few-layered nature of WSe_2 petals thinning down to 1 monolayer at the rims. The overall

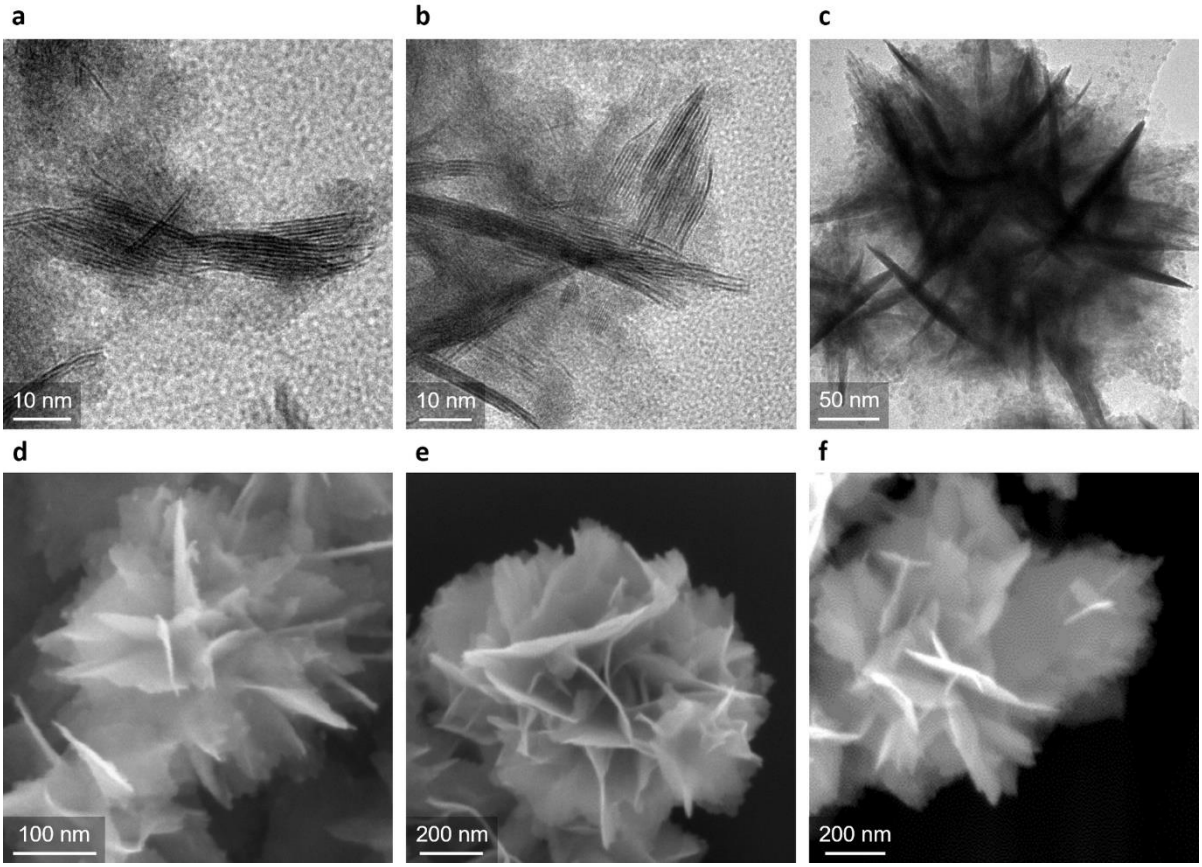


Figure 3.20. Insights into the branching observed in the colloidal WSe_2 nanostructures. **a, b** Representative TEM images of the WSe_2 nanostructures after 30 minutes of growth. **c, d** TEM and SEM images of the final product, obtained after 180 minutes of growth, exhibiting a rich three-dimensional morphology caused by the subsequent nucleation during the growth process. **e, f** SEM images of the branched WSe_2 nanostructures illustrating splitting of the individual petals.

anisotropic morphology of the as produced material is in good agreement with the kinetically-controlled growth regime discussed in Section 3.3.3. However, at this stage we cannot provide a comprehensive study of the branching mechanism as, even in the case of the less branched WSe_2 nanoflowers (Figure 3.19.d), the central core region is usually obscured by the vertical petals, appearing electron-opaque in the TEM images, and as a result the core structure has not been inferred from the microscopy data.

Generally, the formation of hierarchical two-dimensional nanostructures that is not driven by a difference in the growth rates along a certain family of crystallographic directions, as for example was demonstrated in the case of CdTe tetrapods [197] or PbS octahedrons [330], can be due to a secondary heterogeneous nucleation occurring on the surface of the growing material if the synthesis conditions are not optimised to effectively separate the nucleation and growth stages [337,338]. We hypothesise a similar mechanism underlying the formation of colloidal WSe_2 nanoflowers. Presented in Figure 3.20 is a series of TEM images of the WSe_2

nanostructures isolated from the reaction medium at different growth times. After 30 minutes of growth, both quasi-two-dimensional nanosheets (Figure 3.20.a) and nanostructures with secondary petals stemming from a primary nanosheet (Figure 3.20.b) co-exist in the system; these are later overgrown by multiple subsequently nucleated petals (Figure 3.20.c), resulting in the rich three-dimensional morphology of the produced WSe_2 nanoflowers as clearly seen in the SEM images of the final product (Figure 3.20.d).

However, the detailed examination of the lateral sides of growing WSe_2 nanosheets presented in Figure 3.20.a,b suggests that the formation of nanoflowers cannot be solely attributed to the secondary nucleation. This process can be complemented by stacking or an oriented attachment of insufficiently passivated disk-shaped TMD nuclei formed at the early stages of the reaction. Additionally, crystal splitting that is occasionally observed in some minerals, i.e. aragonite, has been recently proposed as the formation mechanism of sheaf-like nanocrystals grown by the colloidal approach [[339]]. The mechanism is described as an individual single crystal splitting apart during the growth process. The reasons for such splitting are not fully understood but are commonly associated with fast crystal growth or with the presence of extra species trapped in the growing crystal and causing its mechanical splitting. We can presume that during the growth process a few-layer WSe_2 single crystal extending in the *ab* plane splits into thinner sub-crystals, resulting in the petal morphologies resembling a stack of paper sheets like the ones shown in Figure 3.20.e,f.

Unlike $MoSe_2$ that in the present work was acquired in the thermodynamically stable 2H phase, the as produced WSe_2 adopted the metastable 1T' phase. In contrast to the 1T' $MoTe_2$ discussed in Section 3.1.1, direct synthesis of the metastable 1T' polymorph of WSe_2 is significantly more challenging as the energy difference between the polymorphs is larger for diselenides than for ditellurides (270 meV vs 40 meV per formula unit for WSe_2 and $MoTe_2$ monolayers, respectively, [[20]]). Possible explanation for the preferential growth of the metastable WSe_2 polymorph in the solution-phase synthesis will be provided in Section 3.3.3. Figure 3.21.a shows the HR TEM image of an individual petal of a WSe_2 nanoflower displaying evident contrasting stripes originating from the zigzag chains of tungsten atoms as highlighted by the overlaid crystal model. Clustering of the metal centres that is accompanied by the formation of quasi-one-dimensional metal chains along the *b* axis of the unit cell is characteristic to the 1T' structure [[29]]. The FFT pattern in Figure 3.21.b further confirms the rectangular unit cell of the produced WSe_2 and can be indexed in the [001] zone axis of the monoclinic 1T' phase (space group $P\,2_1/m$). The high order reflections observed in the

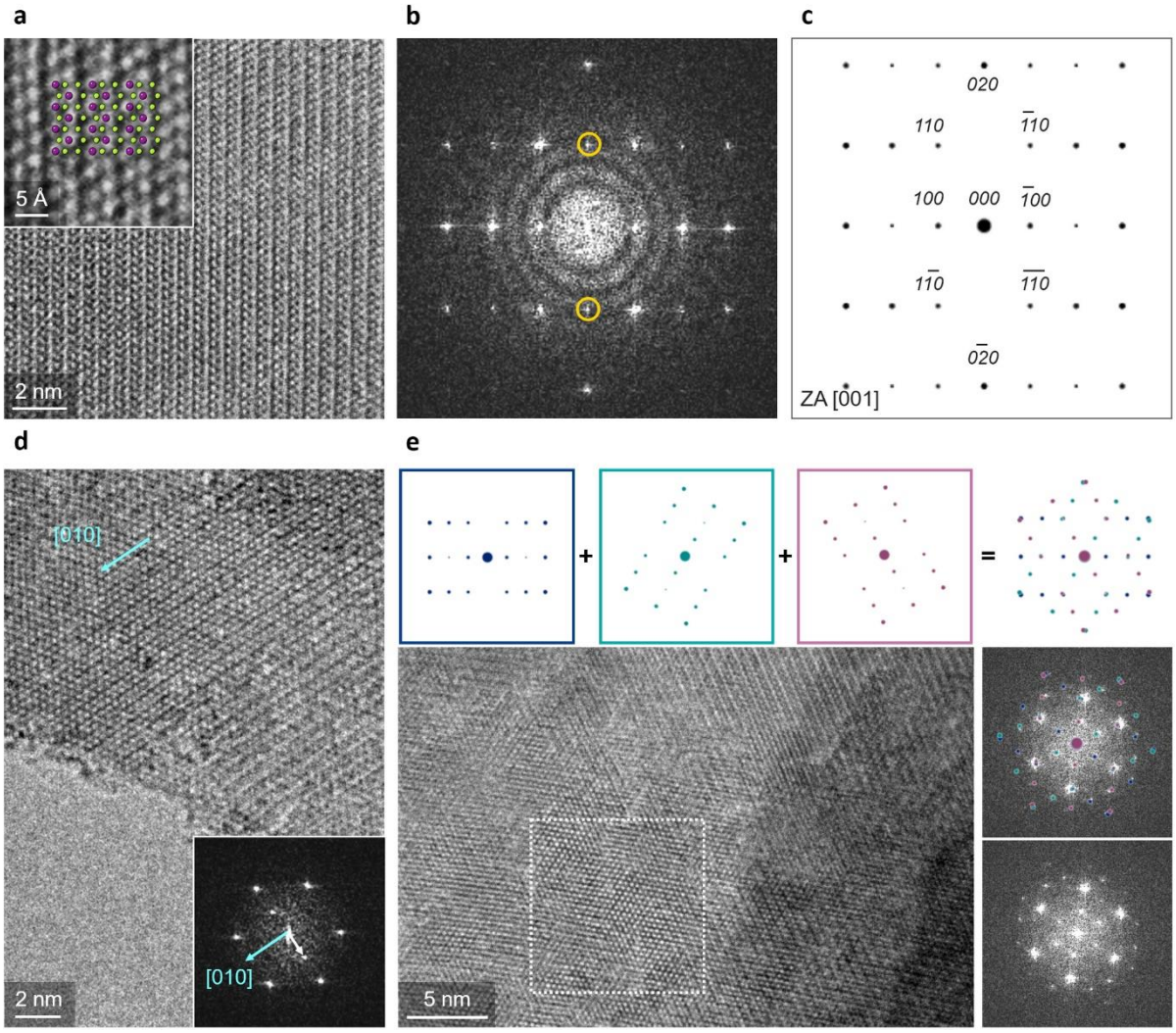


Figure 3.21. TEM characterisation of the 1T' WSe_2 nanosheets. **a** High resolution TEM image of the as produced WSe_2 nanosheets with an overlaid crystal model of the 1T' phase. **b, c** Experimental FFT pattern of the area in **a** and a simulated diffraction pattern indexed in the [001] zone axis of the 1T' phase of WSe_2. **d** Lateral termination of an individual WSe_2 petal. **e** High resolution TEM image, corresponding experimental and simulated FFT patterns of three overlapping 1T' WSe_2 single crystals.

experimental FFT pattern provide an additional evidence of the long-range periodicity in the as grown material, while kinematically-forbidden (010) reflections (highlighted with yellow circles) can be indicative of incomplete layers or antisite defects present in the few-layer WSe_2 nanosheets. The 1T' phase of WSe_2 exhibits the period doubling along the *a* axis (commonly referred to as a $2a \times a$ superstructure with respect to the hexagonal 2H lattice) with the structural parameters $a = 5.76$ Å and $b = 3.30$ Å identified from the results of HR TEM imaging. The lateral extension of growing WSe_2 nanosheets seemingly occurs along the [010] direction as illustrated in Figure 3.21.d. Rigid chains of tungsten atoms running through the ultra-thin WSe_2 nanosheets are likely to cause an increased stiffness along the *b* direction; in this case, scrolling

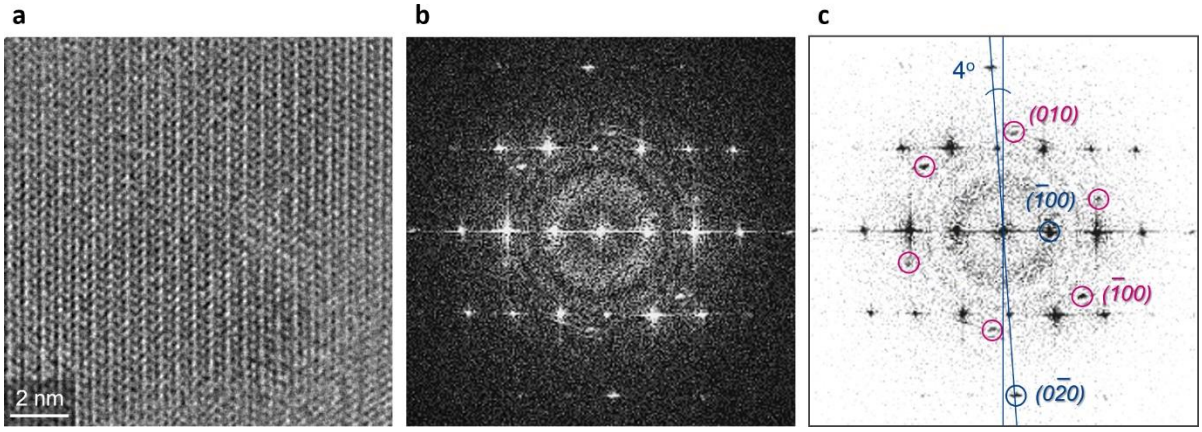


Figure 3.22. Surface distortion of the 1T' phase. **a, b** Experimental high resolution TEM image and the corresponding FFT pattern of an individual 1T' WSe_2 petal. **c** Analysis of the experimental FFT pattern (colours inverted for clarity) showing an angular distortion in the ab plane of 1T' phase (navy lines) and presence of the secondary hexagonal (2H) phase (purple circles).

and folding of the individual flexible petals leads to a lattice compression in the *a* direction (experimentally found 5.76 Å vs the calculated equilibrium value of 5.94 Å [20]).

Interestingly, overlapping of the 1T' single crystal domains can give rise to the apparent three-fold symmetry in the *ab* plane as highlighted with white dashed square in Figure 3.21.e, however the detailed FFT analysis confirms a merohedral triplet of the $2a \times a$ cells rotated by 120°. Formation of a similar $2a \times 2a$ superstructure has been reported in the restacked chemically exfoliated 1T' WS_2 nanosheets [123]. Top panel in Figure 3.21.e depicts the superlattice arising as a superposition of three individual reciprocal 1T' lattices rotated by 120° about the [001] direction and the same superlattice overlaid with the experimental FFT pattern of the region highlighted by the white dashed square. It should be noted that such superstructures were only observed in thick petals of the WSe_2 nanoflowers grown at high supersaturation (in this particular case, the molecular precursor concentrations are 10 times higher than the standard ones; detailed description is provided in Section 3.3.3). These conditions can favour secondary nucleation and potentially epitaxial vertical growth competing with the lateral extension of the primary 1T' nanosheets, leading to formation of the described merohedral triples.

A number of examined 1T' WSe_2 domains (petals) exhibited an angular distortion in the *ab* plane characterised by a shear angle between the *a* and *b* axes. Presented in Figure 3.22 is the HR TEM image and the corresponding FFT pattern of a pristine WSe_2 petal, demonstrating an angular distortion with the shear angle of 4° (panel c). Similar angular distortion with the shear angles varying between 2° and 6° has been previously reported in the STM studies of the 1T'-$MoTe_2$ [340] and 1T'-WTe_2 [341] single crystals and 1T'-WSe_2 single-layers grown by the

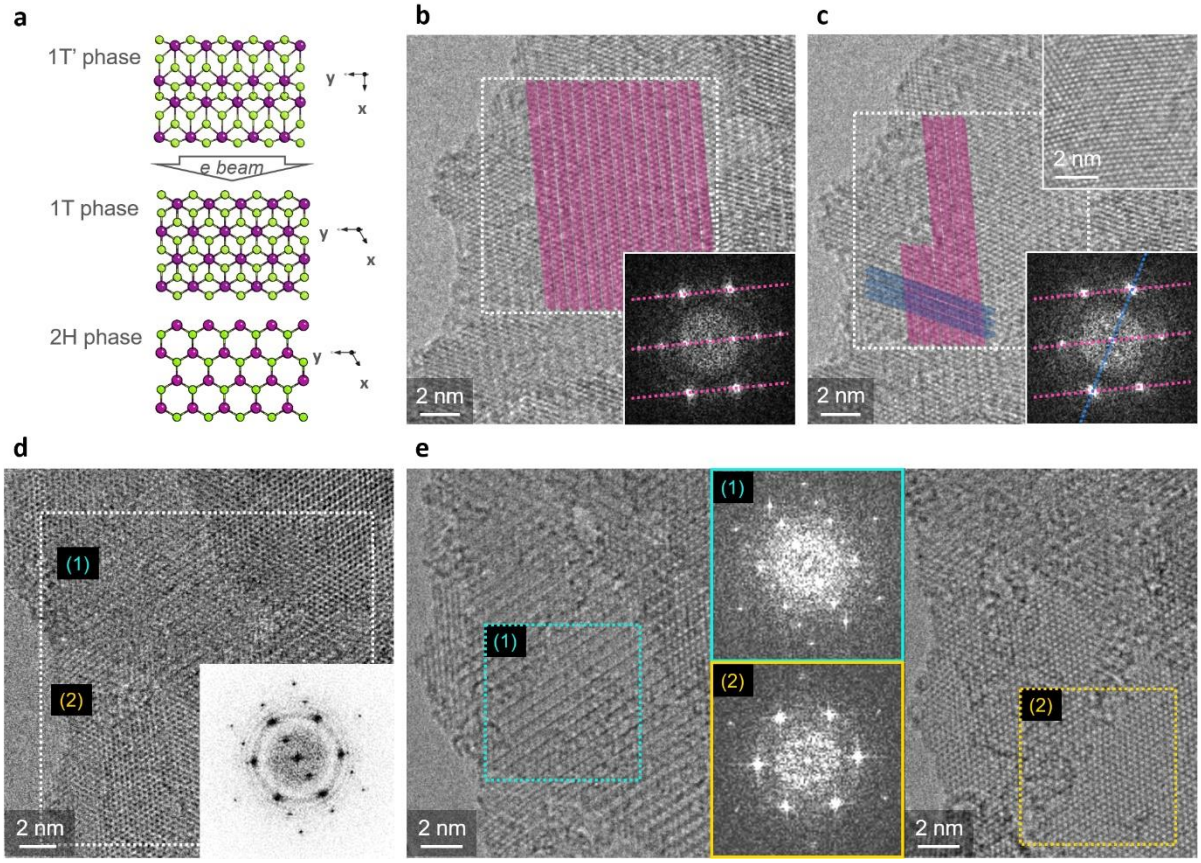


Figure 3.23. Stability of the 1T' WSe_2 phase under TEM imaging conditions. **a** Schematic illustration of a symmetry change in the *ab* plane upon 1T' to 1T or 2H phase transformation. **b, c** High resolution TEM images taken from the same area of the WSe_2 nanosheet demonstrating reorganisation (and complete disappearance, inset) of the contrasting stripes characteristic to the 1T' phase after 5 (10) minutes of beam exposure. **d** High resolution TEM image and the corresponding FFT pattern of a few-layer WSe_2 region, taken after 5 minutes of beam exposure, demonstrating co-existence of the 1T' (few-layer region 1) and the 1T (single-layer region 2) phases. **e** Zoomed in high resolution TEM images and the corresponding FFT patterns of the few-layer region retaining the rectangular symmetry of the 1T' phase and the converted single-layer region exhibiting three-fold symmetry of the 1T phase.

MBE approach [43] and was attributed to the surface reconstruction of the 1T' phase. Interestingly, the second set of diffraction spots matching the (100) planes of the hexagonal 2H phase is (although seldom) found in the experimental FFT patterns of the few-layered petals of the 1T' WSe_2 nanoflowers (highlighted with the purple circles in Figure 3.22.c).

Observed in the chemically exfoliated MoS_2 single layers, the 1T' phase is found to transform into the octahedral 1T phase upon a prolonged electron beam exposure [22]. Similarly, tungsten zigzag chains in the chemically exfoliated WS_2 monolayers were reported to undergo a reorganisation through a tetramer tungsten cluster formation and reorientation of tungsten chains [29]. The change in the *ab* plane symmetry was experimentally observed in the single-layer areas of the produced 1T' WSe_2 nanosheets. Within 5 minutes of beam exposure,

the uniform rectangular lattice of the pristine 1T' phase with the zigzag chains of tungsten atoms highlighted in purple stripes in Figure 3.23.b went through a reconstruction evidenced by the appearance of a second orientation of tungsten chains in the HR TEM image (highlighted in blue in Figure.3.23.c). Eventually, the maze-like lattice composed of shorter tungsten chains relaxed into the hexagonal lattice as illustrated in the inset in Figure 3.23.c. Absence of the angular misalignment in the FFT patterns taken from the same area before and after prolonged beam exposure further confirms that the change in symmetry is likely to be attributed to the dissociation of the W-W bonds and reorientation of tungsten chains and to the ultimate relaxation to the 1T structure. Although the 1T and 2H phases of the group VIB TMD monolayers cannot be distinguished in the TEM mode as both phases possess the three-fold symmetry in the *ab* plane that appears as a hexagonal lattice in HR TEM images, the HAADF STEM studies performed on the chemically exfoliated MoS_2 monolayers have proved that electronic charging of the 1T' phase causes its transformation into the 1T phase [22]. Interestingly, the few-layer domains of the 1T' WSe_2 phase demonstrated better stability under the electron beam irradiation. This is illustrated by the TEM images of a WSe_2 petal consisting of a few- and single-layer 1T' regions (Figure 3.23.d) taken after a prolonged beam exposure. Area 1 (teal square), corresponding to the bi-layer region of the investigated petal, displays the stable chains and retention of the rectangular lattice of the 1T' phase in the FFT pattern, whereas Area 2 (yellow square) highlights the three-fold symmetry of the decayed 1T' phase in the single-layer WSe_2.

3.3.2. Conversion to the thermodynamically stable phase

The synthesised 1T' phase of WSe_2 was found to be stable under ambient conditions. Suspensions of WSe_2 nanoflowers in ethanol were monitored via absorption spectroscopy over one month and did not show any evidence of the phase transformation to the thermodynamically stable 2H phase (Figure 3.24.a). Unlike the semiconducting 2H WSe_2 phase (3), the freshly prepared 1T' WSe_2 nanoflowers (1) and the nanoflowers stored in ethanol for one month (2) do not exhibit excitonic transitions. This agrees well with the predicted metallic behaviour of the few-layer 1T' WSe_2. TEM analysis has further confirmed the retention of the 1T' phase in WSe_2 samples stored in ethanol under ambient conditions (Figure 3.24.b-c). The locking of the metastable phase has previously been shown in colloidal 1T' $MoTe_2$ nanoflowers [171] and has been majorly attributed to the mechanical pinning at grain boundaries as even though the energy difference between the stable and metastable polymorphs was found to be comparable to the room temperature thermal energy (40-42 meV per formula

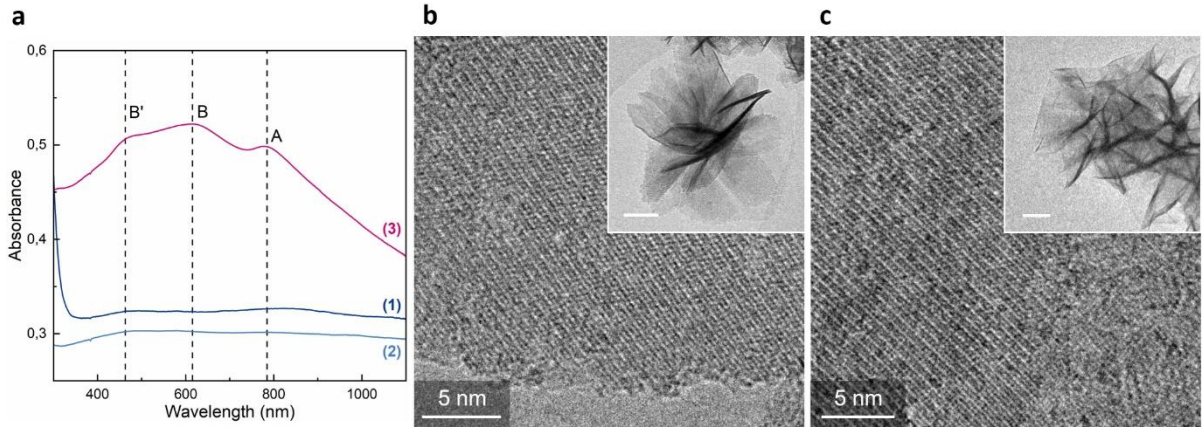


Figure 3.24. Stability of the 1T' phase under ambient conditions in solution. **a** UV-vis absorption spectra of the suspensions of freshly prepared 1T' WSe_2 nanoflowers (1), of the same 1T' WSe_2 nanoflowers after a month in ethanol (2) and of the WSe_2 nanoflowers thermally converted into the semiconducting 2H phase (3) for comparison; optical density recorded for the sample (2) is lower due to partial aggregation (flocculation) and sedimentation of the WSe_2 nanoflowers over a month in solution. **b, c** High resolution TEM images of the freshly prepared WSe_2 nanoflowers (a) and on the 15th day after the synthesis (b); in the corresponding low-magnification TEM images scale bar 50 nm.

unit for $MoTe_2$ monolayers [20,171]) the phase transition would require a simultaneous significant change of both *a* and *b* lattice constants, which is hardly achievable in the polycrystalline material. Despite the larger energy difference (270 meV per formula unit for WSe_2 monolayers [3]), spontaneous 1T'-to-2H phase transition at room temperature is further disfavoured in WSe_2 as the estimated energy barrier associated with the 1T'-to-2H transition is also higher compared to the case of $MoTe_2$ [12].

The metastable 1T' phase can be, however, converted into the thermodynamically stable 2H phase upon thermal annealing. It has previously been shown that the transition from the metallic 1T-MoS_2 produced via chemical exfoliation into the disordered 2H phase occurs at 95 °C at atmospheric pressure [173]. Similarly, the thermodynamically stable 2H phase can be restored in bulk 1T' $MoSe_2$ upon annealing at 120 °C [183]. Being a heavier analogue of MoS_2, WSe_2 would supposedly require higher thermal energy input to overcome the energy barrier to transform from the metastable 1T' to the thermodynamically stable 2H phase. In order to preserve the high surface area morphology of WSe_2 nanoflowers, thermal annealing was performed in the gas phase since solution-phase annealing can lead to a digestive ripening and recrystallisation of the polycrystalline nanostructures as was demonstrated in the case of branched Bi_2Te_3 nanosheets in Section 3.2.1. To achieve this, suspensions of the as produced 1T' WSe_2 nanoflowers in ethanol were drop-cast on Si/SiO_2 substrates and dried at room temperature; the dried powders were pre-annealed in a tube furnace at 200 °C in an argon atmosphere (0.45 mbar) to remove the residual solvent and adsorbed long-chain organic

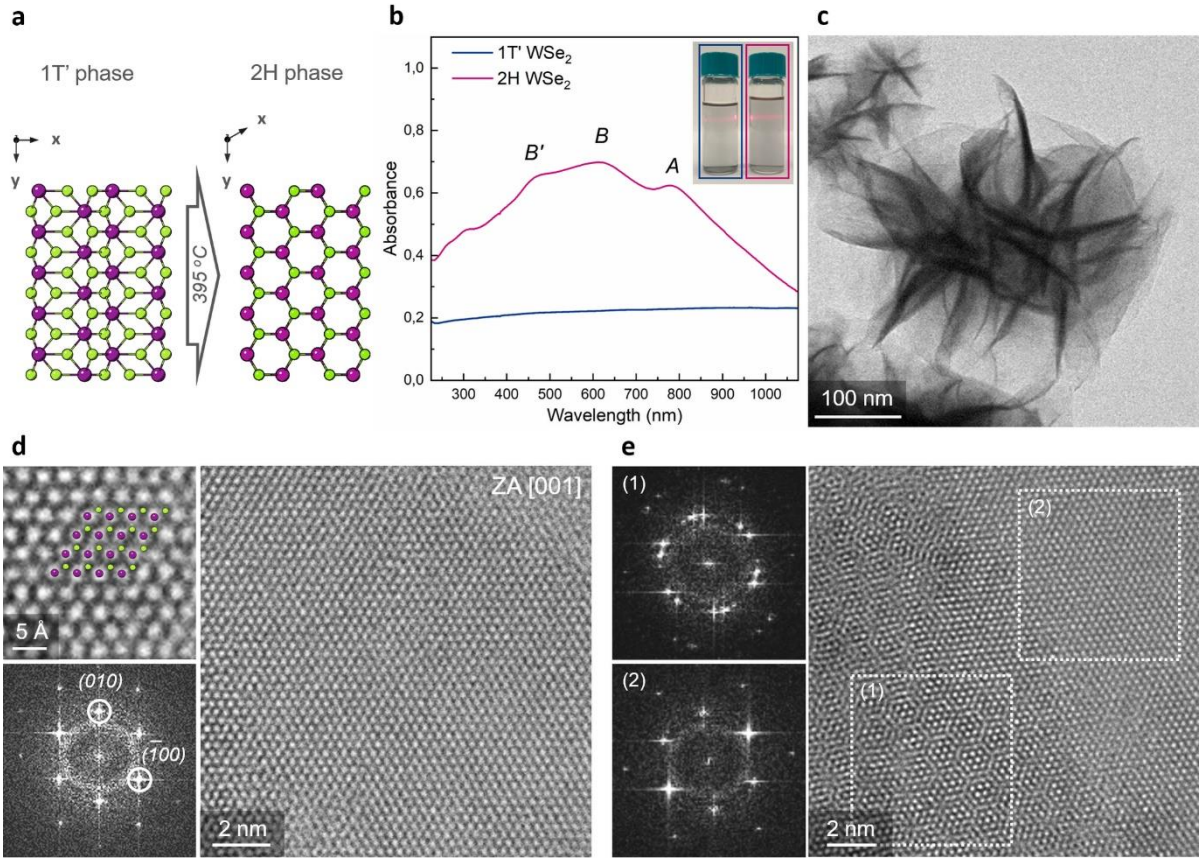


Figure 3.25. 1T' to 2H phase conversion upon thermal annealing of the WSe_2 nanoflowers. **a** Schematic representation of the change in the *ab* plane symmetry accompanying the 1T' to 2H phase transformation. **b** Optical absorption spectra of the suspensions of the as produced 1T' and the annealed 2H WSe_2 nanoflowers in ethanol. **c** TEM image of the WSe_2 nanoflowers after the thermal annealing. **d, e** High resolution TEM images and the corresponding FFT patterns of individual WSe_2 petals after the thermal annealing demonstrating the hexagonal 2H phase of the annealed material (panel **d**, crystal model is overlaid) and the Moiré pattern arising from the superimposed WSe_2 nanosheets (panel **e**).

ligands and then annealed at 400 °C for 2 hours. The annealed WSe_2 nanoflowers were redispersed in ethanol via gentle bath sonication. Thermal annealing of the 1T' WSe_2 nanoflowers was accompanied by the excitonic absorption bands of the semiconducting 2H phase, that are not observed in the spectrum of the pristine metallic 1T' phase, appearing in the visible range (Figure 3.25.b). The absorption spectrum of the annealed WSe_2 nanoflowers exhibits three bands labelled as A, B, and B' excitonic transitions [40] and centred at 778, 617, and 453 nm, respectively. The energies of these transitions are lower than the values reported for the monolayer WSe_2 [55] in agreement with the few-layered nature of the synthesised WSe_2.

TEM imaging has confirmed that the annealed WSe_2 retain the starting flower-like morphology without any notable increase in petal thickness (Figure 3.25.c), while the crystal symmetry in the *ab* plane changes to hexagonal (Figure 3.25.d). The uniform interplanar spacing of 2.84 Å observed in the HR TEM images of the annealed nanoflowers matches the

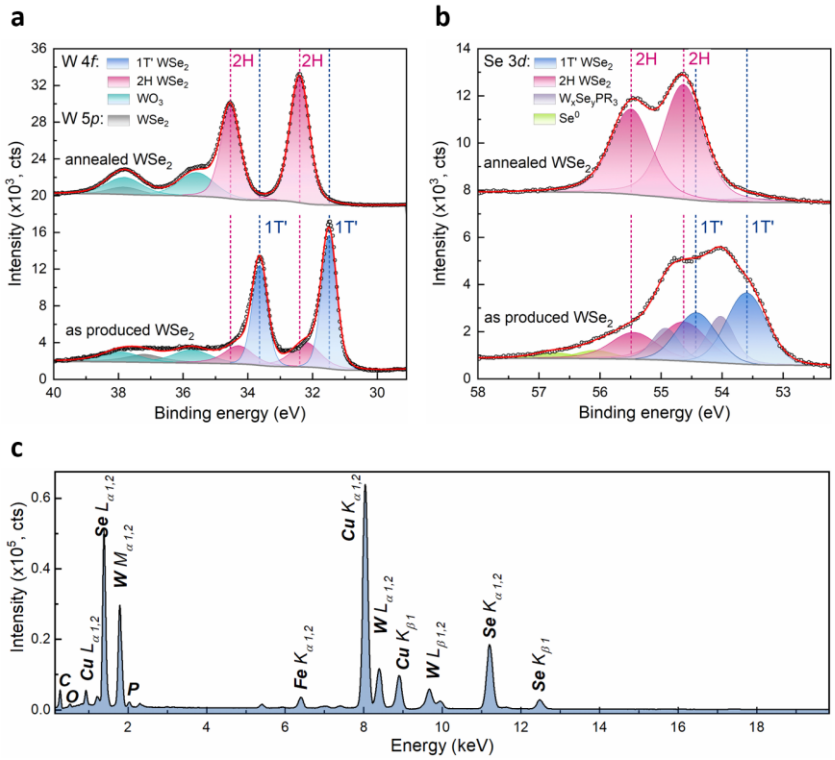


Figure 3.26. Phase purity of the as produced and thermally converted WSe_2 nanoflowers. **a, b** High-resolution XPS spectra of the W 4*f* and the Se 3*d* core level electron shells, respectively. The raw data are presented in open circles, solid red lines correspond to the fitting curves. **c** A representative TEM EDS spectrum of the as produced 1T' WSe_2 nanoflowers.

(100) planes of the 2H WSe_2. The moiré patterns arising in the regions where two single-crystalline WSe_2 domains with different orientations overlap and held by the van der Waals forces can indicate the tendency of the annealed material to restack [342]. Figure 3.25.e illustrates the border between bi- (Area 1) and single-layer (Area 2) regions, in the first case the corresponding FFT pattern displays a doubled set of the three-fold symmetry diffraction spots, while in the latter one a single set of the diffraction spots is present in the FFT pattern.

To evaluate the phase purity of the as produced and the annealed WSe_2 nanoflowers, we performed XPS analysis of the samples. In all cases, the XPS peak positions were calibrated based on the C 1*s* peak (284.6 eV) to minimise variations due to possible surface charging. Thermal annealing was found to induce substantial changes in the XPS spectra of the W 4*f* and the Se 3*d* electron shells of the produced WSe_2 (Figure 3.26.a,b). The XPS spectrum of the W 4*f* electrons of the as produced WSe_2 was fitted with three doublets as shown in Figure 3.26.a. The most prominent pair of peaks found at 31.66 and 33.84 eV was ascribed to the W^{+4} 4*f* doublet. In the annealed sample, the W^{+4} 4*f* doublet appeared at 32.40 and 34.58 eV in a good agreement with the positions commonly reported for the WSe_2. Shifted to lower binding energy the W^{+4} 4*f* doublet was assigned to the 1T' phase of WSe_2. A shift to lower binding

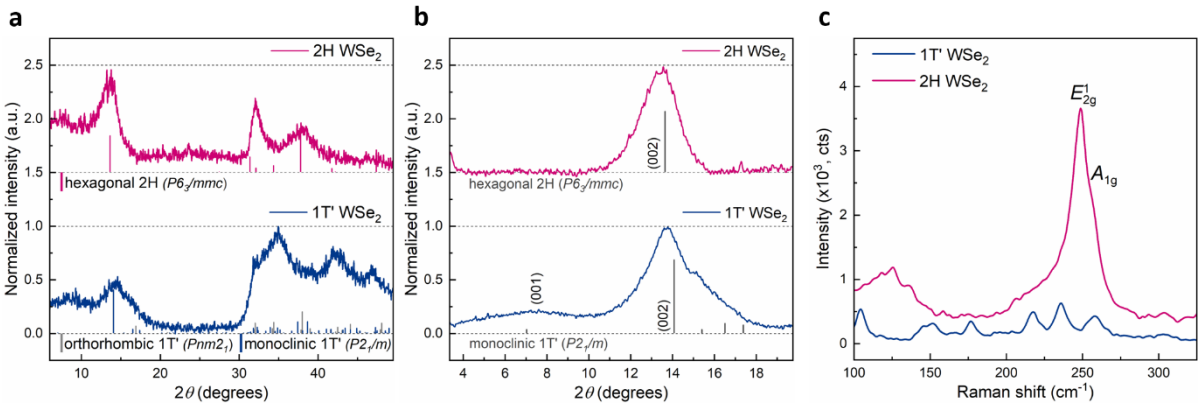


Figure 3.27. Structural characterisation of the as produced and the annealed WSe_2 nanoflowers. **a, b** XRD patterns and small-angle diffraction patterns of the as produced 1T' and the annealed 2H WSe_2 nanoflowers. **c** Raman spectra of the as produced 1T' and the annealed 2H WSe_2 nanoflowers. Raman spectra are offset for clarity.

energy has previously been observed in the polycrystalline films of few-layered MoS_2 and $MoSe_2$ upon conversion from the 2H phase into the metallic 1T phase induced by the *n*-butyllithium treatment [[178]]. The second W^{+4} 4*f* doublet found at 32.22 and 34.30 eV indicated a minor fraction of the 2H phase (20 at.%) present in the as produced WSe_2 nanoflowers. It should be noted that the lower binding energy doublet was absent in the spectrum of the WSe_2 nanoflowers annealed at 400 °C in an argon atmosphere, proving the conversion into the semiconducting 2H phase was complete. The as produced material also contained a trace amount of the oxidized tungsten (15 at.%) as is evidenced by the W^{+6} 4*f* doublet at 35.74 and 37.92 eV; the oxide content increased to 25 at.% after the thermal annealing. Similar trends were found in the XPS spectra of the Se 3*d* core level electrons (Figure 3.26.b). The unresolved spectrum of the as produced WSe_2 nanoflowers was fitted with four doublets corresponding to the 1T' Se^{-2} (53.60 and 54.46 eV), 2H Se^{-2} (54.63 and 55.49 eV), amorphous surface selenium (56.06 and 56.92 eV), and the additional doublet at 54.04 and 54.94 eV was ascribed to the long-chain organic substituted WSe_x derivatives analogous to [[343]]. The presence of phosphorus-containing compounds at the surface of the as produced WSe_2 nanoflowers was proved by the elemental analysis (Figure 3.26.c). After the annealing, only the 2H Se^{-2} doublet is observed in the 3*d* Se spectrum.

The distorted octahedral polymorphs of the group VIB TMDs belong to either the orthorhombic, as in case of the T_d $MoTe_2$ [[31]] and WTe_2 [[21,344]], or the monoclinic syngony, like the 1T' $MoTe_2$ [[31,310]] with the only difference being the stacking order of the octahedrally coordinated monolayers. To date, the crystal structure of the bulk 1T' polymorph of WSe_2 remains unreported in literature; however, it is likely to belong to the monoclinic syngony

similar to the 1T' phase of $MoTe_2$, while the orthorhombic $MoTe_2$ is found to be a low-temperature polymorph existing at cryogenic temperatures [31]. The experimental diffractograms of the as produced 1T' and the annealed 2H WSe_2 nanoflowers are shown in Figure 3.27.a. The overall symmetry of the 1T' phase differs significantly from that of the 2H phase produced via thermal annealing of the synthesised material. The strong reflection at ~13.8 $^{o}2\theta$ corresponds to the (002) planes and confirms the few-layered nature of the bulk of the produced material in agreement with the TEM results discussed above. The annealed WSe_2 nanoflowers demonstrate strong diffraction peaks at ~32.0 and 37.9 $^{o}2\theta$ matching the (100) and (103) reflections of the bulk 2H WSe_2 (standard reference pattern of the bulk WSe_2 ICDD 38-1388 is provided in Figure 3.27.a). The reference diffraction patterns of the 1T' phase of WSe_2 were simulated using the CrystalDiffract software package based on the bulk orthorhombic T_d WTe_2 (space group P $nm2_1$) and the monoclinic 1T' $MoTe_2$ (space group P $2_1/m$) reported in literature; lattice parameters *a* and *b* were estimated from the results of HR TEM imaging, whereas the *c* parameter has not been measured directly, instead it was adjusted until the simulated patterns matched the experimental position of the (002) diffraction peak. Despite the similarity of their diffraction patterns, the two phases can potentially be distinguished by the differences in the small-angle region as, unlike the orthorhombic phase, the monoclinic phase possesses the inversion symmetry that implies that all (00*l*) reflections are allowed, while in the orthorhombic phase only the (00*l*) where *l* = 2n reflections are allowed. The experimental small-angle diffraction patterns of the as produced and the annealed WSe_2 nanoflowers are shown in Figure 3.27.b. Broad reflection centred around 7 $^{o}2\theta$ that is reproducibly found in the diffractograms of the 1T' WSe_2 samples and is absent in the annealed 2H nanoflowers can be assigned to the (001) planes of the monoclinic phase.

The differences in the symmetry of the 1T' and 2H phases become evident from the results of Raman spectroscopy. The Raman spectrum of the 1T' WSe_2 nanoflowers is shown in Figure 3.27.c and exhibits a set of Raman-active modes clearly distinct from that of the semiconducting 2H phase. Six well-resolved peaks are observed at 104.5, 149, 177, 218, 236.3, and 258 cm^{-1}. The wider set of Raman modes is indicative of the lower symmetry of the 1T' polymorph compared to the higher symmetry hexagonal (2H) phase and is generally reported for the 1T' and T_d phases of WTe_2 and $MoTe_2$ [21,31,307,345]. Moreover, the appearance of additional vibration modes, commonly referred to as J_1, J_2, and J_3, is observed in the 1T' MoS_2 and $MoSe_2$ crystals [183]. The lower intensity of Raman signal of the metallic 1T' phase compared to the semiconducting 2H phase and can be attributed to the poor interaction with

light was experimentally observed in the WSe_2 monolayers treated with *n*-butyllithium [180]. In contrast to the 1T' phase, the Raman spectrum of the annealed WSe_2 nanoflowers demonstrates a broad peak at ~250 cm^{-1} corresponding to the unresolved in-plane E^1_{2g} and out-of-plane A_{1g} modes of the hexagonal WSe_2 similar to [346,347].

3.3.3. Parametric study of the synthesis conditions: Insights into the growth mechanism

Observing the formation of branched morphologies described in Section 3.3.1 possibly due to secondary heterogeneous nucleation (as shown in Figure 3.20.b) led us to an assumption that under the proposed synthesis conditions (Section 2.2.3) the growth of WSe_2 nanostructures occurs at high supersaturation, i.e. kinetically-controlled growth regime, that can shed some light on the crystallisation of the metastable 1T' phase. The formation of metastable crystal phases under non-equilibrium growth conditions (kinetically-controlled regime) has been previously reported, for example, in the colloidal tetrapod-shaped $A^{II}B^{VI}$ nanocrystals. In this case, the material nucleates selectively in the metastable zinc-blende structure, while during the growth stage the relative stability of the crystal phases is effectively swapped due to the interaction with the capping ligand that eventually leads to the growth of four tetrapod arms in the wurtzite phase [197]. The key requirement for achieving the nucleation of the metastable crystal phase under non-equilibrium synthesis conditions is the energy difference between the thermodynamically stable and the metastable polymorphs being small. In case of bulk $MoTe_2$ and WSe_2, the 2H-1T' energy difference[9] is rather low (40 and 270 meV per formula unit, respectively) and can explain the formation of the 1T' polymorphs in both these cases as discussed in Sections 3.1.1, 3.1.3, and 3.3.1. For comparison, in bulk $MoSe_2$ this energy difference is only a few meV higher (330 meV per formula unit), however, growth of the thermodynamically stable 2H phase was only achieved via the synthesis method proposed in this work (Section 3.1.1). It should be noted that the 2H-1T' energy difference calculated in [20] corresponds to the pristine polymorphs, while, in solution-phase synthesis, the crystal phase energetics can be altered due to interaction with the reaction medium, e.g. solvent, capping ligand.

We have performed a parametric study of the growth conditions, such as reactivity of the transition metal or of the chalcogen precursors, type of solvent, and growth time, while the precursor concentrations and growth temperature were kept fixed. Shown in Figure 3.28.a are

[9] Equilibrium energy differences between the 2H and 1T' polymorphs are taken from ref. [20].

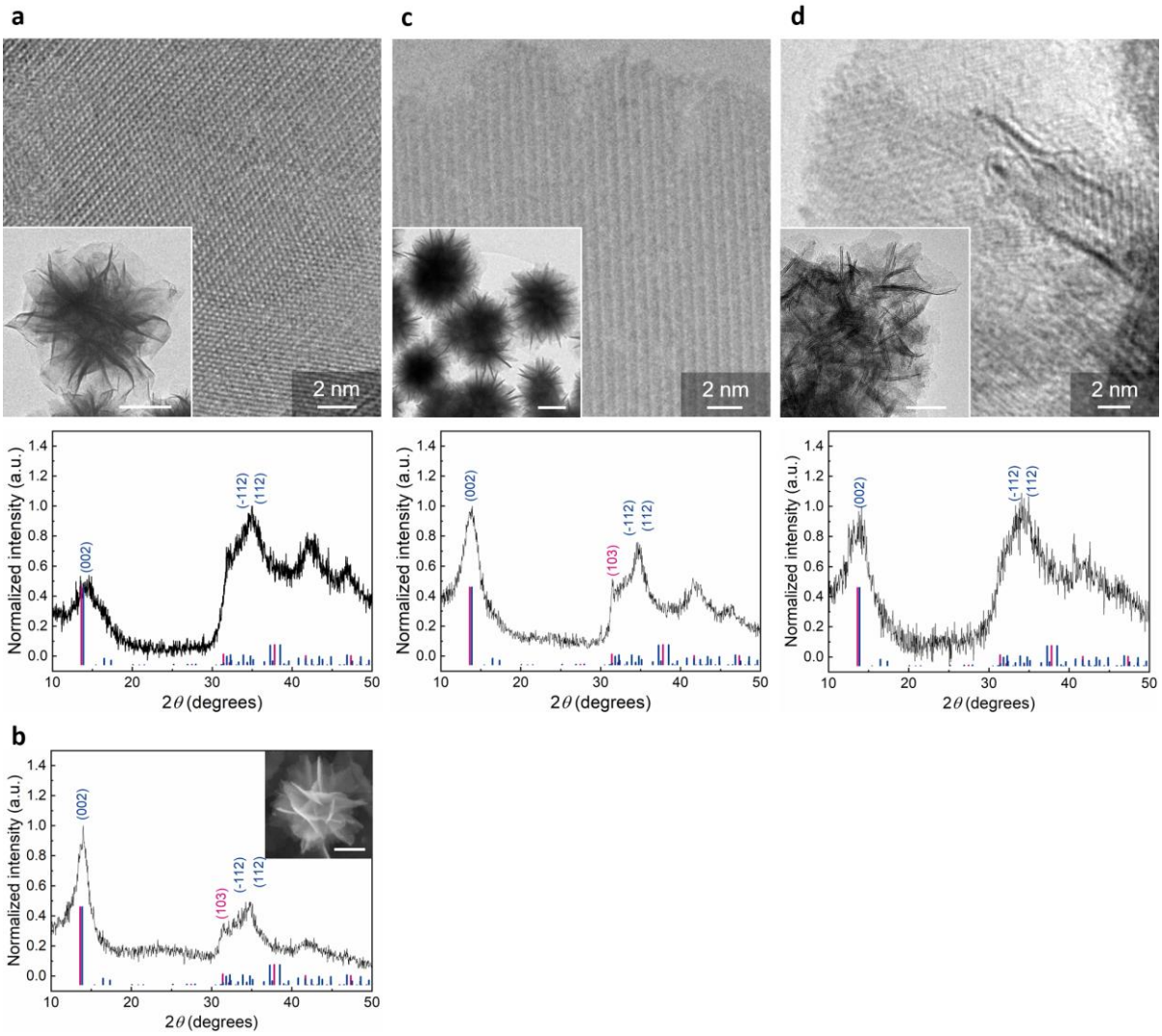


Figure 3.28. Effect of various growth conditions on the crystal phase and morphology of the colloidal WSe_2 nanostructures. High resolution TEM images and the corresponding XRD patterns of the WSe_2 nanostructures grown through a reaction between **a** $W(CO)_6$ and TOP:Se in OlAc (standard, 3 hours), **b** same but growth time extended to 15 hours, **c** $W(CO)_6$ and Se powder in OlAc, and **d** WCl_6 and Se powder in OlAm. Insets show TEM (panels **a**, **c**, **d**) and SEM (panel **b**) images of the individual WSe_2 nanostructures; scale bars: **a-c** 100 nm, **d** 20 nm. Reference diffraction patterns of the monoclinic 1T' (blue) and hexagonal 2H (purple) phases of WSe_2 are shown in the experimental diffractograms.

the XRD pattern and the corresponding high-resolution TEM images of the 1T' WSe_2 nanoflowers that were obtained through a reaction between $W(CO)_6$ and 1M TOP:Se in oleic acid (standard synthesis). Increasing the growth time from 3 to 15 hours resulted in the WSe_2 nanoflowers with thicker petals as evidenced by the intense (002) reflection at 13.9 º2θ in the corresponding XRD pattern (Figure 3.28.b). Interestingly, the absence of well-resolved (100) and (103) reflections, commonly found at ~32 and ~38 º2θ in the 2H phase WSe_2 samples, suggests the retention of the metastable 1T' phase even after 15 hours in hot solution.

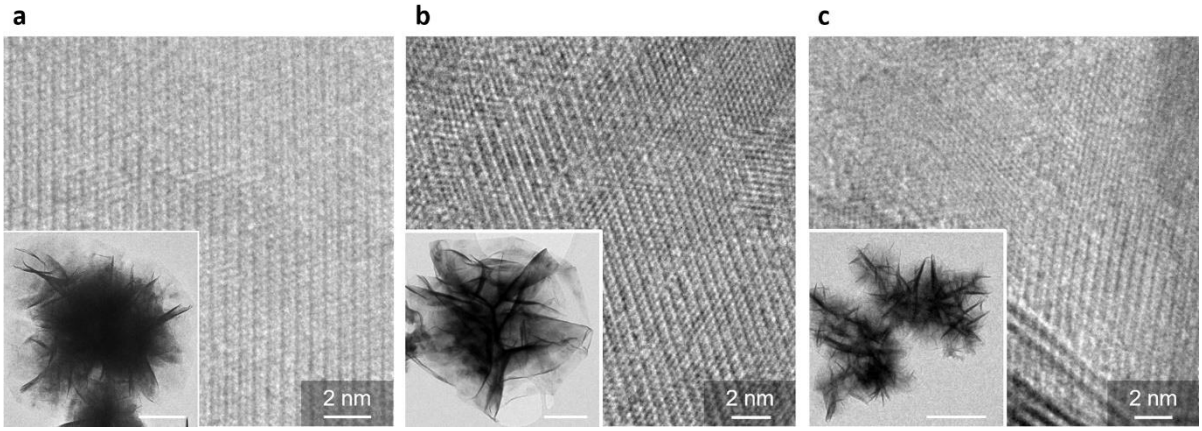


Figure 3.29. Effect of activity of tungsten complex on the crystal phase and morphology of the colloidal WSe_2 nanostructures. High resolution TEM images of the WSe_2 nanostructures grown through a reaction between **a** WCl_6 and TOP:Se in OlAc, **b** $W(CO)_6$ and TOP:Se in OlAc in presence of hexamethyldisilazane (HMDS), **c** $W(CO)_6$ and TOP:Se in OlAc in presence of tetradecylphosphonic acid (TDPA). Insets show TEM images of the individual WSe_2 nanostructures; scale bars 100 nm.

Another growth parameter under study was the activity of the selenium precursor. Taking into account the Se-Se and P-Se bond dissociation energies, selenium powder is expected to be a less reactive precursor compared to TOP:Se [[348]], however quite the opposite behaviour was observed experimentally. This can be explained by the *in situ* generation of H_2Se that is more reactive than TOP:Se. The presence of the *in situ* formed H_2Se was deduced based on the amorphous selenium residues found on the glassware walls as discussed in Section 2.2.2. The WSe_2 nanostructures grown from $W(CO)_6$ and Se powder display the morphology of branched nanospheres composed of densely packed two-dimensional nanosheets, while the individual petals reveal the 1T' crystal structure of the grown material (Figure 3.28.c). The increased thickness of the WSe_2 petals is evidenced by the (002) peak becoming more pronounced in the corresponding diffractogram (Figure 3.28.c).

The reactivity of tungsten precursor was modified by replacing $W(CO)_6$ with WCl_6 (Figure 3.29.a) or more finely tuned by partially complexing tungsten carbonyl complex with two additives, namely hexamethyldisilazane (HMDS) and tetradecylphosphonic acid (TDPA), as shown in Figure 3.29.b,c, respectively. In contrast to the clear changes in morphology observed in the colloidal $MoSe_2$ nanostructures, when $Mo(CO)_6$ was replaced by $MoCl_5$ (Section 3.1.2), the WSe_2 nanostructures grown from WCl_6 precursor exhibit well-defined morphology of nanoflowers similar to those produced via a standard $W(CO)_6$-TOP:Se reaction; moreover, no change in the crystal structure was observed (Figure 3.29.a). Further, forming tungsten complex in oleic acid in the presence of either HMDS or TDPA is expected to lead to partial substitution of the carbonyl/oleate groups thus modulating the activity of the tungsten

complex. Compared to carboxylic acid, HMDS is a weaker binding ligand [156], while TDPA is a stronger binding ligand [258] and so complexing tungsten with HMDS(TDPA) is expected to increase(decrease) its reactivity. In the recent work on the 1T/2H WS_2 nanostructures [156], the higher activity of tungsten precursor caused the predominate formation of the 2H phase of WS_2, although we have not observed similar effect on the crystal structure of the grown WSe_2 material. The WSe_2 samples synthesised in the presence of either HMDS or TDPA display the 1T' crystal structure in their petals (Figure 3.29.b,c). The reactivity of transition metal precursor has, however, led to noticeable changes in the lateral size of WSe_2 nanostructures with larger nanoflowers, reaching 800 nm in diameter, grown in the presence of HMDS, while smaller (~100 nm in diameter) highly branched nanoflowers were formed in the presence of strongly binding TDPA.

Similarly to $MoSe_2$, the WSe_2 nanostructures grown from the respective metal chloride dissolved in oleylamine instead of oleic acid appear as agglomerated nanosheets with much smaller lateral dimensions of the individual WSe_2 petals (10-20 nm) compared to the standard synthesis (Figure 3.28.d). HR TEM imaging was significantly complicated by high degree of polycrystallinity in these structures, however, the XRD data provided along with TEM results in Figure 3.28.d suggest that the material has acquired the 1T' phase. It should be noted that, unlike the case of colloidal $MoTe_2$ nanostructures (Section 3.1.3), no nucleation of either WSe_2 or $MoSe_2$ was observed when the transition metal complexes were formed by dissolving the respective metal carbonyl in minimum amount of oleic acid and the solvent was changed to non-coordinating octadecene.

To study the effect of precursor concentration on the growth of colloidal WSe_2 nanostructures through the reaction between $W(CO)_6$ and TOP:Se in hot oleic acid, we have run a series of express tests varying the concentration in the range from 10[C] to 0.01[C], where [C] is a standard precursor concentration (7.5 mmol/L of W, 15 mmol/L of Se) as discussed in Section 2.2.3. In these experiments, all other growth parameters, such as growth temperature (300 ºC), growth time (3 hours), and cooling rate (rapid quenching), were kept fixed. To successfully work with low quantities of the precursors, the injection step was eliminated. Instead, the nucleation reaction in supersaturated solution was initiated by rapid heating to the growth temperature. To achieve this, tungsten complex in oleic acid was formed at 200 ºC under vacuum and then cooled down to room temperature. Once it reached room temperature, the tungsten complex was mixed with 1M TOP:Se and then diluted with degassed oleic acid to the required concentration. The total volume of the reaction solution was kept fixed and as low

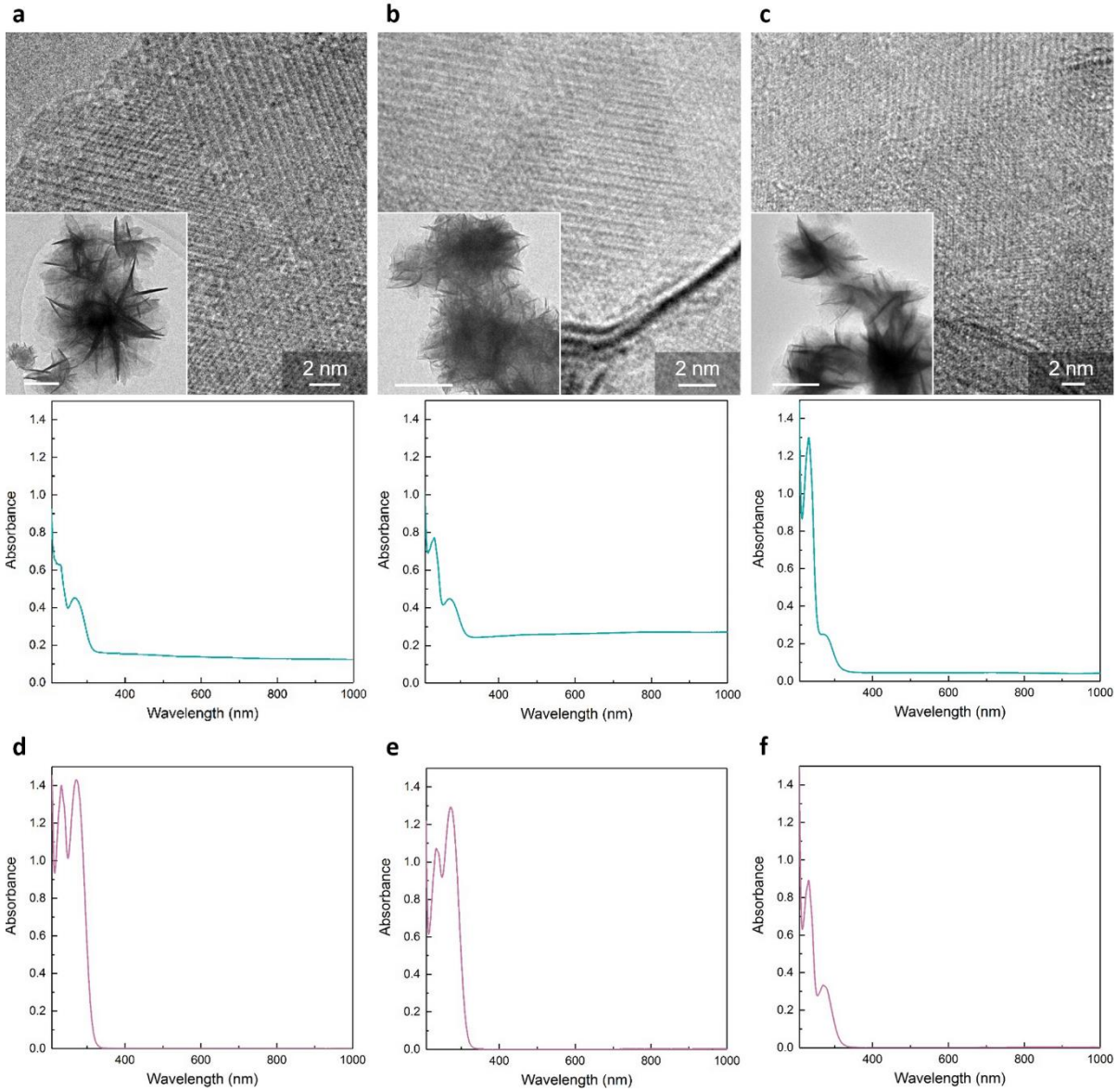


Figure 3.30. Effect of the precursor concentration on the crystal phase of WSe_2 nanostructures. TEM images and optical absorption spectra of the WSe_2 nanostructures synthesised at various precursor concentrations: **a** 10[C], **b** 1[C], **c** 0.1[C], **d** 0.05[C], **e** 0.03[C], and **f** 0.01[C]. Scale bars 100 nm.

as possible (4 mL in total) throughout this series of experiments in order to exclude possible effects of uneven heating. Importantly, $W(CO)_6$ and TOP:Se do not react at room temperature even in a course of a week, therefore nucleation of the WSe_2 nanostructures was initiated only by heating the reaction mixture. The flask containing the mixture of precursors was placed in a preheated to 300 ^oC heating mantle and kept at this temperature for three hours. The growth was quenched by rapidly cooling the reaction flask to room temperature and the nanoparticles were precipitated by 1:1 ethanol/acetone mixture following the standard procedure described in Section 2.2.3. The collected precipitate was washed only once and was dispersed in ethanol straight after in order to keep the lightest fraction of the WSe_2 nanosheets/nanoflowers. In cases

when the final precipitate was not obtained, the supernatant was analysed instead. Importantly, initiating nucleation of the WSe_2 nanoflowers via rapid heating of the metal-chalcogen mixture instead of injection at high temperature did not affect the phase and morphology of the final product as shown in Figure 3.30.b.

The final products obtained in the range of precursor concentrations 0.01-10[C] were analysed with optical absorption spectroscopy and the corresponding spectra are presented in Figure 3.30.a-f. No material was precipitated from the growths performed at 0.01-0.05[C], while optical spectra of the final reaction mixtures (supernatants) display only strong absorption bands of oleic acid at ~240-280 nm (Figure 3.30.d-f). The absence of either the excitonic transitions or the characteristic light scattering suggests that nucleation of either the 2H or 1T' phases of WSe_2 did not occur at these low precursor concentrations. It should be noted that due to the metallic nature of the 1T' phase, the nucleated material can only be detected when the dimensions of the nanoflowers are big enough to cause scattering of light in the visible range. The growth of WSe_2 nanostructures was observed in the range of concentrations from 0.1[C] to 10[C]. According to the TEM data shown in Figure 3.30.a-c, the material produced under these growth conditions exhibits the same flower-like morphology, while the crystal phase is the distorted octahedral 1T'. Featureless scattering in the visible range further confirms the metallic nature of the final products.

Although we have not been able to adjust the synthesis parameters in a way to achieve the thermodynamically-controlled growth mode and so to unambiguously prove the kinetically-driven growth mechanism of the metastable 1T' phase of WSe_2, we performed additional experiments to rule out possible stabilisation of the 1T' phase by the precursor residues. Specifically, we performed ζ-potential measurements to determine the net surface charge of the WSe_2 nanoparticles. Since the synthesised WSe_2 nanoflowers were found to be insoluble in water, suspensions in ethanol were studied instead. We have prepared ethanol suspensions of the as produced 1T' and annealed 2H WSe_2 nanoflowers, while suspensions of the liquid-phase exfoliated (via sonication, no added surfactants) 2H WSe_2 nanosheets in ethanol and in DI water were used as control. A fresh suspension of the synthesised 1T' WSe_2 nanoflowers displays negative ζ-potential of -10.2 mV (average of 3 measurements) indicative of the negative surface charge. This charge can be attributed to the negatively-charged selenium vacancies present in the basal plane of the two-dimensional nanosheets [349] rather than to the charged residues trapped between the layers, since the exfoliated 2H WSe_2 nanosheets exhibit similar negative ζ-potentials (-19.7 mV in ethanol and -40.5 mV in DI water) as shown in

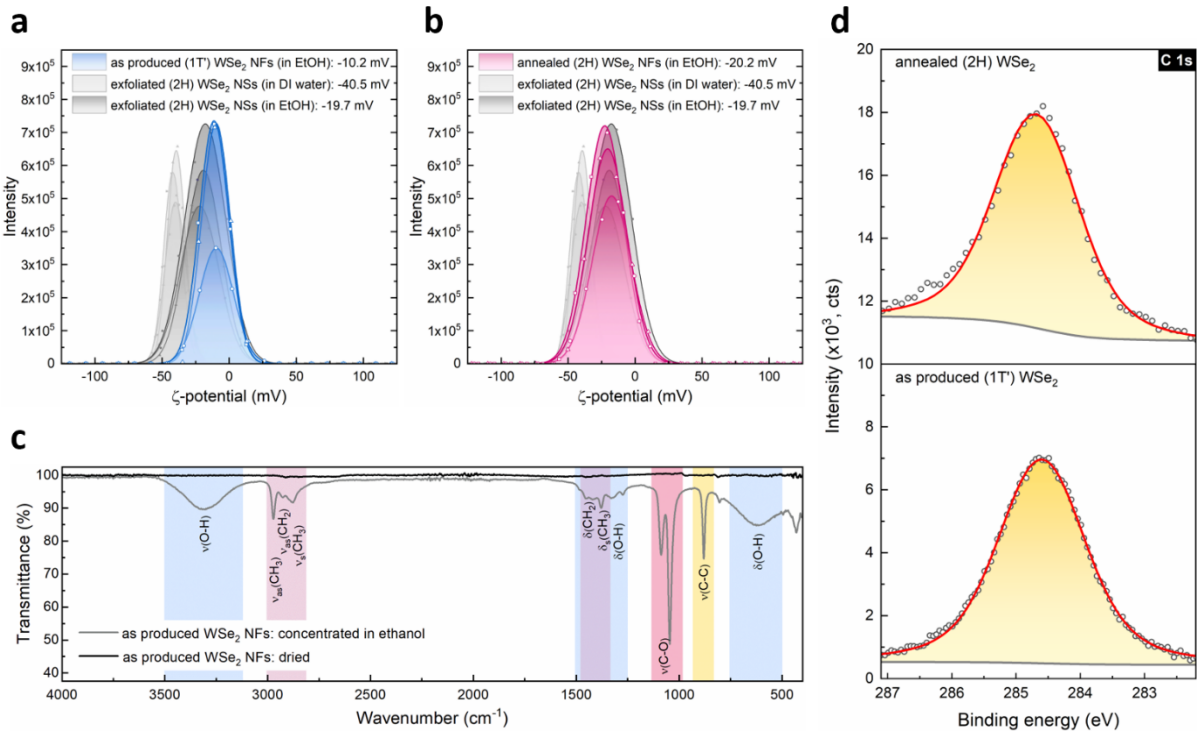


Figure 3.31. Evidence of absence of the intercalated charged species. **a, b** ζ-potential distributions for the suspensions of the 1T' and 2H WSe_2 nanoflowers, respectively. **c** ATR-FTIR spectra of a concentrated suspension and of dried powder of 1T' WSe_2 nanoflowers. **d** High-resolution XPS C 1*s* spectra of the as produced 1T' (bottom panel) and the annealed 2H (WSe_2 nanoflowers.

Figure 3.31.a. Recent reports on the ammonium stabilised 1T phases of WS_2 and MoS_2 have shown that the intercalated species can be removed via mild annealing that eventually leads to the transition into the thermodynamically stable 2H phase [160,163]. The annealed 2H WSe_2 nanoflowers exhibit slightly lower ζ-potential (-20.2 mV), that can be caused by a loss of selenium during the thermal annealing performed in vacuum (Figure 3.31.b). The FTIR study of the concentrated suspensions of the 1T' WSe_2 nanoflowers and their dried powder counterpart does not provide any further insights about the surface functionalisation or about the intercalated species possibly present in the synthesised material. The FTIR spectrum of the concentrated suspension shows the characteristic vibrations of ethanol molecules only, while only very weak vibrations at ~1500 cm^{-1} are present in the FTIR spectrum of the dried 1T' WSe_2 powder (Figure 3.31.c), these can be tentatively assigned to the WSe_2 analogously to [350]. Also, in contrast to the covalently functionalised TMD flakes [351], high-resolution XPS spectra of the C 1*s* electrons of both the as produced 1T' and the annealed 2H WSe_2 nanoflowers contain a single component only ascribed to the C-C bonds of the adventitious carbon (Figure 3.31.d) that can imply absence of other carbon containing species, for example CO residues.

3.4. Conclusions

Developing a high-throughput solution-phase synthesis of nanostructured layered metal chalcogenides is crucial for their successful implementation in catalysis and novel electrochemical energy storage devices. Here, we have demonstrated colloidal synthesis of binary metal chalcogenides ($MoSe_2$, $MoTe_2$, Bi_2Te_3, and WSe_2) from molecular precursors. The obtained material displays a well-developed morphology of nanoflowers composed of multiple atomically-thin petals. Such morphology is particularly beneficial for catalysis as it provides numerous accessible catalytically-active edge sites.

The absence of dangling bonds in the basal planes of transition metal dichalcogenides makes them especially difficult to synthesise in the form of free-standing two-dimensional nanosheets since the direct passivation of the basal planes, and therefore suppression of the vertical growth mode, are not feasible. We found that using a weakly coordinating solvent (oleic acid) instead of a strongly-binding one (oleylamine) helps to facilitate the lateral extension of TMD nanostructures as was demonstrated for the WSe_2 and $MoSe_2$ nanoflowers. Moreover, in the system of highly reactive bismuth and tellurium precursors, removing the coordinating solvent (free oleic acid) from the reaction mixture entirely allowed us to exclusively produce two-dimensional Bi_2Te_3 nanosheets.

The designed synthesis approach allows for the formation of metastable polymorphs, such as the 1T' phase of WSe_2 and $MoTe_2$, directly in solution phase. We suggest that under the synthesis conditions described in this work the nanocrystal growth occurs in the kinetically-controlled regime, i.e. limited by the kinetics of the monomer deposition/desorption on the growing crystal surface. Achieving the metastable polymorphs (1T' WSe_2) by varying the reactivity of molecular precursors offers an extra tool to directly control the electronic properties of the solution-processable material. Furthermore, we demonstrated that switching between the kinetically- and thermodynamically-controlled reaction regimes, which was achieved in the Bi_2Te_3 system by varying the growth temperature, allowed us to controllably modify the morphology and lateral termination of colloidal Bi_2Te_3 nanosheets.

Chapter 4:
Doped WSe_2 and ternary $W_xMo_{1-x}Se_2$ nanostructures

In this Chapter we demonstrate how the solution-phase synthesis approach developed in Chapter 3 can be further modified in order to achieve the compositional variation of the growing material. In general, modification of the material composition through doping or alloying is highly appealing for designing materials with specific magnetic properties or to enable formation of p-n junctions. Moreover, the electronic structure modulation achieved through compositional variation has been successfully employed for enhancement of the catalytic activity of a given material either via improving the electronic conductivity or through local strain induced rearrangement of the crystal lattice. Here, we attempt colloidal synthesis of doped (Cu, Fe) WSe_2 nanoflowers and ternary $W_xMo_{1-x}Se_2$ branched nanosheets.

4.1. Doped WSe_2 nanoflowers

The intentional doping of TMDs falls into either of three categories – substitutional doping, in which case the dopant displaces a host atom in the crystal lattice (in either metal or chalcogen sublattice) and occupies its place; interstitial doping, when the atomic size of the dopant is much smaller than that of the host atom and so the dopant occupies normally unoccupied voids in the crystal structure; and surface doping, when the adatoms are held by the unsaturated bonds around the surface vacancy sites [352]. Dopants can be introduced into the crystal lattice of the material either during the growth process, as substitutions and interstitial species, or during the post-growth treatment, mostly as surface adatoms bound to the vacancy sites.

Doping of the group VIB TMDs with the group VB (Nb) and group VIIB (Mn, Re) elements has been attempted to achieve the p-type and n-type of conductivity, respectively, in MoS_2 and WS_2. For example, Nb doping of WS_2 monolayers has been demonstrated during the CVD process performed in the presence of Nb salt. Despite of its high content (over 6 at.%), in the WS_2 lattice, Nb is present in a form of isolated atomic inclusions and small clusters [353]. Similarly, the incorporation of well-dispersed Mn (2 at.%) [354] and individual Re (0.3-0.6 at.%) [353,355] atoms has been reported in the CVD grown MoS_2 single layers. The electronic properties of doped material, however, are not solely defined by the electron count on the *d*-orbitals of the dopant; for instance, although doping of the WSe_2 monolayers with Cr^{3+} formally should give rise to p-type conductivity, it has been shown that double Se vacancies tend to

cluster around substitutional Cr sites leading to net n-type doping of WSe_2 [356]. Moreover, a transition to the metallic 1T WSe_2 phase has been observed in highly doped samples, similar to the electron doped group VIB TMDs [356].

The dopants, whose size or coordination manner significantly differ from that of the host phase, tend to form surface bound single atom sites or small clusters. Such type of doping can be beneficial for catalytic applications since the dopants can potentially provide the additional active sites. An improved catalytic activity has been demonstrated for chemically exfoliated MoS_2 nanosheets doped with Co [357] and Ni [358] via the hydrothermal post-exfoliation treatment. Interestingly, doping of the MoS_2 nanosheets, synthesised by solvothermal approach, with Pd initially led to the anchoring of individual Pd atoms at the basal plane and was followed by their building into the MoS_2 lattice via the redox reaction with Mo^{3+}, occurring at the structural defect sites [106].

Both Fe and Cu are suitable for tailoring the magnetic properties of the group VIB TMDs; moreover, Fe was identified as a potentially perspective dopant to enable the catalytic CO reduction [359]. Further, the catalytically inert basal planes of the 2H MoS_2 [89] can be activated by substitutional doping as demonstrated by the first principle calculations. In particular, Fe is expected to replace molybdenum in the transition metal sublattice, retaining the trigonal-prismatic coordination to six sulphur atoms, and to increase the free energy of proton adsorption at the neighbouring S site, while Cu, on the other hand, is predicted to shift from the trigonal coordination, binding to four sulphur atoms instead and lowering the adsorption free energy [111]. It should be pointed out, however, that no information on the oxidation states of the considered dopants is provided in the cited work. For the metallic 1T polymorph, doping with Mn, Cr, Cu, Ni, or Fe was predicted to facilitate the hydrogen adsorption reaction at the basal planes of MoS_2, thus leading to an improvement in the catalytic activity for the HER [92].

In this work, only a preliminary study of the feasibility to dope the colloidal WSe_2 nanoflowers has been carried out with the main focus being put on achieving the single-phased system. The oxidation states as well as local coordination of dopants in the host lattice or around the defect sites in the colloidal WSe_2 nanosheets have not been investigated. The dopants were introduced by modifying the transition metal precursor before the reaction with chalcogen as described in Section 2.2.3. Three salts – CuCl, $Cu(CH_3COO)_2$, and $FeCl_3$ – were used as a source of the doping transition metal. The other synthesis conditions, including concentrations of the tungsten and selenium precursors, type of solvent, and temperature regimes of the metal complex formation and the material growth, were kept unchanged.

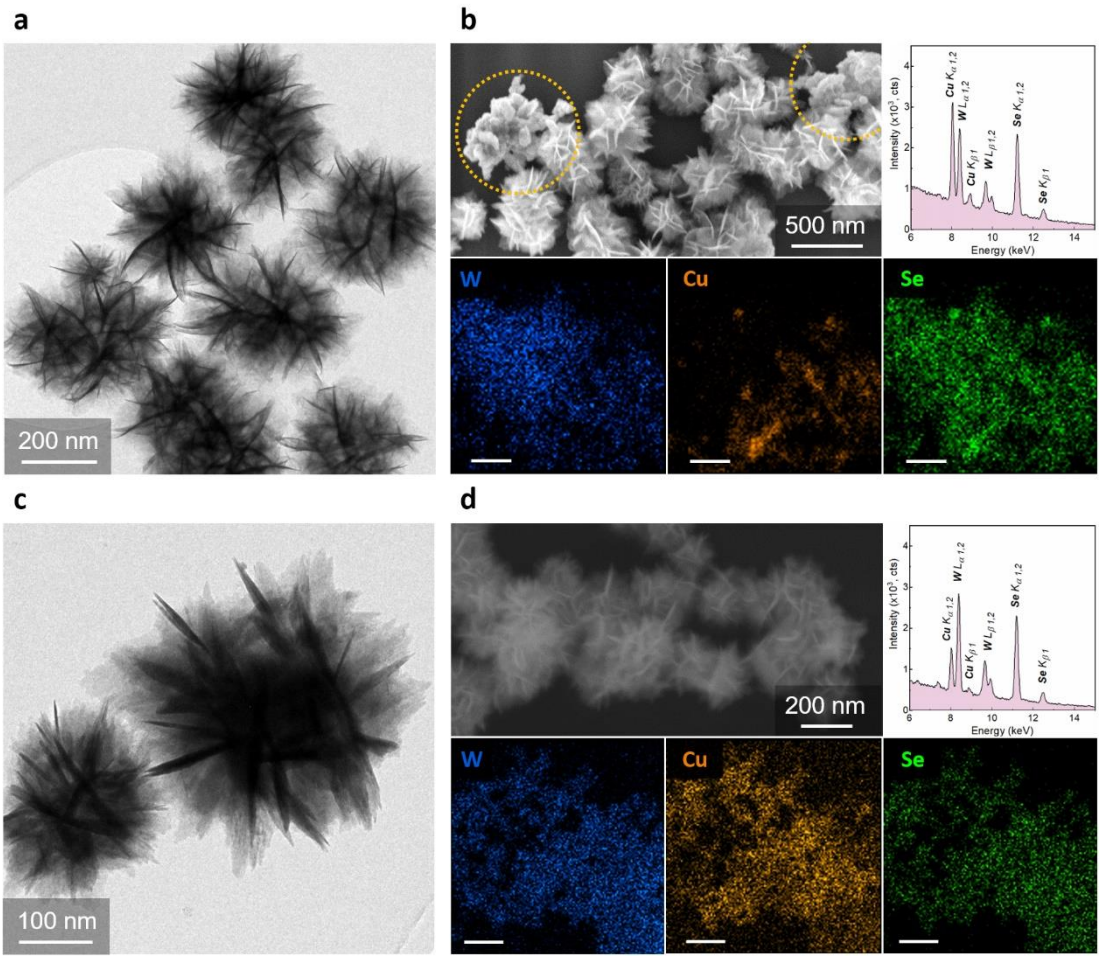


Figure 4.1. Cu-doped colloidal WSe_2 nanoflowers. **a, c** TEM images and **b, d** overview SEM images, corresponding sum EDX spectra and elemental maps (W L, Cu K, and Se K lines; scale bars 2 μm) of the Cu-doped WSe_2 nanoflowers synthesised in presence of Cu^{I} (panels **a, b**) and Cu^{II} (panels **c, d**) salts, respectively.

The results of TEM and SEM analysis of the Cu-doped WSe_2 nanoflowers synthesised in the presence of CuCl and $Cu(CH_3COO)_2$ are summarised in panels a, b and c, d in Figure 4.1, respectively. TEM imaging reveals that the material synthesised in the presence of Cu dopant retains the flower-like morphology with the average diameter of individual flowers close to 300 nm. In order to confirm the presence of copper in the synthesised doped WSe_2, SEM EDS analysis was performed on the ensembles of nanoflowers drop-cast onto Si/SiO_2 substrates. SEM EDS analysis was performed instead of TEM EDS in order to exclude the false-positive results attributed to Cu signal, arising from the carbon-coated copper grids used in this work. The representative SEM images and the corresponding EDS spectra are presented in panels b and d in Figure 4.1. Both elemental spectra display strong signal of Cu in the final product regardless of the copper salt used as a source of dopant. When $Cu^{I}Cl$ is used as a starting copper precursor, SEM imaging reveals the formation of a secondary phase as

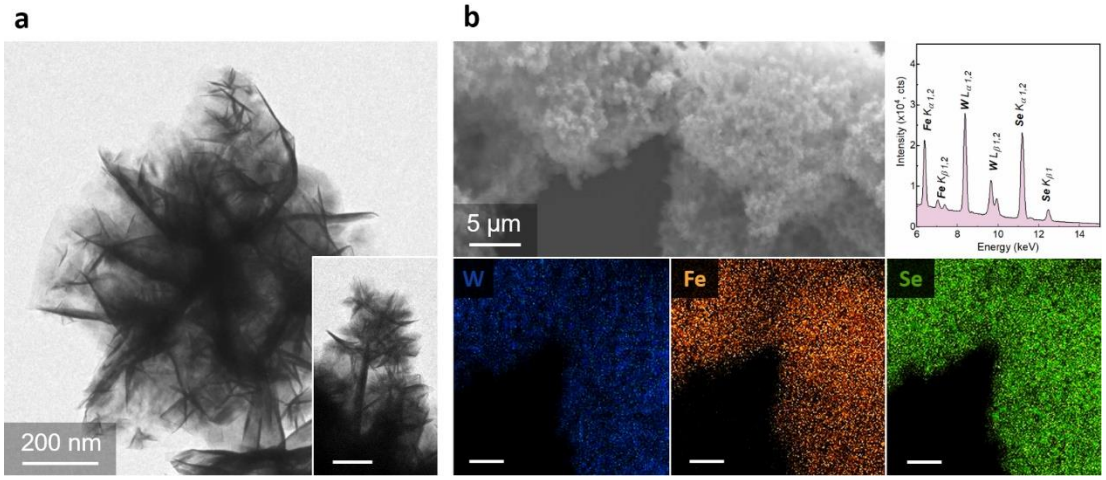


Figure 4.2. Fe-doped colloidal WSe_2 nanoflowers. **a** TEM images and **b** overview SEM image, corresponding sum EDX spectrum and elemental maps (W L, Cu K, and Se K lines; scale bar 5 µm) of the Fe-doped WSe_2 nanoflowers. Inset in panel **a** is a zoomed in TEM image illustrating high degree of branching in the Fe-doped WSe_2 nanoflowers (scale bar 100 nm).

evidenced by the irregular shaped micron-sized crystallites highlighted with dashed orange circles in SEM image in panel b of Figure 4.1. On the other hand, $Cu^{II}(CH_3COO)_2$ has seemingly led to the formation of uniformly shaped Cu-doped WSe_2 nanoflowers only (panel d in Figure 4.1). In the latter case, elemental mapping of the Cu-doped WSe_2 nanostructures has further proved the homogeneity of their composition, displaying uniform distribution of all three elements (W, Cu, and Se) across the nanoflowers (panel d in Figure 4.1). Whereas in the case of $Cu^{I}Cl$ additive, distinct localisation of the $CuSe_x$ phase is clearly evident in the elemental maps shown in panel b in Figure 4.1. In Cu^{II}-doped WSe_2 samples, the average [W]:[Cu]:[Se] molar ratio estimated from the results of SEM EDS is 1:0.52:2.93; copper content, however, significantly exceeds the expected one (nominal W:Cu atomic ratio in all cases was kept not higher than 1:0.2). This can be due to the formation of ternary Cu-W-Se phases as a side-product as evidenced by the XRD data discussed below.

In a similar way, Fe doping, achieved directly during the synthesis of the WSe_2 nanostructures in the presence of $Fe^{III}Cl_3$, does not substantially affect the branched morphology of the pristine WSe_2 nanoflowers (Figure 4.2). The average diameter of the Fe-doped WSe_2 nanoflowers reaches 700 nm. Moreover, the presence of Fe ions in the crystal lattice of the growing WSe_2 seems to promote nucleation of the secondary petals (Figure 4.2, inset) in contrast to the morphology of pristine WSe_2 nanoflowers made of multiple single-crystalline petals stemming from the central core. It should also be noted that no other morphologies, different from that of branched nanoflowers, were observed in the SEM images of the ensembles of Fe-doped WSe_2 nanostructures. Shown in Figure 4.2.b the EDS spectrum

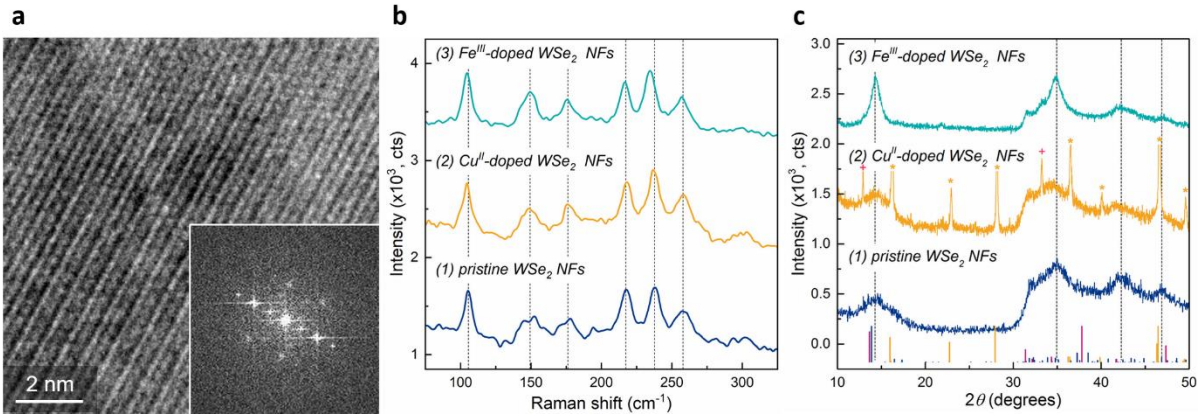


Figure 4.3. Crystal phase of the doped WSe_2 nanoflowers. **a** High-resolution TEM image of a Fe^{III}-doped WSe_2 nanoflower revealing the 1T' phase of the doped material. **b** Raman spectra of the pristine (1), Cu^{II}- (2), and Fe^{III}-doped (3) WSe_2 nanoflowers confirming the retention of the 1T' crystal phase. **c** XRD patterns of the pristine (1), Cu^{II}- (2), and Fe^{III}-doped (3) WSe_2 nanoflowers. The secondary Cu_2WSe_4 phase present in the Cu^{II}-doped material is highlighted with asterisks. The simulated reference patterns of the 1T' (navy) and 2H (purple) WSe_2 and Cu_2WSe_4 (orange) are provided under the experimental diffractograms.

and the corresponding elemental (W, Fe, and Se) maps acquired form the doped nanoflower sample confirm the presence and uniform distribution of iron in the colloidal WSe_2 branched nanostructures. According to the results of SEM EDS analysis, the averaged [W]:[Fe]:[Se] molar ratio is 1:0.44:3.15, indicating significantly higher content of iron in the obtained doped nanostructures than could be expected from the loaded precursor amounts (nominal W:Fe molar ratio is 1:0.2).

The doped material retains the metastable 1T' crystal structure of pristine WSe_2 nanoflowers synthesised via colloidal approach. A representative TEM image of a single-crystalline area of an Fe-doped WSe_2 nanoflower shown in Figure 4.3.a displays contrasting stripes characteristic to the 1T' phase of the group VIB TMDs. Estimated from the results of HR TEM imaging, the approximate cell constants a = 6.31 Å and b = 3.76 Å differ from that of the pristine material (5.76 Å and 3.3 Å, respectively). The observed change in cell constants of the doped material can be attributed to the insertion of Fe ions displacing tungsten in the crystal lattice. This is supported by the results of Raman spectroscopy. Raman spectra of doped WSe_2 nanoflowers were acquired from at least 10 random spots across each of the deposited samples and the representative spectra are presented in Figure 4.3.b. Both Cu^{II}- and Fe^{III}-doped WSe_2 nanoflowers display similar sets of six Raman modes at the frequencies close to that of the pristine 1T' WSe_2, thus confirming that the metastable crystal phase is preserved in the doped material.

The findings on the crystal phase of doped nanostructures derived from the local probe analysis (TEM, Raman spectroscopy) were complemented by X-ray diffraction employed to study the phase purity at macroscopic scale. The diffraction patterns of the Cu^{II}- and Fe^{III}-doped WSe_2 nanoflowers are shown in Figure 4.3.c. The Fe^{III}-doped WSe_2 nanoflowers are acquired in the 1T' phase, although a small fraction of the 2H phase is evidenced by a shoulder peak at 31.5° 2θ, corresponding to the (100) planes of the 2H WSe_2 and normally observed in the pristine 1T' WSe_2 nanoflowers. Higher intensity of the (002) peak at 14.3° 2θ and of the $(\bar{1}12)$, and (112) reflections, appearing as a broad unresolved peak at ~35° 2θ, suggests the increased thickness as well as lateral size of the Fe^{III}-doped WSe_2 nanoflowers as compared to pristine WSe_2. This agrees well with the TEM data. However, considerable broadening of the diffraction peaks impeded the direct confirmation of the lattice expansion caused by the inclusion of Fe cations. On the other hand, the XRD pattern of the Cu^{II}-doped WSe_2 nanoflowers clearly demonstrates at least two distinct phases present in the sample, one of which is the 1T' WSe_2. The second set of narrow diffraction peaks, marked with asterisks, was assigned to the non-layered Cu_2WSe_4 phase. This ternary phase has been obtained only recently via a hydrothermal reaction [360]. The experimental diffraction peaks match well the simulated diffraction pattern of the primitive Cu_2WSe_4 lattice (space group $P\bar{4}2m$) shown in Figure 4.3.c. The lattice parameters of the P-Cu_2WSe_4 were taken from [360,361].

Overall, Cu- and Fe-doped WSe_2 branched nanostructures were obtained via solution-phase reaction in the presence of $Cu^{II}(CH_3COO)_2$ and $Fe^{III}Cl_3$. Using $Cu^{I}Cl$ as a source of dopant led to the formation of a considerable fraction of highly-crystalline Cu-Se phase as a side product. The Cu- and Fe-doped WSe_2 nanostructures exhibit the uniform flower-like morphology similar to that of the pristine WSe_2 and are attained in the 1T' phase. The elemental analysis performed on the Cu- and Fe-doped WSe_2 nanoflowers has demonstrated the dopant content approaching nearly 33 at.% (W:Cu is 1:0.52, W:Fe is 1:0.44), while the dopant fraction in the reaction mixture did not exceed 16 at.% in all cases. This may suggest that the ternary phases, such as Cu_2WSe_4 observed as a side-product, may be preferentially formed during a solution-phase reaction. This might potentially limit the range of compositions achievable in the solution-phase synthesis of doped group VIB TMD nanostructures.

4.2. Ternary $W_xMo_{1-x}Se_2$ nanoflowers

Achieving tunable compositions via the isovalent alloying is gaining attention since this approach holds a great promise to effectively modulate the electronic properties of TMD materials to further expand the range of their applications. The term isovalent alloying encompasses both mixing chalcogen atoms in the anion sublattice as well as mixing the same group transition metals in the cation sublattice. Recent calculations have demonstrated that in the MoS_2-$MoSe_2$-$MoTe_2$ system, the anion mixing enthalpies (at 0 K) are negative in the entire range of the S-Se compositions and only slightly negative in the Se-Te and S-Te. Taking into consideration the entropic contribution, this renders the random anion-mixed alloys in the molybdenum dichalcogenides system stable over phase segregation at ambient temperature [362]. Similarly, formation of random alloys, displaying no tendency to preferential segregation or local ordering, is expected for the cation-mixed $W_xMo_{1-x}S_2$ due to chemical similarity of W and Mo cations. Moreover, isovalent cation and anion mixing in the $W_xMo_{1-x}S_{2y}Se_{2(1-y)}$ system also exhibits consistently negative mixing enthalpies implying formation of random alloys to be favourable [363].

Synthesis of the atomically-thin alloyed TMD flakes has been majorly achieved by mechanical exfoliation of the bulk alloys produced via physical (PVD) or chemical vapour transport (CVT) approaches with a few recent examples of the direct growth of the alloyed materials via the CVD or wet chemistry approaches. Thus, the formation of a random alloy in the CVT grown $W_xMo_{1-x}S_2$ crystals has been demonstrated in the whole range of compositions x = 0-1 [364]. Similarly, no evidence of a preferential segregation was observed in the 2H $Mo_xW_{1-x}Se_2$ and $WS_{2y}Se_{2(1-y)}$ alloys synthesised via the solution-phase approach [260]. Furthermore, formation of a hetero-phased random alloy has been reported in the CVD grown $W_xMo_{1-x}S_2$ monolayers. In this case, the produced material displayed a 1T/2H phase heterogeneity, while the detailed microscopic analysis of the areas in the vicinity of the 1T/2H borders has unambiguously proved the random distribution of both transition metals across the co-existing 1T and 2H phases [365]. Interestingly, the metastable 1T phase was only present in the alloyed monolayers, while the pristine WS_2 and MoS_2, grown under the same conditions, exhibited the 2H phase only. The maximum content of the 1T phase was achieved when the molar ratio [W]:[Mo] was approaching 1:1. Composition-dependant crystallisation of the metastable phase under the conditions when the individual components adopt the thermodynamically stable phase only was attributed to the lowest mixing enthalpy and the highest strain in the crystal lattice.

Alloying the group VIB transition metal disulphides and diselenides with tellurium opens up a way for varying the electronic properties of the alloys in a wider range since both ditellurides, $MoTe_2$ and WTe_2, can be attained in the semimetallic 1T' polymorph and so the composition-dependent 2H-to-1T' transition in the corresponding alloys can be exploited. Fully random alloys with the Se_2, Te_2, and Se-Te units uniformly distributed across the 2H $MoSe_{2(1-x)}Te_{2x}$ monolayers with x reaching 0.28 were recently reported by the CVD growth approach [366]. At higher tellurium content, the 2H-to-T_d phase transition has been observed in the CVT grown $WSe_{2(1-x)}Te_{2x}$ monolayers; notably, up to x = 0.5 the material retained the 2H phase, whereas at x = 0.5-0.6 the transition into the semimetallic T_d occurred with the stable T_d phase being produced at higher tellurium concentrations [367]. Interestingly, although the 2H phase telluride-based alloys exhibit isotropic distribution of both chalcogen anions across the alloyed material, anisotropic ordering has been shown in the 1T' type $WSe_{2x}Te_{2(1-x)}$ and $MoS_{2x}Te_{2(1-x)}$ alloys with either S_2 or Se_2 units, preferentially occupying the chalcogen sites next to the metal chains [368].

Due to the chemical similarity of tungsten and molybdenum cations, formation of a ternary alloy is expected in a wide range of compositions in W-Mo dichalcogenide systems. Moreover, in the mixed-cation diselenides, tungsten cations are predicted to occupy the lattice nodes next to molybdenum since such configuration is stabilised by energy gain due to the electron density redistribution from the weak Mo-Se to the strong W-Se bonds [363]. Such local W-Se-Mo ordering is likely to cause the formation of a random $W_xMo_{1-x}Se_2$ alloy stable over phase segregation. In this work, we synthesise the $W_xMo_{1-x}Se_2$ (x ~0.5) nanostructured alloy via the colloidal approach described in Section 2.2.3. Under these growth conditions, $MoSe_2$ is acquired in the thermodynamically stable 2H phase, while WSe_2 nanostructures are produced in the metastable 1T'phase. Therefore, the stabilisation of the 1T' phase can potentially be achieved in colloidal $W_xMo_{1-x}Se_2$ alloys.

The representative TEM images of the produced $W_xMo_{1-x}Se_2$ (x ~0.5) nanostructures are shown in Figure 4.4.a,b. The synthesised material predominantly exhibits the morphology of distinct nanoflowers, consisting of densely packed atomically-thin petals similar to the colloidal WSe_2 nanoflowers discussed in Section 3.3.1. According to the TEM results, the mean diameter of the $W_xMo_{1-x}Se_2$ (x ~0.5) nanoflowers varies in the range 100-150 nm approaching 200 nm in some cases (Figure 4.4.a). Although the diameter of the alloyed $W_xMo_{1-x}Se_2$ (x ~0.5) nanoflowers is noticeably smaller than that of the pristine WSe_2 nanoflowers, the overall shape

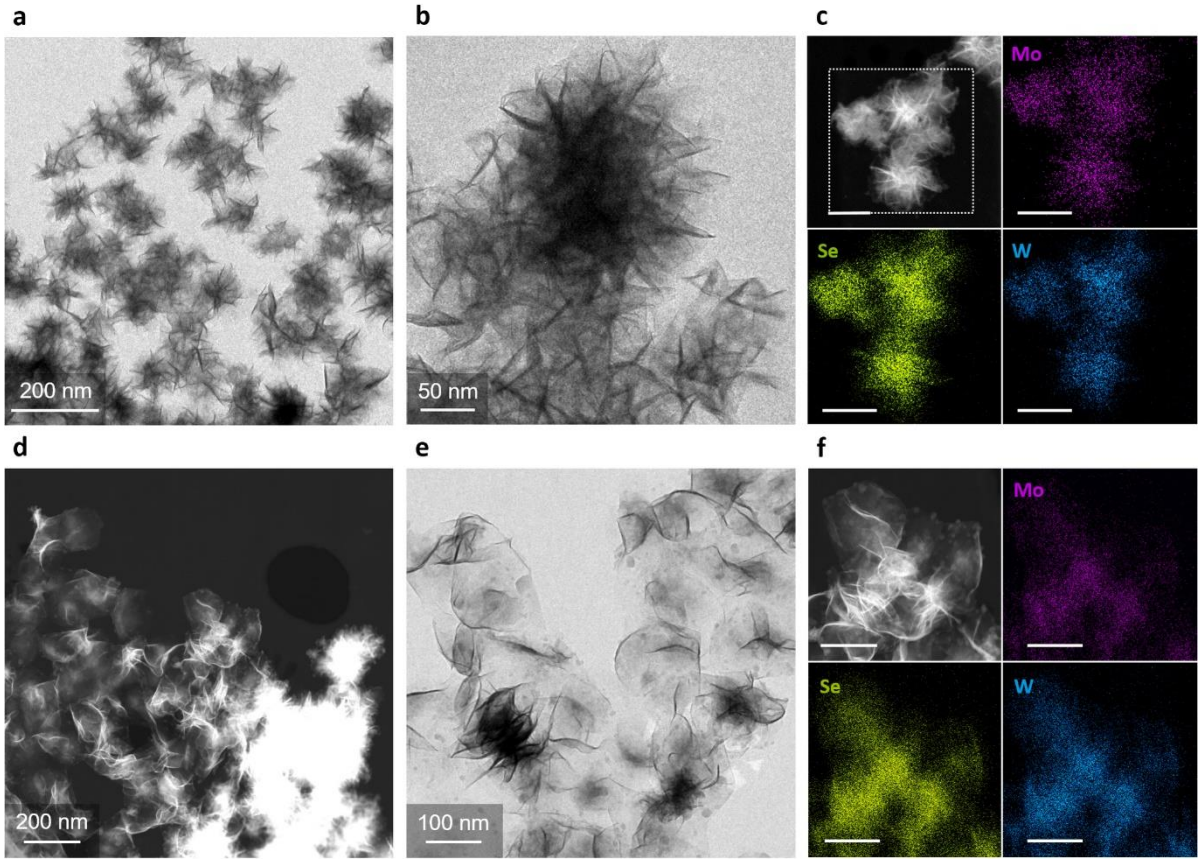


Figure 4.4. Characterisation of the alloyed $W_xMo_{1-x}Se_2$ (x ~0.5) nanoarchitectures. **a, b** TEM images of the ensemble and of an individual alloyed $W_xMo_{1-x}Se_2$ nanoflower; **c** ADF STEM image and the corresponding elemental maps (W, Mo, and Se) of the branched nanoflowers; scale bars 100 nm. **d, e** ADF STEM and a zoomed in TEM images of the alloyed $W_xMo_{1-x}Se_2$ nanosheets; **f** ADF STEM image and the corresponding elemental maps (W, Mo, and Se) of the alloyed $W_xMo_{1-x}Se_2$ nanosheets; scale bars 100 nm.

of the branched nanostructures (Figure 4.4.b) is nevertheless closer to that of the well-defined WSe_2 nanoflowers than of the $MoSe_2$ continuous "brushes" described in Section 3.1.1.

STEM EDS analysis supports the uniform distribution of all three elements across the colloidal $W_xMo_{1-x}Se_2$ (x ~0.5) nanoflowers as is evident from the corresponding elemental maps shown in panel c in Figure 4.4. Estimated from the intensities of the W M lines and Mo L lines, the [W]:[Mo] atomic ratio differs from the nominal 1:1 and reaches 1:1.4. The majority of individual $W_xMo_{1-x}Se_2$ (x ~0.5) nanoflowers also exhibit a slight selenium excess with the average [W]:[Mo]:[Se] atomic ratio being 1:1.2:4.2.

In addition to well-defined nanoflowers, a fraction of ultra-thin nanosheets was occasionally observed in the alloyed $W_xMo_{1-x}Se_2$ (x ~0.5) samples. Compared to the nanoflowers, these branched nanosheets are composed of fewer individual two-dimensional petals with the lateral size of a few hundreds of nm as shown in Figure 4.4.c,d. STEM EDS

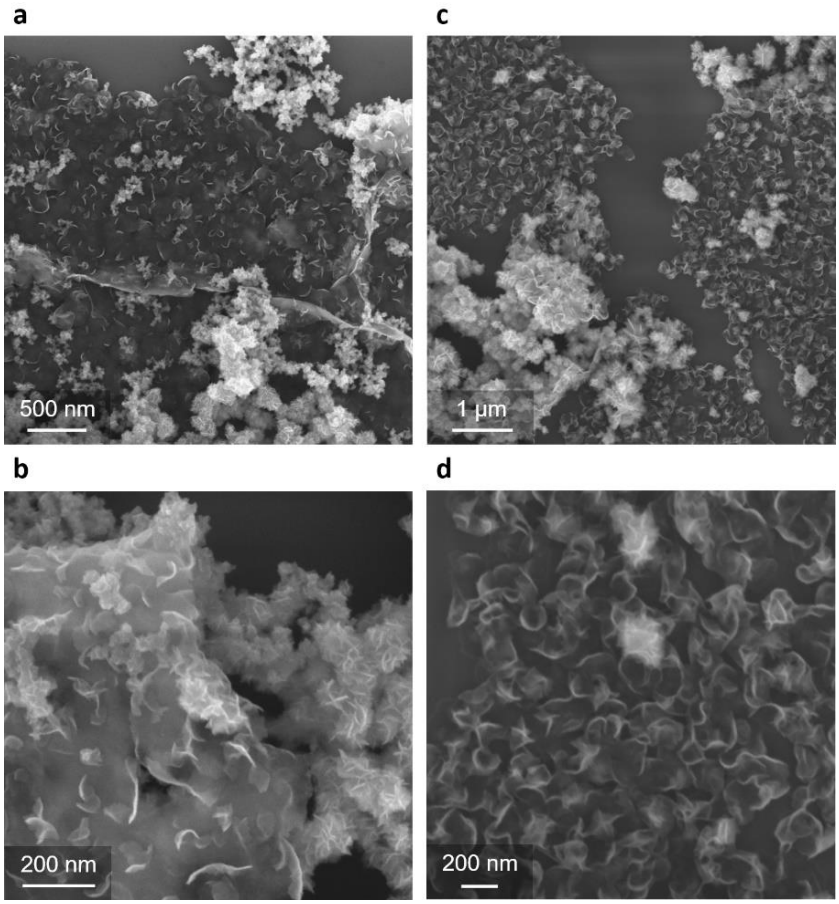


Figure 4.5. Comparison of the $MoSe_2$ and $W_xMo_{1-x}Se_2$ (x ~0.5) branched nanosheets. **a, b** SEM images of the colloidal $MoSe_2$ branched nanosheets. **c, d** SEM images of the $W_xMo_{1-x}Se_2$ (x ~0.5) branched nanosheets.

mapping performed on the branched nanosheets (Figure 4.4.e) has confirmed presence of all three elements homogeneously spread through the nanoarchitecture with no localisation of either tungsten- or molybdenum-rich areas being observed. Elemental composition of the $W_xMo_{1-x}Se_2$ (x ~0.5) branched nanosheets was determined via TEM EDS and on average the individual nanosheets exhibit a measurable tungsten overstoichiometry with the [W]:[Mo]:[Se] atomic ratio close to 1:0.52:3. Analogous branched nanosheets forming quasi-continuous structures over micron-sized areas were, albeit rarely, seen in some $MoSe_2$ samples (Figure 4.5.a,b) and were never observed in WSe_2 samples. The origin of these branched nanosheets found in the $MoSe_2$ (Figure 4.5.a,b) and $W_xMo_{1-x}Se_2$ (Figure 4.5.c,d) samples is not clear at the moment, however, their continuous nature can be indicative of a templated growth. Unsaturated fatty acids, and oleic acid in particular, are known to undergo a heat induced polymerisation at ~300 ^oC; moreover, the polymerisation process is reported to be considerably promoted in the presence of heavy metals [369]. Proving the proposed templated growth mechanism and elucidating the role of molybdenum carbonyl (since the branched nanosheets

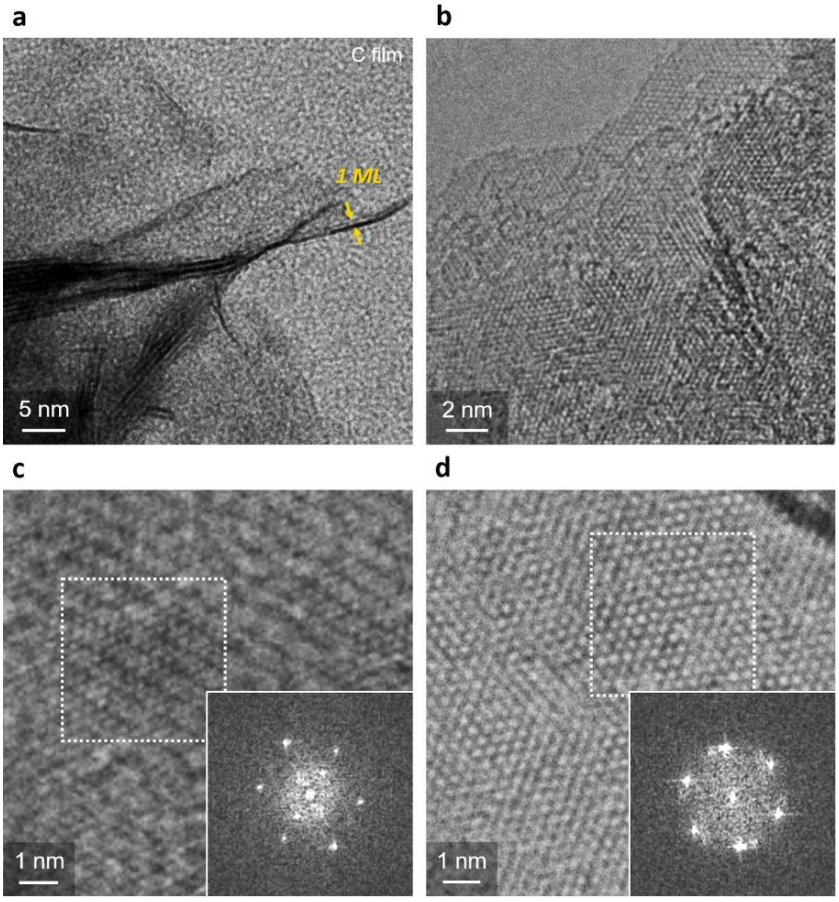


Figure 4.6. TEM characterisation of the $W_xMo_{1-x}Se_2$ (x ~0.5) nanoflowers. **a** Representative TEM image of an individual petal of a $W_xMo_{1-x}Se_2$ nanoflower illustrating its ultra-thin nature. **b** Overview HR TEM image of an individual petal demonstrating its polycrystalline nature. **c, d** HR TEM images and the corresponding FFT patterns of the 1T' and 2H areas of the $W_xMo_{1-x}Se_2$ alloy, respectively.

were seen in $MoSe_2$ and $W_xMo_{1-x}Se_2$ samples only) in formation of the templates themselves would, however, require a separate dedicated study and remain speculative in the context of present work.

The alloyed $W_xMo_{1-x}Se_2$ (x ~0.5) nanosheets exhibit the same ultra-thin nature as seen in the parent WSe_2 nanostructures, progressively thinning down to a single layer towards the rims (Figure 4.6.a). At the same time, unlike the single crystalline petals of parent WSe_2 nanoflowers, the nanosheets comprising the alloyed $W_xMo_{1-x}Se_2$ (x ~0.5) nanoflowers are made of a few nm^2-sized domains (Figure 4.6.b) much alike the produced $MoSe_2$ nanosheets (Section 3.1.1). High resolution TEM imaging reveals areas of the 1T' and 2H phases present in both the alloyed nanoflowers (Figure 4.6.c,d).

The Raman spectrum of the alloyed $W_xMo_{1-x}Se_2$ (x ~0.5) nanoflowers presented in Figure 4.7.a exhibits two well-resolved vibration modes at 240 and 283.9 cm^{-1}. Due to the similarity of the $MoSe_2$ and WSe_2 crystal lattice, Raman active modes in the alloyed material

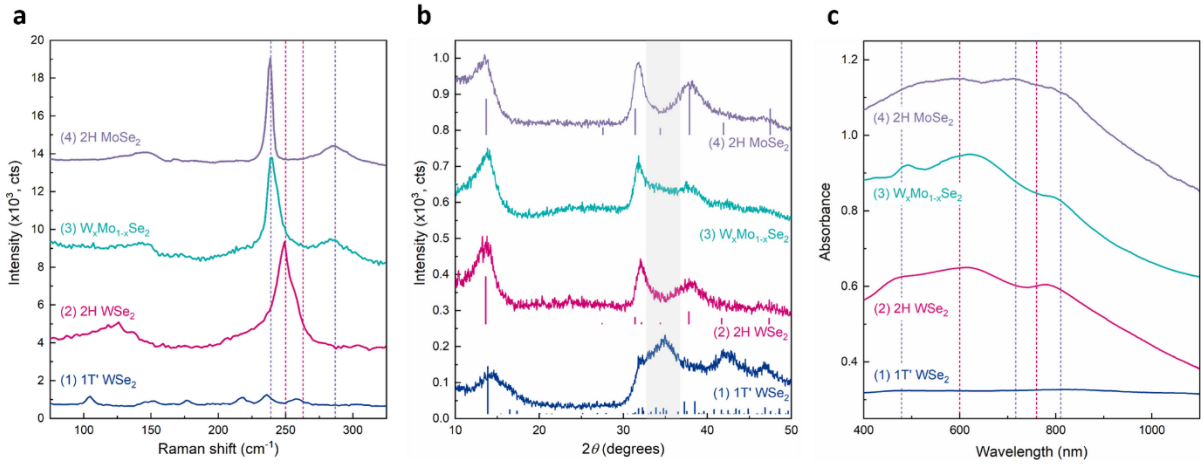


Figure 4.7. Structural characterisation of the alloyed $W_xMo_{1-x}Se_2$ (x ~0.5) nanoflowers. **a, b, c** Typical Raman spectra, XRD patterns, and optical absorption spectra of the 1T' (navy) and 2H (purple) WSe_2, 2H $MoSe_2$ (violet), and the alloyed $W_xMo_{1-x}Se_2$ (teal) nanoflowers. Vertical dashed lines in panel **a** correspond to the A'$_1$ and E' frequencies of the single layer $MoSe_2$ (violet, from ref. [302]) and A_{1g}+E^1_{2g} and 2LA(M) modes of the single layer WSe_2 (purple, from ref. [396]). Reference XRD patterns of the 1T' (navy) and 2H (purple) WSe_2 as well as of the 2H $MoSe_2$ (violet) are provided under the experimental diffractograms in panel **b**. Vertical dashed lines in panel **c** correspond to the A, B, and C excitonic transitions of the single layer $MoSe_2$ (violet, from ref. [302]) and A and B excitons of the single layer WSe_2 (purple, from ref. [55]).

are expected to appear at intermediate frequencies. Indeed, Raman signatures appear slightly shifted from the frequencies characteristic for the pristine 2H $MoSe_2$ nanosheets (239 and 285.6 cm^{-1}, respectively) towards the unresolved $E^1_{2g} + A_{1g}$ mode of the 2H WSe_2 observed at ~250 cm^{-1} in the annealed WSe_2 samples. Similar shift has been previously reported for CVT grown and micromechanically exfoliated $W_xMo_{1-x}Se_2$ monolayers [370] and for colloidal $W_xMo_{1-x}Se_2$ few-layered nanostructures [260]. Such shift was attributed to the random mixing of transition metal cations in the crystal lattice. The absence of doubled set of peaks, corresponding to the separate domains of the $MoSe_2$ and WSe_2 phases, is a good indication of the uniformity of the achieved ternary composition. The presence or absence of the metallic 1T' phase in the synthesised alloyed samples cannot be inferred from the Raman spectroscopy data since the characteristic Raman modes of the 1T' phase exhibit a very low intensity at the frequencies between 100-300 cm^{-1} (discussed in Section 3.3.2), and so are possibly obscured by the strong scattering of the semiconducting 2H phase.

Powder X-ray diffraction was employed to study the crystal phase of the produced alloyed material. A representative XRD pattern of the colloidal $W_xMo_{1-x}Se_2$ (x ~0.5) nanosheets is shown in Figure 4.7.b along with the experimental patterns of the synthesised $MoSe_2$ and WSe_2 nanoflowers. Three pronounced reflections centred at ~13.8, 31.8, and

38.3 $^{o}2\theta$ match well the (002), (100) and (103) planes of the hexagonal phase of either $MoSe_2$ or WSe_2. A broad feature observed at ~34.8 $^{o}2\theta$ (this region is highlighted with a grey rectangle in Figure 4.7.b) can, however, arise from the $(\bar{1}12)$ and (112) planes of the 1T' phase, as seen in the diffractograms of the as produced WSe_2 nanoflowers, and so be indicative of the 1T' phase present in the alloyed $W_xMo_{1-x}Se_2$ (x ~0.5) samples consistent with the result of the HR TEM imaging. This reflection is absent in the diffractograms of the as synthesised 2H $MoSe_2$ and the thermally converted into the 2H phase WSe_2 nanoflowers. Precise determination of the 1T' phase is complicated due to the broadening of the diffraction peaks due to polycrystallinity of the alloyed $W_xMo_{1-x}Se_2$ (x ~0.5) nanosheets, although it is worth mentioning that no reflection at this diffraction angle has been observed in the pure 2H phase $W_xMo_{1-x}Se_2$ nanostructures [155,260].

The presence of the semiconducting 2H phase in the alloyed $W_xMo_{1-x}Se_2$ (x ~0.5) nanoflowers is further confirmed by the results of optical absorption spectroscopy (Figure 4.7.c). A typical UV-vis absorption spectrum of the alloyed nanoflowers exhibits excitonic transitions of the semiconducting phase centred around 800 and 620 nm. The energies of these optical transitions are quite close to that of the A and B excitons of the 2H WSe_2 nanoflowers found at 780 and 617 nm, respectively, rather than of the as produced 2H $MoSe_2$ nanoflowers (805 and 710 nm, respectively).

Since the macroscopic techniques discussed above (XRD, Raman and UV-vis spectroscopies) do not provide a conclusive evidence of the presence or absence of the 1T' phase in the colloidal $W_xMo_{1-x}Se_2$ (x ~0.5) ternary alloys, X-ray photoemission spectroscopy was employed to study the coordination environment of transition metal cations in the crystal lattice of the alloyed nanoflowers. High-resolution XPS spectra of the W 4*f*, Mo 3*d*, and Se 3*d* core level electrons of pristine colloidal WSe_2 and $MoSe_2$, and alloyed $W_xMo_{1-x}Se_2$ (x ~0.5) nanoflowers are presented in Figure 4.8. As discussed in Section 3.3.1, under the growth conditions used throughout this work, the WSe_2 nanostructures are acquired in the metastable 1T' phase, and the W^{+4} 4*f* doublet appeared at 31.66 and 33.84 eV in the corresponding XPS spectra. Upon thermal annealing, the 1T' phase of WSe_2 is fully converted into the thermodynamically stable 2H phase, this phase transformation is accompanied by a shift of the W^{+4} 4*f* doublet to the higher binding energies up to 32.40 and 34.58 eV. On the other hand, in the high-resolution XPS spectrum of the as produced $MoSe_2$ nanostructures, the doublet corresponding to the Mo^{+4} 3*d* core level electrons is found at 228.7 and 231.9 eV that is in a good agreement with the values reported for the 2H phase of $MoSe_2$ [183,170]. XPS spectrum of

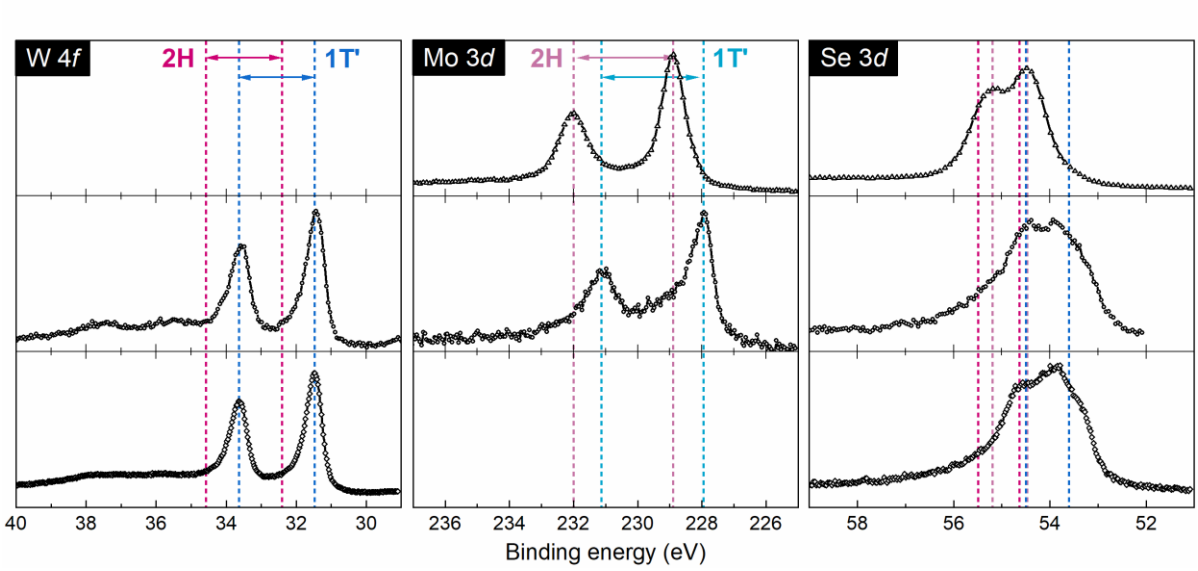


Figure 4.8. XPS study of the produced $W_xMo_{1-x}Se_2$ nanoflowers. High resolution XPS spectra of the W 4*f*, Mo 3*d*, and Se 3*d* core electrons of the as synthesised WSe_2 (predominantly 1T' phase; bottom row), $MoSe_2$ (2H phase; top row), and the $W_xMo_{1-x}Se_2$ (x ~0.5; middle row) nanoflowers.

the alloyed $W_xMo_{1-x}Se_2$ (x ~0.5) nanoflowers, however, displays the W^{+4} 4*f* doublet at the binding energies close to that found in the 1T' phase of WSe_2 (31.5 and 33.6 eV), while the most prominent doublet in the Mo 3*d* core level spectrum also appears shifted to the lower binding energies compared to the peak positions in the 2H phase and is observed at 227.9 and 231.1 eV (Figure 4.8). These energies are comparable to the Mo^{4+} (228.1 and 231.2 eV) reported for the metallic 1T' $MoSe_2$ [183]. Appearance of the Mo^{+4} and W^{+4} doublets shifted to the lower binding energies compared to the corresponding 2H phases can be indicative of a fraction of both molybdenum and tungsten cations, exhibiting the 1T' phase coordination, present in the alloyed $W_xMo_{1-x}Se_2$ (x ~0.5) nanoflowers.

Formation and investigation of ternary $W_xMo_{1-x}Se_2$ alloys is particularly interesting since can potentially allow the lateral heterostructures being synthesised via the induced phase segregation. Similar process was reported for the $Mo_xW_{1-x}S_{2y}Se_{2-2y}$ flakes obtained via CVD approach that formed $MoS_{2y}Se_{2-2y}/WS_{2z}Se_{2-2z}$ heterostructures upon thermal annealing [371].

4.3. Conclusions

As a general strategy, varying the composition of a given material is appealing for tailoring its electronic properties due to either introducing localised defect states or achieving gradual modulation of the electronic structure. Here, we have demonstrated that the incorporation of Cu and Fe species into the WSe_2 nanostructures can be achieved during a solution phase reaction. Cu and Fe have been selected as potential dopants since both, according to the first principle calculations, are expected to alter the hydrogen adsorption free energy in both the semiconducting 2H and metallic 1T phases, thus facilitating the catalytic hydrogen reduction.

The growth of Cu- and Fe-doped WSe_2 nanoflowers has been achieved in the presence of Cu^{II} and Fe^{III} salts. According to the results of SEM imaging and Raman spectroscopy, the final product is morphologically uniform, and elemental analysis confirmed the presence of doping species in the nanoflowers. However, the stoichiometry of final products strongly deviates from the nominal, possibly suggesting the preferential formation of ternary Cu-W-Se and Fe-W-Se phases. These phases are rarely reported in literature, and the range of potentially achievable compositions, whilst maintaining the overall layered crystal structure of the parent TMD phase, needs to be thoroughly investigated.

In the mixed W-Mo dichalcogenides, the effective formation of random ternary alloys is expected in a wide range of compositions owing to the similarity of W and Mo cations. Moreover, by alloying the components, that under the same conditions tend to preferentially crystallise in different polymorphs (2H and 1T'), allows the crystal phase of the alloyed material to be selectively targeted as was demonstrated in $MoS_{2x}Te_{2-2x}$ and $WSe_{2x}Te_{2-2x}$ alloys.

In this work, we have demonstrated that ternary $W_xMo_{1-x}Se_2$ nanostructures can be obtained through a reaction between the corresponding molecular precursors. The alloyed material retained the nanoflower morphology, although the individual atomically-thin nanosheets were composed of smaller single-crystalline patches, unlike the single crystalline petals of the parent WSe_2 structures. Elemental analysis clearly demonstrated the uniform distribution of both cations within individual ternary nanostructures; this was further confirmed by Raman spectroscopy. The observed splitting of the W^{+4} and Mo^{+4} doublets in the core level electron spectra suggests that in the alloyed material two types W and Mo cations are present. Therefore, structurally, the produced ternary $W_xMo_{1-x}Se_2$ nanoflowers are a 2H/1T' bi-phased, although compositionally uniform, alloy.

Chapter 5:
Application in electrochemical devices

In this Chapter we study the electrocatalytic performance of the colloidal inorganic nanoflowers for the hydrogen evolution reaction. First, we discuss the methods to assemble the active material on various conductive support platforms essential for testing its catalytic properties. We demonstrate that the developed solution-phase synthesis approach can be modified to grow the active material directly on a chosen functional substrate. Compared to the deposition from colloidal suspensions, this yields more uniform and stable coatings. Remarkably, the methods developed to achieve the control over the crystal phase, as in the case of direct synthesis of the metastable 1T' polymorph of WSe_2 discussed in Section 3.3.1, or the catalyst composition, as illustrated by the ternary alloyed $W_xMo_{1-x}Se_2$ nanoflowers introduced in Section 4.2, can be applied to attain functional coatings of the respective modified catalysts on a support platform. Furthermore, the heterogeneous nucleation on the substrate surface does not affect the phase purity or the precision over the composition control achieved via the solution-phase reaction. Considering the colloidal WSe_2 nanoflowers as a model system, we discuss how the access to metastable polymorphs, such as the metallic 1T' phase of WSe_2, or to the ternary compositions, i.e. by alloying with molybdenum, can be beneficial for improving the catalytic performance of chosen material. We discuss the efficiency of the nanostructured catalysts grown by colloidal approach compared to other members of the group VIB TMD family suggested for the catalytic hydrogen evolution reaction (HER). Finally, we perform the prolonged electrolysis tests to assess the durability of colloidal TMD catalysts.

5.1. Approaches to assemble colloidal TMD nanostructures on conductive supports for electrocatalytic hydrogen reduction

In order to assess the catalytic activity of colloidal nanoflowers for the hydrogen reduction, the produced material was assembled on a conductive support platform and the performance was evaluated in acidic electrolytes using a three-electrode cell configuration as described in Section 2.4.2.1. Two approaches to assemble the active material on functional substrates, namely, drop-casting from colloidal suspensions and a solution-phase growth of the active material directly on a conductive substrate, are introduced and compared in this Section.

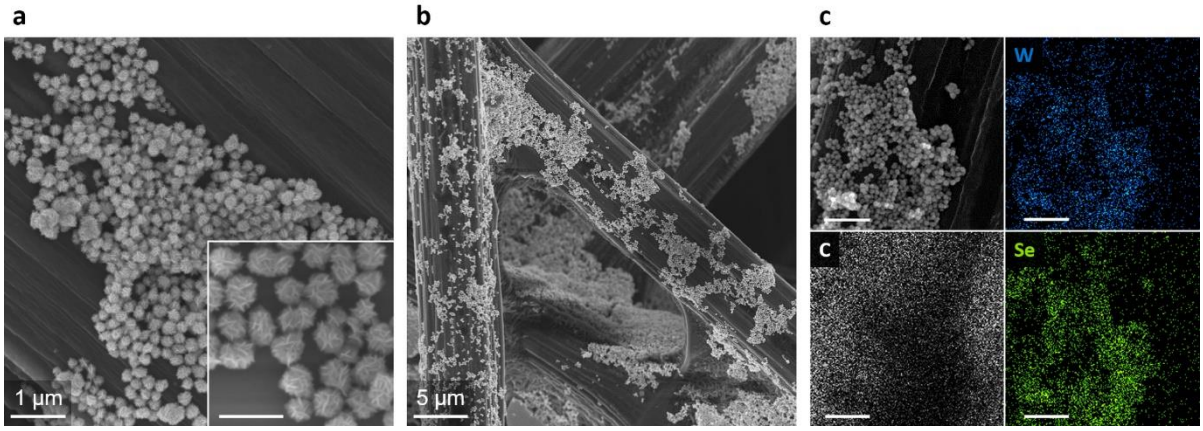


Figure 5.1. Working electrodes produced via drop-casting of the active material (colloidal WSe_2 nanoflowers) onto a functional substrate (CP). **a**, **b** SEM images of the WSe_2 nanoflowers coating the fibres of CP. Inset is a zoomed in SEM image demonstrating the morphology of the colloidal WSe_2 nanoflowers, scale bar 500 nm. **c** SEM image and the corresponding elemental (W, Se, and C) maps of the WSe_2 nanoflowers drop-cast on CP; scale bar 20 µm.

Drop-casting onto conductive substrates is a simple deposition technique allowing for a quick preparation of the working electrodes for express evaluation of the catalytic properties of the material under study. Carbon paper (CP) was chosen as a conductive support material as it has low intrinsic resistance and does not exhibit a significant catalytic activity for the hydrogen evolution reaction. To make the working electrodes via drop-casting, 1 mL of an ethanol suspension of colloidal nanoflowers (i.e. in a standard synthesis, the WSe_2 NFs were obtained as 0.1 mg/mL suspensions) was pipetted onto a strip of carbon paper over a 0.5×0.5 cm^2 geometric area, resulting in a nominal catalyst loading of 0.4 mg/cm^2. It should be noted that the desired amount of the active material was loaded onto the CP surface in portions allowing each layer to dry out completely before the following portions were deposited to minimise spreading of the active material beyond the active area of the working electrode, which normally was 0.5×0.5 cm^2.

Representative SEM images of the WSe_2 working electrodes produced via drop-casting are shown in Figure 5.1. Casting approach does not allow for the uniform spreading of the active material since driven by the capillary forces the nanoflowers tend to agglomerate when the solvent evaporates, leaving a substantial part of the substrate unfunctionalized and hence inert for the catalytic reaction. Additionally, the depth distribution of the loaded catalyst also varies as the major fraction of colloidal nanoflowers is deposited onto the topmost layer of CP only. The SEM images and the corresponding elemental maps shown in Figure 5.1.a,c demonstrate the non-uniform distribution of the WSe_2 active material drop-cast onto CP. In spite of these problems, this deposition method allows for potentially high mass loading as the

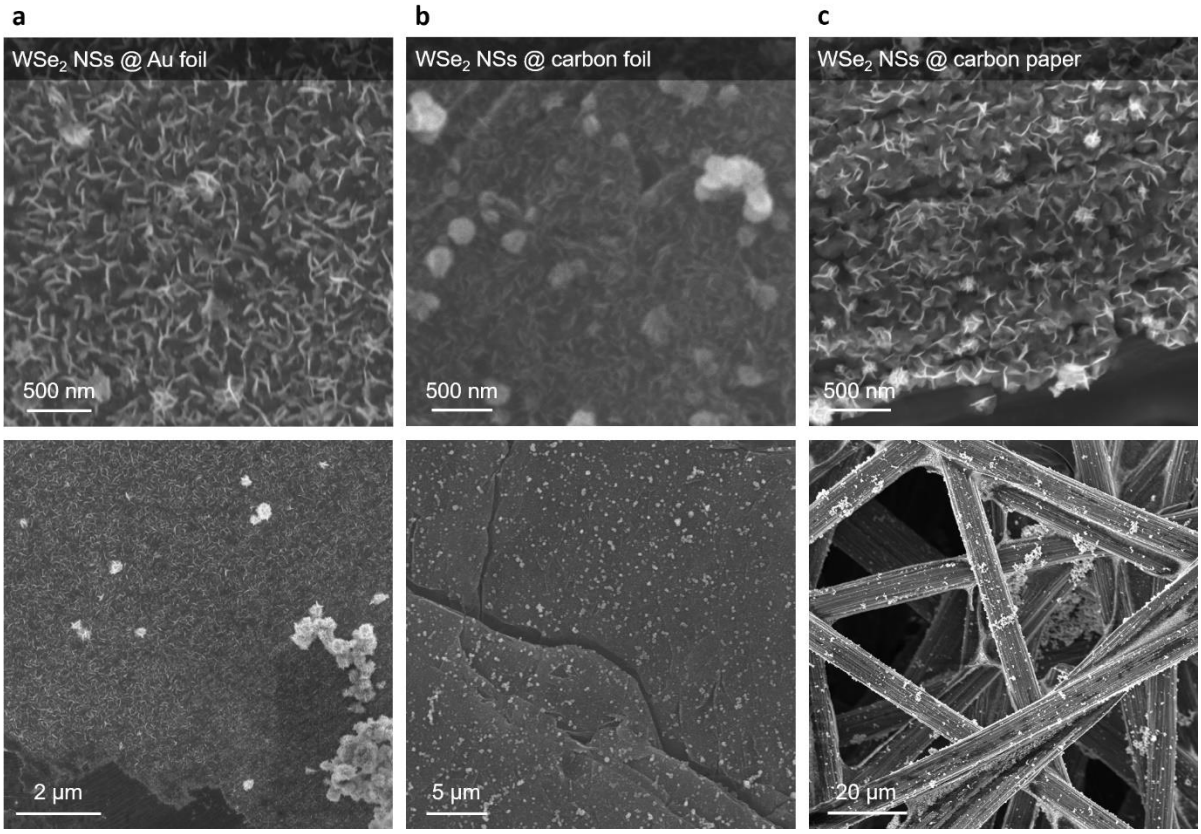


Figure 5.2. Bottom-up synthesis of the TMD nanosheets growing directly on functional substrates. SEM images of dense arrays of the vertically aligned WSe_2 nanosheets (top row) uniformly covering large areas (bottom row) of **a** gold foil, **b** carbon foil, and **c** carbon paper chosen as conductive substrates.

material can accumulate in the pockets between the carbon fibres as shown in Figure 5.1.b. However, it is worth mentioning that too much agglomeration of the nanostructured WSe_2 catalyst has a disadvantageous effect on its performance since the number of catalytically-active edge sites per mass of loaded material is significantly reduced because the nanoflowers inside the lumps of agglomerated particles are inaccessible to the electrolyte and therefore are not involved in the catalytic reaction. Moreover, these can potentially lead to an increase in resistive losses attributed to the interparticle charge transfer.

On the other hand, solution-phase synthesis approach developed in Chapter 3 allows growing the active material directly on an arbitrary functional substrate such as carbon paper (CP), carbon foil (CF) and gold foil (Figure 5.2). The only growth limitation is that the substrate must be wettable by the solvent. This fabrication method results in a continuous coating of large areas of the functional support with the excellently adhered active material and is potentially compatible with batch production of the working electrodes. Direct bottom-up synthesis of the catalyst is also favourable since, in contrast to deposition techniques, it ensures

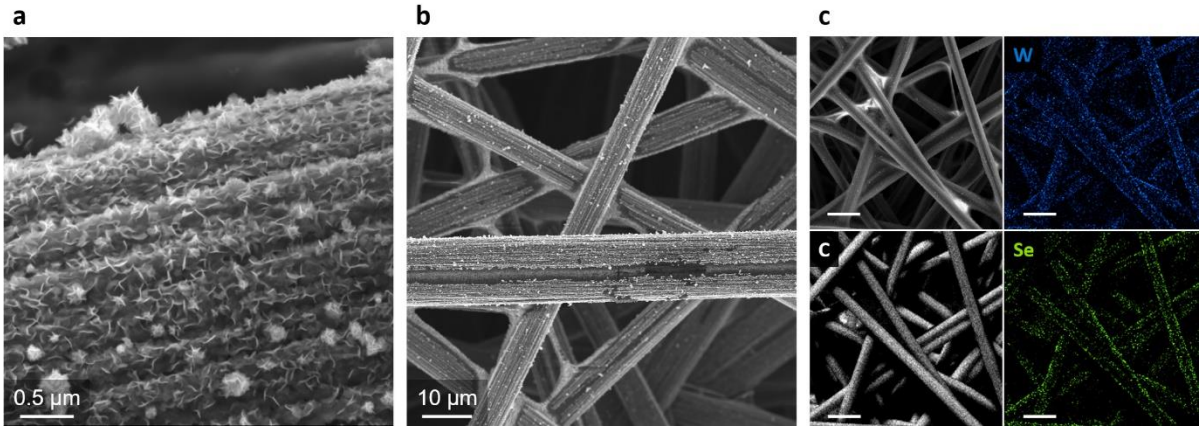


Figure 5.3. Working electrodes produced via direct growth of the active material (WSe_2 nanosheets) on a functional substrate (CP). **a**, **b** SEM images of the vertically aligned WSe_2 nanosheets coating the fibres of CP. **c** SEM image and the corresponding elemental (W, Se, and C) maps of the WSe_2 nanosheets grown directly on CP; scale bar 20 µm.

good electrical connection between the active material and the underlying substrate, thus reducing the resistive losses. The contact resistance was demonstrated to play a key role in the catalytic performance of the semiconducting MoS_2 [94,96].

Carbon paper was chosen as a support material since compared to other highly conductive carbon-based substrates it provides a three-dimensional porous framework with high surface area accessible to the electrolyte. Direct solution-phase growth of WSe_2 on CP resulted in a dense array of vertically aligned nanosheets, uniformly covering the accessible surface area of the substrate as illustrated by low magnification SEM images and the corresponding elemental maps in Figure 5.3.b,c. The vertical growth preserves the edge-abundant morphology of the free-standing WSe_2 nanoflowers grown in colloidal solution. Therefore, the high number of catalytically-active sites of the nanostructured active material is preserved during the direct growth. The observable lateral dimensions of the vertically aligned WSe_2 nanosheets varied from 20 to 100 nm and were comparable to the size of individual petals of the free-standing WSe_2 nanoflowers (Figure 5.3.a). Interestingly, not only the edge-rich morphology of the colloidal WSe_2 nanoflowers but also the metastable 1T' crystal structure (will be discussed in Section 5.2) was preserved when the solution-phase growth was confined to the surface of a substrate instead of occurring in the free-standing state in solution. Thus, the performance of the working electrodes produced via drop-casting and via solution-phase growth of the active material can be directly compared. In case of direct growth of the active material, the mass loading is theoretically limited by the density of the nanosheet array and by the lateral dimensions of individual nanosheets. Estimated from the results of ICP OES, the mass loading of the WSe_2 nanosheets grown on CP was in the range of 40-120 µg/cm^2.

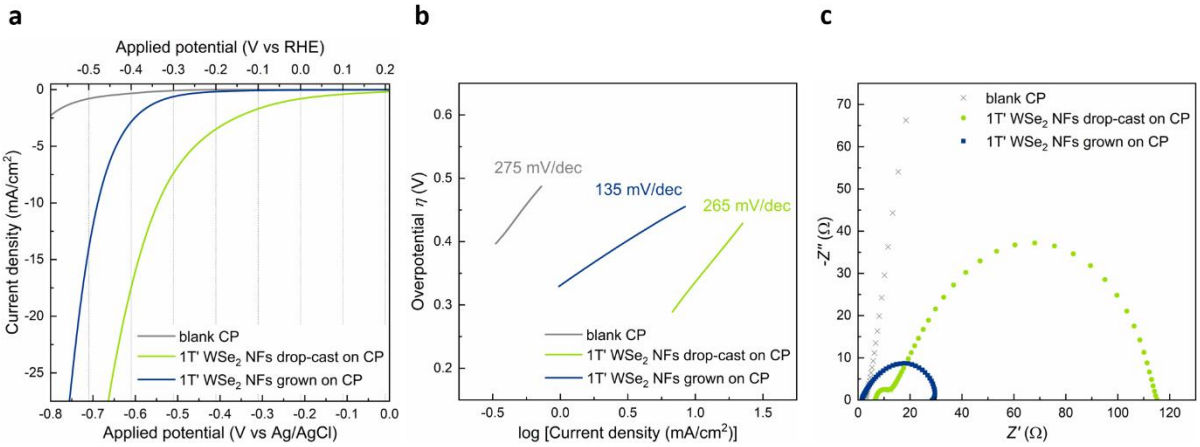


Figure 5.4. Comparison of catalytic performance of the WSe_2 working electrodes produced via drop-casting and via direct growth of active material on CP. **a** Polarisation curves, **b** the corresponding Tafel slopes, and **c** Nyquist plots of the 1T' WSe_2 nanosheets grown directly on CP and deposited (drop-cast) on CP from the colloidal suspension.

The parameter most commonly used to compare the performance of various catalysts is the overpotential required to achieve a certain current density on the working electrode. The current density of -10 mA/cm^2 has been widely accepted as a benchmarking value [290]. LSV was performed to assess the catalytic performance of the WSe_2 nanostructures, and the applied potential was swept cathodically from 0 to -0.8 V (vs Ag/AgCl $_{3M\ KCl}$ reference electrode). The polarisation curves of the working electrodes prepared via drop-casting and via direct growth of the WSe_2 nanosheets on CP are presented in Figure 5.4.a. Although the drop-cast working electrodes achieve the benchmarking cathodic current density of -10 mA/cm^2 at measurably lower overpotentials compared to the material grown directly on CP (350 mV vs 480 mV, respectively), this apparent efficiency can be mostly attributed to the higher mass loading in case of the drop-cast electrodes (0.4 mg/cm^2 vs 0.12 mg/cm^2, respectively). The Tafel slope of 265 mV/dec demonstrates poor catalytic reaction kinetics in the case of drop-cast electrodes (Figure5.4.b). On the other hand, the electrodes produced via the direct growth of the 1T' WSe_2 nanosheets display much better reaction kinetics with the Tafel slope as low as 135 mV/dec. The electrode kinetics was also studied using electrochemical impedance spectroscopy (EIS). The vertically aligned WSe_2 nanosheets grown directly on CP demonstrate a quite low charge transfer resistance R_c of ~30 Ω, suggesting excellent charge transfer kinetics (Figure 5.4.c). In contrast to that, the Nyquist plot of the drop-cast working electrodes reveals two distinct semicircles, with the low frequency one corresponding to the charge transfer resistance, while the higher frequency semicircle can be attributed to the interparticle charge transfer or to the charge dissipation, occurring at the grain boundaries in the branched WSe_2 nanoflowers. This higher frequency semicircle is normally not observed in the case of electrodes produced via

direct growth. This can be attributed to a significantly lower fraction of the agglomerated nanoflowers compared to that in the drop-cast electrodes as the directly grown material predominantly exhibited the morphology of vertically-aligned two-dimensional flakes, growing off the substrate. Overall, the higher charge transfer resistance observed in the drop-castWSe_2 film (~108 Ω) is indicative of a slower electron transfer during the catalytic hydrogen reduction, which corroborates the results of the Tafel slope analysis. Moreover, much lower uncompensated series resistance R_u of ~1.5-4.5 Ω (Figure 5.4.c, Figure 5.7.c, Figure 5.9.c), consistently observed for all the directly synthesised samples, suggests an improved electrical connection of the catalytic material to the conductive substrate compared to the drop-cast films (R_u ~7-7.5 Ω). These findings are in good agreement with the electron transport study in the semiconductor MoS_2 nanosheets, where the improved electrical contact has led to a great increase in the catalytic activity for HER reflected by lower Tafel slopes [96].

To summarise, the drop-casting technique provides an easy and straightforward way to deposit active material on functional substrates, potentially allowing for high mass loadings. The drawback of the deposition approach is a non-uniform distribution of the active material, agglomeration of the deposited nanoflowers, and poor contact with the conductive substrate. All these aspects impede the reaction kinetics and reduce the electrode lifetime. In contrast to that, the solution-phase approach, developed to grow free-standing TMD hierarchical nanosheets, can be employed to produce functional coatings directly on conductive substrates as we demonstrated for the WSe_2 nanosheets. The higher uniformity of such functional coatings, abundance of catalytically-active edge sites achieved in the arrays of vertical nanosheets, and chemical bonding to the conductive support lead to the improved catalytic performance. Thus, we have chosen the direct growth as a preferential approach to produce working electrodes for the hydrogen reduction.

5.2. Phase engineering for improved catalytic performance: 1T' WSe_2

In the previous Section we have demonstrated that colloidal growth can be employed to form functional coatings directly on conductive substrates, while maintaining the edge-rich morphology of the free-standing hierarchal nanosheets. Here, we confirm that the metastable 1T' phase of WSe_2 is preserved when the growth is initiated heterogeneously on the surface of a conductive substrate (CP). Further, we compare the performance of the 1T' WSe_2 nanosheets and their 2H counterpart for the catalytic hydrogen reduction. The metallic 1T(1T') phases of the group VIB TMDs have been reported to exhibit higher catalytic activity compared to the semiconducting 2H polymorph. However, these metallic phases were generally produced through lithiation of the 2H phase. The gradual loss of the charged species stabilising the 1T(1T') phase cause deterioration of the catalytic performance over time [[112,186]]. We highlight the benefits of the solution-phase growth since the described method provides a direct access to the metastable, more catalytically active, polymorph.

Working electrodes were prepared by growing the WSe_2 nanosheets on CP as described in Section 2.4.1. The 1T' WSe_2 was tested for the HER as produced, while the 2H counterpart was obtained by annealing the electrodes in a tube furnace at 400 ºC for two hours (0.45 mbar, argon atmosphere). It should be pointed out that the thermal treatment did not affect the morphology of the WSe_2 nanosheets assembled on CP as illustrated by the SEM images taken before and after annealing (Figure 5.5.a,b). To rule out the effect of catalyst mass loading on the electrode performance, both the 1T' and the corresponding 2H WSe_2 working electrodes were produced in the same synthesis. The active material loading was determined via ICP OES and was as low as ~40 μg/cm^2. It should be noted that no noticeable loss of the material occurred during the annealing.

Typical Raman spectra of the WSe_2 nanosheets grown on CP taken before and after thermal annealing are presented in Figure 5.5.c,d. The Raman spectrum of the as produced material (Figure 5.5.c) displays six peaks at 104.8, 151, 180, 217, 238.7, and 258.2 cm^{-1} characteristic to the 1T' phase as was stated in Section 3.3.2. After annealing, only the unresolved pair of the E^1_{2g} and A_{1g} peaks, centred at 249 cm^{-1}, is observed in the Raman spectrum (Figure 5.5.d). The broad peak at ~125 cm^{-1}, which was also observed in the few-layered 2H WSe_2 nanoflowers, was tentatively assigned to the resonance $A_{1g} - LA(M)$ mode analogously to [[139,347]]. To better illustrate the phase purity, sections of the 1T' and 2H WSe_2 working electrodes were mapped in three spectral regions – 80-125(150), 170-200, and 200-

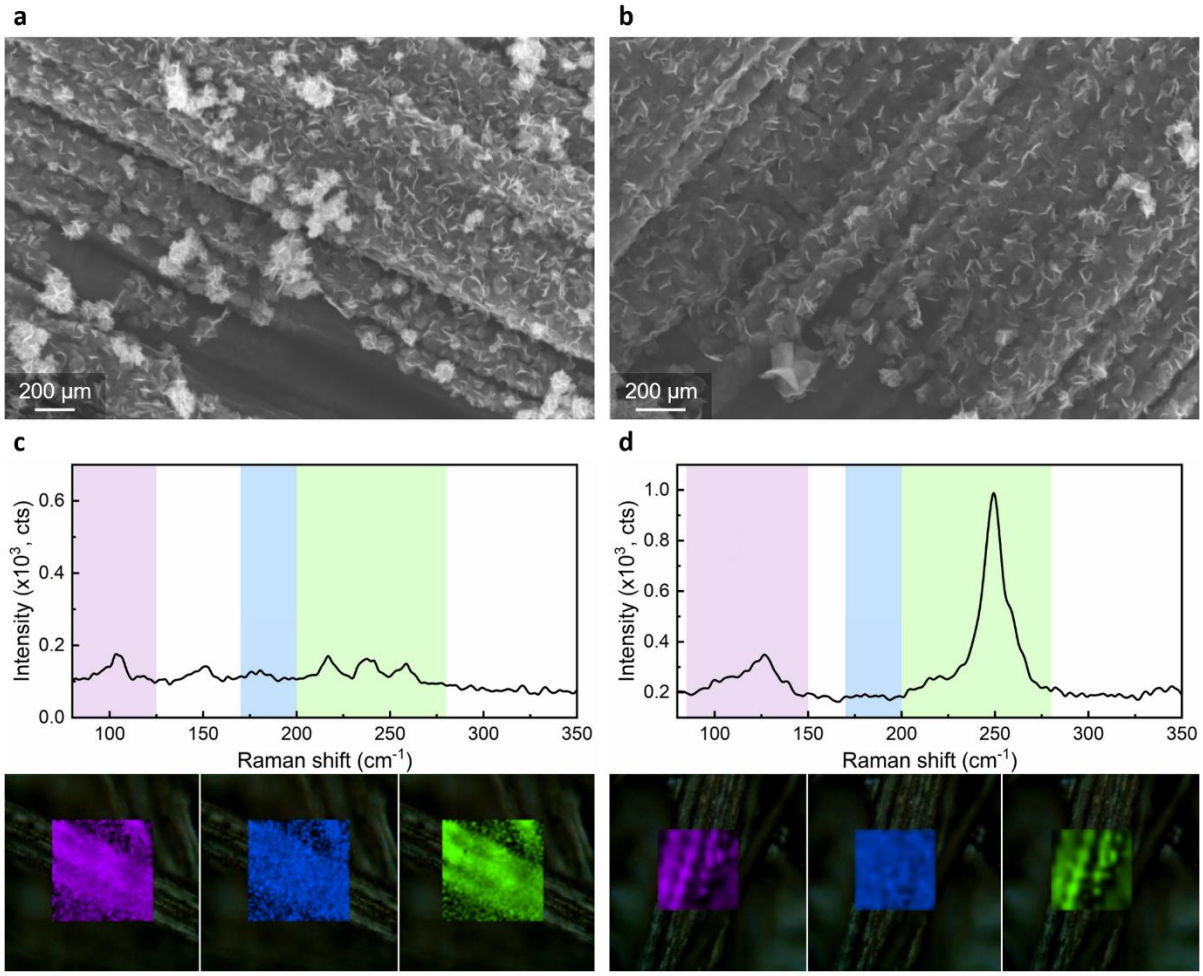


Figure 5.5. Structural characterisation of the as produced 1T' and the converted 2H WSe_2 working electrodes. **a, b** Representative SEM images and **c, d** Raman spectra of the WSe_2 nanosheets grown on CP confirming the 1T' phase of the as produced material and the 2H phase of the thermally annealed working electrode. Raman maps presented below correspond to the 80-125 (purple), 170-200 (blue), and 200-275 (green) cm^{-1} spectral range and demonstrate the uniform coverage of the CP with WSe_2 nanosheets in the 1T' (**c**) and the 2H (**d**) phase.

275 cm^{-1}. In the case of the as produced electrode, all three maps exhibit a strong Raman signal conformal to carbon fibres, suggesting the uniform coverage of CP with the 1T' WSe_2 nanosheets. After annealing, a clear difference in Raman signal is observed. In the 2H phase, Raman-active modes are absent in the spectral range 170-200 cm^{-1}. Indeed, the corresponding Raman map displays a background signal only, while two other maps, acquired in the range 80-150 and 200-275 cm^{-1}, demonstrate a high intensity signal of the 2H WSe_2, coating carbon fibres. This confirms that upon thermal annealing the material is fully converted into the thermodynamically stable 2H phase.

In contrast to the semiconducting 2H phase, the few-layered 1T' phase was predicted to exhibit metallic (semimetallic) behaviour, however, unlike the majorly studied 1T' WTe_2 [21]

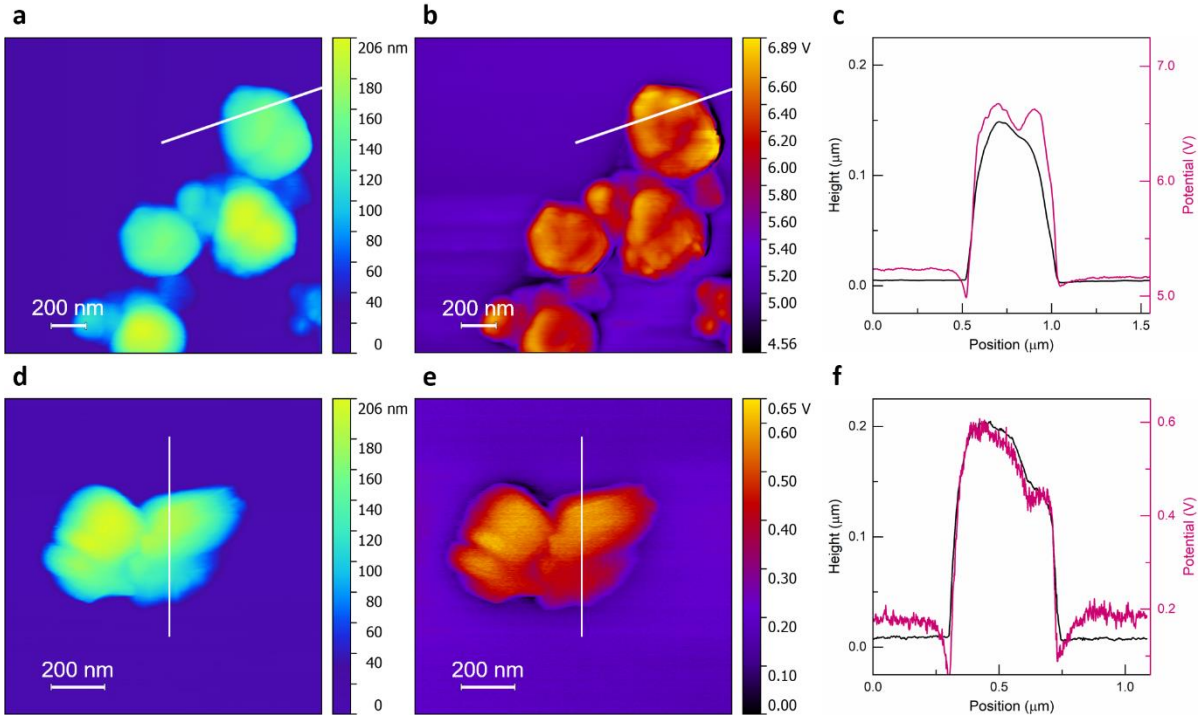


Figure 5.6 Electronic properties of the few-layered 1T' and 2H WSe_2 nanoflowers. **a, d** Tapping mode AFM images, **b, e** KPFM images, and **c, f** corresponding line scans (height profiles and contact potential difference variation) of the as produced 1T' (top row) and annealed 2H WSe_2 (bottom row) nanoflowers assembled on p-doped Si wafers, respectively.

and 1T' $MoTe_2$ [310], the electronic properties of the few-layered 1T' WSe_2 not stabilised by the intercalated charged species remain unexplored. We performed Kelvin probe force microscopy (KPFM) to investigate the electronic structure of the as produced 1T' and annealed 2H WSe_2 nanoflowers (Figure 5.6). For this, the 1T' and 2H WSe_2 nanoflowers were deposited on p-doped Si wafers and the corresponding work functions were determined from the measured contact potential difference based on the known work function of p-doped Si as described in Section 2.3.9. Thus found work functions of the as produced and the annealed material were close to 2.6 and 4.2 eV, respectively. These values match work functions of the metallic 1T' (2.36 eV) the semiconducting 2H WSe_2 bilayer (4.08 eV) reported in [372].

Further, we investigate how the phase control achieved through the wet-chemical synthesis approach can be employed to improve the catalytic activity of a given material. The polarisation curves of the metallic 1T' and semiconducting 2H WSe_2 polymorphs are shown in Figure 5.7.a. The 1T' WSe_2 nanosheets demonstrated a good activity for the hydrogen reduction, reaching the catalytic current density of -10 mA/cm^2 at lower reaction overpotential compared to that of the semiconducting 2H counterpart (510 vs 640 mV, respectively). Since the 1T' and 2H WSe_2 working electrodes had virtually identical morphology and catalyst mass

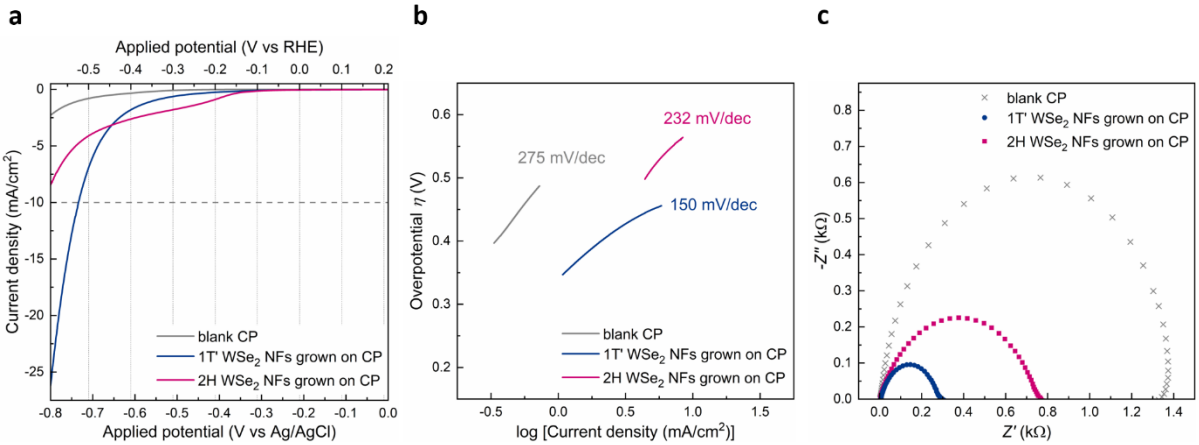


Figure 5.7. Comparison of catalytic activity of the 1T' and 2H WSe_2 working electrodes. **a** Polarisation curves, **b** the corresponding Tafel slopes, and **c** Nyquist plots of the as produced 1T' WSe_2 and the annealed 2H WSe_2 nanosheets grown directly on CP.

loading, the observed lowering of the reaction overpotential is likely to be attributed to higher catalytic activity of the 1T' polymorph. In addition to that, Tafel slope analysis has revealed faster reaction kinetics with the Tafel slope of 150 mV/dec in the 1T' WSe_2 compared to 230 mV/dec of the 2H phase (Figure 5.7.b). Electrochemical impedance spectroscopy (Figure 5.7.c) confirmed better conductivity of the metallic 1T' WSe_2 phase, showing a decreased charge transfer resistance (280 Ω) compared to the semiconducting 2H phase (750 Ω). In fact, enhanced catalytic activity of the 1T(1T') phases of WS_2, MoS_2 and $MoSe_2$ compared to the respective 2H phases has been attributed to the faster charge transfer in the metallic polymorph [112,159,373]. Secondly, it is assumed that the improved activity can be attributed to the activation of inert basal planes of the 1T' phase [109]. Indeed, the hydrogen adsorption free energy on the basal plane of the 1T' MoS_2 was predicted to be closer to thermoneutral (0.18 eV) than in the case of the 2H phase (1.6 eV) [373].

5.3. Ternary $W_xMo_{1-x}Se_2$ alloys for electrocatalytic hydrogen reduction

In addition to the phase engineering discussed in the previous section, a significant improvement in the electrocatalytic performance can be achieved through variation of the material composition, such as through doping and alloying. For the electrocatalytic hydrogen reduction, both approaches are generally applied to optimise the hydrogen adsorption free energy (ΔG_H). This is achieved due to the effective modulation of the electronic structure of the catalyst [358,374]. Substitutional doping can play an important role in the enhancement of catalytic activity of hybrid materials by providing additional catalytic sites as, for example, it was demonstrated in P-doped (8 wt.%) $CoSe_2$ nanobelts [375], where the P dopant sites exhibited ΔG_H close to thermoneutral. Further, the improved electrical transport achieved via local conversion into the metallic 1T polymorph was reported to enhance the catalytic performance of the group VIB TMDs. This was shown in Pd-doped (1 wt.%) MoS_2 nanosheets, where Pd dopant sites only induced local transformation of the host lattice and were not involved in the catalytic reaction [106]. Similar stabilisation of the favourable phase can be attained by alloying with the element, for which this phase is thermodynamically stable. This has been demonstrated for the $Re_xMo_{1-x}S_2$ alloys, which acquired the 1T' phase at high Re content [376]. An alternative approach to achieve the enhanced catalytic activity can rely on introducing structural defects in the basal plane of the group VIB TMDs to increase the number of active edge sites as reported for the porous (holey) MoS_2 nanosheets [100] and oxygen plasma etched MoS_2 [102] monolayers. It has been reported, however, that during a prolonged electrolysis, the evolving gas bubbles may lead to significant changes in the TMD catalyst morphology, including peeling and fracturing [377], and even to delamination of the active material from the surface of a working electrode [378]. From a practical point of view, altering the catalyst composition seems preferable since its structural integrity remains uncompromised, hence longer electrode durability can be expected. Here, we discuss how formation of the cation-mixed $W_xMo_{1-x}Se_2$ alloy can be employed to enhance the catalytic activity of the pristine counterparts.

A set of the $W_xMo_{1-x}Se_2$ working electrodes divided into three types: pristine WSe_2 (x = 1), pristine $MoSe_2$ (x = 0), and alloyed $W_xMo_{1-x}Se_2$ (x ~0.5); was prepared by growing the active material directly on a conductive substrate (CP). The growth of the WSe_2 and $MoSe_2$ nanosheets on CP was performed in a similar way as the solution-phase synthesis of the respective free-standing hierarchical nanosheets discussed in Chapter 3. A piece of CP (~4 cm^2) was put into a hot solution of the transition metal complex prior to the injection of the

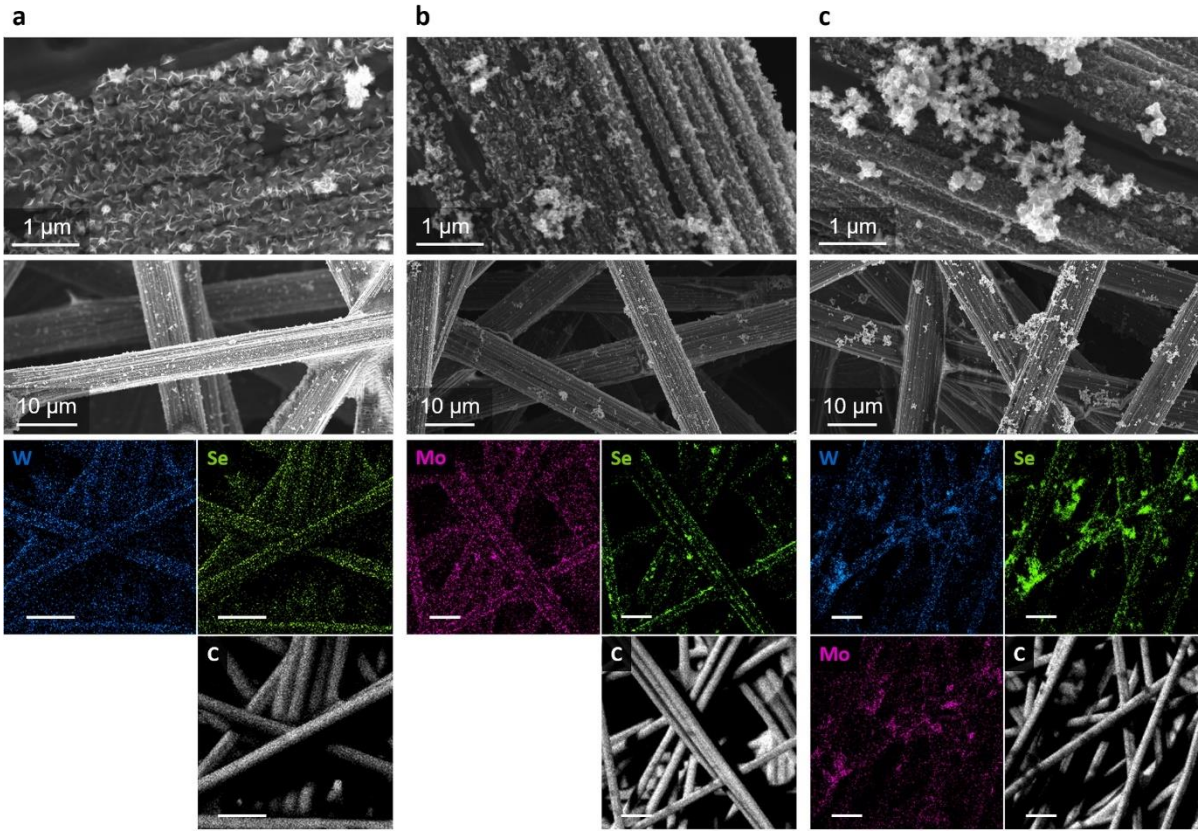


Figure 5.8. Structural characterisation of the as produced $W_xMo_{1-x}Se_2$ (x = 0-1) working electrodes. SEM images (top row) of the dense arrays of the **a** WSe_2, **b** $MoSe_2$, and **c** $W_xMo_{1-x}Se_2$ (x ~0.5) vertically aligned nanosheets grown directly on CP; corresponding low magnification SEM images and elemental (W, Mo, Se, and C) maps confirming uniformity of the functional coatings achieved via the direct growth approach are presented in the middle and bottom rows, respectively. Scale bars in SEM EDS maps are 20 µm.

chalcogen precursor. To achieve the ternary composition, tungsten precursor was partially substituted by molybdenum precursor, while keeping the transition metal to chalcogen [W+Mo]:[Se] molar ratio fixed at 1:2.

Grown directly on CP, both WSe_2 and $MoSe_2$ predominantly form dense arrays of vertically oriented nanosheets, uniformly coating carbon fibres over the entire area of the substrate as illustrated by the high- and low-magnification SEM images in Figure 5.8.a,b. In the corresponding elemental maps, the recorded signal of transition metal (W or Mo) and selenium matches that of carbon from carbon fibres, further confirming uniformity of the attained functional coating (Figure 5.8.a,b). Interestingly, SEM images of the alloyed $W_xMo_{1-x}Se_2$ (x ~0.5) samples reveal a significant fraction of the agglomerated nanoflowers in addition to the vertical nanosheets (Figure 5.8.c). Secondary nucleation, leading to the formation of branched nanoflowers on top of the primary vertical nanosheets, results in a significantly higher mass loading per working electrode compared to the individual WSe_2 and $MoSe_2$. This is in a

good agreement with the higher reaction yield consistently observed in the synthesis of free-standing $W_xMo_{1-x}Se_2$ (x ~0.5) nanoflowers. The reaction yield estimated from the results of ICP OES reaches~17% (vs 2% and 4% for the WSe_2 and $MoSe_2$ nanoflowers, respectively). The reasons why the ternary alloy formation reaction is characterised by a measurably higher yield are not clear at this stage and require a more dedicated study.

Table 8. Main characteristics of the $W_xMo_{1-x}Se_2$@CP working electrodes.

Parameter \ Active material		WSe_2	$MoSe_2$	$W_xMo_{1-x}Se_2$
Mass loading	(ICP, μg/cm$^2_{Se}$)	114	21	128
Composition [W]:[Mo]:[Se]	(TEM, free-standing)	1:1.8	-	1:0.92:4.27
	(SEM, @CP - as produced)	1:2.5	1:2.25	1:1:4.2
Surface area	(BET, free-standing; m^2/g)	57.4	62.7	104.5
	(BET, on CP; m^2/g)[10]	258	-	-

ICP OES analysis, however, does not allow for the direct quantitative determination of the composition of the produced $W_xMo_{1-x}Se_2$ (x = 0-1) electrodes. This is due to an unavoidable loss of the transition metal that forms insoluble oxides in strong mineral acids as discussed in Section 2.3.7. In contrast to tungsten and molybdenum, selenium is likely to form highly-soluble selenous acid upon digestion in strong acids. Therefore, catalyst mass loading per working electrode (in μg/cm^2) was estimated from the measured selenium concentration presuming the transition metal to selenium molar ratio being stoichiometric 1:2. The approximate W:Mo:Se molar ratio was determined from the results of SEM EDS (the material grown directly on CP) and TEM EDS (the free-standing nanoflowers formed in solution as a side product) and the averaged values are listed in Table 7. It should be noted that a slight selenium excess was measured in all cases. Interestingly, [W]:[Mo] molar ratio in the alloyed $W_xMo_{1-x}Se_2$ (x ~0.5) nanosheets was found to be close to the nominal 1:1, similarly to the case of the free-standing alloyed nanoflowers (Section 4.2). The main characteristics of the produced electrodes are summarised in Table 8.

Thus produced working electrodes with relatively low catalyst mass loading (20-130 μg/cm^2) were tested for the catalytic hydrogen reduction. It should be noted that the synthesised TMD nanoflowers are characterised by a high specific surface area (57-105 m^2/g). These values are very close to the reported for the nanostructured (66 m^2/g) [153] and mesoporous group VIB TMDs (87-105 m^2/g) [379]. Moreover, using CP as a support allowed

[10] Specific surface area of the unfunctionalized carbon paper is 191.3 m^2/g. The nitrogen adsorption data is unavailable for the $MoSe_2$ and $W_xMo_xSe_2$ (x ~0.5) functionalised carbon paper.

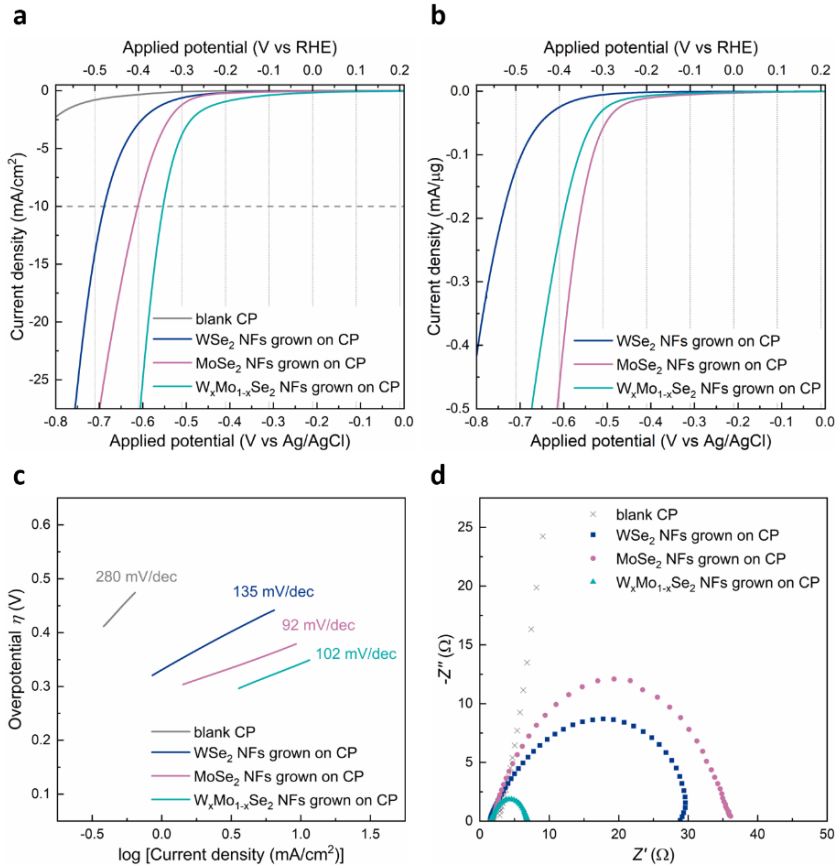


Figure 5.9. Comparison of catalytic performance of the $W_xMo_{1-x}Se_2$ (x = 0-1) working electrodes. **a, b** Polarisation curves, **c** the corresponding Tafel slopes, and **d** Nyquist plots of the as produced 1T' WSe_2, 2H $MoSe_2$, and mixed-phase $W_xMo_{1-x}Se_2$ (x ~0.5) nanosheets grown directly on CP.

us to further increase the area accessible to the electrolyte; the specific surface area of the working electrodes reached 258 m^2/g. Similarity in the catalyst morphology allowed us to study the effect of the composition variation on the catalytic performance. Compared in Figure 5.9.a are the polarisation curves of the produced $W_xMo_{1-x}Se_2$ (x = 0-1) nanosheets. The alloyed $W_xMo_{1-x}Se_2$ (x ~0.5) material reaches the benchmarking current density of - 10 mA/cm^2 at a substantially lower overpotential (350 mV) than the corresponding pristine $MoSe_2$ and WSe_2 nanosheets (400 and 480 mV, respectively). Additionally, alloying was found to significantly improve the reaction kinetics. This is evidenced by the Tafel slope lowering from 135 mV/dec in the pristine WSe_2 to 102 mV/dec in the $W_xMo_{1-x}Se_2$ (x ~0.5) that is close to that of the pristine $MoSe_2$ (92 mV/dec) as shown in Figure 5.9.c. The results of electrochemical impedance spectroscopy (Figure 5.9.d) indicate the unexpectedly low charge transfer resistance of only 5.5 Ω in the case of the alloyed nanosheets compared to 30 Ω of the metallic 1T' WSe_2 and 35 Ω of the semiconducting 2H $MoSe_2$ nanosheets.

The enhancement of catalytic activity has been reported recently for the ternary alloyed $W_xMo_{1-x}S_2$ nanosheets [160,380,381] and colloidal $W_xMo_{1-x}Se_2$ nanoflowers [155]. In two of these

reports, the improved activity has been attributed to the presence of the metallic phase, stabilised by ammonium ions in the $W_xMo_{1-x}S_2$ nanosheets synthesised by hydrothermal approach [160,381]. While an explanation for the improved activity in the purely 2H phase ternary alloy is still missing, it has been hypothesised that in a polycrystalline 2H ternary alloy material, a subtle variation of the electronic structure caused by local strain at the grain boundaries may lead to a decrease in ΔG_H and so to the optimised hydrogen adsorption for the effective catalytic HER [380].

To summarise, we have shown that the electrocatalytic activity of the colloidal WSe_2 can be significantly enhanced via partial isoelectronic substitution of tungsten with molybdenum atoms in the transition metal sublattice. The formation of mixed-cation ternary $W_xMo_{1-x}Se_2$ composition results in a lowering of the reaction overpotential by about 130 mV. Taking into account nearly equal mass loadings, tentatively estimated from the results of ICP OES – 128 μg/cm^2 in the $W_xMo_{1-x}Se_2$ (x ~0.5) compared to 114 μg/cm^2 in the pristine WSe_2; we can assume that the observed effect is mostly attributed to the modification of the electronic structure of the active material. The improvement in the catalytic activity becomes apparent when the catalytic current is being normalised to the mass of active material as shown in Figure 5.9.b. The free-standing $MoSe_2$ and WSe_2 nanoflowers discussed in Chapter 3 are acquired in the semiconducting 2H and the metallic 1T' phases, respectively, while the ternary $W_xMo_{1-x}Se_2$ (x ~0.5) alloy was found to be mixed-phased (Section 4.2). Heterogeneous nucleation of the nanoflowers on carbon paper did not affect the crystal phase of the growing material (Section 5.2). The presence of the metallic phase in the ternary $W_xMo_{1-x}Se_2$ (x ~0.5) alloy can cause the experimentally observed superior catalytic performance and faster reaction kinetics compared to the respective pristine counterparts.

5.4. Efficiency of colloidal TMD nanosheets for catalytic hydrogen reduction

The efficiency of the nanostructured catalyst strongly depends on the balance of many factors. For example, having a branched morphology is considered beneficial for catalysis since such morphology provides high surface area accessible to the electrolyte or, what is more important in the case of group VIB TMDs, high number of active edge sites involved in the catalytic hydrogen reduction [89]. At the same time, the increased resistive losses due to charge carriers dissipation at the grain boundaries and hydrophobicity (hence poor wettability) attributed to the high surface roughness [131,140] can impede the performance of the edge-enriched catalyst. The lateral size of TMD nanosheets has also been identified as a parameter, influencing the catalytic efficiency. Thus, the decrease in lateral size of the mechanically exfoliated WS_2 nanosheets and so the decrease in the fraction of catalytically-inert basal planes led to the improved catalysis [99]. However, for the metallic 1T' phase material, the opposite might be beneficial since the 1T' basal planes were shown to be catalytically-active [94]. In the previous sections, we have compared the WSe_2-based catalysts of similar morphology to point out the advantages of the phase control (metallic 1T' phase vs semiconducting 2H) and composition variation (pristine WSe_2 vs alloyed $W_xMo_{1-x}Se_2$) that led to the improved catalytic performance. Here, we compare the performance of the synthesised colloidal WSe_2, $MoSe_2$, and $W_xMo_{1-x}Se_2$ (x ~0.5) nanoflowers with the reported group VIB TMD catalysts.

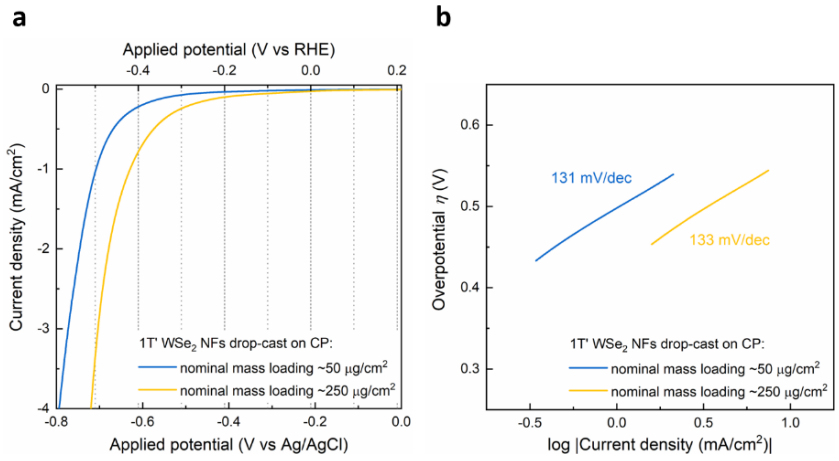


Figure 5.10. Effect of the catalyst mass loading on performance of the working electrodes. **a** Polarisation curves and **b** the corresponding Tafel slopes of the 1T' WSe_2 working electrodes with different mass loading produced via drop-casting approach.

The parameter chosen as a metrics for comparison is the commonly accepted reaction overpotential required to achieve the catalytic current density of -10 mA/cm^2 [290,295]. The current density at the working electrode is proportional to the number of active sites involved

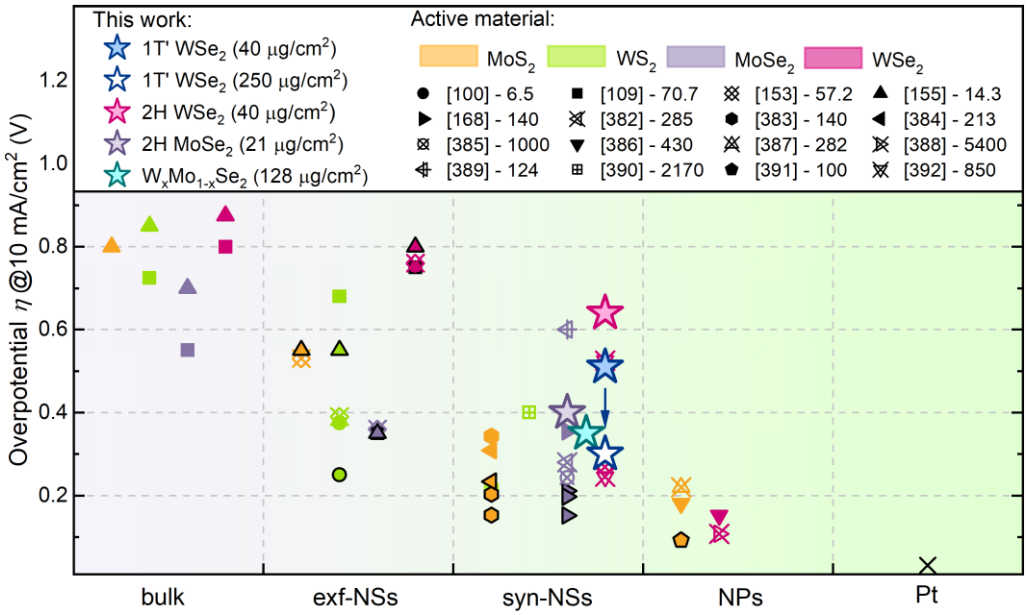


Figure 5.11. Comparison with the reported group VIB TMD electrocatalysts.

in the catalytic reaction and hence to the mass loading of active material. To illustrate this, we prepared two working electrodes by drop-casting a suspension of the 1T' WSe_2 nanoflowers on carbon paper, achieving the mass loading of 50 and 250 μg/cm^2. Compared in Figure 5.10.a are the respective polarisation curves, illustrating a clear decrease in overpotential when the catalyst mass loading increases from 50 to 250 μg/cm^2, while the Tafel slope, characterising the reaction kinetics, remains unchanged (Figure 5.10.b).

We compared the catalytic performance of our $W_xMo_{1-x}Se_2$ working electrodes with the literature, where the performance was evaluated in similar conditions (1M H_2SO_4 electrolyte) and where the catalyst mass loading was clearly stated (Figure 5.11). Comparative data points, representing various group VIB TMD catalyst morphologies: bulk material, mechanically and chemically exfoliated nanosheets (exf-NSs), nanosheets obtained via solution-phase approaches (syn-NSs), and nanoparticles (NPs); were taken from [100,109,387–392,153,155,168,382–386]. For this comparative study, nanoparticles are distinguished from nanosheets based on the reported lateral dimensions of the corresponding TMD nanostructures. Typically, the lateral size of TMD nanoparticles is about 10 nm [391], whereas in the case of nanosheets, it generally varies from a few hundreds of nm [168] to a few microns [109]. In each category, the data points, corresponding to the metallic 1T(1T') phases, have black borders, while the data points without borders represent the semiconducting 2H phase. For each reference data point, the catalyst mass loading (in μg/cm^2) is listed in the legend. The overpotentials, at which the working electrodes composed of the colloidal 1T' and 2H WSe_2 (40 μg/cm^2), 2H $MoSe_2$ (21 μg/cm^2),

and mixed-phase $W_xMo_{1-x}Se_2$ (x ~0.5, 128 μg/cm^2) nanosheets reach the current density of -10 mA/cm^2, are shown with filled stars.

The overall trend illustrated in Figure 5.11 for each given group VIB TMD material is that the catalytic activity scales inversely with the catalyst lateral dimensions. This is expected due to the increased density of accessible catalytically-active edge sites as the catalyst lateral dimensions are decreasing from bulk to 2D nanosheets and eventually to 0D nanoparticles that allows achieving the benchmarking catalytic current density (-10 mA/cm^2) at lower reaction overpotentials. Recently, this trend has been proved empirically in a series of experiments where WS_2 nanosheets produced via liquid phase exfoliation were sorted by cascade centrifugation into batches with progressively decreasing lateral size [99]. On the other hand, within each category, metallic group VIB TMD catalysts generally demonstrate an enhanced catalytic performance compared to the 2H counterparts provided that the mass loading of active material is the same. This is due to the improved electrical conductivity [96] and activation of basal planes in the 1T(1T') polymorph [94].

Our colloidal 1T' WSe_2 and 2H $MoSe_2$ nanosheets demonstrate the catalytic performance comparable to that of chemically exfoliated 1T $MoSe_2$ and 1T WS_2 nanosheets [384] and better than that of synthesised 2H $MoSe_2$ [153] and exfoliated 2H $MoSe_2$ and 2H WSe_2 nanosheets [383]. Although it should be mentioned that the activity is slightly lower than that of the ammonium-stabilised 1T WS_2 [109] and 1T $MoSe_2$ [385] nanosheets synthesised via hydrothermal reaction. In the previous section, we have demonstrated that modifying the catalyst composition by forming an alloy can be attempted in order to enhance the catalytic performance. In Figure 5.11, this is illustrated by the data point (teal star) corresponding to the mixed-phase $W_xMo_{1-x}Se_2$ (x ~0.5) nanosheets. It should be mentioned that the available data on the group VIB TMD catalysts with ternary compositions is limited in literature [155,160,381,393]. Compared to the reported ternary $W_xMo_{1-x}Se_2$ catalysts [155], our colloidal $W_xMo_{1-x}Se_2$ (x ~0.5) nanosheets require a higher overpotential to achieve the benchmarking catalytic current density (350 mV in this work vs 209 mV in [155]); however, in the cited work the mass loading of active material is nearly an order of magnitude higher (1000 μg/cm^2) than achieved in our system (128 μg/cm^2). The direct comparison with other ternary TMD catalysts, such as $WS_{2x}Se_{2(1-x)}$ and $W_xMo_{1-x}S_2$, was not done at this stage due to the lack of information about the catalyst mass loading [393] or about the ternary-composition-dependant metallic phase content [160,381] in the respective reports.

5.5. Stability of the active material under electrochemical testing conditions

Apart from the apparent activity for the catalytic hydrogen reduction, the long-term durability of the solution processed $W_xMo_{1-x}Se_2$ (x = 0-1) nanosheets under the electrocatalytic testing conditions is an important factor to assess. Here, we compare the short-term stability of the working electrodes produced via direct growth and drop-casting approaches and then study the long-term durability of the former ones. For this, we repeatedly swept the applied potential cathodically from 0 to -0.8 V vs $Ag/AgCl_{(3M\ KCl)}$ reference electrode at a scan rate of 10 mV/s; then the polarisation curves of the working electrodes before cycling and after a certain number of cycles were compared in order to visualise changes in the catalytic performance. Normally, the performance of the working electrodes was monitored during 10-20 polarisation cycles for the basic characterisation and during ~3000 cycles for the long-term stability testing. Basic testing was performed in a standard three-electrode cell configuration with a carbon foil counter electrode and a Ag/AgCl reference electrode in 1M H_2SO_4 electrolyte unless stated otherwise.

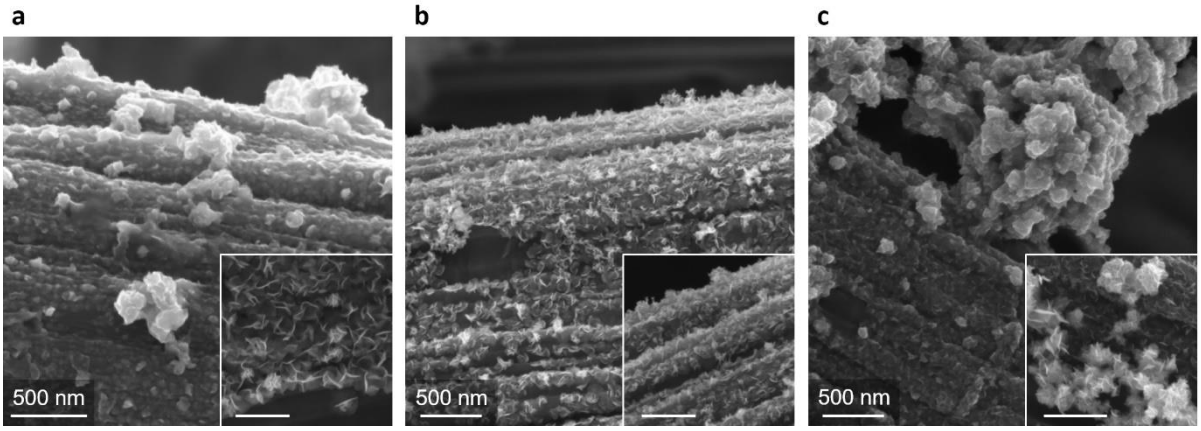


Figure 5.12. Change in morphology of the active material after a short (10-20 cycles) electrochemical testing. **a**, **b**, **c** – SEM images of the WSe_2, $MoSe_2$, and alloyed $W_xMo_{1-x}Se_2$ (x ~0.5) nanosheets grown directly on CP after EC testing, respectively. SEM images of the corresponding working electrodes before the EC testing are presented in insets, scale bars 500 nm.

Shown in Figure 5.12 are the representative SEM images of the $W_xMo_{1-x}Se_2$ (x = 0-1) nanosheets grown on CP after the basic electrochemical testing. The functional coatings grown directly on conductive carbon paper appear to be stable under the electrochemical testing conditions, displaying a continuous coverage of the carbon fibres with the well-adhered vertically aligned $W_xMo_{1-x}Se_2$ (x = 0-1) nanosheets preserved after ~20 catalytic cycles. However, the morphology of individual $W_xMo_{1-x}Se_2$ nanosheets deteriorates slightly as evidenced by the nanosheet edges appearing fused. The SEM images of the respective working electrodes before testing are presented in insets in panels a-c Figure 5.12.

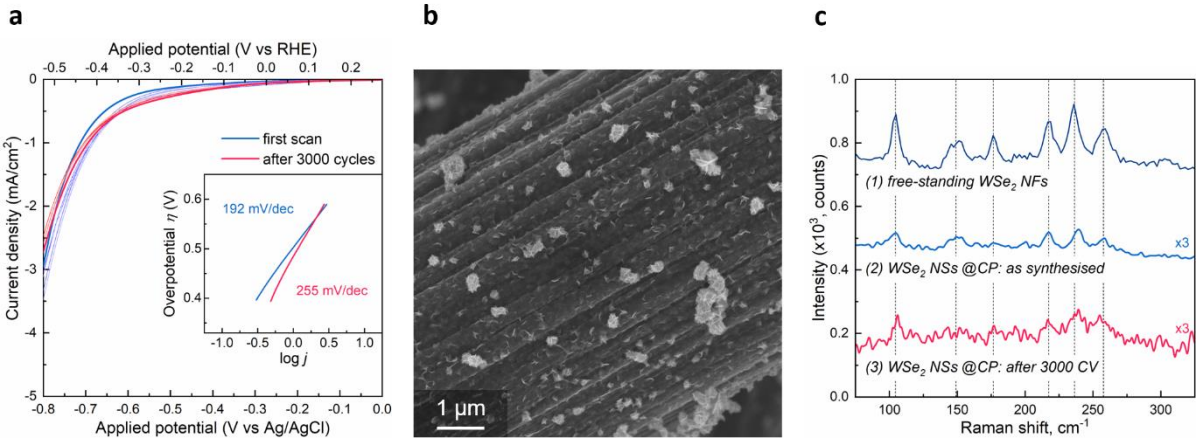


Figure 5.13. Durability test of the WSe_2 on CP working electrodes for the HER. **a** Evolution of the current density at the working electrode during the long-term cycling in 1M H_3PO_4 electrolyte. Solid lines correspond to the initial (blue) and the final (3000 cycles, red) polarisation curves; corresponding Tafel slopes are shown in insets; the intermediate (100, 500, 1000, 1500, 2000, 2500) scans are represented by dashed lines. **b** SEM image of the electrode surface after 3000 catalytic cycles. **c** Raman spectra of the pristine 1T' WSe_2 free-standing nanoflowers (1), pristine 1T' WSe_2 vertical nanosheets grown on CP (2), and WSe_2 vertical nanosheets on CP after 3000 of the catalytic HER cycles (3).

The long-term durability (3000 cycles) of the working electrodes (WSe_2) produced via direct growth approach was assessed in 1M H_3PO_4. Phosphoric acid was used as an electrolyte to exclude any errors, arising from the gradual deposition of impurities during the prolonged cycling at reducing potentials as discussed in Section 2.4.3. The approaches to test the long-term stability of active material reported for the nanostructured TMDs vary greatly and no consensus about the best procedure has been reached so far. In many works, the screening was carried out by repeating cycling voltammetry (CV) at high scan rates (50-100 mV/s), reaching the bias potential required to achieve the benchmarking current density [104,375,377]. Alternatively, either potentiostatic or galvanostatic electrolysis can be performed over a course of 12-60 hours to monitor either the delivered current density or the required potential variation [104,108,290,394]. The repeating CV, which is also known as accelerated degradation, is often preferred as this approach requires less time to assess the material stability under electrolysis conditions. The variation in current density or drop in overpotential after a certain number of catalytic cycles is reported, however, the number of cycles is not strictly defined and typically varies between 1000 [103,395] and 5000 [111,377].

To perform the durability testing, we repeatedly cycled working electrodes in the applied potential window from 0 to -0.8 V vs Ag/AgCl reference electrode at a scan rate of 50 mV/s. The polarisation curves before cycling and after a certain number of cycles were then compared. Continuous cycling in 1M H_3PO_4 reveals only a minor decline in the catalytic

current density as shown in Figure 5.13.a, suggesting the overall good stability of the WSe_2 functional coating under the prolonged electrocatalytic operation conditions. After 3000 catalytic cycles, the working electrode demonstrated 92% retention of the current density at the -0.8 V vs Ag/AgCl applied potential. This value is comparable to that reported for metallic MoS_2 nanosheets, retaining about 88% of the catalytic current density after 1000 cycles of continuous operation [[159]]. Lower current densities and higher Tafel slopes achieved in the electrolysis in phosphoric acid are most likely to be caused by considerably lower concentration of protons in the electrolyte[11]; however, the increase in the Tafel slope values repeatedly observed after the prolonged catalytic testing can be caused by degradation of the catalyst morphology. SEM imaging performed on the working electrode reveals that the active material uniformly coats the carbon fibres even after 3000 catalytic cycles in H_3PO_4, indicating a strong covalent binding between the active material and functional substrate. Achieving such a good connection without an aid of binding additives is essential to design a catalyst that can withstand the harsh corrosive conditions of prolonged electrolysis. The individual vertical nanosheets, however, appear slightly fused compared to the morphology of pristine material (Figure 5.13.b). These changes may lead to a decrease of the number of catalytically-active edge sites and so to the minor decrease in the delivered catalytic current density during prolonged electrolysis as reported in Figure 5.13.a. Raman spectroscopy confirms the retention of the 1T' phase in active material after the prolonged catalytic testing as shown in Figure 5.13.c. It should be mentioned that the overall lower Raman signal intensity is typical for the structures grown on carbon fibres compared to the ones deposited on Si/SiO_2 substrates. This can be attributed to lower material mass loading and to the roughness of the CP surface making it difficult to focus at the topmost layer of the sample.

Overall, we have shown that the nanostructured WSe_2 catalyst grown on CP demonstrates a good stability for at least 3000 catalytic HER cycles performed in 1M H_3PO_4.

[11] $pK_{a1}(H_3PO_4) = 2.16$, $pK_{a2}(H_2SO_4) = 1.99$ [[251]].

5.6. Conclusions

The great interest in nanostructured, edge-abundant TMDs for catalysis is attributed to the high number of catalytically-active edge sites per mass unit available for the reaction. Growing the active material directly on conductive support platforms allowed us to fabricate nanostructured working electrodes, suitable for using in electrolysis as produced. During such growth, the edge-rich morphology, crystal phase, and ternary composition of the active material were preserved in the functional coating. Moreover, we have demonstrated that growing active material directly on a substrate instead of depositing it, for example, via drop-casting, from a colloidal suspension has allowed us to achieve much better adhesion and electrical connection to the substrate. This is manifested in significantly reduced resistive losses (lower charge transfer resistance) and measurably faster catalytic reaction kinetics (lower Tafel slopes).

The crystal phase engineering and composition tailoring, feasible in a solution-phase process via regulating the activity of molecular precursors, have allowed us to enhance the catalytic activity of WSe_2. Firstly, we demonstrated that the metastable 1T' polymorph of WSe_2 exhibits higher activity for the HER compared to the 2H counterpart. The higher activity and faster reaction kinetics were evidenced by lowering the overpotential, Tafel slope and charge transfer resistance in the 1T' phase. By keeping the catalyst morphology and mass loading equal in both the 1T' and 2H WSe_2 electrodes, we were able to assign the observed catalytic enhancement to the higher conductivity of the metallic phase and to the activation of inert basal planes in the 1T' phase, which led to the increased number of catalytically-active sites. Moreover, alloying the 1T'-phased WSe_2 with molybdenum has led to further lowering the reaction overpotential. We found that the cation-mixed $W_xMo_{1-x}Se_2$ alloy is structurally heterogeneous, consisting of nm^2-sized patches of the 1T' and 2H phases, while displaying high compositional homogeneity. The presence of the metallic phase in the ternary colloidal nanoflowers can facilitate the catalytic hydrogen reduction as was supported by faster reaction kinetics and lower reaction overpotential.

Finally, we compared the evaluated catalytic activity of the nanostructured TMDs with the group VIB TMD catalysts reported in literature. We found that the colloidal nanoflowers outperform the majority of the mechanically exfoliated and synthesised via hydrothermal route 2H-TMD counterparts, while demonstrating performance comparable to that of the chemically exfoliated and synthesised 1T-TMD materials.

Chapter 6:
Concluding remarks and outlook

6.1. Concluding remarks

The objective of this work was to develop a solution-phase protocol to controllably grow nanostructured binary metal chalcogenides for application in electrocatalysis. We have demonstrated that colloidal $MoSe_2$, $MoTe_2$, and WSe_2 nanoflowers can be successfully synthesised through a solution-phase reaction between the transition metal (carbonyl or chloride) and chalcogen (trioctylphosphine selenide or telluride complex) molecular precursors. We have systematically investigated the effect of reaction conditions on the morphology and crystal phase of the obtained material. In particular, we have demonstrated that using a more reactive metal precursor (chloride) is crucial to achieve any measurable nucleation and growth of $MoTe_2$ nanosheets. Whereas, such high reactivity is not necessary for the diselenide systems and changing the metal precursor to less reactive carbonyl allowed us to control the nucleation of the solid phase that led to the formation of well-defined WSe_2 and $MoSe_2$ nanoflowers. Furthermore, the coordinating solvent in the colloidal synthesis of binary layered metal chalcogenides needs to be chosen carefully. Due to their chemical inertness, the chalcogen basal planes are not suitable for the covalent functionalisation and the majority of capping ligands coordinate the transition-metal-rich lateral surfaces. Performing the reactions in a weakly coordinating solvent (oleic acid) allowed us to achieve a considerable lateral extension of the atomically-thin petals of WSe_2 and $MoSe_2$ nanoflowers. Moreover, removing the coordinating solvent (free oleic acid) entirely and carrying out the reaction from a stoichiometric bismuth oleate precursor in a non-coordinating solvent (octadecene) resulted into the atomically-thin Bi_2Te_3 nanosheets being synthesised at temperatures as low as 20 ^oC. Removing the excess of capping ligand was especially important in the low-temperature syntheses since the slow ligand dynamics on the growing surface leads to its effective passivation and inhibits the lateral growth of Bi_2Te_3 nanostructures.

The colloidal synthesis approach designed within this work allowed us to obtain the 1T' phases of WSe_2 and $MoTe_2$ directly through the solution-phase reaction. The controllable synthesis of the metastable metallic polymorphs over the thermodynamically stable semiconducting ones achieved in the solution phase is appealing for producing the free-standing nanostructures with the desired electronic properties. This becomes possible in the

systems with a small energy difference between the polymorphs. We attribute the formation of the metastable 1T' phases of WSe_2 and $MoTe_2$ to the fact that under the descried synthesis conditions the reaction is likely to occur in the kinetically-controlled regime. The produced metastable 1T' phase is locked due to the numerous grain (petal) boundaries present in the branches flower-like structures and therefore is stable under ambient conditions. However, the post-growth thermal annealing at 400 ºC in an argon atmosphere led to the restoration of the thermodynamically stable 2H phase, while preserving the branched morphology of the atomically-thin WSe_2 nanoflowers. We have demonstrated that a complete 1T'-to 2H phase conversion was achieved that allowed us to compare the electronic properties and the catalytic activity of both the 1T' and 2H nanostructured WSe_2 polymorphs.

A controllable switching between the kinetically- and thermodynamically-driven growth modes can in principle be achieved via tuning the supersaturation in the reaction medium. In the case of Bi_2Te_3 growth, we demonstrated that the kinetic control can prevail over the diffusion-limited regime when the growth temperature is optimised. Thus, we have shown the formation of highly branched Bi_2Te_3 nanoflowers, exhibiting the uncommon high-index lateral termination, when the reaction was carried out under high supersaturation (low temperature). Whereas the uniformly-shaped hexagonal Bi_2Te_3 nanoplates were obtained under low supersaturation when the reaction is supposedly thermodynamically-controlled.

The composition of the colloidal TMD nanoflowers can be modulated during the solution phase without sacrificing their edge-abundant morphology. In this work, we have shown that the formation of Cu- and Fe-doped WSe_2 nanoflowers and cation-mixed ternary $W_xMo_{1-x}Se_2$ alloys is feasible in the solution phase. The ternary compositions were achieved by simply combining the precursors of both transition metals in the reaction mixture. The composition of the ternary alloys can be altered by varying the ratio between the respective transition metal precursors.

Finally, the developed solution-phase growth approach allowed for the rational design of catalyst material via the crystal phase engineering and tailoring the composition. In this work, we demonstrated that well-adhered functional coatings of nanostructured TMDs can be synthesised directly on conductive support platforms. Moreover, the kinetically-controlled growth of the metastable 1T' polymorph allowed us to enhance the catalytic activity of the nanostructured WSe_2. Further improvement in catalytic performance was achieved in the 1T'/2H mixed-phased $W_xMo_{1-x}Se_2$ alloys, demonstrating the superior activity compared to the parent 1T' WSe_2 nanoflowers.

6.2. Future work

6.2.1. Solution-phase synthesis of atomically-thin binary metal chalcogenides

- The formation mechanism of branched flower-like nanostructures remains unclear. Although we have demonstrated that the well-defined morphologies can be achieved in the syntheses carried out in a weakly coordinating solvent, while subtle tuning of the transition metal complex led to a significant lateral extension of the atomically-thin petals, the principle understanding of the branching process, which would allow tuning the degree of branching in these nanostructures, is still lacking. A follow up work developing an understanding of the very early stages of solution-phase nucleation and growth of binary layered metal chalcogenides is envisioned.
- A precise control over the two-dimensional growth in layered metal chalcogenides is lacking due to the chemical inertness of their basal planes. A templated solution-phase growth of two-dimensional nanosheets in ordered lamellar micelles can potentially allow for supressing the vertical growth mode, always competing with lateral extension, by confining the growing material between the micelle layers. Cetyltrimethylammonium bromide may be a potential surfactant of choice, forming ordered two-dimensional micelles in ternary mixtures with water and organic solvents.
- It is emerging that aliphatic thiols can be used to heal chalcogen vacancies in the basal planes of TMDs. Using these thiols as additives during a solution-phase reaction would therefore be of great interest since they might allow for an effective passivation of the basal planes of growing TMD nanosheet, thus inhibiting the vertical growth. However, the potential problems associated with such growth control include unintentional sulphur doping of the material.
- In order to effectively control the balance between the lateral extension and vertical growth in the synthesis of two-dimensional layered metal chalcogenides, a wider range of capping ligands needs to be screened. To rationally outline such a study, a prior modelling of the surfactant dynamics on various lateral and basal surfaces of the nanocrystal is required.
- We have attributed the formation of the metastable 1T' phase of WSe_2 and $MoTe_2$ to the kinetically-driven reaction between the molecular precursors. Further investigation of possible switching into the thermodynamically-controlled mode is of great interest. To induce nucleation under low supersaturation, a slow accumulation of highly reactive precursor, which can be achieved via a dropwise injection, may be beneficial.

6.2.2. Composition variation via a solution-phase processing

- We have demonstrated that the incorporation of Cu and Fe species in the colloidal WSe_2 nanoflowers can be achieved, however, the chemical states and local coordination of dopants in the host lattice or around the defect sites in the colloidal WSe_2 nanosheets needs to be investigated.
- We mentioned that the achievable doping levels are limited by the composition of ternary phases existing in the Fe-W-Se and Cu-W-Se systems. Examination of the highest achievable dopant concentrations is crucial for establishing reliable protocols to synthesise single-phased uniformly-doped TMD material.
- We have demonstrated the formation of 1T'/2H mixed-phased, compositionally uniform, ternary alloys. The most crucial part of future work would be investigating the range, in which the phase composition can be varied. In particular, alloying with molybdenum may provide a route to stabilise the hexagonal crystal phase in WSe_2 nanosheets.
- We found that the reaction yield is always higher in the synthesis of ternary alloys than for the individual $MoSe_2$ and WSe_2 nanostructures. This might be due to the reduced facet dissolution rate in the mixed-cation TMD lattice. The nucleation and growth kinetics of the alloyed phase in comparison to that of the binary counterparts shall be explored.

6.2.3. Application in heterogeneous catalysis

- In this work, the TMD electrodes were tested for the catalytic HER as produced. However, the lateral sides of the synthesised nanostructures are likely to be partially passivated with organic capping ligands. The post-synthesis treatment with mild agents, such as Meerwein salt, may reduce the coverage of active edge-sites with the residual organics, leading to an improvement in the performance of TMD catalysts.
- Chemical treatment of functional substrates (CP) prior the material deposition might be beneficial for achieving higher nucleation density, and therefore higher mass loading of the active material. Short chain aliphatic dithiols would be suitable linkers, forming densely-packed monolayers on the surface of functional support. However, potential deterioration of the electrical contact between the catalyst and the substrate (current collector) needs to be mitigated.
- It is emerging that Cu-doped nanostructured material can be potentially perspective for the electrocatalytic CO_2 reduction.

Bibliography

1. Cheng, R. *et al.* Few-layer molybdenum disulfide transistors and circuits for high-speed flexible electronics. *Nat. Commun.* **5**, 5143 (2014).
2. Zhu, X., Li, D., Liang, X. & Lu, W. D. Ionic modulation and ionic coupling effects in MoS_2 devices for neuromorphic compu*t*ing. *Nat. Mater.* **18**, 141–148 (2019).
3. Acerce, M., Voiry, D. & Chhowalla, M. Metallic 1T phase MoS_2 nanosheets as supercapacitor electrode materials. *Nat. Nanotechnol.* **10**, 313–318 (2015).
4. Pomerantseva, E. & Gogotsi, Y. Two-dimensional heterostructures for energy storage. *Nat. Energy* **2**, 17089 (2017).
5. Xiong, P. *et al.* Interface modulation of two-dimensional superlattices for efficient overall water splitting. *Nano Lett.* **19**, 4518–4526 (2019).
6. Radisavljevic, B., Radenovic, A., Brivio, J., Giacometti, V. & Kis, A. Single-layer MoS_2 transistors. *Nat. Nanotechnol.* **6**, 147–150 (2011).
7. Unuchek, D. *et al.* Room-temperature electrical control of exciton flux in a van der Waals *h*eterostructure. *Nature* **560**, 340–344 (2018).
8. Jaramillo, T. F. *et al.* Identification of active edge sites for electrochemical H_2 evolution from MoS_2 nanocatalysts. *Science* **317**, 100–102 (2007).
9. Jin, W. *et al.* Direct measurement of the thickness-dependent electronic band structure of MoS_2 using angle-resolved photoemission spectroscopy. *Phys. Rev. Lett.* **111**, 106801 (2013).
10. Dawson, W. G. & Bullett, D. W. Electronic structure and crystallography of $MoTe_2$ and WTe_2. *J. Phys. C Solid State Phys.* **20**, 6159–6174 (1987).
11. Zhang, H. *et al.* Topological insulators in Bi_2Se_3, Bi_2Te_3 and Sb_2Te_3 with a single Dirac cone on the surface. *Nat. Phys.* **5**, 438–442 (2009).
12. Qian, X., Liu, J., Fu, L. & Li, J. Quantum spin Hall effect in two-dimensional transition metal dichalcogenides. *Science* **346**, 1344–1347 (2014).
13. Zhou, W. *et al.* Intrinsic structural defects in monolayer molybdenum disulfide. *Nano Lett.* **13**, 2615–2622 (2013).
14. Bos, J. W. G., Zandbergen, H. W., Lee, M.-H., Ong, N. P. & Cava, R. J. Structures and thermoelectric properties of the infinitely adaptive series $(Bi_2)_m(Bi_2Te_3)_n$. *Phys. Rev. B* **75**, 195203 (2007).
15. Chhowalla, M. *et al.* The chemistry of two-dimensional layered transition metal dichalcogenide nanosheets. *Nat. Chem.* **5**, 263–275 (2013).
16. Wang, Q. H., Kalantar-Zadeh, K., Kis, A., Coleman, J. N. & Strano, M. S. Electronics and optoelectronics of t*w*o-dimensional transition metal dichalcogenides. *Nat. Nanotechnol.* **7**, 699–712 (2012).
17. Cotton, F. A. & Wilkinson, G. *Advanced inorganic chemistry*. (Wiley, 1988).
18. Yang, H., Kim, S. W., Chhowalla, M. & Lee, Y. H. Structural and quantum-state phase transition in van der Waals layered materials. *Nat. Phys.* **13**, 931–937 (2017).
19. Schutte, W. J., De Boer, J. L. & Jellinek, F. Crystal structures of tungsten disulfide and

diselenide. *J. Solid State Chem.* **70**, 207–209 (1987).

20. Duerloo, K.-A. N., Li, Y. & Reed, E. J. Structural phase transitions in two-dimensional Mo- and W-dichalcogenide monolayers. *Nat. Commun.* **5**, 1–9 (2014).
21. Lee, C.-H. *et al.* Tungsten ditelluride: a layered semimetal. *Sci. Rep.* **5**, 10013 (2015).
22. Eda, G. *et al.* Coherent atomic and electronic heterostructures of single-layer MoS_2. *ACS Nano* **6**, 7311–7317 (2012).
23. Li, Y., Duerloo, K.-A. N., Wauson, K. & Reed, E. J. Structural semiconductor-to-semimetal phase transition in two-dimensional materials induced by electrostatic gating. *Nat. Commun.* **7**, 10671 (2016).
24. Kertesz, M. & Hoffmann, R. Octahedral vs. trigonal-prismatic coordination and clustering in transition-metal dichalcogenides. *J. Am. Chem. Soc.* **106**, 3453–3460 (1984).
25. Lin, Y.-C., Dumcenco, D. O., Huang, Y.-S. & Suenaga, K. Atomic mechanism of the semiconducting-to-metallic phase transition in single-layered MoS_2. *Nat. Nanotechnol.* **9**, 391–396 (2014).
26. Heising, J. & Kanatzidis, M. G. Structure of restacked MoS_2 and WS_2 elucidated by electron crystallography. *J. Am. Chem. Soc.* **121**, 638–643 (1999).
27. Qin, X. R., Yang, D., Frindt, R. F. & Irwin, J. C. Real-space imaging of single-layer MoS_2 by scanning tunneling microscopy. *Phys. Rev. B* **44**, 3490–3493 (1991).
28. Tsai, H. L., Heising, J., Schindler, J. L., Kannewurf, C. R. & Kanatzidis, M. G. Exfoliated-restacked phase of WS_2. *Chem. Mater.* **9**, 879–882 (1997).
29. Amara, K. K. *et al.* Dynamic structural evolution of metal–metal bonding network in monolayer WS_2. *Chem. Mater.* **28**, 2308–2314 (2016).
30. Brown, B. E. The crystal structures of WTe_2 and high-temperature $MoTe_2$. *Acta Crystallogr.* **20**, 268–274 (1966).
31. Chen, S., Goldstein, T., Venkataraman, D., Ramasubramaniam, A. & Yan, J. Activation of new Raman modes by inversion symmetry breaking in type II Weyl semimetal candidate T′-$MoTe_2$. *Nano Lett.* **16**, 5852–5860 (2016).
32. Qi, Y. *et al.* Superconductivity in Weyl semimetal candidate $MoTe_2$. *Nat. Commun.* **7**, 11038 (2016).
33. Rhodes, D. *et al.* Engineering the structural and electronic phases of $MoTe_2$ through W substitution. *Nano Lett.* **17**, 1616–1622 (2017).
34. Zhou, Y. *et al.* Pressure-induced T*d* to 1T′ structural phase transition in WTe_2. *AIP Adv.* **6**, 075008 (2016).
35. Xia, J. *et al.* Pressure-induced phase transition in Weyl semimetallic WTe_2. *Small* **13**, 1701887 (2017).
36. Murray, R. B., Bromley, R. A. & Yoffe, A. D. The band structures of some transition metal dichalcogenides. II. Group IVA; octahedral coordination. *J. Phys. C Solid State Phys.* **5**, 746–758 (1972).
37. Zhao, X., Ning, S., Fu, W., Pennycook, S. J. & Loh, K. P. Differentiating polymorphs in molybdenum disulfide via electron microscopy. *Adv. Mater.* **30**, 1802397 (2018).
38. Wang, Z. *et al.* $MoTe_2$: A type-II Weyl topological metal. *Phys. Rev. Lett.* **117**, 056805

(2016).

39. Zeng, Z. *et al.* Controlled vapor growth and nonlinear optical applications of large-area 3R phase WS_2 and WSe_2 atomic layers. *Adv. Funct. Mater.* **1806874**, 1806874 (2019).

40. Wilson, J. A. & Yoffe, A. D. The transition metal dichalcogenides discussion and interpretation of the observed optical, electrical and structural properties. *Adv. Phys.* **18**, 193–335 (1969).

41. Xu, H. *et al.* Observation of gap opening in 1T′ phase MoS_2 nanocrystals. *Nano Lett.* **18**, 5085–5090 (2018).

42. Cheng, F. *et al.* Interface engineering of Au(111) for the grow*t*h of 1T′-$MoSe_2$. *ACS Nano* (2019). doi:10.1021/acsnano.8b09054

43. Ugeda, M. M. *et al.* Observation of topologically protected states at crystalline phase boundaries in single-layer WSe_2. *Nat. Commun.* **9**, 3401 (2018).

44. Chen, S., Lu, S. & Chang, J. Bi-In-Te phase diagram. *J. Alloys Compd.* **722**, 499–508 (2017).

45. Concepción, O. *et al.* Controlling the epitaxial growth of Bi_2Te_3, BiTe, and Bi_4Te_3 pure phases by physical vapor transport. *Inorg. Chem.* **57**, 10090–10099 (2018).

46. Teweldebrhan, D., Goyal, V. & Balandin, A. A. Exfoliation and characterization of bismuth telluride atomic quintuples and quasi-two-dimensional crystals. *Nano Lett.* **10**, 1209–1218 (2010).

47. Yamana, K., Kihara, K. & Matsumoto, T. Bismuth tellurides: BiTe and Bi_4Te_3. *Acta Crystallogr. Sect. B Struct. Crystallogr. Cryst. Chem.* **35**, 147–149 (1979).

48. Bullett, D. W. Electronic band structure and bonding in transition metal layered dichalcogenides by atomic orbital meth*o*ds. *J. Phys. C Solid State Phys.* **11**, 4501–4514 (2001).

49. Coehoorn, R. *et al.* Electronic structure of $MoSe_2$, MoS_2, and WSe_2. I. Band-structure calculations and photoelectron spectroscopy. *Phys. Rev. B* **35**, 6195–6202 (1987).

50. Bromley, R. A., Murray, R. B. & Yoffe, A. D. The band structures of some transition metal dichalcogenides. III. Group VIA: trigonal prism materials. *J. Phys. C Solid State Phys.* **5**, 759–778 (1972).

51. Yoffe, A. D. Layer compounds. *Annu. Rev. Mater. Sci.* **3**, 147–170 (1973).

52. Calandra, M. Chemically exfoliated single-layer MoS_2: Stability, lattice dynamics, and catalytic adsorption from first principles. *Phys. Rev. B* **88**, 245428 (2013).

53. Coehoorn, R., Haas, C. & de Groot, R. A. Electronic structure of $MoSe_2$, MoS_2, and WSe_2. II. The nat*u*re of the optical band gaps. *Phys. Rev. B* **35**, 6203–6206 (1987).

54. Li, H. *et al.* From bulk to monolayer MoS_2: Evolution of Raman scattering. *Adv. Funct. Mater.* **22**, 1385–1390 (2012).

55. Zhao, W. *et al.* Evolution of electronic structure in atomically thin sheets of WS_2 and WSe_2. *ACS Nano* **7**, 791–797 (2013).

56. Backes, C. *et al.* Edge and confinement effects allow in situ measurement of size and thickness of liquid-exfoliated nanosheets. *Nat. Commun.* **5**, 1–10 (2014).

57. Splendiani, A. *et al.* Emerging photoluminescence in monolayer MoS_2. *Nano Lett.* **10**, 1271–1275 (2010).

58. Klein, A., Tiefenbacher, S., Eyert, V., Pettenkofer, C. & Jaegermann, W. Electronic band structure of sing*l*e-crystal and single-layer WS_2: Influence of interlayer van der Waals interactions. *Phys. Rev. B* **64**, 205416 (2001).

59. Neville, R. A. & Evans, B. L. The band edge excitons in 2H-MoS_2. *Phys. Status Solidi* **73**, 597–606 (1976).

60. Xiao, D., Liu, G.-B., Feng, W., Xu, X. & Yao, W. Coupled spin and valley physics in monolayers of MoS_2 and other group-VI dichalcogenides. *Phys. Rev. Lett.* **108**, 196802 (2012).

61. Jones, A. M. *et al.* Optical generation of excitonic valley coherence in monolayer WSe_2. *Nat. Nanotechnol.* **8**, 634–638 (2013).

62. Böker, T. *et al.* Band structure of MoS_2, $MoSe_2$, and a-$MoTe_2$: Angle-resolved photoelectron spectroscopy and ab inition calculations. *Phys. Rev. B* **64**, 235305 (2001).

63. Kam, K. K. & Parkinson, B. A. Detailed photocurrent spectroscopy of the semiconducting group VIB transition metal dichalcogenides. *J. Phys. Chem.* **86**, 463–467 (1982).

64. Mak, K. F., Lee, C., Hone, J., Shan, J. & Heinz, T. F. Atomically thin MoS_2: A new *d*irect-gap semiconductor. *Phys. Rev. Lett.* **105**, 136805 (2010).

65. Beal, A. R. & Hughes, H. P. Kramers-Kronig analysis of the reflectivity spectra of 2H-MoS_2, 2H-$MoSe_2$ and 2H-$MoTe_2$. *J. Phys. C Solid State Phys.* **12**, 881–890 (1979).

66. Beal, A. R., Knights, J. C. & Liang, W. Y. Transmission spectra of some transition metal dichalcogenides. II. Group VIA: trigonal prismatic coordination. *J. Phys. C Solid State Phys.* **5**, 3540–3551 (1972).

67. Tonndorf, P. *et al.* Photoluminescence emission and Raman response of monolayer MoS_2, $MoSe_2$, and WSe_2. *Opt. Express* **21**, 4908 (2013).

68. Upadhyayula, L. C., Loferski, J. J., Wold, A., Giriat, W. & Kershaw, R. Semiconducting properties of single crystals of n- and p-type tungsten diselenide (WSe_2). *J. Appl. Phys.* **39**, 4736–4740 (1968).

69. Beal, A. R., Liang, W. Y. & Hughes, H. P. Kramers-Kronig analysis of the reflectivity spectra of 3R-WS_2 and 2H-WSe_2. *J. Phys. C Solid State Phys.* **9**, 2449–2457 (1976).

70. Ma, J. *et al.* Experimental progress on layered topological semimetals. *2D Mater.* **6**, 032001 (2019).

71. Liu, P., Williams, J. R. & Cha, J. J. Topological nanomaterials. *Nat. Rev. Mater.* **4**, 479–496 (2019).

72. Das, P. K. *et al.* Electronic properties of candidate type-II Weyl semimetal WTe_2. A review perspective. *Electron. Struct.* **1**, 014003 (2019).

73. Pulkin, A. & Yazyev, O. V. Ro*b*ustness of the quantum spin Hall insulator phase in monolayer 1T′ transition metal dichalcogenides. *J. Electron Spectros. Relat. Phenomena* **219**, 72–76 (2017).

74. Murakami, S., Hirayama, M., Okugawa, R. & Miyake, T. Emergence of topological semimetals in gap closing in semiconductors without inversion symmetry. *Sci. Adv.* **3**, e1602680 (2017).

75. Sun, Y., Zhang, Y., Felser, C. & Yan, B. Strong intrinsic spin Hall Effect in the TaAs

family of Weyl semimetals. *Phys. Rev. Lett.* **117**, 146403 (2016).

76. Okugawa, R. & Murakami, S. Dispersion of Fermi arcs in Weyl semimetals and their evolutions to Dirac cones. *Phys. Rev. B* **89**, 235315 (2014).

77. Wu, Y. *et al.* Observation of Fermi arcs in the type-II Weyl semimetal candidate WTe_2. *Phys. Rev. B* **94**, 121113 (2016).

78. Sun, Y., Wu, S.-C., Ali, M. N., Felser, C. & Yan, B. Prediction of Weyl semimetal in orthorhombic $MoTe_2$. *Phys. Rev. B* **92**, 161107 (2015).

79. Jiang, J. *et al.* Signature of type-II Weyl semimetal phase in $MoTe_2$. *Nat. Commun.* **8**, 13973 (2017).

80. Tang, S. *et al.* Quantum spin Hall state in monolayer 1T'-WTe_2. *Nat. Phys.* **13**, 683–687 (2017).

81. Chen, P. *et al.* Large quantum-spin-Hall gap in single-layer 1T′ WSe_2. *Nat. Commun.* **9**, 2003 (2018).

82. Zhang, F. *et al.* Electric-field induced structural transition in vertical $MoTe_2$- and $Mo_{1-x}W_xTe_2$-based resistive memories. *Nat. Mater.* **18**, 55–61 (2019).

83. Shinagawa, T., Garcia-Esparza, A. T. & Takanabe, K. Insight on Tafel slopes from a microkinetic analysis of aqueous electrocatalysis for energy conversion. *Sci. Rep.* **5**, 13801 (2015).

84. Chia, X., Eng, A. Y. S., Ambrosi, A., Tan, S. M. & Pumera, M. Electrochemistry of nanostructured layered transition metal dichalcogenides. *Chem. Rev.* **115**, 11941–11966 (2015).

85. Nørskov, J. K. *et al.* Trends in the exchange current for hydrogen evolution. *J. Electrochem. Soc.* **152**, J23 (2005).

86. Voiry, D., Yang, J. & Chhowalla, M. Recent strategies for improving the catalytic activity of 2D TMD nanosheets toward the hydrogen evolution reaction. *Adv. Mater.* **28**, 6197–6206 (2016).

87. Hinnemann, B. *et al.* Biomimetic hydrogen evolution: MoS_2 nanoparticles as catalyst for hydrogen evolution. *J. Am. Chem. Soc.* **127**, 5308–5309 (2005).

88. Parija, A. *et al.* Mapping catalytically relevant edge electronic states of MoS_2. *ACS Cent. Sci.* **4**, 493–503 (2018).

89. Tsai, C., Chan, K., Abild-Pedersen, F. & Nørskov, J. K. Active edge sites in $MoSe_2$ and WSe2 catalysts for the hydrogen evolution reaction: a density functional study. *Phys. Chem. Chem. Phys.* **16**, 13156–13164 (2014).

90. Tsai, C., Chan, K., Nørskov, J. K. & Abild-Pedersen, F. Theoretical insights into the hydrogen evolution activity of layered transition metal dichalcogenides. *Surf. Sci.* **640**, 133–140 (2015).

91. Tsai, C. *et al.* Electrochemical generation of sulfur vacancies in the basal plane of MoS_2 for hydrogen evolution. *Nat. Commun.* **8**, 15113 (2017).

92. Tang, Q. & Jiang, D. Mechanism of hydrogen evolution reaction on 1T-MoS_2 from first principles. *ACS Catal.* **6**, 4953–4961 (2016).

93. Lukowski, M. a. *et al.* Enhanced hydrogen evolution catalysis from chemically exfoliated metallic MoS_2 nanosheets. *J. Am. Chem. Soc.* **135**, 10274–10277 (2013).

94. Voiry, D. *et al.* Conducting MoS_2 nanosheets as catalysts for hydrogen evolution reaction. *Nano Lett.* **13**, 6222–6227 (2013).

95. Chen, S. *et al.* Reaction mechanism with thermodynamic structural screening for electrochemical hydrogen evolution on monolayer 1T′ phase MoS_2. *Chem. Mater.* **30**, 5404–5411 (2018).

96. Zhou, Y. *et al.* Revealing the contribution of individual factors to hydrogen evolution reaction catalytic activity. *Adv. Mater.* **30**, 1706076 (2018).

97. Voiry, D. *et al.* The role of electronic coupling between substrate and 2D MoS_2 nanosheets in electrocatalytic production of hydrogen. *Nat. Mater.* **15**, 1003–1009 (2016).

98. Xiao, J., Kou, L., Yam, C.-Y., Frauenheim, T. & Yan, B. Toward rational design of catalysts supported on a topological insulator substrate. *ACS Catal.* **5**, 7063–7067 (2015).

99. Gholamvand, Z., McAteer, D., Harvey, A., Backes, C. & Coleman, J. N. Electrochemical applications of two-dimensional nanosheets: The effect of nanosheet length and thickness. *Chem. Mater.* **28**, 2641–2651 (2016).

100. Yin, Y. *et al.* Contributions of phase, sulfur vacancies, and edges to the hydrogen evolution reaction catalytic activity of porous molybdenum disulfide nanosheets. *J. Am. Chem. Soc.* **138**, 7965–7972 (2016).

101. Li, L. *et al.* Role of sulfur vacancies and undercoordinated Mo regions in MoS_2 nanos*h*eets toward the evolution of hydrogen. *ACS Nano* (2019). doi:10.1021/acsnano.9b01583

102. Ye, G. *et al.* Defects engineered monolayer MoS_2 for improved hydrogen evolution reaction. *Nano Lett.* **16**, 1097–1103 (2016).

103. Kong, D. *et al.* Synthesis of MoS_2 and $MoSe_2$ films with vertically aligned layers. *Nano Lett.* **13**, 1341–1347 (2013).

104. Yan, Y. *et al.* Vertically oriented MoS_2 and WS_2 nanosheets directly grown on carbon cloth as efficient and stable 3-dimensional hydrogen-evolving cathodes. *J. Mater. Chem. A* **3**, 131–135 (2015).

105. Najafi, L. *et al.* Doped-$MoSe_2$ nanoflakes/3d metal oxide-hydr(oxy)oxides hybrid catalysts for pH-universal electrochemical hydrogen evolution reaction. *Adv. Energy Mater.* **1801764**, 1801764 (2018).

106. Luo, Z. *et al.* Chemically activating MoS_2 via spontaneous atomic palladium interfacial doping towards efficient hydrogen evolution. *Nat. Commun.* **9**, 2120 (2018).

107. Xu, K. *et al.* Component-controllable $WS_{2(1-x)}Se_{2x}$ nanotubes for efficient hydrogen evolution reaction. *ACS Nano* **8**, 8468–8476 (2014).

108. Zou, M. *et al.* WSe_2 and $W(Se_xS_{1-x})_2$ nanoflakes grown on carbon nanofibers for the electrocatalytic hydrogen evolution reaction. *J. Mater. Chem. A* **3**, 18090–18097 (2015).

109. Voiry, D. *et al.* Enhanced catalytic activity in str*a*ined chemically exfoliated WS_2 nanosheets for hydrogen evolution. *Nat. Mater.* **12**, 850–855 (2013).

110. Attanayake, N. H. *et al.* Effect of intercalated metals on the electrocatalytic activity of 1T-MoS_2 for the hydrogen evolution reaction. *ACS Energy Lett.* **3**, 7–13 (2018).

111. Deng, J. *et al.* Triggering the electrocatalytic hydrogen evolution activity of the inert two-dimensional MoS_2 surface via single-atom metal doping. *Energy Environ. Sci.* **8**, 1594–1601 (2015).

112. Ambrosi, A., Sofer, Z. & Pumera, M. 2H → 1T phase transition and hydrogen evolution activity of MoS_2, $MoSe_2$, WS_2 and WSe_2 strongly depends on the MX_2 composition. *Chem. Commun.* **51**, 8450–8453 (2015).

113. Novoselov, K. S. *et al.* Two-dimensional gas of massless Dirac fermions in graphene. *Nature* **438**, 197–200 (2005).

114. Novoselov, K. S. *et al.* Two-dimensional atomic crystal*s*. *Proc. Natl. Acad. Sci. U. S. A.* **102**, 10451–10453 (2005).

115. Velický, M. *et al.* Mechanism of gold-assisted exfoliation of centimeter-sized transition-metal dichalcogenide monolayers. *ACS Nano* **12**, 10463–10472 (2018).

116. O'Neill, A., Khan, U. & Coleman, J. N. Preparation of high concentration dispersions of exfoliated MoS_2 with increased flake size. *Chem. Mater.* **24**, 2414–2421 (2012).

117. Coleman, J. N. *et al.* Two-dimensional nanosheets produced by liquid exfoliation of layered materials. *Science* **331**, 568–71 (2011).

118. Smith, R. J. *et al.* Large-scale exfoliation of inorganic layered compounds in aqueous surfactant solutions. *Adv. Mater.* **23**, 3944–3948 (2011).

119. Cunningham, G. *et al.* Solvent exfoliation of transition metal dichalcogenides: dispersibility of exfoliated nanosheets varies only weakly between compounds. *ACS Nano* **6**, 3468–3480 (2012).

120. Backes, C. *et al.* Equipartition of energy defines the size–thickness relationship in liquid-exfoliated nanosheets. *ACS Nano* (2019). doi:10.1021/acsnano.9b02234

121. Backes, C. *et al.* Production of highly monolayer enriched dispersions of liquid-exfoliated nanosheets by liquid cascade centrifugation. *ACS Nano* **10**, 1589–1601 (2016).

122. Kelly, A. G. *et al.* All-printed thin-film transistors from networks of liquid-exfoliated nanosheets. *Science (80-.).* **356**, 69–73 (2017).

123. Heising, J. & Kanatzidis, M. G. Exfoliated and restacked MoS_2 and WS_2 - Ionic or neutral species? Enc*a*psulation and ordering of hard electropositive cations. *J. Am. Chem. Soc.* **121**, 11720–11732 (1999).

124. Voiry, D. *et al.* Covalent functionalization of monolayered transition metal dichalcogenides by phase engineering. *Nat. Chem.* **7**, 45–49 (2014).

125. Lin, Z. *et al.* Solution-processable 2D semiconductors for high-performance large-area electronics. *Nature* **562**, 254–258 (2018).

126. Reale, F. *et al.* High-mobility and high-optical quality atomically thin WS2. *Sci. Rep.* **7**, 1–10 (2017).

127. Yang, P. *et al.* Batch production of 6-inch uniform monolayer molybdenum disulfide catalyzed by sodium in glass. *Nat. Commun.* **9**, 979 (2018).

128. Li, S. *et al.* Edge-enriched 2D MoS_2 thin films grown by chemical vapor deposition for enhanced catalytic performance. *ACS Catal.* **7**, 877–886 (2017).

129. Wang, H. *et al.* High-quality monolayer superconductor $NbSe_2$ grown by chemical

vapour deposition. *Nat. Commun.* **8**, 394 (2017).

130. Zhou, J. *et al.* Large-area and high-quality 2D transition metal telluride. *Adv. Mater.* **29**, 1603471 (2017).

131. Agrawal, A. V. *et al.* Controlled growth of MoS_2 flakes from in-plane to edge-enriched 3D network and their surface-energy studies. *ACS Appl. Nano Mater.* **1**, 2356–2367 (2018).

132. Huang, J.-K. *et al.* Large-area synthesis of highly crystalline WSe_2 monolayers and device applications. *ACS Nano* **8**, 923–930 (2014).

133. Kim, S., Kwak, J., Ciobanu, C. V. & Kwon, S. Recent developments in controlled vapor-phase growth of 2D group 6 transition metal dichalcogenides. *Adv. Mater.* **31**, 1804939 (2019).

134. Prabakaran, A. *et al.* WS_2 2D nanosheets in 3D nanoflowers. *Chem. Commun.* **50**, 12360–12362 (2014).

135. Gao, Z. *et al.* In situ-generate*d* volatile precursor for CVD growth of a semimetallic 2D dichalcogenide. *ACS Appl. Mater. Interfaces* **10**, 34401–34408 (2018).

136. Ling, X. *et al.* Role of the seeding promoter in MoS_2 growth by chemical vapor deposition. *Nano Lett.* **14**, 464–472 (2014).

137. Kang, K. *et al.* High-mobility three-atom-thick semiconducting films with wafer-scale homogeneity. *Nature* **520**, 656–660 (2015).

138. Kim, H., Ovchinnikov, D., Deiana, D., Unuchek, D. & Kis, A. Suppressing nucleation in metal–organic chemical vapor deposition of MoS_2 monolayers by alkali metal halides. *Nano Lett.* **17**, 5056–5063 (2017).

139. Eichfeld, S. M. *et al.* Highly scalable, atomically thin WSe_2 grown via metal–organic chemical vapor deposition. *ACS Nano* **9**, 2080–2087 (2015).

140. Bhimanapati, G. R. *et al.* Growth and tunable surface wettability of vertical MoS_2 layers for improved hydrogen evolution reactions. *ACS Appl. Mater. Interfaces* **8**, 22190–22195 (2016).

141. Tarasov, A. *et al.* Highly uniform trilayer molybdenum disulfide for wafer-scale device fabrication. *Adv. Funct. Mater.* **24**, 6389–6400 (2014).

142. Chow, P. K. *et al.* Wetting of mono and few-layered WS_2 and MoS_2 films sup*p*orted on Si/SiO_2 substrates. *ACS Nano* **9**, 3023–3031 (2015).

143. Wang, H. *et al.* $MoSe_2$ and WSe_2 nano fi*l*ms with vertically aligned molecular layers on curved and rough surfaces. *Nano Lett.* **13**, 3426–3433 (2013).

144. Zhou, L. *et al.* Large-area synthesis of high-quality uniform few-layer $MoTe_2$. *J. Am. Chem. Soc.* **137**, 11892–11895 (2015).

145. van der Zande, A. M. *et al.* Grains and grain boundaries in highly crystalline monolayer molybdenum disulphide. *Nat. Mater.* **12**, 554–561 (2013).

146. Najmaei, S. *et al.* Vapour phase growth and grain boundary structure of molybdenum disulphide atomic layers. *Nat. Mater.* **12**, 754–759 (2013).

147. Fan, X. *et al.* Controllable growth and formation mechanisms of dislocated WS_2 spirals. *Nano Lett.* **18**, 3885–3892 (2018).

148. Kong, D. *et al.* Few-layer n*a*noplates of Bi_2Se_3 and Bi_2Te_3 with highly tunable

chemical potential. *Nano Lett.* **10**, 2245–2250 (2010).

149. Son, D. *et al.* Colloidal synthesis of uniform-sized molybdenum disulfide nanosheets for wafer-scale flexible nonvolatile memory. *Adv. Mater.* **28**, 9326–9332 (2016).

150. Huang, Q. *et al.* Flower-like molybdenum disulfide for polarity-triggered accumulation/release of small molecules. *ACS Appl. Mater. Interfaces* **9**, 36431–36437 (2017).

151. Li, W. *et al.* Flowerlike WSe_2 and WS_2 microspheres - one-pot synthesis, formation mechanism and application in heavy metal ion sequestration. *Chem. Commun.* **52**, 4481–4484 (2016).

152. Liu, M. *et al.* Synthesis of few-layer 1T′-$MoTe_2$ ultrathin nanosheets for high-performance pseudocapacitors. *J. Mater. Chem. A* **5**, 1035–1042 (2017).

153. Zhou, X. *et al.* Fast colloidal synthesis of scalable Mo-rich hierarchical ultrathin $MoSe_{2-x}$ nanosheets for high-performance hydrogen evolution. *Nanoscale* **6**, 11046–11051 (2014).

154. Liu, Z. *et al.* Colloidal synthesis of 1T' phase dominated WS_2 towards endurable electrocatalysis. *Nano Energy* **50**, 176–181 (2018).

155. Meiron, O. E., Kuraganti, V., Hod, I., Bar-Ziv, R. & Bar-Sadan, M. Improved catalytic activity of $Mo_{1-x}W_xSe_2$ alloy nanoflowers promotes efficient hydrogen evolution reaction in both acidic and alkaline aqueous solutions. *Nanoscale* **9**, 13998–14005 (2017).

156. Mahler, B., Hoepfner, V., Liao, K. & Ozin, G. A. Colloidal synthesis of 1T-WS_2 and 2H-WS_2 nanosheets: Applications for photocatalytic hydrogen evolution. *J. Am. Chem. Soc.* **136**, 14121–14127 (2014).

157. Samadi, M. *et al.* Group 6 transition metal dichalcogenide nanomaterials: synthesis, applications and future perspectives. *Nanoscale Horizons* **3**, 90–204 (2018).

158. Qu, B. *et al.* Ultrathin MoSe2 nanosheets decorated on carbon fiber cloth as binder-free and high-performance electrocatalyst for hydrogen evolution. *ACS Appl. Mater. Interfaces* **7**, 14170–14175 (2015).

159. Geng, X. *et al.* Pure and stable metallic phase molybdenum disulfide nanosheets for hydrogen evolution reaction. *Nat. Commun.* **7**, 10672 (2016).

160. Yang, K. *et al.* Composition- and phase-controlled synthesis and applications of alloyed phase heterostructures of transition metal disulphides. *Nanoscale* **9**, 5102–5109 (2017).

161. Ding, W. *et al.* Highly ambient-stable 1T-MoS_2 and 1T-WS_2 by hydrothermal synthesis under high magnetic fields. *ACS Nano* (2019). doi:10.1021/acsnano.8b07744

162. Liu, Q. *et al.* Gram-scale aqueous synthesis of stable few-layered 1T-MoS_2: Applications for visible-light-driven photocatalytic hydrogen evolution. *Small* **11**, 5556–5564 (2015).

163. Liu, Q. *et al.* Stable metallic 1T-WS_2 nanoribbons intercalated with ammonia ions: The correlation between structure and electrical/optical properties. *Adv. Mater.* **27**, 4837–4844 (2015).

164. Fei, F. *et al.* Solvothermal synthesis of lateral heterojunction Sb_2Te_3-Bi_2Te_3 nanoplates. *Nano Lett.* **15**, 5905–5911 (2015).

165. Park, G. *et al.* Eventual chemical transformation of metals and chalcogens into metal chalcogenide nanoplates through a surface nucleation-detachment-reorganization mechanism. *Chem. Mater.* **29**, 3219–3227 (2017).

166. Song, J. *et al.* Solvothermal growth of bismuth chalcogenide nanoplatelets by the oriented attachment mechanism - an in situ PXRD study. *Chem. Mater.* **27**, 3471–3482 (2015).

167. Yoo, D., Kim, M., Jeong, S., Han, J. & Cheon, J. Chemical synthetic strategy for single-layer transition-metal chalcogenides. *J. Am. Chem. Soc.* **136**, 14670–14673 (2014).

168. Zhou, M. *et al.* Colloidal preparation and electrocatalytic hydrogen production of MoS_2 and WS_2 nanosheets with controllable lateral sizes and layer numbers. *Nanoscale* **8**, 15262–15272 (2016).

169. Jung, W. *et al.* Colloidal synthesis of single-layer MSe_2 (M = Mo, W) nanosheets via anisotropic solution-phase growth approach. *J. Am. Chem. Soc.* **137**, 7266–7269 (2015).

170. Sun, D., Feng, S., Terrones, M. & Schaak, R. E. Formation and interlayer decoupling of colloidal $MoSe_2$ nanoflowers. *Chem. Mater.* **27**, 3167–3175 (2015).

171. Sun, Y. *et al.* Low-temperature solution synthesis of few-layer 1T′-$MoTe_2$ nanostructures exhibiting lattice compression. *Angew. Chemie Int. Ed.* **55**, 2830–2834 (2016).

172. Cheng, L. *et al.* Ultrathin WS2 nanoflakes as a high-performance electrocatalyst for the hydrogen evolution reaction. *Angew. Chemie - Int. Ed.* **53**, 7860–7863 (2014).

173. Wypych, F. & Schöllhorn, R. 1T-MoS_2, a new metallic modification of molybdenum disulfide. *J. Chem. Soc., Chem. Commun.* 1386–1388 (1992). doi:10.1039/C39920001386

174. Yang, D., Sandoval, S. J., Divigalpitiya, W. M. R., Irwin, J. C. & Frindt, R. F. Structure of single-molecular-layer MoS_2. *Phys. Rev. B* **43**, 12053–12056 (1991).

175. Jiménez Sandoval, S., Yang, D., Frindt, R. F. & Irwin, J. C. Raman study and lattice dynamics of single molecular layers of MoS_2. *Phys. Rev. B* **44**, 3955–3962 (1991).

176. Tan, S. J. R. *et al.* Chemical stabilization of 1T′ phase transition metal dichalcogenides with giant optical Kerr nonlinearity. *J. Am. Chem. Soc.* **139**, 2504–2511 (2017).

177. Xiong, F. *et al.* Li intercalation in MoS_2: In situ observation of its dynamics and tuning optical and electrical properties. *Nano Lett.* **15**, 6777–6784 (2015).

178. Naz, M. *et al.* A new 2H-2H′/1T cophase in polycrystalline MoS_2 and $MoSe_2$ thin films. *ACS Appl. Mater. Interfaces* **8**, 31442–31448 (2016).

179. Sun, L. *et al.* Layer-dependent chemically induced phase transition of two-dimensional MoS_2. *Nano Lett.* **18**, 3435–3440 (2018).

180. Ma, Y. *et al.* Reversible semiconducting-to-metallic phase transition in chemical vapor deposition grown monolayer WSe_2 and applications for devices. *ACS Nano* **9**, 7383–7391 (2015).

181. Friedman, A. L. *et al.* Evidence for chemical vapor induced 2H to 1T phase transition in MoX_2 (X = Se, S) transition metal dichalcogenide films. *Sci. Rep.* **7**, 3836 (2017).

182. Peng, J. *et al.* High phase purity of large-sized 1T′-MoS_2 monolayers with 2D

superconductivity. *Adv. Mater.* **31**, 1900568 (2019).

183. Yu, Y. *et al.* High phase-purity 1T′-MoS_2- and 1T′-$MoSe_2$-layered crystals. *Nat. Chem.* **10**, 638–643 (2018).

184. Liu, L. *et al.* Phase-selective synthesis of 1T′ MoS_2 monolayers and heterophase bilayers. *Nat. Mater.* **17**, 1108–1114 (2018).

185. Lin, Y.-C. *et al.* Stable 1T tungsten disulfide monolayer and its junctions: Growth and atomic structures. *ACS Nano* (2018). doi:10.1021/acsnano.8b04979

186. Ekspong, J. *et al.* Stable sulfur-intercalated 1T′ MoS_2 on graphitic nanoribbons as hydrogen evolution electrocatalyst. *Adv. Funct. Mater.* **28**, 1802744 (2018).

187. Liu, Q. *et al.* Electron-doped 1T-MoS_2 via interface engineering for enhanced electrocatalytic hydrogen evolution. *Chem. Mater.* **29**, 4738–4744 (2017).

188. Peng, Z. A. & Peng, X. Formation of high-quality CdTe, CdSe, and CdS nanocrystals using CdO as precursor. *J. Am. Chem. Soc.* **123**, 183–184 (2001).

189. Urban, J. J., Talapin, D. V., Shevchenko, E. V. & Murray, C. B. Self-assembly of PbTe quantum dots into nanocrystal superlattices and glassy films. *J. Am. Chem. Soc.* **128**, 3248–3255 (2006).

190. Murray, C. B., Norris, D. J. & Bawendi, M. G. Synthesis and characterization of nearly monodisperse CdE (E = sulfur, selenium, tellurium) semiconductor nanocrystallites. *J. Am. Chem. Soc.* **115**, 8706–8715 (1993).

191. Beberwyck, B. J., Surendranath, Y. & Alivisatos, A. P. Cation exchange: A versatile tool for nanomaterials synthesis. *J. Phys. Chem. C* **117**, 19759–19770 (2013).

192. Li, H. *et al.* Sequential cation exchange in nanocrystals: Preservation of crystal phase and formation of metastable phases. *Nano Lett.* **11**, 4964–4970 (2011).

193. Xie, Y. *et al.* Metallic-like stoichiometric copper sulfide nanocrystals: Phase- and shape-selective synthesis, near-infrared surface plasmon resonance properties, and their modeling. *ACS Nano* **7**, 7352–7369 (2013).

194. Akkerman, Q. A., Rainò, G., Kovalenko, M. V. & Manna, L. Genesis, challenges and opportunities for colloidal lead halide perovskite nanocrystals. *Nat. Mater.* **17**, 394–405 (2018).

195. Pang, C. *et al.* Colloidal synthesis and magnetic properties of anisotropic-shaped spinel $CuCr_2Se_4$ nanocrystals. *RSC Adv.* **7**, 31173–31179 (2017).

196. Peng, Z. A. & Peng, X. Mechanisms of the shape evolution of CdSe nanocrystals. *J. Am. Chem. Soc.* **123**, 1389–1395 (2001).

197. Manna, L., Milliron, D. J., Meisel, A., Scher, E. C. & Alivisatos, A. P. Controlled growth of tetrapod-branched inorganic nanocrystals. *Nat. Mater.* **2**, 382–385 (2003).

198. Brescia, R., Miszta, K., Dorfs, D., Manna, L. & Bertoni, G. Birth and growth of octapod-shaped colloidal nanocrystals studied by electron tomography. *J. Phys. Chem. C* **115**, 20128–20133 (2011).

199. Joo, J., Son, J. S., Kwon, S. G., Yu, J. H. & Hyeon, T. Low-temperature solution-phase synthesis of quantum well structured CdSe nanoribbons. *J. Am. Chem. Soc.* **128**, 5632–5633 (2006).

200. Liu, Y.-H., Wayman, V. L., Gibbons, P. C., Loomis, R. A. & Buhro, W. E. Origin of

high photoluminescence efficiencies in CdSe quantum belts. *Nano Lett.* **10**, 352–357 (2010).

201. Ithurria, S. & Dubertret, B. Quasi 2D colloidal CdSe platelets with thicknesses controlled at the atomic level. *J. Am. Chem. Soc.* **130**, 16504–16505 (2008).

202. Son, J. S. *et al.* Large-scale soft colloi*d*al template synthesis of 1.4 nm thick CdSe nanosheets. *Angew. Chemie* **121**, 6993–6996 (2009).

203. Schliehe, C. *et al.* Ultrathin PbS sheets by two-dimensional oriented attachment. *Science* **329**, 550–553 (2010).

204. Shamsi, J. *et al.* Colloidal synthesis of quantum confined single crystal $CsPbBr_3$ nanosheets with lateral size control up to the micrometer range. *J. Am. Chem. Soc.* **138**, 7240–7243 (2016).

205. Park, J., Joo, J., Kwon, S. G., Jang, Y. & Hyeon, T. Synthesis of monodisperse spherical nanocrystals. *Angew. Chemie - Int. Ed.* **46**, 4630–4660 (2007).

206. Thanh, N. T. K., Maclean, N. & Mahiddine, S. Mechanisms of nucleation and growth of nanoparticles in solution. *Chem. Rev.* **114**, 7610–7630 (2014).

207. LaMer, V. K. & Dinegar, R. H. Theory, production and mechanism of formation of monodispersed hydrosols. *J. Am. Chem. Soc.* **72**, 4847–4854 (1950).

208. Klimov, V. I. *Semiconductor and metal nanocrystals: Synthesis and electronic and optical properties*. (CRC Press, 2003).

209. Adamson, A. W. & Gast, A. P. *Physical chemistry of surfaces*. (Wiley, 1997).

210. Xie, R., Li, Z. & Peng, X. Nucleation kinetics vs chemical kinetics in the initial formation of semiconductor nanocrystals. *J. Am. Chem. Soc.* **131**, 15457–15466 (2009).

211. Wang, L. *et al.* Precursor self-assembly identified as a general pathway for colloidal semiconductor magic-size clusters. *Adv. Sci.* **5**, 1800632 (2018).

212. Zhang, J. *et al.* Evolution of self-assembled ZnTe magic-sized nanoclusters. *J. Am. Chem. Soc.* **137**, 742–749 (2015).

213. Yang, J. *et al.* Chemical synthesis, doping, and transformation of magic-sized semiconductor alloy nanoclusters. *J. Am. Chem. Soc.* **139**, 6761–6770 (2017).

214. Zhang, H. & Banfield, J. F. Understanding polymorphic phase transformation behavior during growth of nanocrystalline aggregates: Insights from TiO2. *J. Phys. Chem. B* **104**, 3481–3487 (2000).

215. Gao, Y. & Peng, X. Crystal structure control of CdSe nanocrystals in growth and nucleation: Dominating effects of surface versus interior structure. *J. Am. Chem. Soc.* **136**, 6724–6732 (2014).

216. Reiss, H. The growth of uniform colloidal dispersions. *J. Chem. Phys.* **19**, 482–487 (1951).

217. Yin, Y. & Alivisatos, A. P. Colloidal nanocrystal synthesis and the o*r*ganic-inorganic interface. *Nature* **437**, 664–670 (2005).

218. Peng, X., Wickham, J. & Alivisatos, A. P. Kinetics of II-VI and III-V colloidal semiconductor nanocrystal growth: 'Focusing' of size distributions. *J. Am. Chem. Soc.* **120**, 5343–5344 (1998).

219. Peng, X. *et al.* Shape control of CdSe nanocrystals. *Nature* **404**, 59–61 (2000).

220. Lee, S.-M., Cho, S.-N. & Cheon, J. Anisotropic shape control of colloidal inorganic nanocrystals. *Adv. Mater.* **15**, 441–444 (2003).

221. Lee, S.-M., Jun, Y., Cho, S.-N. & Cheon, J. Single-crystalline star-shaped nanocrystals and their evolution: Programming the geometry of nano-building blocks. *J. Am. Chem. Soc.* **124**, 11244–11245 (2002).

222. Yin, X. & Wang, X. Kinetics-driven crystal facets evolution at the tip of nanowires: A new implementation of the Ostwald-Lussac law. *Nano Lett.* **16**, 7078–7084 (2016).

223. Zeng, J. *et al.* Controlling the shapes of silver nanocrystals with different capping *a*gents. *J. Am. Chem. Soc.* **132**, 8552–8553 (2010).

224. Niu, Z., Peng, Q., Gong, M., Rong, H. & Li, Y. Oleylamine-mediated shape evolution of palladium nanocrystals. *Angew. Chemie Int. Ed.* **50**, 6315–6319 (2011).

225. Bealing, C. R., Baumgardner, W. J., Choi, J. J., Hanrath, T. & Hennig, R. G. Predicting nanocrystal shape through consideration of surface-ligand interactions. *ACS Nano* **6**, 2118–2127 (2012).

226. Manna, L., Scher, E. C. & Alivisatos, A. P. Synthesis of soluble and processable rod-, arrow-, teardrop-, and tetrapod-shaped CdSe nanocrystals. *J. Am. Chem. Soc.* **122**, 12700–12706 (2000).

227. Li, Z. & Peng, X. Size/shape-controlled synthesis of colloidal CdSe quantum disks: Ligand and temperature effects. *J. Am. Chem. Soc.* **133**, 6578–6586 (2011).

228. Rempel, J. Y., Trout, B. L., Bawendi, M. G. & Jensen, K. F. Density functional theory study of ligand binding on CdSe (0001), (000-1), and (11-20) single crystal relaxed and reconstructed surfaces: Implications for nanocrystalline growth. *J. Phys. Chem. B* **110**, 18007–18016 (2006).

229. Cozzoli, P. D., Pellegrino, T. & Manna, L. Synthesis, properties and perspectives of hybrid nanocrystal structures. *Chem. Soc. Rev.* **35**, 1195–1208 (2006).

230. Reiss, P., Protiere, M. & Li, L. Core/shell semiconductor nanocrystals. *Small* **5**, 154–168 (2009).

231. Talapin, D. V. *et al.* Seeded growth of highly luminescent CdSe/CdS nanoheterostructures with rod and tetrapod morphologies. *Nano Lett.* **7**, 2951–2959 (2007).

232. Carbone, L. & Cozzoli, P. D. Colloidal heterostructured nanocrystals: Synthesis and growth mechanisms. *Nano Today* **5**, 449–493 (2010).

233. Gong, Y. *et al.* Two-step growth of two-dimensional WSe_2-$MoSe_2$ heterostructures. *Nano Lett.* **15**, 6135–6141 (2015).

234. Gong, Y. *et al.* Vertical and in-plane heterostructures from WS_2-MoS_2 monolayers. *Nat. Mater.* **13**, 1135–1142 (2014).

235. Sahoo, P. K., Memaran, S., Xin, Y., Balicas, L. & Gutiérrez, H. R. One-pot growth of two-dimensional lateral heterostructures via sequential edge-epitaxy. *Nature* **553**, 63–67 (2018).

236. Son, D. H., Hughes, S. M., Yin, Y. & Alivisatos, A. P. Cation exchange reactions in ionic nanocrystals. *Science* **306**, 1009–1012 (2004).

237. Sadtler, B. *et al.* Selective facet reactivity during cation exchange in cadmium sulfide nanorods. *J. Am. Chem. Soc.* **131**, 5285–5293 (2009).

238. Fenton, J. L., Steimle, B. C. & Schaak, R. E. Exploiting crystallographic regioselectivity to engineer asymmetric three-component colloidal nanoparticle isomers using partial cation exchange reactions. *J. Am. Chem. Soc.* (2018). doi:10.1021/jacs.8b03338

239. Beberwyck, B. J. & Alivisatos, A. P. Ion exchange synthesis of III–V nanocrystals. *J. Am. Chem. Soc.* **134**, 19977–19980 (2012).

240. Dutt, M. B. & Sharma, B. L. 3 Diffusion in compound semiconductors. in *Diffusion in Semiconductors* 1–63 (Springer-Verlag, 1998).

241. Fainblat, R. *et al.* Quantum confinement-controlled exchange coupling in manganese(II)-doped CdSe two-dimensional quantum well nanoribbons. *Nano Lett.* **12**, 5311–5317 (2012).

242. Schlenskaya, N. N. *et al.* Scroll-like alloyed CdS_xSe_{1-x} nanoplatelets - Facile synthesis and detailed analysis of tunable optical properties. *Chem. Mater.* (2017). doi:10.1021/acs.chemmater.6b03876

243. Zingaro, R. A. & Mcglothlin, R. E. Some phosphines, phosphine sulfides, and phosphine selenides. *J. Chem. Eng. Data* **8**, 226–229 (1963).

244. Garcia-Rodriguez, R., Hendricks, M. P., Cossairt, B. M., Liu, H. & Owen, J. S. Conversion reactions of cadmium chalcogenide nanocrystal precursors. *Chem. Mater.* **25**, 1233–1249 (2013).

245. Sun, H., Wang, F. & Buhro, W. E. Tellurium precursor for nanocrystal synthesis: tris(dimethylamino)phosphine telluride. *ACS Nano* (2018). doi:10.1021/acsnano.8b06468

246. Socrates, G. *Infrared and Raman Characteristic Group Frequencies*. (Wiley, 2004).

247. Young, A. G., Al-Salim, N., Green, D. P. & McQuillan, A. J. Attenuated total reflection infrared studies of oleate and trioctylphosphine oxide ligand adsorption and exchange reactions on CdS quantum dot films. *Langmuir* **24**, 3841–3849 (2008).

248. Bullen, C. *et al.* High activity phosphine-free selenium precursor solution for semiconductor nanocrystal growth. *Chem. Mater.* **22**, 4135–4143 (2010).

249. Thomson, J. W., Nagashima, K., MacDonald, P. M. & Ozin, G. A. From sulfur-amine solutions to metal sulfide nanocrystals: Peering into the oleylamine-sulfur black box. *J. Am. Chem. Soc.* **133**, 5036–5041 (2011).

250. Deng, Z., Cao, L., Tang, F. & Zou, B. A new route to zinc-blende CdSe nanocrystals: Mechanism and synthesis. *J. Phys. Chem. B* **109**, 16671–16675 (2005).

251. *CRC handbook of chemistry and physics*. (CRC Press, 2009).

252. Antunez, P. D., Webber, D. H. & Brutchey, R. L. Solution-phase synthesis of highly conductive tungsten diselenide nanosheets. *Chem. Mater.* **25**, 2385–2387 (2013).

253. Li, J., Schreckenbach, G. & Ziegler, T. First bond dissociation energy of $M(CO)_6$ (M = Cr, Mo, W) revisited: The performance of density functional theory and the influence of relativistic effects. *J. Phys. Chem.* **98**, 4838–4841 (1994).

254. Stark, J. G. The oxidation states of molybde*n*um. *J. Chem. Educ.* **46**, 505 (1969).

255. Louhichi, B., Bensalash, N. & Gadri, A. Electrochemical oxidation of benzoic acid derivatives on boron doped diamond: Voltammetric study and galvanostatic electrolyses. *Chem. Eng. Technol.* **29**, 944–950 (2006).

256. Zheng, H. *et al.* Nanostructured tungsten oxide - Properties, synthesis, and applications. *Adv. Funct. Mater.* **21**, 2175–2196 (2011).

257. Luo, Y.-R. *Comprehensive handbook of chemical bond energies*. (Boca Raton, FL : Taylor & Francis, 2007).

258. Puzder, A. *et al.* The effect of organic ligand binding on the growth of CdSe nanoparticles probed by ab initio calculations. *Nano Lett.* **4**, 2361–2365 (2004).

259. Sun, Y., Fujisawa, K., Terrones, M. & Schaak, R. E. Solution synthesis of few-layer WTe_2 and $Mo_xW_{1-x}Te_2$ nanostructures. *J. Mater. Chem. C* **5**, 11317–11323 (2017).

260. Sun, Y. *et al.* Low-temperature solution synthesis of transition metal dichalcogenide alloys with tunable optical properties. *J. Am. Chem. Soc.* **139**, 11096–11105 (2017).

261. Scheele, M. *et al.* Synthesis and thermoelectric characterization of Bi_2Te_3 nanoparticles. *Adv. Funct. Mater.* **19**, 3476–3483 (2009).

262. Yashina, L. V. *et al.* Negligible surface reactivity of topological insulators Bi_2Se_3 and Bi_2Te_3 towards oxygen and water. *ACS Nano* **7**, 5181–5191 (2013).

263. Egerton, R. F. *Physical principles of electron microscopy*. (Springer, 2005).

264. Goldstein, J. *Practical scanning electron microscopy: Electron and ion microprobe analysis*. (Plenum Press, 1977).

265. Kumagai, K. & Sekiguchi, T. Sharing of secondary electrons by in-lens and out-lens detector in low-voltage scanning electron microscope equipped with immersion lens. *Ultramicroscopy* **109**, 368–372 (2009).

266. Griffin, B. J. A comparison of conventional Everhart-Thornley style and in-lens secondary electron detectors-a further variable in scanning electron microscopy. *Scanning* **33**, 162–173 (2011).

267. Reimer, L. *Scanning electron microscopy*. (Springer, 1998).

268. Oxford Instruments application note - Silicon drift detectors explained. Available at: https://nano.oxinst.com/assets/uploads/products/nanoanalysis/documents/Brochures/SDD Explained.pdf.

269. Williams, D. B. & Carter, C. B. *Transmission electron microscopy: A textbook for materials science*. (Plenum Press, 1996).

270. Rice, S. B. *et al.* Particle size distributions by transmission electron microscopy: An interlaboratory comparison case study. *Metrologia* **50**, 663–678 (2013).

271. Carbone, L. *et al.* Synthesis and micrometer-scale assembly of colloidal CdSe/CdS nanorods prepared by a seeded growth approach. *Nano Lett.* **7**, 2942–2950 (2007).

272. Pyrz, W. D. & Buttrey, D. J. Particle size determination using TEM: A discussion of image acquisition and analysis for the novice microscopist. *Langmuir* **24**, 11350–11360 (2008).

273. de Ruijter, W. J., Sharma, R., McCartney, M. R. & Smith, D. J. Measurement of lattice-fringe vectors from digital HREM images: Experimental precision. *Ultramicroscopy* **57**, 409–422 (1995).

274. Biskupek, J. Practical considerations on the determination of the accuracy of the lattice parameters measurements from digital recorded diffractograms. *J. Electron Microsc. (Tokyo).* **53**, 601–610 (2004).

275. Pecharsky, V. K. & Zavalij, P. Y. *Fundamentals of powder diffraction and structural characterization of materials*. (Springer, 2009).

276. Moulder, J. F. & Chastain, J. *Handbook of X-ray photoelectron spectroscopy: A reference book of standard spectra for identification and interpretation of XPS data*. (Physical Electronic Division, Perkin-Elmer Corporation, 1995).

277. Watts, J. F. & Wolstenholme, J. *An introduction to surface analysis by XPS and AES*. (Wiley, 2003).

278. Nakamoto, K. *Infrared and Raman spectra of inorganic and coordination compounds*. (Wiley, 1986).

279. Rousseau, D. L., Bauman, R. P. & Porto, S. P. S. Normal mode determination in crystals. *J. Raman Spectrosc.* **10**, 253–290 (1981).

280. Zhang, J. Z. *Optical properties and spectroscopy of nanomaterials*. (World Scientific, 2009).

281. Srivastava, S. K. & Avasthi, B. N. Layer type tungsten dichalcogenide compounds: Their preparation, structure, properties and uses. *J. Mater. Sci.* **20**, 3801–3815 (1985).

282. Thommes, M. *et al.* Physisorption of gases, with special reference to the evaluation of surface area and pore size distribution (IUPAC technical report). *Pure Appl. Chem.* **87**, 1051–1069 (2015).

283. Rouquerol, F. *Adsorption by powders and porous solids: Principles, methodology and applications*. (Academic Press, 2013).

284. Binnig, G., Quate, C. F. & Gerber, C. Atomic force microscope. *Phys. Rev. Lett.* **56**, 930–933 (1986).

285. Melitz, W., Shen, J., Kummel, A. C. & Lee, S. Kelvin probe force microscopy and its application. *Surf. Sci. Rep.* **66**, 1–27 (2011).

286. Pfeiffer, C. *et al.* Interaction of colloidal nanoparticles with their local environment: The (ionic) nanoenvironment around nanoparticles is different from bulk and determines the physico-chemical properties of the nanoparticles. *J. R. Soc. Interface* **11**, 20130931 (2014).

287. Lowry, G. V. *et al.* Guidance to improve the scientific value of zeta-potential measurements in nanoEHS. *Environ. Sci. Nano* **3**, 953–965 (2016).

288. Hunter, R. J. *Zeta potential in colloid science: Principles and applications*. (Academic Press, 1981).

289. Zetasizer Nano user manual. Available at: https://www.malvernpanalytical.com/en/.

290. Anantharaj, S. *et al.* Precision and correctness in the evaluation of electrocatalytic water splitting: revisiting activity parameters with a critical assessment. *Energy Environ. Sci.* **11**, 744–771 (2018).

291. Binninger, T., Fabbri, E., Kötz, R. & Schmidt, T. J. Determination of the electrochemically active surface area of metal-oxide supported platinum Catalyst. *J. Electrochem. Soc.* **161**, H121–H128 (2014).

292. Wei, C. *et al.* Approaches for measuring the surface areas of metal oxide electrocatalysts for determining their intrinsic electrocatalytic activity. *Chem. Soc. Rev.* **48**, 2518–2534 (2019).

293. Xu, J. *et al.* Carbon dioxide electroreduction into syngas boosted by a partially delocalized charge in molybdenum sulfide selenide alloy monolayers. *Angew. Chemie Int. Ed.* **56**, 9121–9125 (2017).

294. Benck, J. D., Hellstern, T. R., Kibsgaard, J., Chakthranont, P. & Jaramillo, T. F. Catalyzing the hydrogen evolution reaction (HER) with molybdenum sulfide nanomaterials. *ACS Catal.* **4**, 3957–3971 (2014).

295. McCrory, C. C. L. *et al.* Benchmarking hy*d*rogen evolving reaction and oxygen evolving reaction electrocatalysts for solar water splitting devices. *J. Am. Chem. Soc.* **137**, 4347–4357 (2015).

296. Bard, A. J. & Faulkner, L. R. *Electrochemical methods: Fundamentals and applications*. (Wiley, 1980).

297. Barsoukov, E. & Macdonald, J. R. *Impedance spectroscopy: Theory, experiment, and applications*. (Wiley, 2005).

298. Potentiostatic EIS tutorial. Available at: https://www.gamry.com/application-notes/EIS/potentiostatic-eis-tutorial/.

299. Basics of electrochemical impedance spectroscopy. Available at: https://www.gamry.com/application-notes/EIS/basics-of-electrochemical-impedance-spectroscopy/.

300. Roger, I. & Symes, M. D. Silver leakage from Ag/AgCl reference electrodes as a potential cause of interference in the electrocatalytic hydrogen evolution reaction. *ACS Appl. Mater. Interfaces* **9**, 472–478 (2017).

301. Sekine, T., Izumi, M., Nakashizu, T., Uchinokura, K. & Matsuura, E. Raman Scattering and infrared reflectance in 2H-$MoSe_2$. *J. Phys. Soc. Japan* **49**, 1069–1077 (1980).

302. Smithe, K. K. H. *et al.* Nanoscale heterogeneities in monolayer $MoSe_2$ revealed by correlated scanning probe microscopy and tip-enhanced Raman spectroscopy. *ACS Appl. Nano Mater.* **1**, 572–579 (2018).

303. Lu, X. *et al.* Rapid and nondestructive identification of polytypism and stacking sequences in few-layer molybdenum diselenide by Raman spectroscopy. *Adv. Mater.* **27**, 4502–4508 (2015).

304. Zhang, X., Tan, Q.-H., Wu, J.-B., Shi, W. & Tan, P.-H. Review on the Raman spectroscopy of different types of layered materials. *Nanoscale* **8**, 6435–6450 (2016).

305. Kozawa, D. *et al.* Photocarrier relaxation pathway in two-dimensional semiconducting transition metal dichalcogenides. *Nat. Commun.* **5**, 4543 (2014).

306. Pine, A. S. & Dresselhaus, G. Raman spectra and lattice dynamics of tellurium. *Phys. Rev. B* **4**, 356–371 (1971).

307. Chen, S.-Y., Naylor, C. H., Goldstein, T., Johnson, A. T. C. & Yan, J. Intrinsic phonon bands in high-quality monolayer T' molybdenum ditelluride. *ACS Nano* (2016). doi:10.1021/acsnano.6b07260

308. Zhou, L. *et al.* Sensitive phonon-based probe for structure identification of 1T′ $MoTe_2$.

J. Am. Chem. Soc. **139**, 8396–8399 (2017).

309. Ruppert, C., Aslan, O. B. & Heinz, T. F. Optical properties and band gap of single- and few-layer $MoTe_2$ crystals. *Nano Lett.* **14**, 6231–6236 (2014).

310. Keum, D. H. *et al.* Bandgap opening in few-layered monoclinic $MoTe_2$. *Nat. Phys.* **11**, 482–486 (2015).

311. Kobylinski, M. M., Ruhmlieb, C., Kornowski, A. & Mews, A. Hexagonally shaped two-dimensional tin(II) sulfide nanosheets: Growth model and controlled structure formation. *J. Phys. Chem. C* **122**, 5784–5795 (2018).

312. Ma, C., Yan, J., Huang, Y., Wang, C. & Yang, G. The optical duality of tellurium nanoparticles for broadband solar energy harvesting and efficient photothermal conversion. *Sci. Adv.* **4**, eaas9894 (2018).

313. Deng, Z., Chen, D., Tang, F. & Mansuripur, M. Growth of single-crystal double-directional tellurium nanoneedles from CdTe nanocrystals in solution. *Cryst. Growth Des.* **9**, 1823–1828 (2009).

314. Chen, L., Zhao, Q. & Ruan, X. Facile synthesis of ultra-small Bi_2Te_3 nanoparticles, nanorods and nanoplates and their morphology-dependent Raman spectroscopy. *Mater. Lett.* **82**, 112–115 (2012).

315. Stavila, V. *et al.* Wet-chemical synthesis and consolidation of stoichiometric bismuth telluride nanoparticles for improving the thermoelectric figure-of-merit. *ACS Appl. Mater. Interfaces* **5**, 6678–6686 (2013).

316. Jeong, S., Yoo, D., Jang, J., Kim, M. & Cheon, J. Well-defined colloidal 2D layered transition metal chalcogenide nanocrystals via generalized synthetic protocols. *J. Am. Chem. Soc.* **134**, 18233–18236 (2012).

317. Wu, C., Yu, S.-H. & Antonietti, M. Complex concaved cuboctahedrons of copper sulfide crystals with highly geometrical symmetry created by a solution process. *Chem. Mater.* **18**, 3599–3601 (2006).

318. Chen, H., Wu, L., Zhang, L., Zhu, Y. & Grey, C. P. $LiCoO_2$ concaved cuboctahedrons from symmetry-controlled topological reactions. *J. Am. Chem. Soc.* **133**, 262–270 (2011).

319. Zhao, Y. *et al.* Interlayer vibrational modes in few-quintuple-layer Bi_2Te_3 and Bi_2Se_3 two-dimensional crystals. *Phys. Rev. B* **90**, 245428 (2014).

320. Russo, V. *et al.* Raman spectroscopy of Bi-Te thin films. *J. Raman Spectrosc.* **39**, 205–210 (2008).

321. Xu, H. *et al.* Vibrational properties of epitaxial Bi_4Te_3 films as studied by Raman spectroscopy. *AIP Adv.* **5**, 087103 (2015).

322. Park, D. *et al.* Thermal and electrical conduction of single-crystal Bi_2Te_3 nanostructures grown using a one step process. *Sci. Rep.* **6**, 19132 (2016).

323. Buha, J., Gaspari, R., Del Rio Castillo, A. E., Bonaccorso, F. & Manna, L. Thermal stability and anisotropic sublimation of two-dimensional colloidal Bi_2Te_3 and Bi_2Se_3 nanocrystals. *Nano Lett.* **16**, 4217–4223 (2016).

324. Hashibon, A. & Elsässer, C. First-principles density functional theory study of native point defects in Bi_2Te_3. *Phys. Rev. B* **84**, 144117 (2011).

325. Oh, M. W. *et al.* Antisite defects in n-type $Bi_2(Te,Se)_3$: Experimental and theoretical

studies. *J. Appl. Phys.* **115**, 133706 (2014).

326. Han, J. H., Lee, S. & Cheon, J. Synthesis and structural transformations of colloidal 2D layered metal chalcogenide nanocrystals. *Chem. Soc. Rev.* **42**, 2581–2591 (2013).

327. Buha, J. & Manna, L. Solid state intercalation, deintercalation, and cation exchange in colloidal 2D Bi_2Se_3 and Bi_2Te_3 nanocrystals. *Chem. Mater.* **29**, 1419–1429 (2017).

328. Ma, J. *et al.* First-principles study of the structures and electronic band properties of Bi_2Te_3 {01-15} nanoribbons. *AIP Adv.* **5**, 067133 (2015).

329. Mehta, R. J. *et al.* A new class of doped nanobulk high-figure-of-merit thermoelectrics by scalable bottom-up assembly. *Nat. Mater.* **11**, 233–240 (2012).

330. Li, L. *et al.* A self-defined intermediate product captured from the evolution process from a six-pod to an octahedral PbS sub-micrometer particle. *CrystEngComm* **19**, 2195–2201 (2017).

331. Wang, Y., He, J., Liu, C., Chong, W. H. & Chen, H. Thermodynamics versus kinetics in nanosynthesis. *Angew. Chemie Int. Ed.* **54**, 2022–2051 (2015).

332. Wang, N. *et al.* Stability investigations on the non-vdW-exfoliated surfaces of the topological insulator Bi_2Te_3: A first-principles study. *Phys. Rev. B* **93**, 115306 (2016).

333. Jiang, Y. *et al.* Vertical-planar growth and surface orientation of Bi_2Te_3 and Bi_2Se_3 topological insulator nanoplates. *Nano Lett.* **15**, 3147–3152 (2015).

334. Purkayastha, A. *et al.* Synthesis and thermoelectric properties of thin film assemblies of bismuth telluride nanopolyhedra. *Chem. Mater.* **23**, 3029–3031 (2011).

335. Son, J. S. *et al.* n-Type nanostructured thermoelectric materials prepared from chemically synthesized ultrathin Bi_2Te_3 nanoplates. *Nano Lett.* **12**, 640–647 (2012).

336. Yuan, Q., Radar, K. & Hussain, M. M. Acetic acid-confined synthesis of uniform three-dimensional (3D) bismuth telluride nanocrystals consisting of few-quintuple-layer nanoplatelets. *Chem. Commun.* **47**, 12131 (2011).

337. Liu, K. K. *et al.* Growth of large-area and highly crystalline MoS_2 thin layers on insulating substrates. *Nano Lett.* **12**, 1538–1544 (2012).

338. Zhu, J. *et al.* Formation of chiral branched nanowires by the Eshelby twist. *Nat. Nanotechnol.* **3**, 477–481 (2008).

339. Tang, J. & Alivisatos, A. P. Crystal splitting in the growth of Bi_2S_3. *Nano Lett.* **6**, 2701–2706 (2006).

340. Hla, S. W., Marinković, V., Prodan, A. & Muševič, I. STM/AFM investigations of β-$MoTe_2$, α-$MoTe_2$ and WTe_2. *Surf. Sci.* **352**–**354**, 105–111 (1996).

341. Das, P. K. *et al.* Layer-dependent quantum cooperation of electron and hole states in the anomalous semimetal WTe_2. *Nat. Commun.* **7**, 10847 (2016).

342. Jeon, J. *et al.* Layer-controlled CVD growth of large-area two-dimensional MoS_2 films. *Nanoscale* **7**, 1688–1695 (2015).

343. Xie, X. & McCarley, R. E. Synthesis, structure, and characterization of N-ligated tungsten selenide cluster complexes $W_6Se_8L_6$. *Inorg. Chem.* **34**, 6124–6129 (1995).

344. Fei, Z. *et al.* Edge conduction in monolayer WTe_2. *Nat. Phys.* **13**, 677–682 (2017).

345. Ma, X. *et al.* Raman scattering in the transition-metal dichalcogenides of 1T′-$MoTe_2$,

Td-$MoTe_2$, and Td-WTe_2. *Phys. Rev. B* **94**, 214105 (2016).

346. del Corro, E. *et al.* Excited Excitonic States in 1L, 2L, 3L, and Bulk WSe_2 Observed by Resonant Raman Spectroscopy. *ACS Nano* **8**, 9629–9635 (2014).

347. Zhao, W. *et al.* Lattice dynamics in mono- and few-layer sheets of WS_2 and WSe_2. *Nanoscale* **5**, 9677 (2013).

348. Lobana, T. S. Structure and bonding of metal complexes of tertiaryphosphine-arsine chalcogenides including analytical, catalytic, and other applications of the complexes. in *Progress in Inorganic Chemistry* **37**, 495–588 (1989).

349. Park, J. H. *et al.* Defect passivation of transition metal dichalcogenides via a charge transfer van der Waals interface. *Sci. Adv.* **3**, e1701661 (2017).

350. Manjunatha, S., Rajesh, S., Vishnoi, P. & Rao, C. N. R. Reaction with organic halides as a general method for the covalent functionalization of nanosheets of 2D chalcogenides and related materials. *J. Mater. Res.* **32**, 2984–2992 (2017).

351. Sim, D. M. *et al.* Long-term stable 2H-MoS_2 dispersion: Critical role of solvent for simultaneous phase restoration and surface functionalization of liquid-exfoliated MoS_2. *ACS Omega* **2**, 4678–4687 (2017).

352. Wang, S., Robertson, A. & Warner, J. H. Atomic structure of defects and dopants in 2D layered transition metal dichalcogenides. *Chem. Soc. Rev.* **47**, 6764–6794 (2018).

353. Gao, J. *et al.* Transition-metal substitution doping in synthetic atomically thin semiconductors. *Adv. Mater.* **28**, 9735–9743 (2016).

354. Zhang, K. *et al.* Manganese doping of monolayer MoS_2: The substrate is critical. *Nano Lett.* **15**, 6586–6591 (2015).

355. Lin, Y.-C. *et al.* Properties of individual dopant atoms in single-layer MoS_2: Atomic structure, migration, and enhanced reactivity. *Adv. Mater.* **26**, 2857–2861 (2014).

356. Ho, C.-H. *et al.* Interplay between Cr dopants and vacancy clustering in the structural and optical properties of WSe_2. *ACS Nano* (2017). doi:10.1021/acsnano.7b05426

357. Liu, G. *et al.* MoS2 monolayer catalyst doped with isolated Co atoms for the hydrodeoxygenation reaction. *Nat. Chem.* **9**, 810–816 (2017).

358. Lau, T. H. M. *et al.* Transition metal atom doping of the basal plane of MoS_2 monolayer nanosheets for electrochemical hydrogen evolution. *Chem. Sci.* **9**, 4769–4776 (2018).

359. Ma, D. *et al.* CO catalytic oxidation on iron-embedded monolayer MoS_2. *Appl. Surf. Sci.* **328**, 71–77 (2015).

360. Crossland, C. J., Hickey, P. J. & Evans, J. S. O. The synthesis and characterisation of Cu_2MX_4 (M = W or Mo; X = S, Se or S/Se) materials prepared by a solvothermal method. *J. Mater. Chem.* **15**, 3452 (2005).

361. Gan, L.-Y. & Schwingenschlögl, U. Two-dimensional square ternary Cu_2MX_4 (M = Mo, W; X = S, Se) monolayers and nanoribbons predicted from. *Phys. Rev. B* **89**, 125423 (2014).

362. Komsa, H. P. & Krasheninnikov, A. V. Two-dimensional transition metal dichalcogenide alloys: Stability and electronic properties. *J. Phys. Chem. Lett.* **3**, 3652–3656 (2012).

363. Yang, J.-H. & Yakobson, B. I. Unusual negative formation enthalpies and atomic ordering in isovalent alloys of transition metal dichalcogenide monolayers. *Chem. Mater.* **30**, 1547–1555 (2018).

364. Dumcenco, D. O., Kobayashi, H., Liu, Z., Huang, Y.-S. & Suenaga, K. Visualization and quantification of transition metal atomic mixing in $Mo_{1-x}W_xS_2$ single layers. *Nat. Commun.* **4**, 1351 (2013).

365. Wang, Z. *et al.* Chemical vapor deposition of monolayer $Mo_{1-x}W_xS_2$ crystals with tunable band gaps. *Sci. Rep.* **6**, 21536 (2016).

366. Apte, A. *et al.* Telluride-based atomically thin layers of ternary two-dimensional transition metal dichalcogenide alloys. *Chem. Mater.* (2018). doi:10.1021/acs.chemmater.8b03444

367. Yu, P. *et al.* Metal-semiconductor phase-transition in $WSe_{2(1-x)}Te_{2x}$ monolayer. *Adv. Mater.* **29**, 1603991 (2017).

368. Lin, J. *et al.* Anisotropic ordering in 1T′ molybdenum and tungsten ditelluride layers alloyed with sulfur and selenium. *ACS Nano* (2018). doi:10.1021/acsnano.7b08782

369. Goebel, C. G. Polymerization of unsaturated fatty acids. *J. Am. Oil Chem. Soc.* **24**, 65–68 (1947).

370. Zhang, M. *et al.* Two-dimensional molybdenum tungsten diselenide alloys: Photoluminescence, Raman scattering, and electrical transport. *ACS Nano* **8**, 7130–7137 (2014).

371. Susarla, S. *et al.* Thermally induced 2D alloy-heterostructure transformation in quaternary alloys. *Adv. Mater.* **30**, 1804218 (2018).

372. Lei, B. *et al.* Direct observation of semiconductor–metal phase transition in bilayer tungsten d*i*selenide induced by potassium surface functionalization. *ACS Nano* **12**, 2070–2077 (2018).

373. Chou, S. S. *et al.* Understanding catalysis in a multiphasic two-dimensional transition metal dichalcogenide. *Nat. Commun.* **6**, 8311 (2015).

374. Tan, S. M. & Pumera, M. Two-Dimensional materials on the rocks: Positive and negative role of dopants and impurities in electrochemistry. *ACS Nano* (2019). doi:10.1021/acsnano.8b07795

375. Zheng, Y.-R. *et al.* Doping-induced structural phase transition in cobalt diselenide enables enhanced hydrogen evolution catalysis. *Nat. Commun.* **9**, 2533 (2018).

376. Yang, S.-Z. *et al.* Rhenium-doped and stabilized MoS_2 atomic layers with basal-plane catalytic activity. *Adv. Mater.* **30**, 1803477 (2018).

377. Liu, Y. *et al.* Self-optimizing, highly surface-active layered metal dichalcogenide catalysts for hydrogen evolution. *Nat. Energy* **2**, 17127 (2017).

378. Gholamvand, Z. *et al.* Comparison of liquid exfoliated transition metal dichalcogenides reveals MoSe2 to be the most effective hydrogen evolution catalyst. *Nanoscale* **8**, 5737–5749 (2016).

379. Lee, Y. Y. *et al.* Mesoporous transition metal dichalcogenide ME_2 (M = Mo, W; E = S, Se) with 2D layered crystallinity as anode materials for lithium ion batteries. *RSC Adv.* **6**, 14253–14260 (2016).

380. Gan, X. *et al.* Pyrolytic carbon supported alloying metal dichalcogenides as free-

standing electrodes for efficient hydrogen evolution. *Carbon N. Y.* **132**, 512–519 (2018).

381. He, Q. *et al.* High-metallic-phase-concentration $Mo_{1-x}W_xS_2$ nanosheets with expanded interlayers as efficient electrocatalysts. *Nano Res.* **11**, 1687–1698 (2018).

382. Eng, A. Y. S., Ambrosi, A., Sofer, Z., Šimek, P. & Pumera, M. Electrochemistry of transition metal dichalcogenides: Strong dependence on the metal-to-chalcogen composition and exfoliation method. *ACS Nano* **8**, 12185–12198 (2014).

383. Chia, X., Ambrosi, A., Sofer, Z., Luxa, J. & Pumera, M. Catalytic and charge transfer properties of transition metal dichalcogenides arising from electrochemical pretreatment. *ACS Nano* **9**, 5164–5179 (2015).

384. Tan, S. M., Sofer, Z., Luxa, J. & Pumera, M. Aromatic-exfoliated transition metal dichalcogenides: Implications for inherent electrochemistry and hydrogen evolution. *ACS Catal.* **6**, 4594–4607 (2016).

385. Yin, Y. *et al.* Synergistic phase and disorder engineering in 1T-$MoSe_2$ nanosheets for enhanced hydrogen-evolution reaction. *Adv. Mater.* **29**, 1700311 (2017).

386. Wang, D. *et al.* Phase engineering of a multiphasic 1T/2H MoS_2 catalyst for highly efficient hydrogen evolution. *J. Mater. Chem. A* **5**, 2681–2688 (2017).

387. Vrubel, H., Moehl, T., Grätzel, M. & Hu, X. Revealing and accelerating slow electron transport in amorphous molybdenum sulphide particles for hydrogen evolution reaction. *Chem. Commun.* **49**, 8985 (2013).

388. Zhou, H. *et al.* Highly efficient hydrogen evolution from edge-oriented $WS_{2(1-x)}Se_{2x}$ particles on three-dimensional porous NiSe2 foam. *Nano Lett.* **16**, 7604–7609 (2016).

389. Zhang, C. *et al.* Phosphine-free synthesis and shape evolution of $MoSe_2$ nanoflowers for electrocatalytic hydrogen evolution reactions. *CrystEngComm* **20**, 2491–2498 (2018).

390. Huang, G. *et al.* Hierarchical architecture of WS_2 nanosheets on graphene frameworks with enhanced electrochemical properties for lithium storage and hydrogen evolution. *J. Mater. Chem. A* **3**, 24128–24138 (2015).

391. Chen, W. *et al.* Quantum dots of 1T phase transition metal dichalcogenides generated via electrochemical Li intercalation. *ACS Nano* **12**, 308–316 (2018).

392. Sun, Y., Zhang, X., Mao, B. & Cao, M. Controllable selenium vacancy engineering in basal planes of mechanically exfoliated WSe_2 monolayer nanosheets for efficient electrocatalytic hydrogen evolution. *Chem. Commun.* **52**, 14266–14269 (2016).

393. Fu, Q. *et al.* Synthesis and enhanced electrochemical catalytic performance of monolayer $WS_{2(1-x)}Se_{2x}$ with a tunable band gap. *Adv. Mater.* **27**, 4732–4738 (2015).

394. Gao, M.-R., Chan, M. K. Y. & Sun, Y. Edge-terminated molybdenum disulfide with a 9.4-Å interlayer spacing for electrochemical hydrogen production. *Nat. Commun.* **6**, 7493 (2015).

395. Huan, Y. *et al.* Vertical 1T-*Ta*S_2 synthesis on nanoporous gold for high-performance electrocatalytic applications. *Adv. Mater.* **1705916**, 1705916 (2018).

396. Yamaoka, T. *et al.* Efficient photocarrier transfer and effective photoluminescence enhancement in type I monolayer $MoTe_2/WSe_2$ heterostructure. *Adv. Funct. Mater.* **28**, 1801021 (2018)

Appendix

[12] Legend to the Appendix tables is provided in the footnote.

A1. List of $MoSe_2$ samples

Sample		Metal precursor			Chalcogen precursor			Solvent		Injection			Growth	
			ν, mmol	m, mg		ν, mmol	V (*m*), ml (*mg*)		V, ml	M or X	T_{inj}, °C	rate, µl/min	T_{gr}, °C	t_{gr}, min
01		[d] $MoCl_5$	0.37	100	1M TOP:Se	1	1	†OlAc	9	X	300	swift	305	90+30↓
02		[d] $MoCl_5$	0.37	100	1M TOP:Se	1	1	†ODE	9	X	270	swift	268-280	90+30↓
03		[c] $MoCl_5$	0.37	100	1M TOP:Se	1	1	†ODE	9	X	280	swift	280-320	90+30↓
04		[c] $MoCl_5$	0.37	100	[f] Se:OlAm	1	1	†OlAm	9	M	300	swift	300	90+30↓
05		[g] $MoCl_5$	0.5	136	[g] Se powder	1	*79*	OlAm	2				300	30
06		[g] $MoCl_5$	0.5	136	[g] Se powder	1	*79*	†OlAm + ODE	2 + 10				300	30
07		[g] $MoCl_5$	0.5	136	1M Se:OlAm	1	1	†OlAc + ODE	1 + 10	X	300	swift	300	30
08		[g] $MoCl_5$	0.5	136	1M TOP:Se	1	1	†OlAc + ODE	1 + 10	X	300	swift	300	30
09		[a] $MoCl_5$	0.5	137	1M TOP:Se	1	1	†OlAm + ODE	2 + 10	X	300	swift	300	120
10		[d] $MoCl_5$	0.37	100	1M TOP:Se	1	1	†OlAc	9	X	250	swift	300	90
11		[c] $MoCl_5$	0.37	100	[f] Se:OlAm	1	*79*	OlAm	9	M	300	swift	300	120
12		[a] $Mo(CO)_6$	0.1	26	1M TOP:Se	0.2	0.2	OlAc	8	X	300	swift	300	180
13		[a] $Mo(CO)_6$	0.06	15	1M TOP:Se	0.2	0.2	OlAc	8	X	300	swift	300	180
14		[a] $Mo(CO)_6$	0.04	10	1M TOP:Se	0.2	0.2	OlAc	8	X	300	swift	300	180
15		[b] $Mo(CO)_6$	0.05	13	1M TOP:Se	0.1	0.1	†ODE + OlAc	8 + 0.094	X	300	swift	300	180
16		[b] $Mo(CO)_6$	0.05	13	1M TOP:Se	0.1	0.1	†OlAc	9	X	300	swift	300	180
17		[b] $Mo(CO)_6$	0.05	13	1M TOP:Se	0.2	0.2	OlAc	8	X	300	swift	300	1140
18		[b] $Mo(acac)_2O_2$	0.1	16	1M TOP:Se	0.1	0.1	†OlAc + OlAm	8 + 1	X	300	swift	300	180
19	*HMDS*	[b] $Mo(CO)_6$	0.05	13	1M TOP:Se	0.2	0.2	†OlAc	8	X	300	swift	300	180
20		[b] $Mo(CO)_6$	0.05	13	1M TOP:Se	0.2	0.2	†OlAc	8	X	300	swift	300	180
21	*CuCl*	[b] $Mo(CO)_6$	0.05	13	1M TOP:Se	0.2	0.2	†OlAc	8	X	300	swift	300	180
22	*Cu(ac)₂*	[b] $Mo(CO)_6$	0.05	13	1M TOP:Se	0.2	0.2	†OlAc	8	X	300	swift	300	180
23	CP	[b] $Mo(CO)_6$	0.1	27	1M TOP:Se	0.4	0.4	†OlAc	8	X	300	swift	300	180
24		[b] $Mo(CO)_6$	0.05	14	1M TOP:Se	0.2	0.2	†OlAc	8	X	300	swift	300	180
25	CF	[b] $Mo(CO)_6$	0.05	14	1M TOP:Se	0.2	0.2	†OlAc	8	X	300	swift	300	180
26		[b] $Mo(CO)_6$	0.05	16	1M TOP:Se	0.2	0.2	†OlAc	8	X	300	swift	300	180
27	CP	[b] $Mo(CO)_6$	0.05	14	1M TOP:Se	0.2	0.2	†OlAc	8	X	300	swift	300	180
28		[b] $Mo(CO)_6$	0.05	14	1M TOP:Se	0.2	0.2	†OlAc	8	X	300	swift	300	180

[12] Solvent pre-treatment: ‡ Ar (N_2), RT, 30' and † vac, RT, 30'.
Complex formation:
[a] metal precursor is added into a flask containing solvent → vac, RT-100°C, 30-120' → N_2 (Ar), ↑T_{inj}
[a*] metal precursor is added into a flask containing solvent → vac, RT, 15-30' → N_2, 100-200°C, until dissolution → N_2, ↑↓T_{inj}
[b] metal precursor is added into a flask containing solvent → vac, RT, 30' → vac, 200°C, 30-120' → N_2 (Ar), ↑T_{inj}
[c] metal precursor is mixed with 1 ml OlAc in a glass vial under N_2 ant RT, sonicated until dissolution
[c*] metal precursor is mixed with 0.5 ml OlAc in a glass vial under N_2 at RT, sonicated until dissolution, then diluted with 4 ml of OlAm and injected into the reaction mixture
[c**] metal precursor is mixed with 0.2 ml OlAc in a glass vial at RT, sonicated until dissolution, then injected into the reaction mixture
[d] metal precursor is mixed with 1 ml OlAm in a glass vial under N_2 ant RT, sonicated until dissolution
[e] chalcogen precursor is formed *in situ*: chalcogen powder is mixed with solvent → vac, 100-120°C, 30' → Ar, ↑260°C, 30' → ↑T_{inj}
[f] chalcogen precursor is formed *in situ*: chalcogen powder is mixed with solvent → vac, RT-100°C, 30' → N_2 (Ar), ↑220°C, 60' → ↑T_{inj}
[f*] chalcogen precursor is formed *in situ*: chalcogen powder is mixed with solvent → vac, RT-100°C, 30' → N_2 (Ar), ↑220°C, 60' → ↓RT-80°C → + metal precursor → ↑T_{inj}
[g] metal and/or chalcogen precursors are mixed with solvent in the flask → vac, RT, 10' → N_2, ↑T_{gr}

A2. List of $MoTe_2$ samples

Sample		Metal precursor			Chalcogen precursor			Solvent		Injection			Growth	
			ν, mmol	m, mg		ν, mmol	V (*m*), ml (*mg*)		V, ml	M or X	T_{inj}, °C	rate, µl/min	T_{gr}, °C	t_{gr}, min
01		[c] $MoCl_5$	0.5	120	1M TOP:Te	0.5	0.5	‡OlAc	15	X	250	swift	250	30
02	*TDPA*	[a] $MoCl_5$	0.5	130	1M TOP:Te	0.5	0.5	OlAc	10	X	300	swift	300	120
03	*TDPA*	[a] $MoCl_5$	0.5	130	1M TOP:Te	0.5	0.5	†OlAc	15	X	250	20	260	30↓
04	*TDPA*	[a] $MoCl_5$	0.5	125	1M TOP:Te	0.5	0.5	†OlAm	15	X	250	5	260-280	20↓
05	*TDPA*	[a] $Mo(CO)_6$	0.5	132	1M TOP:Te	0.5	0.5	†OlAc	15	X	250	5	280	20↓
06		[c] $MoCl_5$	0.15	46	[e] TOP:Te	1.2	*156*	OlAm + TOP	7 + 3	M	300	16.6	310	20↓
07		[c] $MoCl_5$	0.15	45	[e] TOP:Te	1.2	*160*	OlAc + TOP	7 + 3	M	320	16.6	320-340	20↓
08		[c] $MoCl_5$	0.15	45	[e] TOP:Te	1.2	*150*	OlAm + TOP	7 + 3	M	300	16.6	315-325	20↓
09		[c] $Mo(CO)_6$	0.15	40	[e] TOP:Te	1.2	*150*	OlAm + TOP	7 + 3	M	300	16.6	300-320	20↓
10	*TDPA*	[a] $MoCl_5$	0.5	136	1M TOP:Te	1	1	†OlAc	7	X	300	8.34	300-330	20↓
11		[c] $MoCl_5$	0.37	100	[e] TOP:Te	0.4	*50*	OlAc + TOP	9 + 1	M	300	swift	305-315	90+30↓
12		[a] $MoCl_5$	0.37	100	1M TOP:Te	1	1	†OlAc	10	X	300	swift	300	90+30↓
13		[b] $Mo(CO)_6$	0.38	100	1M TOP:Te	1	1	†OlAc	10	X	300	swift	300	90+30↓
14		[c] $MoCl_5$	0.37	100	1M TOP:Te	1	1	†OlAm	9	X	300	swift		90+30↓
15		[c] $MoCl_5$	0.37	100	1M TOP:Te	1	1	†OlAm	9	X	300	swift		90+30↓
16		[c] $MoCl_5$	0.37	100	1M TOP:Te	0.6	0.6	†OlAm	9	X	290	swift	300	90+30↓
17		[d] $MoCl_5$	0.37	100	1M TOP:Te	1	1	†OlAc	9	X	300	swift	305	90+30↓
18		[d] $MoCl_5$	0.37	100	1M TOP:Te	1	1	†ODE	9	X	280	swift	280	90+30↓
19		[c] $MoCl_5$	0.37	100	1M TOP:Te	1	1	†ODE	9	X	275	swift	300	90+30↓
20		[a] $MoCl_5$	0.5	137	1M TOP:Te	1	1	†ODE	10	X	300	swift	300	15
21		[b] $Mo(CO)_6$	0.05	14	1M TOP:Te	0.2	0.2	†OlAc	8	X	300	swift	300	180
22		[b] $MoCl_5$	0.18	50	1M TOP:Te	0.5	0.5	†OlAc	8	X	300	swift	300	120

A3. List of WSe_2 samples

Sample		Metal precursor			Chalcogen precursor			Solvent		Injection			Growth	
			ν, mmol	m, mg		ν, mmol	V (*m*), ml (*mg*)		V, ml	M or X	T_{inj}, °C	rate, µl/min	T_{gr}, °C	t_{gr}, min
02		[a] WCl_6	0.5	200	1M TOP:Se + 0.5ml OlAc	1	1	OlAm	10	X	270	swift	260	30
03		[c*] WCl_6	0.25	100	1M TOP:Se	1	1	‡OlAm	Σ20	X	300	swift	320	120
04		[c*] WCl_6	0.25	100	1M TOP:Se	0.5	0.5	‡OlAm	Σ20	M X	300	slow	300-320	240
05		[c] WCl_6	0.13	50	Se powder		*30*	‡OlAc	Σ10	X	330	swift	330	90
06		[a] $W(CO)_6$	0.05	20	1M TOP:Se	0.2	0.2	OlAc	10	X	250	swift	300	60
07		[a] $W(CO)_6$	0.05	20	1M TOP:Se	0.2	0.2	OlAc	8	X	200	swift	230	90
08		[a] $W(CO)_6$	0.05	20	1M TOP:Se	0.2	0.2	‡OlAc	10	X	300	swift	300	180
10	*TDPA*	[a] WCl_6	0.5	200	1M TOP:Se	0.5	0.5	†OlAc	15	X	250	5	270-290	20↓
11	*TDPA*	[a] $W(CO)_6$	0.5	180	1M TOP:Se	0.5	0.5	†OlAc	15	X	250	5	260-280	20↓
12	*TDPA*	[a] $W(CO)_6$	0.5	175	1M TOP:Se	0.5	0.5	† OlAc	12	X	200	5	200	20↓
13		[c] WCl_6	0.15	60	[f] TOP:Se		*95*	OlAm + TOP	7 + 3	M	300	16.67	260-300	20↓
14		[c] WCl_6	0.15	60	[f] TOP:Se		*95*	OlAm + TOP	5 + 3	M	300	16.67	330-360	20↓
15		[g] WCl_6	0.5	198	[g] Se powder	1	*79*	OlAm	2				300	30
16		[g] WCl_6	0.5	198	[g] Se powder	1	*79*	†OlAm + ODE	2 + 10				300	30
17		[a] WCl_6	0.5	198	Se powder	1	*79*	†OlAm + ODE	2 + 10				300	150
18		[a] WCl_6	0.5	198	1M TOP:Se	1	1	†OlAm + ODE	2 + 10	X	300	swift	300	150
19		[g] WCl_6	0.5	198	[g] Se powder	1	*79*	OlAm	2				280-340	30
20		[g] WCl_6	0.5	198	[g] Se powder	1	*79*	OlAm	2				300	30
21		[a] $W(CO)_6$	0.06	20	1M TOP:Se	0.2	0.2	OlAc	8	X	300	swift	300	180
22		[g] WCl_6	0.5	198	[g] Se powder	1	*79*	†OlAm	12				300	30
23		WCl_6	0.5	198	[f*] Se:OlAm	1	*79*	†OlAm	12				300	30
24		[a] $W(CO)_6$	0.1	35	1M TOP:Se	0.2	0.2	OlAc	8	X	300	swift	300	180
25		[a] $W(CO)_6$	0.06	20	1M TOP:Se	0.2	0.2	OlAc	8	X	300	swift	300	180
26		[b] $W(CO)_6$	0.07	24	1M TOP:Se	0.2	0.2	†OlAc	8	X	300	swift	300	180
27		[b] $W(CO)_6$	0.06	20	1M TOP:Se	0.2	0.2	†OlAc	8	X	300	swift	300	120
28		[b] $W(CO)_6$	0.06	20	1M TOP:Se	0.2	0.2	†OlAc	8	X	300	swift	300	180
29		[b] $W(CO)_6$	0.06	20	1M TOP:Se	0.2	0.2	†OlAc	8	X	300	swift	300	900
30		[b] $W(CO)_6$	0.06	17	1M TOP:Se	0.1	0.1	†ODE + OlAc	8+ 0.094	X	300	swift	300	180
31		[b] $W(CO)_6$	0.06	20	0.05M Ph_2Se_2-OlAm	0.1	2	OlAc	8	X	300	swift	300	1140
32		[b] $W(CO)_6$	0.06	20	1M TOP:Se	0.2	0.2	†OlAc	8	X	300	swift	300	180
33		[a] $W(CO)_6$	0.06	20	1M TOP:Se	0.2	0.2	†OlAc	8	X	300	swift	300	180
34		[b] $W(CO)_6$	0.06	20	1M TOP:Se + ODE	0.2	0.2 0.8	†OlAc	8	X	300	4.17	300	180
35	*TDPA*	[b] $W(CO)_6$	0.06	20	1M TOP:Se	0.2	0.2	†OlAc	8	X	300	swift	300	180
36	*HMDS*	[b] $W(CO)_6$	0.06	20	1M TOP:Se	0.2	0.2	†OlAc	8	X	300	swift	300	180
37	*$Cu(ac)_2$*	[b] $W(CO)_6$	0.06	20	1M TOP:Se	0.2	0.2	†OlAc	8	X	300	swift	300	180
38	*$FeCl_3$*	[b] $W(CO)_6$	0.06	20	1M TOP:Se	0.2	0.2	†OlAc	8	X	300	swift	300	180
39	*HMDS*	[b] $W(CO)_6$	0.06	20	1M TOP:Se	0.2	0.2	†OlAc	8	X	300	swift	300	180
40	*CuCl*	[b] $W(CO)_6$	0.06	20	1M TOP:Se	0.2	0.2	†OlAc	8	X	300	swift	300	180
41	*HMDS*	[b] $W(CO)_6$	0.06	20	1M TOP:Se	0.2	0.2	†OlAc	8	X	300	swift	300	180
42		[b] $W(CO)_6$	0.06	20	1M TOP:Se	0.2	0.2	†OlAc	8	X	300	swift	300	180
43		[b] $W(CO)_6$	0.06	20	1M TOP:Se	0.2	0.2	†OlAc	8	X	300	swift	300	180
44		[b] $W(CO)_6$	0.06	20	1M TOP:Se	0.2	0.2	†OlAc	8	X	300	swift	250-315	180
45		[b] $W(CO)_6$	0.06	20	1M TOP:Se	0.2	0.2	†OlAc	8	X	300	swift	300	270
46		[b] $W(CO)_6$	0.06	20	1M TOP:Se	0.2	0.2	†OlAc	8	X	300	swift	300	180
47		[a] $W(CO)_6$	0.06	20	1M TOP:Se	0.2	0.2	†OlAc	8	X	300	swift	300	180
½ 48		[b] $W(CO)_6$	0.06	20	1M TOP:Se	0.2	0.2	†OlAc	8	X	300	swift	300	180
49	CP	[b] $W(CO)_6$	0.06	20	1M TOP:Se	0.2	0.2	†OlAc	8	X	300	swift	300	180
50		[b] $W(CO)_6$	0.06	20	1M TOP:Se	0.2	0.2	†OlAc	8	X	300	swift	300	180
51		[b] $W(CO)_6$	0.06	20	Se powder	0.2	*16*	†OlAc	8	X	300	swift	300	180
52		[g] WCl_6	0.5	198	[g] Se powder	1	*79*	OlAm	2				*350*	30
53		[b] WCl_6	0.5	20	1M TOP:Se	0.2	0.2	†OlAc	8	X	300	swift	300	180
54	CP	[b] $W(CO)_6$	0.06	20	1M TOP:Se	0.2	0.2	†OlAc	8	X	300	swift	300	180
⅓ 55		[b] $W(CO)_6$	0.06	20	1M TOP:Se	0.2	0.2	†OlAc	8	X	300	swift	300	180
56	SG	[b] $W(CO)_6$	0.06	20	1M TOP:Se	0.2	0.2	†OlAc	8	X	300	swift	300	180

57		[b] $W(CO)_6$	0.12	40	1M TOP:Se	0.4	0.4	†OlAc	8	X	300	swift	300	180
58	CP	[b] $W(CO)_6$	0.12	40	1M TOP:Se	0.4	0.4	†OlAc	8	X	300	swift	300	180
59	CP	[b] $W(CO)_6$	0.12	40	1M TOP:Se	0.4	0.4	†OlAc	8	X	300	swift	300	180
60		[b] $W(CO)_6$	0.06	20	Se powder	0.2	*16*	†OlAc	8	X	300	swift	300	180
61		[b] $W(CO)_6$	0.06	20	Se powder	0.2	*16*	†OlAc	8	X	300	swift	300	180
62		[b] $W(CO)_6$	0.06	20	Se powder	0.2	*16*	†OlAc	8	X	300	swift	300	180
63	CF	[b] $W(CO)_6$	0.06	20	1M TOP:Se	0.1	0.1	†OlAc	8	X	300	swift	300	180
½ 64	CP	[b] $W(CO)_6$	0.06	20	1M TOP:Se	0.2	0.2	†OlAc	8	X	300	swift	300	180
65		[b] $W(CO)_6$	0.06	20	1M TOP:Se	0.2	0.2	†OlAc	8	X	300	swift	300	180
½ 66		[b] $W(CO)_6$	0.06	20	1M TOP:Se	0.2	0.2	†OlAc	8	X	300	swift	300	180
67	CP	[b] $W(CO)_6$	0.12	40	1M TOP:Se	0.4	0.4	†OlAc	12	X	300	swift	300	180
69		[b] $W(CO)_6$	0.06	25	1M TOP:Se	0.2	0.2	†OlAc	8	X	300	swift	300	180
70		[b] $W(CO)_6$	0.06	22	Se powder	0.2	*17*	†OlAc	8	X	300	swift	300	180
½ 71		[b] $W(CO)_6$	0.06	20	1M TOP:Se	0.2	0.2	†OlAc	8	X	300	swift	300	180
72		$W(CO)_6$+TOP:Se in OlAc, 300 ºC, 180' – 1[C]; 0.1[C]; 0.03[C]; 0.01[C]												
73		$W(CO)_6$+TOP:Se in OlAc, 180' – 0.05[C] at 300 ºC; 1[C] at 320 ºC; 1[C] at 360 ºC												
74		[b] $W(CO)_6$	0.03	10	1M TOP:Se	0.1	0.1	†OlAc	4	X	360	swift	360	180
75		[b] $W(CO)_6$	0.03	10	1M TOP:Se	0.1	0.1	†OlAc	4	X	320	swift	320	180
76		[b] $W(CO)_6$	0.03	10	1M TOP:Se	0.1	0.1	†OlAc	4	X	360	swift	360	1320
77	*10[C]*	[b] $W(CO)_6$	0.3	100	1M TOP:Se	1	1	†OlAc	4	X	300	swift	300	180
78	*TDPA*	[b] $W(CO)_6$	0.06	20	1M TOP:Se	0.2	0.2	†OlAc	8	X	300	swift	300	180
79	*HMDS*	[b] $W(CO)_6$	0.06	20	1M TOP:Se	0.2	0.2	†OlAc	8	X	300	swift	300	180
80		[b] $W(CO)_6$	0.06	20	Se powder	0.2	*16*	†OlAm	8	X	300	swift	300	180
81	*HMDS*	[b] WCl_6	0.06	22	Se powder	0.2	*16*	†OlAc	8	X	300	swift	300	180
82	$Cu(ac)_2$	[b] $W(CO)_6$	0.06	20	1M TOP:Se	0.2	0.2	†OlAc	8	X	300	swift	300	180
83	$FeCl_3$	[b] $W(CO)_6$	0.06	20	1M TOP:Se	0.2	0.2	†OlAc	8	X	300	swift	300	180

A4. List of Bi_2Te_3 samples

Sample	Metal precursor			Chalcogen precursor			Solvent		Injection			Growth	
		ν, mmol	m, mg		ν, mmol	V (*m*), ml (*mg*)		V, ml	M or X	T_{inj}, °C	rate, µl/min	T_{gr}, °C	t_{gr}, min
01	[a*] $Bi(ac)_3$	0.5	193	1M TOP:Te	0.75	0.75	†ODE + OlAc	10 + 1.1	X	70	swift	70	30
02	[a*] $Bi(ac)_3$	0.5	193	1M TOP:Te	0.75	0.75	†ODE + OlAc	10 + 1.1	X	185	swift	185	1
03	[a*] $Bi(ac)_3$	0.5	193	1M TOP:Te	0.75	0.75	†ODE + OlAc	10 + 1.1	X	180	swift	180	0.25
04	[a*] $Bi(ac)_3$	0.5	196	1M TOP:Te	0.75	0.75	†ODE + OlAc	10 + 1.1	X	50	swift	50	30
05	[a*] $Bi(ac)_3$	0.5	196	1M TOP:Te	0.75	0.75	†ODE + OlAc	10 + 1.1	X	35	swift	35	30
06	[a*] $Bi(ac)_3$	0.5	195	1M TOP:Te	0.8	0.8	†ODE + OlAc	10 + 1.1	X	50	26.7	50	30
07	[a*] $Bi(ac)_3$	0.5	193	1M TOP:Te	0.75	0.75	†ODE + OlAc	10 + 1	X	50	swift	50	30
08	[a*] $Bi(ac)_3$	0.6	230	1M TOP:Te	0.9	0.9	†ODE + OlAc	10 + 10	X	35	swift	35	30
09	[a*] $Bi(ac)_3$	0.5	195	1M TOP:Te	0.75	0.75	†ODE + OlAc	10 + 0.47	X	50	swift	50	30
10	[a*] $Bi(ac)_3$	0.5	193	1M TOP:Te	0.75	0.75	†ODE + OlAc	10 + 1.1	X	50	swift	50	30
11	[a*] $Bi(ac)_3$	0.5	193	1M TOP:Te	0.75	0.75	†ODE + OlAc	10 + 0.16	X	50	swift	50	30
12	[a*] $Bi(ac)_3$	0.5	193	1M TOP:Te	0.75	0.75	†OlAm + OlAc	10 + 0.16	X	50	swift	50	30
13	[a*] $Bi(ac)_3$	0.5	193	1M TOP:Te	0.75	0.75	†ODE + OlAc	10 + 0.16	X	180	swift	180	1
14	[a*] $Bi(ac)_3$	0.5	193	1M TOP:Te	0.75	0.75	†OlAm + OlAc	10 + 0.16	X	180	swift	180	1
15	[a*] $Bi(ac)_3$	0.5	193	1M TOP:Te	0.75	0.75	†ODE + OlAc	10 + 1.47	X	50	drop wise	50	30
16	[a*] $Bi(ac)_3$	0.5	193	1M TOP:Te	0.75	0.75	†ODE + OlAc	10 + 0.47	X	35	swift	35	30
17	[a*] $Bi(ac)_3$	0.5	193	1M TOP:Te	0.75	0.75	†TOP + ODE + OlAc	6 + 4 + 0.5	X	50	swift	50	30
18	[a*] $Bi(ac)_3$	0.5	193	1M TOP:Te	0.75	0.75	†ODE + OlAc	10 + 0.16	X	50	swift	50	150
19	[a*] $Bi(ac)_3$	0.5	193	1M TOP:Te	0.75	0.75	†ODE + OlAc	10 + 0.16	X	35	swift	35	150
20	[b*] $Bi(ac)_3$	0.5	194	1M TOP:Te	0.75	0.75	†ODE + OlAc	10 + 0.47	X	70	swift	70	30
21	[a*] $Bi(ac)_3$	0.5	194	1M TOP:Te	0.75	0.75	†ODE + OlAc	10 + 0.47	X	50	swift	50	30
22	[a*] $Bi(ac)_3$	0.5	194	1M TOP:Te	0.75	0.75	†ODE + OlAc	10 + 1.1	X	70	swift	70	30
23	[a*] $Bi(ac)_3$	0.5	194	1M TOP:Te	0.75	0.75	†ODE + OlAc	10 + 1.1	X	180	swift	180	1
24	[a*] $Bi(ac)_3$	0.5	194	1M TOP:Te	0.75	0.75	†ODE + OlAc	10 + 1.1	X	70	swift	70	30
25	[a*] $Bi(ac)_3$	0.5	194	1M TOP:Te	0.75	0.75	†ODE + OlAc	10 + 1.1	X	50	swift	50	30
26	[c**] $Bi(ac)_3$	0.2	77	1M TOP:Te	0.3	0.3	†TOP	5	M	70	swift	70	30
28	[a*] $Bi(ac)_3$	0.5	194	0.5M TOP:Te	0.75	1.5	†ODE + OlAc	10 + 0.47	X	50	swift	50	30
29	[b*] $Bi(ac)_3$	0.5	194	0.5M TOP:Te	0.75	1.5	†ODE + OlAc	10 + 0.47	X	RT	swift	RT	90
30	[a*] $Bi(ac)_3$	0.5	194	0.5M TOP:Te	0.75	1.5	†ODE + OlAc	10 + 0.47	X	RT	swift	RT	1440
31	[a*] $Bi(ac)_3$	0.4	156	1M TOP:Te	0.6	0.6	†ODE + OlAc	10 + 0.45	X	RT	swift	RT	30
32	[b] $Bi(ac)_3$	0.5	193	1M TOP:Te	0.75	0.75	†ODE + OlAc	10 + 0.47	X	RT	swift	RT	90
33	[b] $Bi(ac)_3$	0.5	193	1M TOP:Te	0.75	0.75	†ODE + OlAc	10 + 0.47	X	70	swift	70	30
34	[b] $Bi(ac)_3$	0.5	193	1M TOP:Te	0.75	0.75	†ODE + OlAc	10 + 0.47	X	180	swift	180	0.5
35	[b] $Bi(ac)_3$	0.5	194	1M TOP:Te	0.75	0.75	†ODE + OlAc	10 + 0.45	X	RT	swift	RT	120
37	[b] $Bi(ac)_3$	0.5	191	1M TOP:Te	0.75	0.75	†ODE + OlAc	10 + 0.47	X	RT	swift	RT	720

38	[b] $Bi(ac)_3$	0.5	193	1M TOP:Te	0.75	0.75	†ODE + OlAc	10 + 0.47	X	70	swift	70	30
39	[b] $Bi(ac)_3$	0.5	193	1M TOP:Te	0.75	0.75	†ODE + OlAc	10 + 0.47	X	180	swift	180	0.5
40	[b] $Bi(ac)_3$	0.5	193	1M TOP:Te	0.3	0.3	†ODE + OlAc	10 + 0.47	X	170	swift	170	0.5
42	[b] $Bi(ac)_3$	0.5	194	1M TOP:Te	0.75	0.75	†ODE + OlAc	10 + 1.1	X	50	swift	50	30
43	[b] $Bi(ac)_3$	0.5	194	1M TOP:Te	0.75	0.75	†ODE + OlAc	10 + 1.1	X	RT	swift	RT	60
45	[b] $Bi(ac)_3$	0.5	193	1M TOP:Te	0.74	0.74	†ODE + OlAc	10 + 0.47	X	170	swift	170	0.3-5
½ 46	[b] $Bi(ac)_3$	0.5	194	1M TOP:Te	0.75	0.75	†ODE + OlAc	10 + 0.47	X	RT	swift	RT	90
48	[b] $Bi(ac)_3$	0.05	19.3	1M TOP:Te	0.075	0.075	†ODE + OlAc	10 + 0.04	X	170	swift	170	0.5
49	[b] $Bi(ac)_3$	0. 5	195	1M TOP:Te	0.75	0.75	†ODE + OlAc	10 + 0.04	X	170	swift	170	2

A5. Full list of publications

P. C. Sherrell, P. Palczynski, M. S. Sokolikova, F. Reale, F. M. Pesci, M. Och, and C. Mattevi, Large-area CVD MoS_2/WS_2 heterojunctions as a photoelectrocatalyst for salt water oxidation, *ACS Applied Energy Materials* (2019), **2**, 5877-5882.

M. S. Sokolikova, P. C. Sherrell, P. Palczynski, V. L. Bemmer, C. Mattevi, Direct solution-phase synthesis of 1T' WSe_2 nanosheets, *Nature Communications* **10** (2019), 712.

P. C. Sherrell, K. Sharda, C. Grotta, J. Ranalli, M. S. Sokolikova, F. M. Pesci, P. Palczynski, V. L. Bemmer, C. Mattevi, Thickness-dependent characterization of chemically exfoliated TiS_2 nanosheets, *ACS Omega* **3** (2018), 8655-8662.

M. S. Sokolikova, P. C. Sherrell, P. Palczynski, V. L. Bemmer, C. Mattevi, Room-temperature growth of colloidal Bi_2Te_3 nanosheets, *Chemical Communications* **53** (2017), 8026-8029.

F. M. Pesci, M. S. Sokolikova, C. Grotta, P. C. Sherrell, F. Reale, K. Sharda, N. Ni, P. Palczynski, C. Mattevi, MoS_2/WS_2 heterojunction for photoelectrochemical water oxidation, *ACS Catalysis* **7** (2017), 4990-4998.

A. G. Vitukhnovsky, V. S. Lebedev, A. S. Selyukov, A. A. Vashchenko, R. B. Vasiliev, M. S. Sokolikova, Electroluminescence from colloidal semiconductor CdSe nanoplatelets in hybrid organic-inorganic light emitting diode, *Chemical Physics Letters* **619** (2015), 185-188.

A. V. Katsaba, V. V. Fedyanin, S. A. Ambrozevich, A. G. Vitukhnovsky, M. S. Sokolikova, R. B. Vasiliev, Density of surface states in colloidal CdSe nanoplatelets, *Semiconductors* **49** (2015), 1323–1326.

A. S. Selyukov, A. G. Vitukhnovskii, V. S. Lebedev, A. A. Vashchenko, R. B. Vasiliev, M. S. Sokolikova, Electroluminescence of colloidal quasi-two-dimensional semiconducting CdSe nanostructures in a hybrid light-emitting diode, *Journal of Experimental and Theoretical Physics* **120** (2015), 595–606.

R. B. Vasiliev, M. S. Sokolikova, A. G. Vitukhnovskii, S. A. Ambrozevich, A. S. Selyukov, V. S. Lebedev, Optics of colloidal quantum-confined CdSe nanoscrolls, *Quantum Electronics* **45** (2015), 853.

Y. Yao, T. Kuroda, D. N. Dirin, M. S. Sokolikova, R. B. Vasiliev, Strain effects on optical properties of tetrapod-shaped CdTe/CdS core-shell nanocrystals, *Superlattices and Microstructures* **76** (2014), 244-252.

M. S. Sokolikova, N. N. Shlenskaya, V. F. Kozlovsky, R. B. Vasiliev, A. M. Gaskov, Synthesis and optical properties of quasi-2D CdS_xSe_{1-x} nanoparticles, *Russian Journal of Inorganic Chemistry* **59** (2014), 1069-1072.

A. A. Vashchenko, A. G. Vitukhnovsky, V. S. Lebedev, A. S. Selyukov, R. B. Vasiliev, M. S. Sokolikova, Organic light-emitting diode with an emitter based on a planar layer of CdSe semiconductor nanoplatelets, *JETP Letters* **100** (2014), 94-97.

M. S. Sokolikova, R. B. Vasiliev, A. M. Gaskov, Synthesis of quasi-two-dimensional colloidal cadmium selenide nanoparticles and formation of sulfide monolayer on their surfaces, *Russian Journal of Inorganic Chemistry* **59** (2014), 413-418.

D. N. Dirin, M. S. Sokolikova, A. M. Gaskov, R. B. Vasiliev, Extinction and luminescence coefficients of CdSe/CdTe, CdTe/CdSe, and CdTe/CdS heterostructures based on colloidal CdSe and CdTe nanocrystals, *Journal of Optical Technology* **78** (2011), 693-698.

R. B. Vasiliev, D. N. Dirin, M. S. Sokolikova, V. V. Roddatis, A. L. Vasiliev, Al. G. Vitukhnovsky and A. M. Gaskov, Facet-selective growth and optical properties of CdTe/CdSe tetrapod-shaped nanocrystal heterostructures, *Journal of Materials Research* **26** (2011), 1621–1626.

D. N. Dirin, R. B. Vasiliev, M. S. Sokolikova, A. M. Gaskov, Synthesis, morphology, and optical properties of colloidal CdTe/CdSe and CdTe/CdS nanoheterostructures based on CdTe tetrapods, *Inorganic Materials* **47** (2011), 23-28.

R. B. Vasiliev, D. N. Dirin, M. S. Sokolikova, S. G. Dorofeev, A. G. Vitukhnovsky, A. M. Gaskov, Growth of near-IR luminescent colloidal CdTe/CdS nanoheterostructures based on CdTe tetrapods, *Mendeleev Communications* **19** (2009), 128-130.

A6. Permissions to reuse content

Page No	Figure in Thesis	Type of work	Source of work	Copyright holder	Permission to reuse
26	1.2.b	figure	Journal of Alloys and Compounds, 722, 25, 499-508 (2017); Figure 5	© 2017 Elsevier	granted
29	1.3.a	figure	Journal of Physics C: Solid State Physics, 5, 7, 759-778 (1972); Figure 5	© 1972 IOP	granted
29	1.3.b	figure	Nano Letters, 10, 4, 1271-1275 (2010); Figure 4	© 2010 American Chemical Society	granted
29	1.3.c	figure	Physical Review Letters, 108, 19, 196802 (2012); Figure 1	© 2012 American Physical Society	granted
31	1.4.a-c	figure	Science Advances, 3, 5, e1602680 (2017); Figure 1	© 2017 AAAS	granted
31	1.4.d	figure	Nature Physics, 5, 6, 438-442 (2009); Figure 4	© 2009 Springer Nature	granted
31	1.4.e	figure	Physical Review Letters, 117, 14, 146403 (2016); Figure 1	© 2016 American Physical Society	granted
35	1.5.a	figure	Advanced Materials, 28, 29, 6197-6206 (2016); Figure 1	© 2016 John Wiley and Sons	granted
35	1.5.c-f	figure	Surface Science, 640, 133140 (2015) Figures 3,5	© 2015 Elsevier	granted
53	2.2	figure	Nature, 437, 664–670 (2005); Figure 2	© 2004 Springer Nature	granted
92	2.17	figure	Surface Science Reports, 66, 1, 1-27 (2011); Figure 3	© 2011 Elsevier	granted
97	2.19.c,d	figure	ACS Catalysis. 4, 11, 3957-3971 (2014); Figure 4	© 2014 American Chemical Society	granted

License Details

This Agreement between Imperial College London -- Maria Sokolikova ("You") and Elsevier ("Elsevier") consists of your license details and the terms and conditions provided by Elsevier and Copyright Clearance Center.

Print Copy

License Number	4638810714490
License date	Jul 30, 2019
Licensed Content Publisher	Elsevier
Licensed Content Publication	Journal of Alloys and Compounds
Licensed Content Title	Bi-In-Te phase diagram
Licensed Content Author	Sinn-wen Chen,Shi-ting Lu,Jui-shen Chang
Licensed Content Date	Oct 25, 2017
Licensed Content Volume	722
Licensed Content Issue	n/a
Licensed Content Pages	10
Type of Use	reuse in a thesis/dissertation
Portion	figures/tables/illustrations
Number of figures/tables/illustrations	1
Format	both print and electronic
Are you the author of this Elsevier article?	No
Will you be translating?	No
Original figure numbers	Figure 5
Title of your thesis/dissertation	Colloidal atomically-thin inorganic nanoflowers for electrocatalytic hydrogen evolution
Expected completion date	Jul 2019
Estimated size (number of pages)	230
Requestor Location	Imperial College London Exhibition Road London, SW7 2AZ United Kingdom Attn: Imperial College London
Publisher Tax ID	GB 494 6272 12
Total	**0.00 GBP**

BACK

Copyright © 2019 Copyright Clearance Center, Inc. All Rights Reserved. Privacy statement . Terms and Conditions . Comments? We would like to hear from you. E-mail us at customercare@copyright.com

Sokolikova, Maria

From: Permissions <permissions@ioppublishing.org>
Sent: 31 July 2019 12:30
To: Sokolikova, Maria
Subject: Re: Permission request

Dear Maria Sokolikova,

Thank you for your request to reproduce IOP Publishing material ***in "Colloidal atomically-thin inorganic nanoflowers for electrocatalytic hydrogen evolution" to be published in your PhD thesis***

Regarding:
Figure 5 - https://iopscience.iop.org/article/10.1088/0022-3719/5/7/007

We are happy to grant permission for the use you request on the terms set out below.

License to publish material published by IOP Publishing

Please provide the below to your new publisher as proof of permission.

Conditions

Non-exclusive, non-transferrable, revocable, worldwide, permission to use the material in print and electronic form will be granted **subject to the following conditions:**

- Permission will be cancelled without notice if you fail to fulfil any of the conditions of this letter.
- You will make reasonable efforts to contact the author(s) to seek consent for your intended use. Contacting one author acting expressly as authorised agent for their co-authors is acceptable.
- You will reproduce the following prominently alongside the material:
    - the source of the material, including author, article title, title of journal, volume number, issue number (if relevant), page range (or first page if this is the only information available) and date of first publication. This information can be contained in a footnote or reference note; or
    - a link back to the article (via DOI); and
    - if practical and IN ALL CASES for works published under any of the Creative Commons licences the words "© IOP Publishing. Reproduced with permission. All rights reserved""
- The material will not, without the express permission of the author(s), be used in any way which, in the opinion of IOP Publishing, could distort or alter the author(s)' original intention(s) and meaning, be prejudicial to the honour or reputation of the author(s) and/or imply endorsement by the author(s) and/or IOP Publishing.
- Payment of £0 is received in full by IOP Publishing prior to use.

This permission does not apply to any material/figure which is credited to another source in our publication or has been obtained from a third party. Express permission for such materials/figures must be obtained from the copyright owner.

Special Conditions – For STM Signatories ONLY (as agreed as part of the STM Guidelines)

Any permissions granted for a particular edition will apply also to subsequent editions and for editions in other languages, provided such editions are for the work as a whole in situ and does not involve the separate exploitation of the permitted illustrations or excerpts.

Kind regards,

Christina

Copyright & Permissions Team
Gemma Alaway – Senior Rights & Permissions Adviser
Christina Colwell - Rights & Permissions Assistant

Contact Details
E-mail: permissions@iop.org
For further information about copyright and how to request permission:
https://publishingsupport.iopscience.iop.org/copyright-journals/
See also: https://publishingsupport.iopscience.iop.org/
Please see our Author Rights Policy https://publishingsupport.iopscience.iop.org/author-rights-policies/
Please note: We do not provide signed permission forms as a separate attachment. Please print this email and provide it to your publisher as proof of permission.

Please note: Any statements made by IOP Publishing to the effect that authors do not need to get permission to use any content where IOP Publishing is not the publisher is not intended to constitute any sort of legal advice. Authors must make their own decisions as to the suitability of the content they are using and whether they require permission for it to be published within their article.

From: Sokolikova, Maria <m.sokolikova15@imperial.ac.uk>
Sent: 30 July 2019 16:31
To: permissions@iop.org <permissions@iop.org>
Subject: Permission request

Dear Sir/Madam,

I would like to request a permission to reproduce a figure published in Journal of Physics C: Solid State Physics in my dissertation. I would be very grateful if you could help me to obtain the permission.

My details are:
1. Maria Sokolikova, Imperial College London
2. Imperial College London, Exhibition Road, London SW7 2AZ, +447596448576

The content I wish to use:

1. Journal of Physics C: Solid State Physics
2. The band structures of some transition metal dichalcogenides. III. Group VIA: trigonal prism materials
3. R.A. Bromley, R.B. Murray and A.D. Yoffe
4. Volume 5, number 7, 759-778, 1972; doi 10.1088/0022-3719/5/7/007
5. Figure 5

The intended use:

1. PhD thesis/dissertation
2. Dissertation title: Colloidal atomically-thin inorganic nanoflowers for electrocatalytic hydrogen evolution
3. Author: Maria Sokolikova
4. My format: both print and electronic
5. Intended use: Reproducing a figure form an original paper

Kind regards,
Maria

IOP Publishing email addresses have changed from @iop.org to @ioppublishing.org, except those of our legal and finance teams, which have changed to @ioplegal.org and @iopfinance.org respectively.

This email (and attachments) are confidential and intended for the addressee(s) only. If you are not the intended recipient please immediately notify the sender, permanently and securely delete any copies and do not take action with it or in reliance on it. Any views expressed are the author's and do not represent those of IOPP, except where specifically stated. IOPP takes reasonable precautions to protect against viruses but accepts no responsibility for loss or damage arising from virus infection. For the protection of IOPP's systems and staff; emails are scanned automatically.

IOP Publishing Limited
Registered in England under Registration No 00467514.
Registered Office: Temple Circus, Bristol BS1 6HG England
Your privacy is important to us. For information about how IOPP uses your personal data, please see our Privacy Policy

Copyright Clearance Center RightsLink®

Home | Account Info | Help | LIVE CHAT

ACS Publications
Most Trusted. Most Cited. Most Read.

Title: Emerging Photoluminescence in Monolayer MoS2

Author: Andrea Splendiani, Liang Sun, Yuanbo Zhang, et al

Publication: Nano Letters

Publisher: American Chemical Society

Date: Apr 1, 2010

Copyright © 2010, American Chemical Society

Logged in as:
Maria Sokolikova
Imperial College London
Account #:
3001493046

LOGOUT

PERMISSION/LICENSE IS GRANTED FOR YOUR ORDER AT NO CHARGE

This type of permission/license, instead of the standard Terms & Conditions, is sent to you because no fee is being charged for your order. Please note the following:

- Permission is granted for your request in both print and electronic formats, and translations.
- If figures and/or tables were requested, they may be adapted or used in part.
- Please print this page for your records and send a copy of it to your publisher/graduate school.
- Appropriate credit for the requested material should be given as follows: "Reprinted (adapted) with permission from (COMPLETE REFERENCE CITATION). Copyright (YEAR) American Chemical Society." Insert appropriate information in place of the capitalized words.
- One-time permission is granted only for the use specified in your request. No additional uses are granted (such as derivative works or other editions). For any other uses, please submit a new request.

If credit is given to another source for the material you requested, permission must be obtained from that source.

BACK | CLOSE WINDOW

Copyright © 2019 Copyright Clearance Center, Inc. All Rights Reserved. Privacy statement. Terms and Conditions.
Comments? We would like to hear from you. E-mail us at customercare@copyright.com

American Physical Society
Reuse and Permissions License

30-Jul-2019

This license agreement between the American Physical Society ("APS") and Maria Sokolikova ("You") consists of your license details and the terms and conditions provided by the American Physical Society and SciPris.

Licensed Content Information

License Number:	**RNP/19/JUL/017195**
License date:	30-Jul-2019
DOI:	10.1103/PhysRevLett.108.196802
Title:	Coupled Spin and Valley Physics in Monolayers of ${\mathrm{MoS}}_{2}$ and Other Group-VI Dichalcogenides
Author:	Di Xiao et al.
Publication:	Physical Review Letters
Publisher:	American Physical Society
Cost:	USD $ 0.00

Request Details

Does your reuse require significant modifications: No

Specify intended distribution locations:	Worldwide
Reuse Category:	Reuse in a thesis/dissertation
Requestor Type:	Student
Items for Reuse:	Figures/Tables
Number of Figure/Tables:	1
Figure/Tables Details:	Figure 1
Format for Reuse:	Print and Electronic
Total number of print copies:	Up to 1000

Information about New Publication:

University/Publisher:	Imperial College London
Title of dissertation/thesis:	Colloidal atomically-thin inorganic nanoflowers for electrocatalytic hydrogen evolution
Author(s):	Maria Sokolikova
Expected completion date:	Jul. 2019

License Requestor Information

Name:	Maria Sokolikova
Affiliation:	Individual
Email Id:	m.sokolikova15@imperial.ac.uk
Country:	United Kingdom

American Physical Society
Reuse and Permissions License

TERMS AND CONDITIONS

The American Physical Society (APS) is pleased to grant the Requestor of this license a non-exclusive, non-transferable permission, limited to Print and Electronic format, provided all criteria outlined below are followed.

1. You must also obtain permission from at least one of the lead authors for each separate work, if you haven't done so already. The author's name and affiliation can be found on the first page of the published Article.
2. For electronic format permissions, Requestor agrees to provide a hyperlink from the reprinted APS material using the source material's DOI on the web page where the work appears. The hyperlink should use the standard DOI resolution URL, http://dx.doi.org/{DOI}. The hyperlink may be embedded in the copyright credit line.
3. For print format permissions, Requestor agrees to print the required copyright credit line on the first page where the material appears: "Reprinted (abstract/excerpt/figure) with permission from [(FULL REFERENCE CITATION) as follows: Author's Names, APS Journal Title, Volume Number, Page Number and Year of Publication.] Copyright (YEAR) by the American Physical Society."
4. Permission granted in this license is for a one-time use and does not include permission for any future editions, updates, databases, formats or other matters. Permission must be sought for any additional use.
5. Use of the material does not and must not imply any endorsement by APS.
6. APS does not imply, purport or intend to grant permission to reuse materials to which it does not hold copyright. It is the requestor's sole responsibility to ensure the licensed material is original to APS and does not contain the copyright of another entity, and that the copyright notice of the figure, photograph, cover or table does not indicate it was reprinted by APS with permission from another source.
7. The permission granted herein is personal to the Requestor for the use specified and is not transferable or assignable without express written permission of APS. This license may not be amended except in writing by APS.
8. You may not alter, edit or modify the material in any manner.
9. You may translate the materials only when translation rights have been granted.
10. APS is not responsible for any errors or omissions due to translation.
11. You may not use the material for promotional, sales, advertising or marketing purposes.
12. The foregoing license shall not take effect unless and until APS or its agent, Aptara, receives payment in full in accordance with Aptara Billing and Payment Terms and Conditions, which are incorporated herein by reference.
13. Should the terms of this license be violated at any time, APS or Aptara may revoke the license with no refund to you and seek relief to the fullest extent of the laws of the USA. Official written notice will be made using the contact information provided with the permission request. Failure to receive such notice will not nullify revocation of the permission.
14. APS reserves all rights not specifically granted herein.
15. This document, including the Aptara Billing and Payment Terms and Conditions, shall be the entire agreement between the parties relating to the subject matter hereof.

Sokolikova, Maria

From: permissions <permissions@aaas.org>
Sent: 13 September 2019 16:13
To: Sokolikova, Maria
Subject: PERMISSION REQUEST - SCI ADVANCES - THESIS USE

Dear Maria:

Thanks very much for getting in touch and for your interest in the material. I apologize for the delay, we have a high volume of requests and it is taking me longer to respond.

If you can still use the material, this article is published under a Creative Commons Attribution license (CC BY), which means, after it is published in Science Advances, anyone may use, distribute, and reproduce it (the full-text published version and/or figures), in any medium under the terms outlined here (https://creativecommons.org/licenses/by/4.0/). I've also summarized the terms below:

To reuse, one must:

1. Credit the author and credit the original Science Advances article.

Appropriate credit lines follow this format: "From/or modified from [INSERT Science Advances REFERENCE CITATION]. © The Authors, some rights reserved; exclusive licensee American Association for the Advancement of Science. Distributed under a Creative Commons Attribution License 4.0 (CC BY) https://creativecommons.org/licenses/by/4.0/.

2. If any modifications are made to the material, those changes must be identified.

3. Use of the material must not imply any endorsement by the authors or by AAAS and Science Advances.

4. No legal terms or technological measures may be applied to the reproduced material that conflicts with CC BY license terms.

Please note: Portions, images, or figures appearing in the original Science Advances article that are attributed to other publishers or individuals are not subject to the article's Creative Commons license. Permission from the credited party should be sought prior to reproduction of such material.

If you have any questions please just let me know.

Kind regards,

Liz
***
Ms. Elizabeth Sandler
Rights & Permissions, Science family of journals
American Association for the Advancement of Science (AAAS)
1200 New York Ave. NW
Washington DC 20005
Tel: 1-202-326-6765

From: Sokolikova, Maria <m.sokolikova15@imperial.ac.uk>
Sent: Tuesday, July 30, 2019 11:24 AM
To: permissions <permissions@aaas.org>
Subject: Requesting permission to reuse

Dear Sir/Madam,

I would like to request a permission to reproduce a figure published in Science Advances in my dissertation.
I would be very grateful if you could help me to obtain the permission.

My details are:

1. Maria Sokolikova, Imperial College London
2. Imperial College London, Exhibition Road, London SW7 2AZ, +447596448576

The content I wish to use:

1. *Science Advances*
2. Emergence of topological semimetals in gap closing in semiconductors without inversion symmetry
3. Shuichi Murakami, Motoaki Hirayama, Ryo Okugawa and Takashi Miyake
4. 3, 5, e1602680
5. Figure 1

The intended use:

1. PhD thesis/dissertation
2. Colloidal atomically-thin inorganic nanoflowers for electrocatalytic hydrogen evolution
3. Maria Sokolikova
4. print and electronic
5. Reproducing a figure form an original paper

Kind regards,
Maria

License Details

This Agreement between Imperial College London -- Maria Sokolikova ("You") and Springer Nature ("Springer Nature") consists of your license details and the terms and conditions provided by Springer Nature and Copyright Clearance Center.

Print Copy

License Number	4638811491096
License date	Jul 30, 2019
Licensed Content Publisher	Springer Nature
Licensed Content Publication	Nature Physics
Licensed Content Title	Topological insulators in Bi2Se3, Bi2Te3 and Sb2Te3 with a single Dirac cone on the surface
Licensed Content Author	Haijun Zhang, Chao-Xing Liu, Xiao-Liang Qi, Xi Dai, Zhong Fang et al.
Licensed Content Date	May 10, 2009
Licensed Content Volume	5
Licensed Content Issue	6
Type of Use	Thesis/Dissertation
Requestor type	academic/university or research institute
Format	print and electronic
Portion	figures/tables/illustrations
Number of figures/tables/illustrations	1
High-res required	no
Will you be translating?	no
Circulation/distribution	<501
Author of this Springer Nature content	no
Title	Colloidal atomically-thin inorganic nanoflowers for electrocatalytic hydrogen evolution
Institution name	n/a
Expected presentation date	Jul 2019
Portions	Figure 4
Requestor Location	Imperial College London Exhibition Road London, SW7 2AZ United Kingdom Attn: Imperial College London
Total	**0.00 GBP**

BACK

Copyright © 2019 Copyright Clearance Center, Inc. All Rights Reserved. Privacy statement . Terms and Conditions . Comments? We would like to hear from you. E-mail us at customercare@copyright.com

American Physical Society
Reuse and Permissions License

30-Jul-2019

This license agreement between the American Physical Society ("APS") and Maria Sokolikova ("You") consists of your license details and the terms and conditions provided by the American Physical Society and SciPris.

Licensed Content Information

License Number:	**RNP/19/JUL/017197**
License date:	30-Jul-2019
DOI:	10.1103/PhysRevLett.117.146403
Title:	Strong Intrinsic Spin Hall Effect in the TaAs Family of Weyl Semimetals
Author:	Yan Sun et al.
Publication:	Physical Review Letters
Publisher:	American Physical Society
Cost:	USD $ 0.00

Request Details

Does your reuse require significant modifications: No

Specify intended distribution locations:	Worldwide
Reuse Category:	Reuse in a thesis/dissertation
Requestor Type:	Student
Items for Reuse:	Figures/Tables
Number of Figure/Tables:	1
Figure/Tables Details:	Figure 1
Format for Reuse:	Print and Electronic
Total number of print copies:	Up to 1000

Information about New Publication:

University/Publisher:	Imperial College London
Title of dissertation/thesis:	Colloidal atomically-thin inorganic nanoflowers for electrocatalytic hydrogen evolution
Author(s):	Maria Sokolikova
Expected completion date:	Jul. 2019

License Requestor Information

Name:	Maria Sokolikova
Affiliation:	Individual
Email Id:	m.sokolikova15@imperial.ac.uk
Country:	United Kingdom

American Physical Society
Reuse and Permissions License

TERMS AND CONDITIONS

The American Physical Society (APS) is pleased to grant the Requestor of this license a non-exclusive, non-transferable permission, limited to Print and Electronic format, provided all criteria outlined below are followed.

1. You must also obtain permission from at least one of the lead authors for each separate work, if you haven't done so already. The author's name and affiliation can be found on the first page of the published Article.
2. For electronic format permissions, Requestor agrees to provide a hyperlink from the reprinted APS material using the source material's DOI on the web page where the work appears. The hyperlink should use the standard DOI resolution URL, http://dx.doi.org/{DOI}. The hyperlink may be embedded in the copyright credit line.
3. For print format permissions, Requestor agrees to print the required copyright credit line on the first page where the material appears: "Reprinted (abstract/excerpt/figure) with permission from [(FULL REFERENCE CITATION) as follows: Author's Names, APS Journal Title, Volume Number, Page Number and Year of Publication.] Copyright (YEAR) by the American Physical Society."
4. Permission granted in this license is for a one-time use and does not include permission for any future editions, updates, databases, formats or other matters. Permission must be sought for any additional use.
5. Use of the material does not and must not imply any endorsement by APS.
6. APS does not imply, purport or intend to grant permission to reuse materials to which it does not hold copyright. It is the requestor's sole responsibility to ensure the licensed material is original to APS and does not contain the copyright of another entity, and that the copyright notice of the figure, photograph, cover or table does not indicate it was reprinted by APS with permission from another source.
7. The permission granted herein is personal to the Requestor for the use specified and is not transferable or assignable without express written permission of APS. This license may not be amended except in writing by APS.
8. You may not alter, edit or modify the material in any manner.
9. You may translate the materials only when translation rights have been granted.
10. APS is not responsible for any errors or omissions due to translation.
11. You may not use the material for promotional, sales, advertising or marketing purposes.
12. The foregoing license shall not take effect unless and until APS or its agent, Aptara, receives payment in full in accordance with Aptara Billing and Payment Terms and Conditions, which are incorporated herein by reference.
13. Should the terms of this license be violated at any time, APS or Aptara may revoke the license with no refund to you and seek relief to the fullest extent of the laws of the USA. Official written notice will be made using the contact information provided with the permission request. Failure to receive such notice will not nullify revocation of the permission.
14. APS reserves all rights not specifically granted herein.
15. This document, including the Aptara Billing and Payment Terms and Conditions, shall be the entire agreement between the parties relating to the subject matter hereof.

License Details

This Agreement between Imperial College London -- Maria Sokolikova ("You") and John Wiley and Sons ("John Wiley and Sons") consists of your license details and the terms and conditions provided by John Wiley and Sons and Copyright Clearance Center.

Print Copy

License Number	4638820356986
License date	Jul 30, 2019
Licensed Content Publisher	John Wiley and Sons
Licensed Content Publication	Advanced Materials
Licensed Content Title	Recent Strategies for Improving the Catalytic Activity of 2D TMD Nanosheets Toward the Hydrogen Evolution Reaction
Licensed Content Author	Damien Voiry, Jieun Yang, Manish Chhowalla
Licensed Content Date	Feb 12, 2016
Licensed Content Volume	28
Licensed Content Issue	29
Licensed Content Pages	10
Type of Use	Dissertation/Thesis
Requestor type	University/Academic
Format	Print and electronic
Portion	Figure/table
Number of figures/tables	1
Original Wiley figure/table number(s)	Figure 1
Will you be translating?	No
Title of your thesis / dissertation	Colloidal atomically-thin inorganic nanoflowers for electrocatalytic hydrogen evolution
Expected completion date	Jul 2019
Expected size (number of pages)	230
Requestor Location	Imperial College London Exhibition Road London, SW7 2AZ United Kingdom Attn: Imperial College London
Publisher Tax ID	EU826007151
Total	**0.00 GBP**

BACK

Copyright © 2019 Copyright Clearance Center, Inc. All Rights Reserved. Privacy statement . Terms and Conditions . Comments? We would like to hear from you. E-mail us at customercare@copyright.com

License Details

This Agreement between Imperial College London -- Maria Sokolikova ("You") and Elsevier ("Elsevier") consists of your license details and the terms and conditions provided by Elsevier and Copyright Clearance Center.

Print Copy

License Number	4638820558969
License date	Jul 30, 2019
Licensed Content Publisher	Elsevier
Licensed Content Publication	Surface Science
Licensed Content Title	Theoretical insights into the hydrogen evolution activity of layered transition metal dichalcogenides
Licensed Content Author	Charlie Tsai,Karen Chan,Jens K. Nørskov,Frank Abild-Pedersen
Licensed Content Date	Oct 1, 2015
Licensed Content Volume	640
Licensed Content Issue	n/a
Licensed Content Pages	8
Type of Use	reuse in a thesis/dissertation
Portion	figures/tables/illustrations
Number of figures/tables/illustrations	2
Format	both print and electronic
Are you the author of this Elsevier article?	No
Will you be translating?	No
Original figure numbers	Figures 3, 5
Title of your thesis/dissertation	Colloidal atomically-thin inorganic nanoflowers for electrocatalytic hydrogen evolution
Expected completion date	Jul 2019
Estimated size (number of pages)	230
Requestor Location	Imperial College London Exhibition Road London, SW7 2AZ United Kingdom Attn: Imperial College London
Publisher Tax ID	GB 494 6272 12
Total	**0.00 GBP**

BACK

Copyright © 2019 Copyright Clearance Center, Inc. All Rights Reserved. Privacy statement . Terms and Conditions . Comments? We would like to hear from you. E-mail us at customercare@copyright.com

License Details

This Agreement between Imperial College London -- Maria Sokolikova ("You") and Springer Nature ("Springer Nature") consists of your license details and the terms and conditions provided by Springer Nature and Copyright Clearance Center.

Print Copy

License Number	4638820697056
License date	Jul 30, 2019
Licensed Content Publisher	Springer Nature
Licensed Content Publication	Nature
Licensed Content Title	Colloidal nanocrystal synthesis and the organic–inorganic interface
Licensed Content Author	Yadong Yin et al
Licensed Content Date	Sep 28, 2004
Type of Use	Thesis/Dissertation
Requestor type	academic/university or research institute
Format	print and electronic
Portion	figures/tables/illustrations
Number of figures/tables/illustrations	1
High-res required	no
Will you be translating?	no
Circulation/distribution	<501
Author of this Springer Nature content	no
Title	Colloidal atomically-thin inorganic nanoflowers for electrocatalytic hydrogen evolution
Institution name	n/a
Expected presentation date	Jul 2019
Portions	Figure 2
Requestor Location	Imperial College London Exhibition Road London, SW7 2AZ United Kingdom Attn: Imperial College London
Total	**0.00 GBP**

BACK

Copyright © 2019 Copyright Clearance Center, Inc. All Rights Reserved. Privacy statement . Terms and Conditions . Comments? We would like to hear from you. E-mail us at customercare@copyright.com

License Details

This Agreement between Imperial College London -- Maria Sokolikova ("You") and Elsevier ("Elsevier") consists of your license details and the terms and conditions provided by Elsevier and Copyright Clearance Center.

Print Copy

License Number	4638820988275
License date	Jul 30, 2019
Licensed Content Publisher	Elsevier
Licensed Content Publication	Surface Science Reports
Licensed Content Title	Kelvin probe force microscopy and its application
Licensed Content Author	Wilhelm Melitz,Jian Shen,Andrew C. Kummel,Sangyeob Lee
Licensed Content Date	Jan 1, 2011
Licensed Content Volume	66
Licensed Content Issue	1
Licensed Content Pages	27
Type of Use	reuse in a thesis/dissertation
Portion	figures/tables/illustrations
Number of figures/tables/illustrations	1
Format	both print and electronic
Are you the author of this Elsevier article?	No
Will you be translating?	No
Original figure numbers	Figure 3
Title of your thesis/dissertation	Colloidal atomically-thin inorganic nanoflowers for electrocatalytic hydrogen evolution
Expected completion date	Jul 2019
Estimated size (number of pages)	230
Requestor Location	Imperial College London Exhibition Road London, SW7 2AZ United Kingdom Attn: Imperial College London
Publisher Tax ID	GB 494 6272 12
Total	**0.00 GBP**

BACK

Copyright © 2019 Copyright Clearance Center, Inc. All Rights Reserved. Privacy statement . Terms and Conditions . Comments? We would like to hear from you. E-mail us at customercare@copyright.com

Copyright Clearance Center RightsLink®

Home | Account Info | Help | LIVE CHAT

ACS Publications Most Trusted. Most Cited. Most Read.

Title: Catalyzing the Hydrogen Evolution Reaction (HER) with Molybdenum Sulfide Nanomaterials

Author: Jesse D. Benck, Thomas R. Hellstern, Jakob Kibsgaard, et al

Publication: ACS Catalysis

Publisher: American Chemical Society

Date: Nov 1, 2014

Copyright © 2014, American Chemical Society

Logged in as:
Maria Sokolikova
Imperial College London
Account #:
3001493046

LOGOUT

PERMISSION/LICENSE IS GRANTED FOR YOUR ORDER AT NO CHARGE

This type of permission/license, instead of the standard Terms & Conditions, is sent to you because no fee is being charged for your order. Please note the following:

- Permission is granted for your request in both print and electronic formats, and translations.
- If figures and/or tables were requested, they may be adapted or used in part.
- Please print this page for your records and send a copy of it to your publisher/graduate school.
- Appropriate credit for the requested material should be given as follows: "Reprinted (adapted) with permission from (COMPLETE REFERENCE CITATION). Copyright (YEAR) American Chemical Society." Insert appropriate information in place of the capitalized words.
- One-time permission is granted only for the use specified in your request. No additional uses are granted (such as derivative works or other editions). For any other uses, please submit a new request.

If credit is given to another source for the material you requested, permission must be obtained from that source.

BACK | CLOSE WINDOW

Copyright © 2019 Copyright Clearance Center, Inc. All Rights Reserved. Privacy statement. Terms and Conditions.
Comments? We would like to hear from you. E-mail us at customercare@copyright.com